Ultrafast Exciton Dynamics of Lead Halide Perovskite Nanocrystals for Light Harvesting

THESIS SUBMITTED FOR THE DEGREE OF
DOCTOR OF PHILOSOPHY (SCIENCE)

OF

JADAVPUR UNIVERSITY

February 2022

BY

Goutam Ghosh

SCHOOL OF MATERIALS SCIENCES

INDIAN ASSOCIATION FOR THE CULTIVATION OF SCIENCE

2A & 2B RAJA S. C. MULLICK ROAD, JADAVPUR

KOLKATA – 700 032

INDIA

इण्डियन एसोसिएशन फॉर द कल्टीवेशन ऑफ़ साइंस
ইণ্ডিয়ান এ্যাসোসিয়েশন ফর দি কালটিভেশন অব সায়েন্স
INDIAN ASSOCIATION FOR THE CULTIVATION OF SCIENCE

CERTIFICATE FROM THE SUPERVISOR

This is to certify that the thesis entitled ***"Ultrafast Exciton Dynamics of Lead Halide Perovskite Nanocrystals for Light Harvesting"*** submitted by Mr. Goutam Ghosh who got his name registered on 25.09.2018 for the award of Ph.D. (Science) degree of Jadavpur University, is absolutely based on his own work under the supervision of Prof. Amitava Patra and that neither this thesis nor any part of it has been submitted for either any degree/ diploma or any other academic award anywhere before.

Amitava Patra
(Prof. Amitava Patra) 08.02.2022
Signature of Supervisor and
Date with Official Seal

Dr. Amitava Patra
Senior Professor
Department of Materials Science
Indian Association for the Cultivation of Science
Jadavpur, Kolkata - 700 032

२ए एण्ड बी, राजा एस. सी. मल्लिक रोड, जादवपुर, कोलकाता-700 032. 2A & B, RAJA S. C. MULLICK ROAD, JADAVPUR, KOLKATA - 700 032
दूरभाष / PHONE : 2473-4971, 3372 3073. फैक्स/FAX : (91) (33) 2473 2805

Dedicated to

my parents & family

Preface

Ubiquitous energy consumption is projected to invent unconventional power source by solar light harvesting. Semiconducting lead halide perovskite nanocrystals have been endowed as potential light harvesting materials due to their plentiful advantages like easy synthetic procedure, broad absorption with extraordinarily high molar extinction coefficient, long carrier diffusion length, higher carrier lifetime, extraordinary brightness, and colour tunability and so on. The designing strategy of efficient light harvesting system and the controlling on the photo generated exciton dynamics in perovskite nanocrystals are the most challenging task to reach optimum efficiency. In addition, hybrid nanomaterials composed of different inorganic and organic semiconducting materials (like CdSe, PbSe, porphyrin) can be employed to achieve high performance in photovoltaic based devices. In this context, the current thesis provides the basic construction and the understanding of the fundamental photophysics of semiconducting lead halide perovskite nanocrystals, worthwhile for versatile applications.

In the first place, I would like to express my profound gratitude and special appreciation to my advisor Professor Amitava Patra, who is an incredible mentor. I would like to thank him for his constant encouragement, guidance, stimulating discussions, and helpful suggestions throughout my doctoral studies. His advice on both researches as well as on my personal life is priceless. His punctuality and discipline are something which I wish to follow throughout my life. I am indebted to him for enlightening my global perspective of scientific and professional view.

Besides my advisor, I would like to thank the members of my research progress monitoring committee: Prof. Swapan Kumar Bhattacharya from Jadavpur University; Dr. Prashant Chandra Singh, School of Chemical Sciences for their insightful comments and encouragement. I gratefully acknowledge the insightful contribution of Prof. Abir De Sarkar, Institute of Nanoscience and Technology, Mohali and Prof. Swapan Kumar Pati, JNCASR, Bangalore during the scientific collaborations. My sincere thanks to Raihan Ahammed (INST) and Raju Kumar Sarkar (JNCASR) for their generous support and helping hand during the theoretical studies.

I take the opportunity to acknowledge my Institute, Indian Association for the Cultivation of Science for providing me suitable platform for my research work and also Council of Scientific & Industrial Research (CSIR) for awarding fellowship. I would like to

thank the Director of our Institute, Prof. Tapas Chakraborty for his kind help and encouragement in the research. I would like to thank all the faculty members of School of Materials science, IACS for their precious help, which I have received directly or indirectly. A special thank goes to Prof. Sreebrata Goswami, and Prof. Abhishek Dey of IACS for their instrumental support in my research work. I would also like to thank Rajib da and Abhijit for their help and support.

It is my great pleasure to thank Mr. Supriya Chakraborty, Mr. Suman Guchait, and Mr. Arunim Pal (TEM operator), Mr. Subrata Das (TCSPC operator), Dr. Manash Ghosh (Raman operator), Mr. Sutopesh and Dr. Bholanath Maity (XRD operator). I am thankful to the non-teaching staffs of the School of Materials Sciences namely, Mr. Subhasis Guha Roy and Mr. Mahadev Das and all the staffs of the workshop and administrations who are very generous to extend their helping hands. Special thanks to Mr. Gopal Krishna Manna for his assistance in graphic design.

I am also very grateful to my alma mater IIT Madras for the teaching me the lifetime lessons which I needed to finish this journey. Specially, I want to mention the monumental contribution in shaping my life by directing me through strict discipline and by building my "never give up" attitude. I am thankful to all my teachers of the Department of Chemistry, IIT Madras, where I completed my post-graduation. I would like to express my sincere gratitude to Prof. Ashok Kumar Mishra for his excellent encouragement and guidance during my master's project work. A special thanks to Dr. Avik Kumar Pati, Dr. Jitendriya Swain, Dr. Alok Tripathi, Dr. Vikram Singh, Dr. Madhumita Tarai, and Dr. Jhili Mishra for being amazing lab mates and sharing wonderful time during my M.Sc project. Without their precious support it would not be possible to get an early taste of whereabouts of a PhD work.

I am very much grateful to the all the captivating teachers I met during this academic journey. I want to thank the Department of Chemistry, Narasinha Dutt College for their excellent facilities and environment. Special thanks to Dr. Indranil Bhattacharya (the head of the chemistry department) and Dr. Suman Das (Jadavpur University) who always believed in me and provided their helping hand whenever I needed. I want to acknowledge my sincere gratitude to all the teachers of my secondary school (Jaynagar Pallisree Vidyaniketan) and higher secondary school (Jujursa P.N.Manna Institution), specially, Mr. Prabir Koley, Mr. Prafulla Roy and Mr. Ananda Dhara for giving the lessons of perseverance and hard work

since childhood. Without their constant support, help and encouragement I would not be able to reach here.

I also express my sincere thanks to all of my school friends (specially, Mainak, Lalu, Sajjan, Pratyay, Suraj, Joyrit, Mantu, Bubai, Sada, Sourav, Debarshi, Injamul, Palash), college friends (notably, Subhabrata, Satyabarata, Sukanya, Arindam, Tonojit), M.Sc. frineds (specially, Malay, Deepayan, Arpan, Chirantan, Dilip, Pradip, Milan, Arunabha, Asesh, Arup, Souvik, Swadhin, Ankush da), IACS friends for your love, support and constant encouragement in my professional and personal life from very early beginning. I would like to express my deepest appreciation to Rituparna for the constant support to accomplish my goals. I extend my sincere thanks to all my roommates (Malay, Dipayan and Apurba) for the glorious time that we spent together will be cherished forever. I have enjoyed the moment spend at IACS sporting events (specially, cricket and football matches) where a special bonding has been formed between seniors and juniors. Especially I should mention some names from this IACS family like Subir da, Debabrata da, Rafikul da, Nabhendu da, Anurag da, Suman da, Debasish da, Jayanta, Shubhankar, Sumitava, Raj, Manotosh, Mintu, Bikash and Sumanta. I cannot list all the names here, but you are always in my mind.

Word is not enough to express the influence of my parents and my family. It is the time to share my happiness with my parents and family. From my childhood days, my parents and my family have done lots of sacrifice for me. Word cannot express my gratitude to my mother Mrs. Ashima Ghosh, whose ambition, strength, and passion for excellence inspire me always in every moment of my life. She is always keen to know what I was doing and how I was proceeding, although it is likely that she has never grabbed what my work was all about! I want to express my heartiest feelings for my father, Mr. Uttam Ghosh. He has devoted his total life for making me a better human being. Without them I cannot reach the place. I would like to convey my deepest appreciation to my beloved younger sister Mamoni Ghosh for all the unconditional love, care and affection who always bring smile in my face even in the difficult times. Again, I specially want to express my gratitude towards my uncle Mr. Sukanta Ray who have always guided me towards a better direction and always watched my back. Thank you all for helping me to realize my hope and ambitions. I also offer my heartiest love to Bitku and Bitan.

Last but not the least, I would like to thank my all ex and present lab mates: Simanta da, Bipattaran da, Soma di, Susmita di, Piyali di, Monoj da, Rajesh da, Bikash da, Sumanta

da, Monojit da, Debarati di, Dipankar da, Bodhisatwa da, Arnab da, Subarna, Avisek, Srijon, Anusri, Kritiman, Sarita, Sikta, and Soubhik for their constant support and togetherness. It was an amazing experience of sharing workspace with all of them, since last five years. Again a special thanks to all my current lab members for proof reading this thesis.

Throughout the wonderful journey, I have come across innumerable generous, brilliant and caring people who impacted my life greatly. It's not my lone voyage; rather it would be impossible without all of my teachers, family, friends and well-wishers. Therefore, it is a great pleasure to conclude the roller-coaster ride by expressing my sincere gratitude to all of them. There must be a few more names which I may have missed out but my sincere thanks and regards remain for all. Thanks for all your encouragement!

Goutam Ghosh

(Goutam Ghosh)

08/02/2022

February 2022

School of Materials Sciences

Indian Association for the Cultivation of Science

Kolkata-700032

CONTENTS

Abstract

The thesis entitled ***"Ultrafast Exciton Dynamics of Lead Halide Perovskite Nanocrystals for Light Harvesting"*** discusses the synthesis and ultrafast carrier dynamics of lead halide perovskite nanocrystals (NCs) for improving artificial light harvesting. The basic understanding of (a) excited state carrier dynamics of lead halide perovskite (LHP) NCs with changing morphology; (b) hot hole transfer dynamics with porphyrin molecules; (c) slow hot carrier (HC) cooling dynamics; and (d) halide composition-dependent tunable electron transfer process with 2D CdSe nanoplatelets (NPLs) have been emphasized.

Chapter 1 illustrates the fundamental concepts and recent findings on different important aspects of lead halide perovskite NCs such as nature of excitons, diverse ultrafast photo-induced phenomenon, and hot carrier cooling mechanisms. Additionally, potential applications of these novel materials have been demonstrated.

Chapter 2 describes basic principle and theories of different spectroscopic and microscopic instruments.

Chapter 3 deals with the influence of different shapes on the carrier relaxation dynamics of $CsPbBr_3$ perovskite NCs using ultrafast transient absorption spectroscopy. The structural transformation of $CsPbBr_3$ NCs from cubic shape to rod shape occurs with changing the solvent from toluene to dichloromethane (DCM). Global and target analysis of TA spectra is being used to decipher the excited state photo-induced processes. We have found that the lifetime of the swallow trap (ST) changes from 25 ps to 45 ps, and the lifetime of the deep trap (DT) state changes from 163 ps to 303 ps with changing the shape of nanocrystals from cubic to rod. The analysis reveals that trap states play a critical role in the carrier relaxation dynamics of cubic and rod-shaped NCs. This work unveils that tuning the crystal phase, shape, and exciton dynamics of $CsPbBr_3$ NCs would be beneficial for designing efficient photovoltaic devices.

Chapter 4 describes the hot hole cooling and transfer dynamics of $CsPbBr_3$ nanocrystals with 5,10,15,20-Tetra(4pyridyl) porphyrin (TpyP) molecules, which can be helpful in the development of suitable hot carrier-based solar cell devices. A combination of density-functional theory (DFT) and femtosecond transient absorption spectroscopy uses to elucidate the mechanism underlying charge extraction and the HC transfer process in the $CsPbBr_3$-TpyP system. The initial hot carrier temperature (T_C) drops significantly from 1140 K to 638 K at 400 nm excitation due to the hot holes transfer from $CsPbBr_3$ NCs to TpyP molecules. It is dependent on the excitation energy, and the maximum transfer efficiency is

42% (for 0.85eV above band edge photo-excitation). Additionally, we have found that the hot hole transfer rate is almost 11 times faster than the band-edge hole transfer rate. The findings would be relevant for the development of next-generation perovskite-based optoelectronic devices.

Chapter 5 illustrates a strategy to retard the HC cooling via charge localization at the $CsPbBr_3$/PbSe heterostructure interface. The transient absorption measurements reveal two times slower HC relaxation time (from 770 fs to 1.4 ps) and much higher initial HC temperature, T_C (1663 K, compared to 900 K) for the heterostructure compared to the pure $CsPbBr_3$ at 3.64 eV excitation, under 1.86×10^{17} cm^{-3} carrier density. Furthermore, a combination of an electron-phonon coupling model and first-principles calculations suggest a retarded relaxation through the Klemens channel due to an appearance of a large energy gap between the longitudinal optical (LO) and longitudinal acoustic (LA) phonon modes. The localization of charge density near the heterojunction is responsible for the up-conversion of LO modes to the higher energy and retards the HC relaxation. The findings highlight a new protocol for achieving long-lived HCs in perovskites at low carrier densities, which would benefit the future of HC photovoltaics.

Chapter 6 outlines the design of nano-heterostructures using $CsPbX_3$ NCs (X = mixture of Br and I or I) and 2D CdSe nanoplatelets (NPls). We investigate the carrier relaxation processes of this heterostructure at different time scales by ultrafast transient absorption spectroscopy. Time-resolved fluorescence upconversion study suggests the composition-dependent electron transfer from CdSe NPLs to $CsPbX_3$. From the transient absorption spectroscopic study, the shortening of faster bleach recovery kinetics of CdSe NPLs and the enhancement of growth time of $CsPbX_3$ NCs in composites indicate the ultrafast electron transfer from CdSe NPLs to $CsPbX_3$ NCs. The ultrafast electron transfer from 2D CdSe NPLs to $CsPbX_3$ NCs enhances in following order: $CsPbI_3$> $CsPbBrI_2$> $CsPbBr_{1.5}I_{1.5}$. The high dark current and photocurrent are 0.04 μA and 62.4 μA in the CdSe-$CsPbI_3$ composite. The photocurrent generation is due to the efficient ultrafast electron transfer from CdSe NPLs to perovskite NCs. It indicates that the heterostructures of 2D CdSe NPLs with perovskite NCs would be useful for perovskite solar cells because of the efficient interfacial charge transfer process.

This thesis provides a detailed understanding of the carrier dynamics of lead-based halide perovskite nanomaterials for optoelectronics, photovoltaics, and other light-harvesting applications.

Chapter 1

Introduction

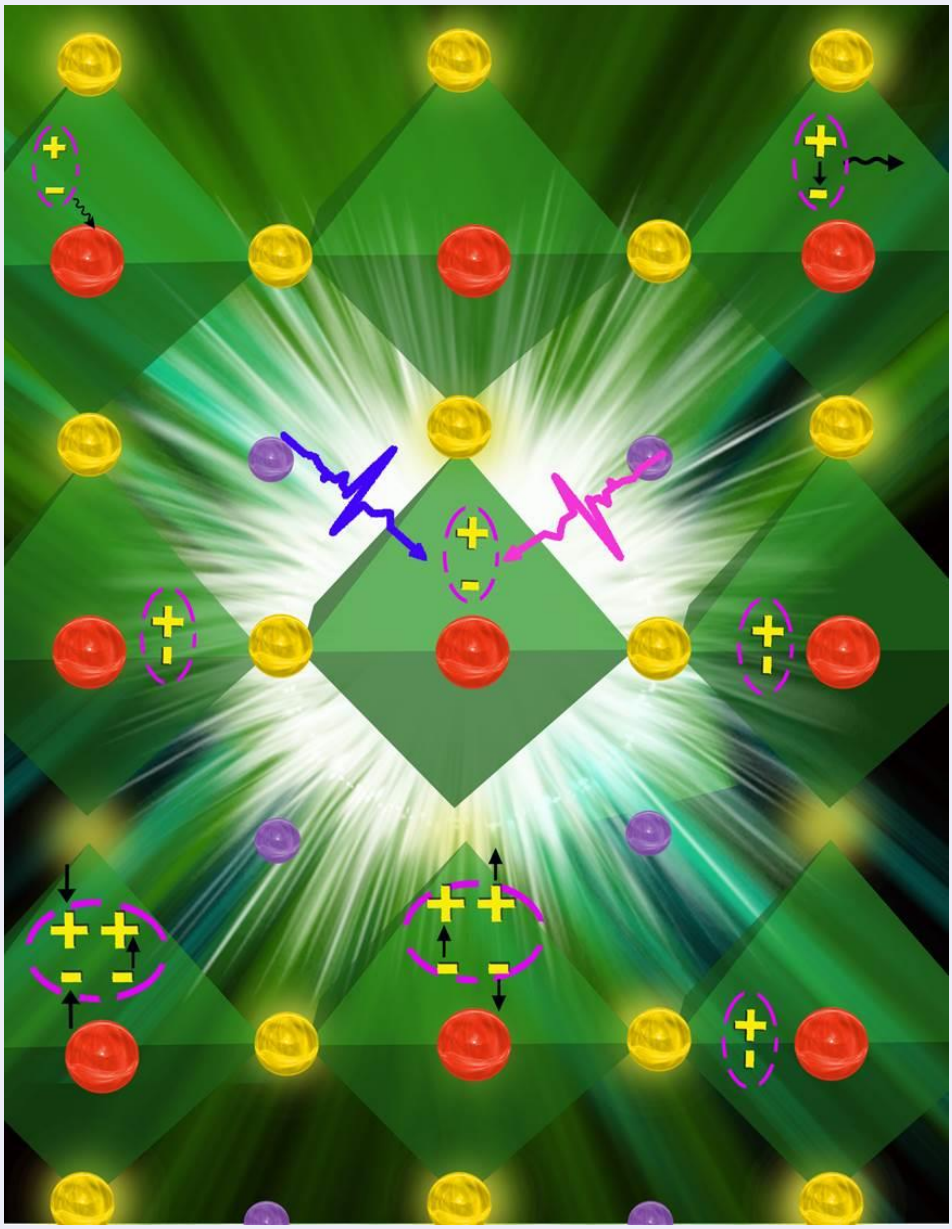

1.1.Overview of Nanomaterials

1.1.1. General concept of nanomaterials

A collection of atoms or molecules with a size range of 1-100 nanometres (nm) is commonly named nanomaterials. The specific word 'Nano' comes from the Greek word "Nanos" or Latin "Nanus," which designates 10^{-9} power, or one billionth. The comparison of nanoscale dimensionality is pictorially represented in Figure 1.1. Nanomaterials are essentially a bridge between bulk materials and atoms/molecules. In the nano dimension, materials gained new physical phenomena compared to bulk form.[1]

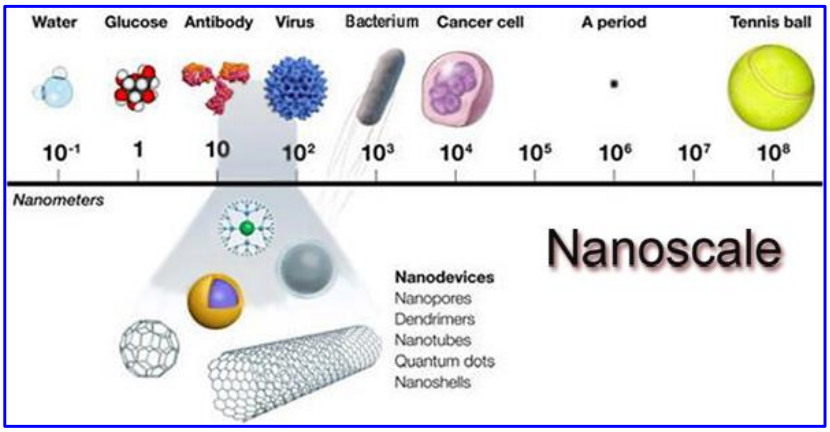

Figure 1.1. *Pictorial Comparison of other dimensions with nano dimension (image is taken from http://introtonanotechnology.weebly.com/uploads/2/5/1/5/25152204/8984028_orig.jpg)*

New physical properties of nanomaterials are arisen due to different types of interactions between atoms and molecules in the nano regime. The nanomaterials exhibit size and shape-dependent properties not shown in bulk materials. In brief, the origin of these properties correspond to two main aspects, i. e. a) surface effect and b) quantum effect. With gradually decreasing the dimension of the materials up to nanoscale, more and more surface atoms are exposed to interact, and therefore surface-related properties become prominent. Accordingly, new physical properties originate due to the spatial confinement of electrons in quantum wells of nanostructures and show efficient electrical, optical, and magnetic properties. There are two broad nanomaterials, i.e., (a) organic nanomaterials and (b) inorganic nanomaterials. Organic nanomaterials are aggregated polymers, porphyrins, and other π-conjugated molecules, and inorganic nanomaterials are semiconducting quantum dots and metal nanoparticles (NPs). To begin with, we briefly discuss organic and inorganic

semiconducting nanomaterials. The detailed structural, optical, and electronic properties of lead halide perovskite (LHP) NCs and their applications will be discussed in this chapter.

1.1.2. Organic semiconducting nanomaterials

The term 'organic semiconductor' is being used to study the photoconductivity of anthracene crystals (prototype of organic semiconductors) in the early 21st century. In 2020, Hegger and his group were awarded for "The discovery and development of conductive polymers," which opened up new areas of application for organic conducting materials. Generally, organic semiconductors can be classified as (a) low molecular weight compounds and (b) polymers. A conjugated system of π bonds formed by p-orbitals of carbon atoms of trigonal hybridisation is the common feature of both groups. In contrast to inorganic semiconductors, occupied and unoccupied molecular orbitals (MOs) in organic semiconductors are not closely packed. Among charge transfers in organic semiconductors, hole transport occurs in the highest occupied molecular orbital (HOMO), which is formed by overlapping molecular π-orbitals. Similarly, electron transport results from the overlap between anti-bonding π-orbitals (π*) and occurs in the lowest occupied molecular orbital (LUMO). The energy required to pump an electron from the HOMO to the LUMO is called the HOMO- LUMO, E_g, and is analogous to the valence-conduction band gap in an inorganic semiconductor (Figure 1.2).[2]

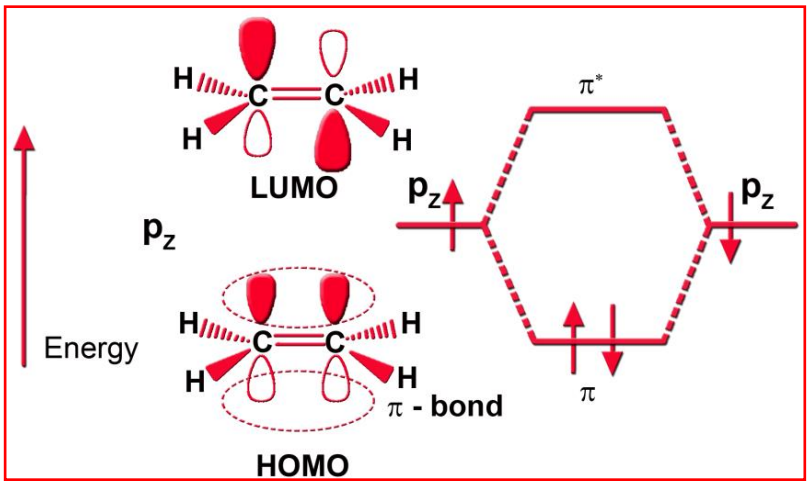

Figure 1.2. *π-bonding and π*antibonding molecular orbital by the constructive and destructive overlap of the two non-hybridized P_z orbital of conjugated system.*[3]

Absorption or emission occurs due to π- π* transition, which is controlled by the degree of conjugation of the individual systems in the macromolecule. The range of screening and

design possibilities for organic semiconductors provides an advantage over inorganic semiconductors. When conjugated molecules are bound into a solid, the overlap of their delocalized π-electron systems gives rise to conductivity.[4-6]

1.1.3. Inorganic semiconducting nanomaterials

The discovery of the quantum size effect in 1981 for inorganic semiconductor nanocrystals (NCs) and the resulting size-dependent optical properties instigated a new branch of research for materials scientists, chemists, and physicists.[7] In 1982, Prof. Louis Bruks envisages and has done the pivotal work on the colloidal semiconductor Quantum dots (QDs), which is marked as the actual birth of a nano science building block.[8-10] In the bulk form of the semiconductor material, the electronic energy levels are continuous, whereas discrete atomic like energy levels appear at the edges of the band due to the limited number of atoms in the QD (typically 100-10000), which is known as quantum confinement effect. QDs have broad absorption, narrow and symmetric emission spectra, slow excited-state decay rates, and broad absorption cross-sections due to the quantum confinement effects.[11-15] Bulk semiconductors are characterized by a composition-dependent band gap energy (E_g), which is the minimum energy required to excite an electron from the ground state valence band (VB) into the conduction band (CB) (Figure 1.3).

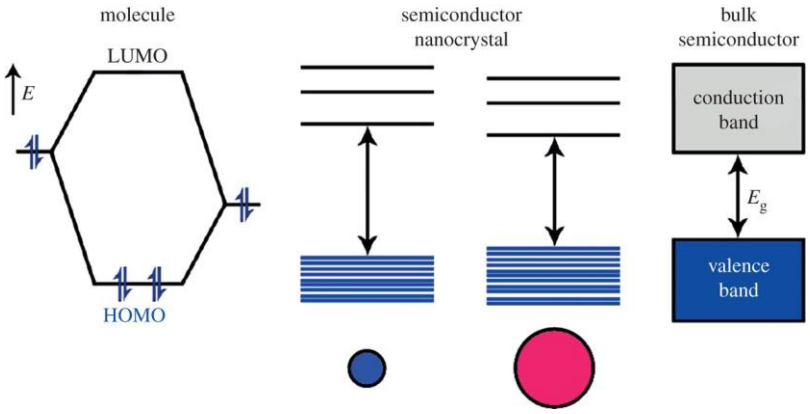

***Figure 1.3**. Schematic presentation of energy level diagram of the molecule, semiconductor nanocrystal, and bulk semiconductor (image taken from http://picshype.com/quantum-dots-band-gap/download-figure/6361)*

The average physical distance between the electron-hole pair is called the exciton Bohr radius, and this distance differs for the different types of semiconductor materials. In the semiconducting nanocrystals, the Bohr radius of the free exciton is determined by the spatial

extension of the wave functions of the conduction band electron and valence band hole. If the particle size becomes of the order of the exciton Bohr radius or smaller, these wave functions are confined by the nanocrystals' edges and the kinetic energy of the charge carriers (electron and hole) increases. This causes the observed shift of the absorption edge to higher energies as the particle size decreases. Equation (1) relates the band gap energy and particle size based on a "particle in a box" model.

$$E_g\,(\text{eff}) = E_g + \hbar^2\pi^2/2\mu R^2 - 1.8e^2/\varepsilon R \qquad (1)$$

The term $\hbar^2\pi^2/2\mu R^2$ is due to confinement effect and $1.8e^2/\varepsilon R$ is related to Coulombic term. E_g (eff) is the effective band gap energy, and E_g is bulk band gap energy, R is the particle radius, and μ = reduced mass $[1/m_e + 1/m_h]$. In addition to the size, the dimensionality of nanocrystals can also strongly influence the electronic spectrum of charge carriers and the optical properties of the nanocrystals. In 2008, Dubertret et al. discovered the first 2-D zinc blende (ZB) CdSe colloidal quantum wells, also widely known as nanoplatelets (NPLs).[16] Unlike bulk semiconductors, where the density of the states (DOS) increases continuously with energy due to continuous bands, the 2D quantum well (QW) confines the motions of electrons in the thickness direction, and carriers can movie in the other two directions (Figure 1.4).

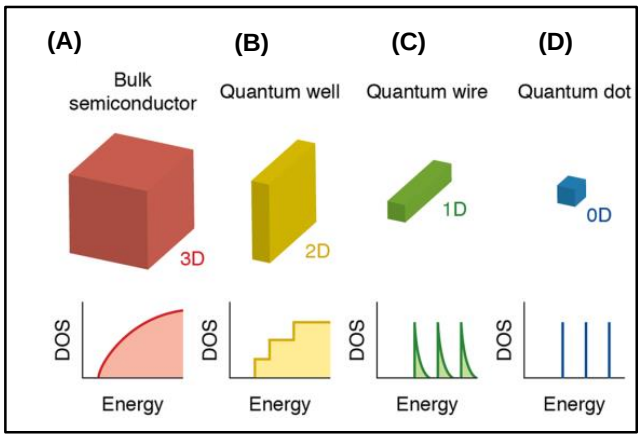

Figure 1.4. *Schematic illustration of the energy level structure of a bulk semiconductor and (semiconductor nanostructures with reduced dimensionality.[17] Reproduced with permission from reference 17 (Copyright 2016 Springer).*

Generally, it is observed that the absorption spectra are red-shifted with increasing thicknesses of the monolayers.[18] Splitting heavy hole (hh) and light hole (lh) excitonic transitions in CdSe NPLs is vital in quantum well structures. The photoluminescence (PL) of

these NPLs arises due to the recombination of an electron at the conduction band with the heavy hole band.

1.2. Lead halide perovskite (LHP) nanocrystals

Gustav Rose first proposed "perovskite" for the $CaTiO_3$ mineral. He named it after the Russian nobleman and mineralogist Count Lev Alekseyevich von Perovski in 1839.[19-20] Later, Victor Goldschmidt first used it as a general term for the crystal structure group in 1926. Over the last two decades, lead halide perovskites (LHP) have been identified as one of the most promising materials in photovoltaic and light-emitting devices, leading to significant breakthroughs in materials science.[19-22] Three dimensional (3D) LHP crystal lattice is defined as a network of corner-sharing BX_6 octahedra that crystallize with a general ABX_3 (or equivalent) stoichiometry, where A is monovalent cations (Cs^+/ FA^+/ MA^+), B is divalent cations (PB^{2+}) and X is monovalent anions (Cl^-, Br^-, I^- or their mixture).[23] Generally, LHP are classified into either organic-inorganic hybrid (OIH) or all-inorganic perovskites, depending on whether the A-site cation is organic or inorganic. Methyl ammonium (MA) or formadinium (FA) are used monovalent A-site cation for OIH perovskite, whereas all-inorganic perovskite has cesium (Cs) or rubidium (Rb) as the cation.[24] Ideally, perovskite crystal structures exist as a cubic lattice, although perovskite with orthorhombic and tetragonal crystal lattice can be found.

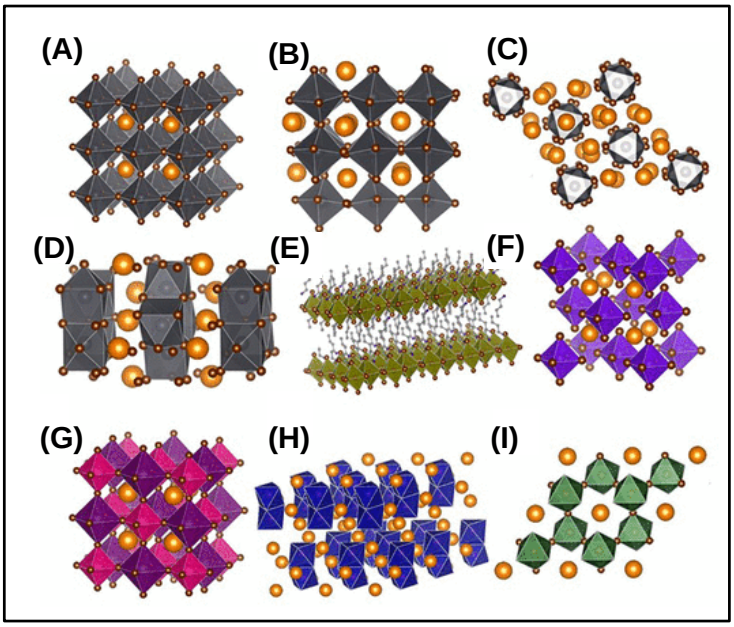

Figure 1.5. *Schematic representation of different metal halide structures.[25] Reproduced with permission from reference 25 (Copyright 2019 American Chemical Society).*

Deviations from this ABX_3 stoichiometry can be obtained when the A and B sites cation become partially or fully vacant (vacancy-ordered perovskites) or replaced by a combination of other cations (with different valences but with an overall neutral charge balance), forming double or quadruple perovskites. Notably, numerous perovskite-related structures with variations of structure and compositions such as pseudocubic ABX_3 (3D), A_4BX_6 (0D), (d) AB_2X_5 (2D), A_2BX_4 (2D), A_2BX_6 (0D), $A_2B^+B^{3+}X_6$ (3D) and $A_3B_2X_9$ (2D) can be found (Figures 1.5).[25] The deviation from the ideal perovskite structure in ABX_3 materials can be predicted through the Goldschmidt tolerance factor, $t= (r_A + r_X)/[\sqrt{2}(r_B + r_X)]$, where r_A, r_B, and r_X are the ionic radii of the corresponding ions, and t is defined as the ratio of the distance A-X to the distance B-X.[26] Only a limited number of A-cations (Cs, MA, and FA) can give rise to stable LHP structures because stable 3D perovskite structures are formed with the tolerance factor range of 0.76-1.1. Additionally, the octahedral factor (μ), defined as $\mu = r_B/r_X$, describes the stability of the BX_6^{2-} octahedral.[25, 27] Hence, the tolerance and octahedral factors are the two most important factors to predict the stability of novel possible perovskite combination. LHP NCs can be done by simply mixing the corresponding precursor solutions under ambient conditions due to their inherent ionic character. The two most common methods of the synthesis of LHP NCs are: (a) hot injection approach and (b) ligand assisted re-precipitation (LARP) methods.[22, 28-31] The detailed synthetic procedures have been described in the methodology chapter (chapter 2). The main difference between the two approaches is the temperature at which the reaction occurs: while the hot injection is performed at high temperatures (in most cases above 100°C), the formation of NCs in LARP occurs at room temperature. Depending on the synthetic conditions, the dimensionality of LHP can be tuned from 3D to 0D (see Figure 1.6 A).[20] The optical and electronic properties of perovskites are tunable across the whole visible region by simple modulation of halide compositions (See Figure 1.6 B).[22] The size and dimensionality of perovskites tune their optical properties, like conventional metal chalcogenide semiconductors.[22, 32-34] Moreover, they show strong quantum confinement effects when their dimensionality changes from 3D to 2D, offering tunability of optical properties.[33, 35-36] Additionally, doping of divalent metal ion (Mn^{2+}, Zn^{2+} etc) is widely used to tune the photophysical properties of LHP.[37-38] Interestingly, recent studies have shown that colloidal perovskite nanocrystals (NCs) can exhibit outstanding opto-electronic properties such as very high photoluminescence quantum yields (PLQY), high absorption coefficient, very narrow full width half maximum (FWHM) of PL emission and long diffusion length.[28, 32, 39-42]

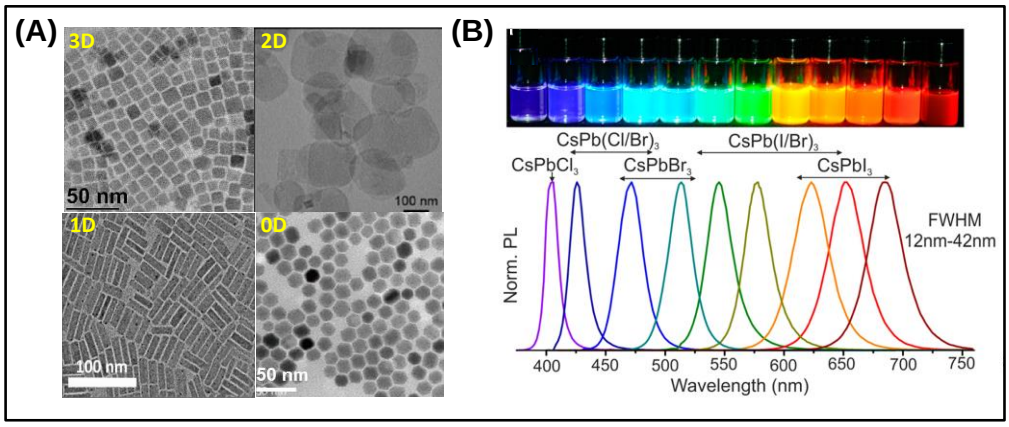

Figure 1.6. *(A) TEM images of different dimensional LHP NCs.[20] Reproduced with permission from reference 20 (Copyright 2021 American Chemical Society) (B) colloidal solution of perovskite NCs under UV-lamp (λ_{ex}=365 nm) and their corresponding PL spectra.[22] Reproduced with permission from reference 22 (Copyright 2015 American Chemical Society)*

It is reported that defect tolerance is an important factor for optical properties related to the shallow of the defect-related energy states. Defect tolerance is low nonradiative recombination rates despite high densities of defects.[20, 43-44] A schematic plot of the band structure of LHP NCs and conventional semiconductor QDs (CdSe, GaAs) is shown in Figure 1.7.[45]

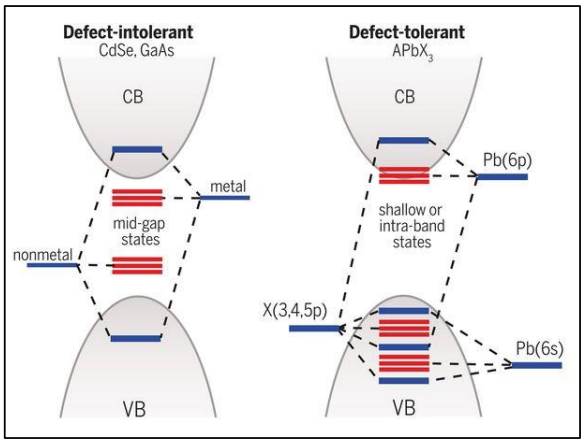

Figure 1.7. *Comparison of the electronic structure of defect-intolerant CdSe/GaAs and defect-tolerant semiconductors (ABX_3).[45] Reproduced with permission from reference 45 (Copyright 2017 American Association for the Advancement of Science)*

Interestingly, it is noticed that the defect states for perovskite NCs lie within the valence and conduction bands, whereas it is formed within the band-gap for conventional semiconductor

QDs.[44] Notably, the band structure of the perovskites shows that the conduction and valence bands are included with orbitals that are anti-bonding in nature. In the subsequent section, we will elaborately discuss the excitonic properties of LHP NCs and their versatile applications.

1.3. Nanophotonics: An exciting frontier in materials science

Nanophotonics deals with the interaction of light with the matter on a nanometer size scale which is an emerging frontier providing challenges for fundamental research and opportunities for new technologies.[46] It is a multidisciplinary field, creating opportunities in physics, chemistry, applied sciences, engineering, biology, and biomedical technology. By adding a new dimension to nanoscale science and technology, nanophotonics provides challenges for fundamental research and creates opportunities for new technologies. The interest in nanoscience is a realization of a famous statement by Feynman that "There's Plenty of Room at the Bottom" (Feynman, 1961). He pointed out that if one takes a length scale of one micrometer and divides it into nanometer segments, which are a billionth of a meter, one can imagine how many segments and compartments become available to manipulate. The critical fact is that nanophotonics deals with interactions between light and matter at a scale shorter than the wavelength of light itself. Nanophotonics can conceptually be divided into three parts.[46] One way to induce interactions between light and matter on a nanometer size scale is to confine light to nanoscale dimensions that are much smaller than the wavelength of light. The second approach is to confine matter to nanoscale dimensions, thereby limiting interactions between light and matter to nanoscopic dimensions. This defines the field of nanomaterials. The last way is nanoscale confinement of a photoprocess where we induce photochemistry or a light-induced phase change. This approach provides methods for nanofabrication of photonic structures and functional units.

Let us look at the nanoscale confinement of radiation. There are several ways to confine the light to a nanometer size scale. One example is lightly squeezed through a metal-coated and tapered optical fiber where the light emanates through a tip opening that is much smaller than the wavelength of light.[46] The nanoscale confinement of matter to make nanomaterials for photonics involves various ways of confining the dimensions of matter to produce nanostructures. For example, one can utilize nanoparticles that exhibit unique electronic and photonic properties. It is gratifying to find that these nanoparticles are already being used for various applications of nanophotonics, such as UV absorbers in sunscreen lotions.[46] Nanoparticles can be made of either inorganic or organic materials. Nanometers,

nanometer-size oligomers (a small number of repeat units) of monomeric organic structures, are organic analogs of nanoparticles.

In contrast, polymers are long-chain structures involving many repeat units. These nanometers exhibit size-dependent optical properties. Metallic nanoparticles exhibit unique optical responses and enhanced electromagnetic fields and constitute the area of "plasmonics." Nanocomposites comprise nanodomains of two or more dissimilar materials that are phase-separated on a nanometer size scale. Each nanodomain in the nanocomposite can impart a particular optical property to the bulk media. Flow of optical energy by energy transfer (optical communications) between different domains can also be controlled. Nanoscale photo processes can be used for nanolithography to fabricate nanostructures. These nanostructures can be used to form nanoscale sensors and actuators.[46] A nanoscale optical memory is one of the exciting concepts of nanofabrication. An essential feature of nanofabrication is that the photo processes can be confined to well-defined nano-regions so that structures can be fabricated in a precise geometry and arrangement.

1.3.1. Excitons in LHP Nanocrystals

In a semiconductor, the absorption of a photon with energy higher or equal to the energy of the bandgap can lead to the formation of a quasiparticle, known as an exciton.[47] The The attractive Coulomb interaction binds Photo-created electron-hole pair. Consequently, the exciton-related absorption or emission appears at energies below the fundamental bandgap. Excitons can be of two types: (a) Frenkel excitons, when the electron and hole are bound so tightly that the exciton is localized within a single unit cell and (b) Wannier-Mott excitons which are weakly bound and extended over many lattice sites (depicted in Figure 1.8).

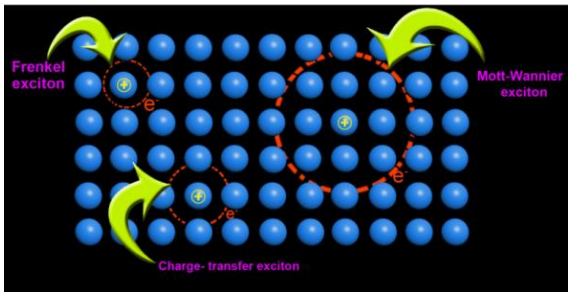

Figure 1.8. *Diagram of the different types of exciton*[48]

Generally, there are two photo-excitations near the band edge for direct bandgap semiconductors: free carriers and excitons. Exciton binding energy that reflects the Coulomb interaction strength between photoexcited electrons and holes determines the balance of the

populations between the two species. Typically, inorganic semiconductors are free-carrier materials with the exciton binding energies only in a few meV at room temperature and their excited states being populated principally by free carriers. While organic semiconductors are excitonic materials with the exciton binding energies in hundreds of meV and thus excitons are prevailing in the excited states.[49] Interestingly, LHP that combine some merits of organic and inorganic semiconductors seem to stand for an exotic class of semiconductors between these two limiting cases, with the experimentally determined exciton binding energy varying in a wide range of 2 to more than 50 meV for the prototype perovskite $MAPbI_3$.[50-52] Such large variations of the exciton binding energies reported for LHP give rise to a strongly debated question, that is, whether free carriers or excitons are generated upon photoexcitation? Most studies showed that the excitons, if formed at room temperature, dissociated rapidly into free carriers on a sub-ps time scale, leading to the free carriers dominating in the subsequent processes.[53-54] However, researchers also revealed that excitonic effects play an important role in defining the optical properties of MHPs since their band edge absorption onsets and the transient absorption spectra were found to be dominated by the exciton resonances.[55] Therefore, understanding the exciton nature in perovskite NCs is critical in guiding their further applications. For instance, semiconductors with high exciton binding energies are more favorable in light-emitting applications since the radiative recombination that occurs through excitons can reach high quantum yields at relatively lower carrier densities. In contrast, additional effort is required in photovoltaics applications to dissociate the excitons for carrier extraction. In contrast, semiconductors with low exciton binding energies significantly below the thermal energy at room temperature are highly desirable in photovoltaic cells, owing to the merit of easy dissociation of excitons or spontaneous generation of free carriers upon photo-excitation. In this context, accurate determination of exciton binding energy is important. Magneto-absorption, the temperature dependence of photoluminescence, optical absorption, and theoretical calculations have been applied to determine the excitons binding energies (E_b) in hybrid and all-inorganic perovskites.[56] However, significant discrepancies of excitons binding energies are found in several previous reports. Although LHP NCs have gained significant attention recently, more efforts are needed to unfold the fundamental physics of these novel materials for the future development of photovoltaics devices.

1.3.2. Ultrafast Photo-induced Processes in LHP NCs: Fate of Excitons

It is essential to understand the fate of the photoexcited charge carriers in a semiconducting material to develop efficient optoelectronic devices. Photoexcitation produces electron-hole pairs whose energy relaxation channels depend on various conditions.[26, 57-58] Followed by initial carrier thermalization, the hot charge carrier loses its energy by emitting optical phonons and successively relaxes down to the electronic band-edge. The charge carriers then either radiatively decay to produce light or recombine non-radiatively. This section discusses the current understanding of different energy relaxation dynamics in LHP NCs under ultrafast photoexcitation. The various sequences of events after photo-excitation within perovskites and various interfaces are schematically shown in Figure 1.9.[44, 59-60]

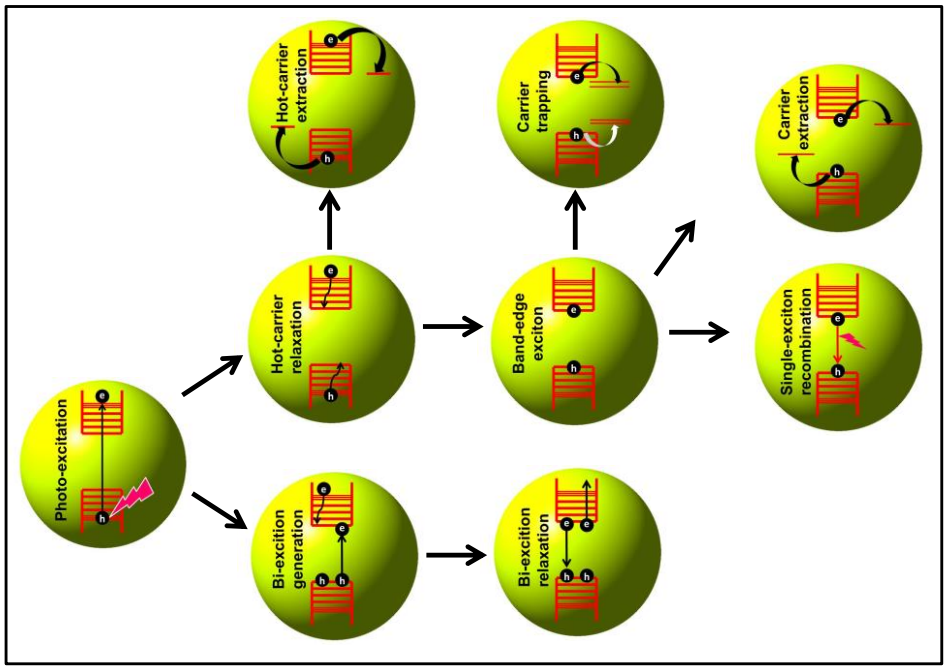

Figure 1.9. *Schematic representation of various modes of relaxation of charge carriers produced on photoexcitation of the perovskites and perovskite composites.*

The photo-induced transients of perovskite NCs have been characterized using optical pump-probe transient absorption (TA) spectroscopy. The pump laser-induced change in excited state population as a function of time (fs to ns).[44, 61] A typical steady-state linear absorption spectrum (red squares) and a TA spectrum (blue circles) of a planar $MAPbI_3$ perovskite thin film is represented in Figure 1.10. It reveals that both excitonic and band to band continuum transitions contribute to the optical band gap in LHP NCs.[62]

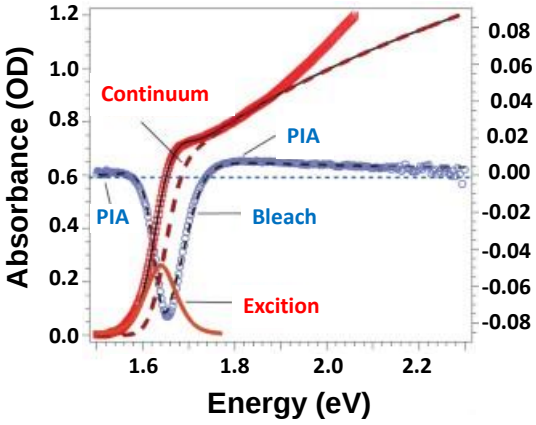

Figure 1.10. *Typical Steady-state (red squares) and transient absorption (TA) (blue circles) spectra of a typical $MAPbI_3$ perovskite thin film.[62] Reproduced with permission from reference 62 (Copyright 2015 Macmillan Publishers Limited)*

The TA spectrum consists of two general features: a sharp photobleach (PB) and broad photoinduced absorption (PIA). The PB signal peaking at ~1.65 eV has been attributed to both band filling and free carrier-induced bleaching of the exciton transition.[62-63] The PIA has been related to several factors such as hot carrier (HC) cooling, polaron formation, and free carrier absorption.[61-62, 64] The derivative like TA feature at an early time scale (<1 ps) for the $CsPbX_3$ NCs have been attributed to the biexciton effect, which arises due to coulombic interaction between the hot-exciton and band-edge exciton produced by the pump and probe laser, respectively.[58-59, 63, 65-66]

❖ Hot-Carrier Relaxation Dynamics

When perovskite NCs are excited by photons with energy higher than the band-gap energy, the charge carriers (electrons and holes) are produced in states much above the band-edge states with a non-equilibrium distribution in the energy. These "hot carriers" thermalize through Carrier-carrier scattering processes within 1 ps. The subsequent process is called "carrier cooling", in which the quasi-equilibrated HCs (at a temperature higher than the lattice temperature and governed by the Fermi-Dirac distribution) dissipate their excess energy as heat via phonon emission and come to the band-edge state.[67-71] The HC cooling can be monitored by following the buildup dynamics of band-edge bleach (PB) and decay of the PIA band. In addition, HC cooling can be probed by measuring the carrier temperature by fitting the high-energy tail of the TA spectra to a Maxwell-Boltzmann distribution.[62, 72] However, the exact estimation of the individual contributions of hot holes and hot electrons to the carrier cooling time is difficult as the excess energy is almost equally distributed between the hot electrons and hot holes.[64]

❖ Carrier Trapping and Recombination Dynamics

Radiative recombination of the charge carriers is one of the most important channels in direct band gap semiconductors that determine their utility in optoelectronic devices. However, multi-exponential PL decay dynamics of most perovskites NCs even at low excitation fluence suggests the existence of sub-band-gap energy levels arising from various defects that act as trap centers.[61, 73-75] These trapped carriers can return to the conduction or valence band and recombine radiatively if the de-trapping process is effective such as in the case of shallow defects.[74, 76] However, when the separation between the trap state and band-edge is significant, the charge carriers relax non-radiatively, as in the case of deep traps.[74] For smaller NCs with a high surface-to-volume ratio, "surface trapping" can also facilitate non-radiative recombination of the charge carriers, resulting in lowering the PL efficiency and acceleration of the PL decay dynamics. Notably, the time constants for the radiative processes are most commonly estimated from the PL decay profiles using the time-correlated single-photon counting (TCSPC) technique, but, the non-radiative recombination processes are much faster and require ultrafast TA and PL measurements. The temporal profile of the photobleach (PB) signal of perovskite NCs represents the dynamics of relaxation of the thermalized/band-edge exciton. It consists of a fast component due to carrier trapping, and a long component is due to radiative recombination of two components.[61] In this context, time constants of ~45 ps and ~2 ps are obtained for the bleach recovery kinetics of $CsPbBr_3$ NCs, where the former has been assigned to the electron trapping.[73] The estimated carrier trapping time constants is ~215-400 ps in the case of $CsPbI_3$ NCs.[73, 77-78] A recent theoretical study shows that halide vacancies in the NCs are the major contributor to the defect energy levels, which are shallow for $CsPbBr_3$ and $CsPbI_3$, but deep in the case of $CsPbCl_3$.[79-80] The high trap density in large band gap $CsPbCl_3$ NCs accounts for its weak luminescence (PLQY <10%), and TA studies show multiple carrier trapping channels with time constants ranging from 3 to 64 ps.[37, 81-82]

❖ Multi-Exciton Dynamics

It is noteworthy that the generation of multiple excitons by absorption of a single photon can enhance the PCE of single-junction photovoltaics. Generally, multi-excitons in semiconductor NCs are generated by utilizing the excess energy available to an HC or by high photon flux. Notably, multi-exciton dynamics is independent of the method of generation which can be applied to improve solar cell applications as the.[44, 83-86] Recently, Makarov *et al.* studied multi-exciton dynamics in $CsPbX_3$ NCs by monitoring the PL kinetics

as a function of the pump fluence, where the appearance of an additional fast decay component at higher laser fluences indicates the formation of multi-excitons (Figure 1.11).[83]

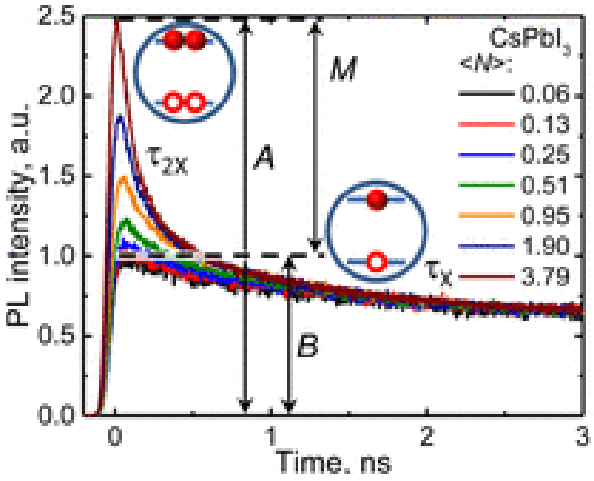

Figure 1.11. *PL decay dynamics of $CsPbI_3$ NCs at different pump laser fluences correspond to a short-lived PL component due to bi-excitons (denoted as τ2X) emerging at higher pump intensities.[83] Reproduced with permission from reference 83 (Copyright 2016 American Chemical Society).*

The generation of a large number of charge carriers in spatially confined NCs enhances the carrier-carrier interaction, which leads to Auger recombination (AR), an additional non-radiative channel for the relaxation of the charge carriers. Multi-exciton generation is limited to bi-excitons as both VB and the CB edge states of the perovskite NCs which accommodate a maximum of two charge carriers (two-fold degeneracy).[83] The bi-exciton lifetime of the pure $CsPbX_3$ NCs varies with the halide composition as $CsPbI_3$ (90-115 ps) > $CsPbBr_3$ (40-74 ps) > $CsPbCl_3$ (~20 ps).[83, 87-90] Bi-exciton lifetime (τ_{xx}) of perovskite NCs strongly depends on the volume of the NCs as, $\tau_{xx} = \gamma V$, where γ is the scaling factor. The systems with a higher bi-exciton lifetime are of great interest as they provide a longer period for the extraction of bi-excitons before nonradiative AR. In a recent study, Mondal *et al*. showed that the biexciton lifetime of $CsPbI_3$ can be almost doubled by doping a small amount of chloride or formamidinium ion into the system.[91]

Another possible non-radiative loss channel is forming a trion, a localized center containing three charged particles.[92-93] A positively charged trion consists of two holes and one electron, and a negatively charged one comprises two electrons and a hole. These species are formed on photo-excitation of NCs, which contain a trapped electron or hole. Recently, Yarita *et al.* had estimated a trion lifetime of 190 ps for $CsPbBr_3$ NCs.[94] Post synthetic surface treatments could suppress the trion recombination process since the trions are formed through surface trapping.[95]

1.3.3. Hot Carrier (HC) Cooling Mechanisms in Lead Halide Perovskite Nanocrystals

Metal halide perovskite is the most exciting and potential material for photovoltaics and optoelectronic applications.[96] The solar energy conversion efficiency has been surpassed over 22% within a concise period, kept behind the conventional silicon solar cells.[20] But, further improvements of perovskite solar cells efficiency have plateaued, which requires exploring the advanced concept like hot-carrier solar cells (HCSC).[68, 97-99] Hot Carriers (HCs) are carriers with initial kinetic energies at least KBT above the conduction (valence) band generated by the above band gap Photoexcitation. This hot carrier exhibits a higher temperature than the lattice temperature. They rapidly relax (within sub-picoseconds) to the band edge by losing their excess kinetic energies to phonons (or as heat) via carrier–phonon scattering. Then they are available for transport to the contacts for charge extraction.[68, 70] For any single-junction solar cells, including perovskite solar cells, the rapid HC cooling is the dominant energy loss channel (see Figure 1.12).[100]

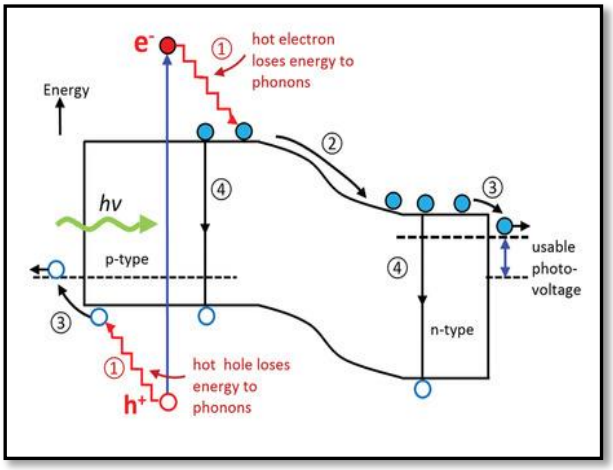

Figure 1.12. *Major energy loss processes in conventional single-junction solar cells.[100] Reproduced with permission from reference 100 (Copyright 2001, John Wiley & Sons, Ltd.)*

The theoretical calculation reveals that the solar cell efficiency can be extended up to 66% for single-junction HCSC under one sun illumination by mitigating the so-called Shockley-Queisser (SQ) limit of 33%.[101-102] However, HC cooling occurs very rapidly (within hundreds of femtoseconds) in most conventional semiconductor nano-materials (such as CdSe, PbSe, CdSe, GaAs etc). Slow HC cooling rate is the critical material criterion in solar absorbers for successful implications of HCSC where excess non-thermalized energy is judiciously extracted before they are lost as heat. The recent emergence of metal halide perovskite shows suitable HC cooling properties such as reduced HC cooling lifetime compared to

conventional semiconductor absorber, long-range hot-carrier transport (up to 600 nm), and highly efficient HC extraction properties.[62, 68, 103] Fundamental photophysical processes of HC cooling in a semiconductor and the corresponding evolution of electron and hole distribution with time following above bandgap pulsed laser excitation are shown in Figure 1.13.[97]

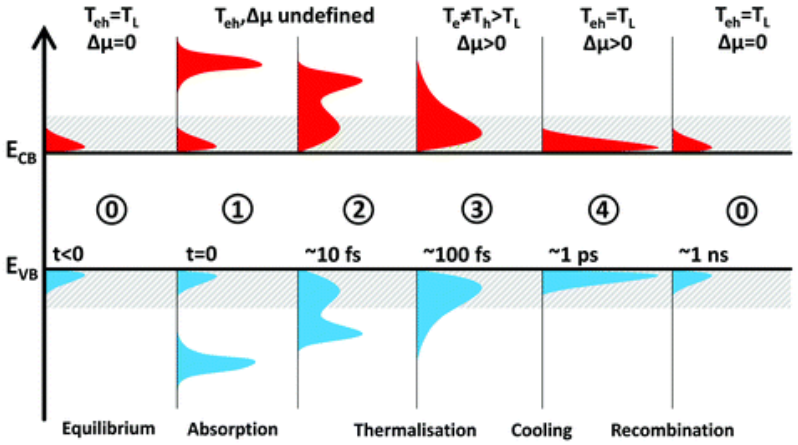

Figure 1.13. *Schematic representation of the evolution of the carrier distribution with time after pulsed laser excitation.[97] Reproduced with permission from reference 97 (Copyright 2019 Royal Societ of Chemistry).*

After absorbing the high-energy photons (process 1), the HCs will redistribute the energy and relax via various pathways to reach thermal equilibrium with the lattice. The hot carriers will thermalize among themselves through carrier–carrier interactions within 100 fs, usually called carrier thermalization (process 2). In this process, the distribution of HCs follows the Fermi-Dirac statistics with a carrier temperature T_c that is larger than the lattice temperature T_L. Richter et al. first observed ultrafast carrier thermalization in perovskites using 2D electronic spectroscopy with a characteristic thermalization time from 10 to 85 fs.[104] The thermalized HCs will start to equilibrate with the lattice mainly through an inelastic carrier–phonon interactions after carrier thermalization, known as "cooling" of HCs, which comprises of processes 3–4. In general, HC cooling in perovskite NCs occurs through dominant Fröhlich interactions (i.e. electron–LO–phonon scattering) within 1 ps due to the polar nature (process 3).[105] Notably, polarons can also be formed during process 3 due to the large electron-phonon interactions coupled with lattice deformations.[106] The electron–LO–phonon scattering process continues till the excess energies of the HCs are less than the LO phonon energy. Then, the emitted LO phonons from electron–LO–phonon scattering can decay into the daughter acoustic phonons and transverse optical phonons, and the

corresponding energy will be lost via decay of acoustic phonon emissions, which usually occurs in hundreds of picoseconds (process 4). Finally, the cooled carriers will recombine in nanosecond timescale (process 5). In this section, we highlight the crucial findings of slow HC cooling and various mechanisms that have been established for perovskite NCs as well as challenges and opportunities in this emerging field. Xing *et al.* first observed slow HC cooling of 0.4 ps in $MAPbI_3$ polycrystalline thin films in 2013 by employing transient absorption spectroscopy.[107] They showed concomitant rise of band edge bleach signal and decay of deeper level bleach signal which originates due to the hot hole relaxation from deeper valence band state to band edge valence band state. Later, Sum *et al.* reported similar concomitant rise and decay of bleach signals (0.4 ps) for the conduction band states due to the slow hot electron cooling.[108] Notably, halide perovskite have similar hot electron and hot hole cooling lifetimes which are essential for developing practical HC optoelectronics.[64] HC cooling dynamics in perovskite NCs depend on photoexcited carrier density, the initial HC excess energy, cation species, morphology, and confinement effects.[36, 62, 67, 71, 109-114] In this context, Chen *et al.* showed that HC cooling dynamics in $MAPbI_{3-x}Cl_x$ films could be further retarded up to 10 ps by increasing pump fluence from 2.3 μJ cm^{-2} to 340 μJ $cm^{-2,}$ which is evident from the substantially prolonged high-energy tail, and delayed build-up of the ground state bleaching signals (Figure 1.14).[114]

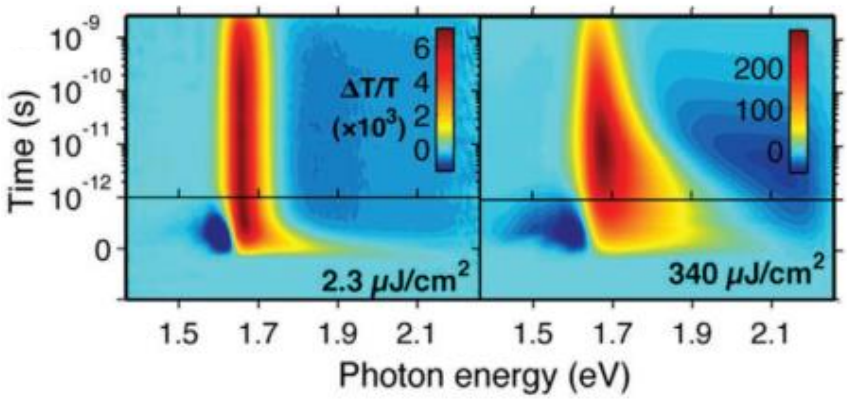

Figure 1.14. *2D pseudo-colour TA spectra of $MAPbI_{3-x}Cl_x$ film under 3.1 eV photoexcitation at low and high pump fluence showing prolonged high energy tail.[114] Reproduced with permission from reference 114 (Copyright 2015 American Chemical Society).*

Recently, the influence of A-site cation on the HC relaxation rate has been examined by Pullerits *et al,* where HC lifetime increases in the following order: $CsPbBr_3$ (390 ± 20 fs) > $MAPbBr_3$ (270 ± 20 fs)> $FAPbBr_3$ (210 ± 20 fs).[71] This has been explained by the fact that organic cations (MA and FA) enhance charge carrier-phonon coupling compared to inorganic

Cs cations, which leads to faster HC cooling in the case of organic cations.[115-116] On the other hand, FA cation-based LHP NCs show fastest HC relaxation among the three types of LHP NCs, indicating that FA cation interacts stronger with Pb-X framework than MA and Cs due to the larger size of FA cations.[71] Kim *et al.* reported the halide composition-dependent HC cooling time of $CsPbX_3$ NCs which varies as follows: $CsPbBr_3$(310 fs) > $CsPbBr_{1.5}I_{1.5}$(380 fs) > $CsPbI_3$ (580 fs) (Figure 1.15).[117] It is shown by density function theory (DFT) calculations that valence band (VB) electronic structures are perturbed by the orbitals of the halide ions while those of conduction band (CB) show halide-independent behavior. Thus, a significant dependence of HC relaxation rate on the halide composition is mainly attributable to the density of states for holes in the VB of $CsPbX_3$ NCs.[45]

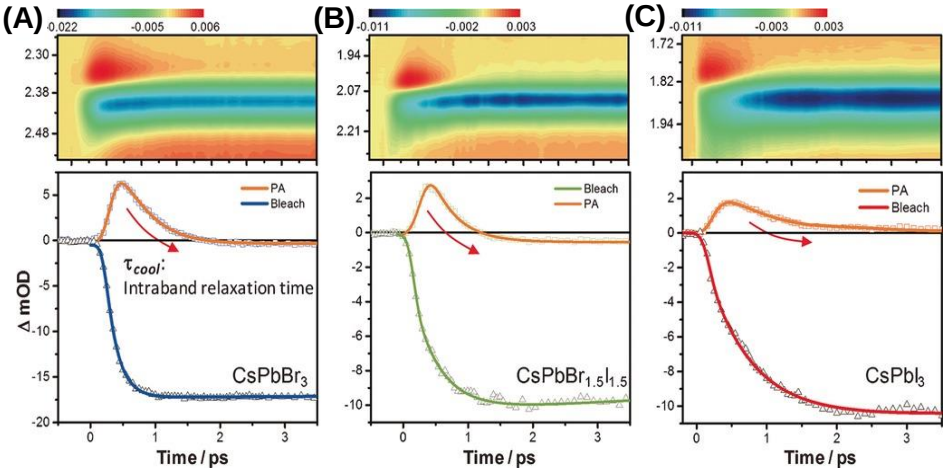

Figure 1.15. *2D pseudo-color TA map (top) and early time TA dynamics probed at the positions of PA and bleach features (bottom) for (A) $CsPbBr_3$, (B) $CsPbBr_{1.5}I_{1.5}$ and (C) $CsPbI_3$ NCs showing the halide dependence of HC cooling rate.[117] Reproduced with permission from reference 117 (Copyright (2017) John Wiley & Sons).*

Li *et al.* showed that two orders slower HC cooling times and about four times larger hot-carrier temperatures in colloidal $MAPbBr_3$ NCs than perovskites bulk films.[67] It is important to note that HC cooling rates depend on the photoexcited carrier density, the initial HC excess energy, and the resolution of the instrument used. Sometimes comparison of HC cooling dynamics between various groups may create confusion. HC temperature (T_C) of perovskite NCs is calculated by fitting the high energy tail of band edge photobleaching (PB) TA spectrum using the following Maxwell–Boltzmann distribution function:[62, 72, 118]

$$\Delta T(\hbar\omega) = -T_0 exp\left(\frac{E_F - \hbar\omega}{k_B T_C}\right) \quad (2)$$

Where ΔT stands for the amplitude of bleach at a particular probe wavelength, E_F is the quasi-Fermi energy level, K_B is the Boltzmann constant, and T_C is the HC temperature. T_C represents the average temperature of electron and hole since the average effective mass of electron and hole are almost equal in LHP NCs. The actual reason behind the slow HC cooling of perovskite NCs is still under debate. Various mechanisms, including hot-phonon (HP) bottleneck, acoustic-optical phonon upconversion, Auger-heating (AH), band-filling effect, large polaron formation, and intrinsic phonon bottleneck effects have been proposed, which will be discussed briefly to get a clear overview:[62, 67, 112, 116, 119]

❖ Hot-Phonon Bottleneck Effect

The longitudinal (LO) hot-phonon bottleneck effect is widely used to account for the slow HC cooling effect in polar semiconductors, including perovskite NCs.[120-121] This bottleneck effect usually occurs in the presence of a non-equilibrium LO-phonon population that leads to reduced net LO-phonon emission and re-heating of carriers, thus slowing the HC cooling.[62, 104, 112] The HC cooling phenomenon is a cascade process between carrier–LO–phonon scattering and LO-phonon decay. The presence of the hot-phonon effect is determined by the competition between the phonon decay rate and the carrier density-dependent carrier– LO–phonon scattering rate. In the absence of the hot-phonon effect, the HC cooling dynamics can be modelled using the Fröhlich interaction model with the energy loss rate (J_r) of the HCs as follows:[105, 118, 122]

$$J_r = \frac{3}{2}\frac{\hbar\omega}{\tau_{LO}}\left(e^{\frac{\hbar\omega}{K_B T_a}} - e^{\frac{\hbar\omega}{K_B T_c}}\right)\frac{N_{LO}(T_a)}{N_{LO}(T_c)}\left(\frac{K_B T_c}{\hbar\omega}\right)^2 e^{\frac{-\hbar\omega}{K_B T_c}} \quad (3)$$

where $\hbar\omega$ is the LO-phonon energy, τ_{LO} is the characteristics LO-phonon time, T_a is the temperature of acoustics phonon and $N_{LO}(T)$ is the LO-phonon occupation number for specific temperature T. At high pump fluence (>10^{18} cm^{-3}), HC cooling dynamics are significantly deviated from the calculated curves based on the above equation, indicating the presence of the hot-phonon effect. Such a hot-phonon bottleneck has been observed in organic-inorganic hybrid perovskites such as a film of $MAPbI_3$ and $FAPbI_3$. It shows the more considerable electron–phonon interaction than conventional semiconductors to a more rapid build-up of a hot LO-phonon population and a slower conversion rate of LO-phonons to acoustic phonons.[112, 123] A recent report by Yang et al. showed approximately ten times longer LO-phonon emission lifetime in highly excited $FAPbI_3$ films than their all inorganic counterparts with the same 3.1 eV photoexcitation energy. They attributed the hot-phonon

effect to originate from acoustic optical phonon upconversion, where the overlapping phonon branches by organic cations enhanced the up-transition of low-energy phonon modes.[109]

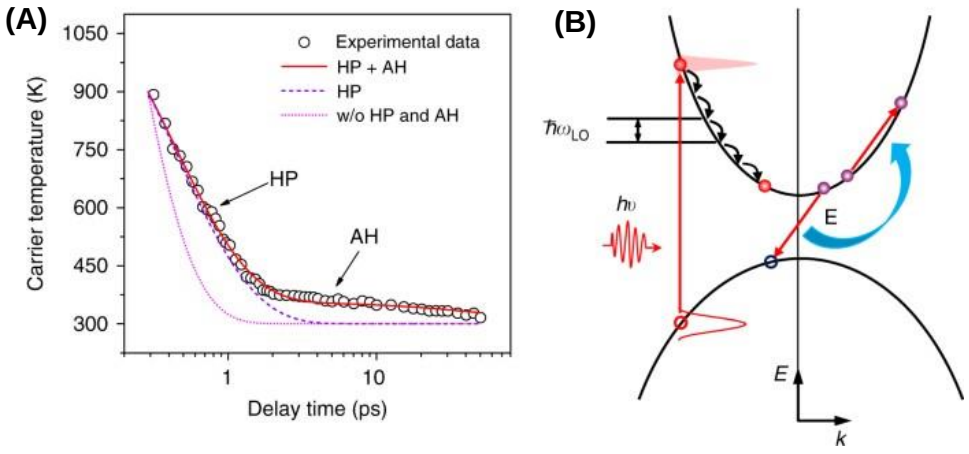

Figure 1.16. *(A) HC cooling in the presence of hot-phonon (HP) and Auger heating (AH) effects and (B) schematic representation of hot electron cooling in the presence of hot phonon and Auger-heating effect.[112] Reproduced with permission from reference 112 (Copyright 2017, Nature Publishing Group).*

❖ Auger Heating Effect

The multi-particle Auger-heating effect can further retard the HC cooling to several hundreds of picoseconds in hybrid perovskites films at higher HC densities (≈10^{19} cm^{-3}), apart from the hot-phonon bottleneck effect.[112] The non-radiative Auger-heating process involves the transfer of the electron-hole recombination energy to another carrier that leads to the excitation of this carrier to an even higher energetic state (Figure 1.16).[112, 124] The recombination energy transferred to the electronic system is proportional to $E_g + E$, where E_g is the bandgap.[125] The HC cooling dynamics, including the Auger heating effect, is described by the following equation:

$$< \frac{dE}{dt} >_{tot} = < \frac{dE}{dt} >_{e\text{-}ph} + k_3 n^2 \, (E_g + E) \qquad (4)$$

$$\frac{dn}{dt} = k_1 \, n - k_2 n^2 - k_3 n^3 \qquad (5)$$

where k_1 the monomolecular recombination co-efficient, k_2 is the free carrier bimolecular recombination co-efficient, and k_3 the Auger recombination co-efficient, which is larger for

smaller bandgap and higher carrier temperature.[126] The first term on the right side of Equation (5) refers to the energy loss rate via electron–LO–phonon interaction, while the second term corresponds to the Auger-heating contribution. The strong Auger heating effect on HC cooling in lead iodide perovskites is due to its relatively small bandgap and the significant hot-phonon effect.[112]

❖ Large Polaron Formation

HC cooling in halide perovskites may arise due to large polaron formation.[127] Zhu *et al.* proposed that this particular mechanism is severely distinct from the hot phonon bottleneck effect mechanism and mainly occurs at low carrier density (<10^{18} cm^{-3}).[106] Previously, long-lived HC photoluminescence (PL) with ≈150 ps lifetime and initial electronic temperature of ≈580K is observed in $MAPbBr_3$ and $FAPbBr_3$ (Figure 1.17).[106] However, such long-lived hot-PL emission was not observed in all-inorganic $CsPbBr_3$ counterparts. It has been explained that the dynamical screening from the re-orientational motions of the dipolar molecular cations and the large polaron formation give rise to the long-lived HCs in organic-inorganic hybrid perovskites.[128 129]

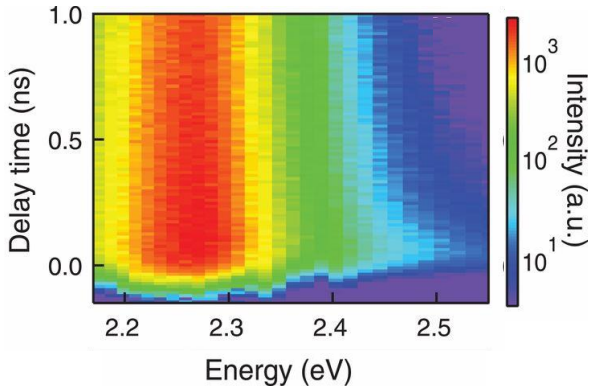

Figure 1.17. *Pseudo-color plot of TR-PL spectra for a single-crystal $FAPbBr_3$ microplate at 3.08 eV excitation with excitation density 1.7 μJ/cm^2, showing hot PL emission.[106] Reproduced with permission from reference 106 (Copyright 2016, American Association for the Advancement of Science).*

In another report, Zhu *et al.* reported a polaron formation time of ≈0.3 ps in $MAPbBr_3$ and 0.7 ps in $CsPbBr_3$, respectively.[103, 106] They suggested that the significant polaron formation rate competes favorably with the initial LO-phonon cooling time to slow down the HC cooling in $MAPbBr_3$ considerably. Also, they reported that the high energy tail of the initial PL spectra and HC temperature reduces with increasing pump fluence as for $MAPbI_3$ film.

This striking observation (as compared to the reports based on TA measurements) was explained by the fact that HC cooling rate becomes faster because of the destabilization of the large polarons caused by greater inter-polaron repulsive interaction[68] Hence, it is necessary to conduct more studies to confirm the contrasting trends for the HC temperatures and to understand better the transition of HC cooling from the large polaron protection model at very low carrier densities ($\approx 10^{16}$ cm^{-3}) to the hot-phonon bottleneck effect at high carrier densities ($\geq 10^{18}$ cm^{-3}).

❖ Band Filling Effect at High Carrier Density

Band filling effects are also responsible for the retardation of HC cooling time at higher carrier densities (>10^{18} cm^{-3}).[130-131] Recently, longer HC emissions with ns lifetimes are observed for $FASnI_3$ thin films at high carrier densities (>10^{18} cm^{-3}).[131] It has been observed that the emission peak shifts toward high energy (up to 75 meV) and an increased contribution of higher energy hot-PL with increasing pump intensity. Such long-lived HCs with few-ns lifetimes and a significant blue shift of the band edge emission energy were attributed to the band-filling effect (Figure 1.18).[130]

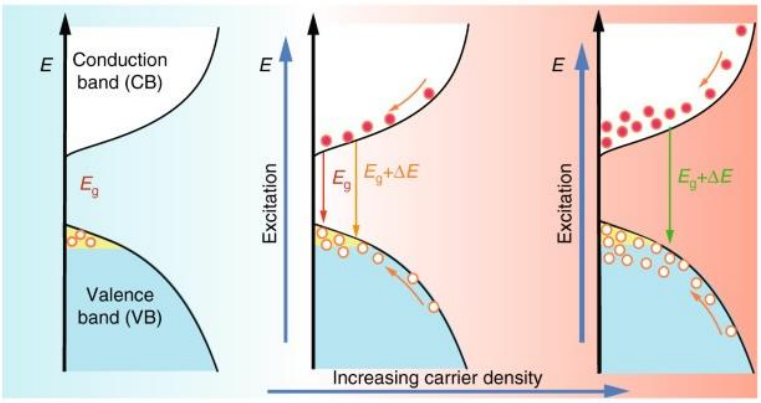

Figure 1.18. *Schematic representation mechanism for the blue shift of the PL resulting from band filling.[131] Reproduced with permission from reference 131 (Copyright 2017, Nature Publishing Group).*

Notably, the high pump fluence used contrasts with the polaron protection model (a low pump fluence effect). Under similar excitation conditions, the observed blue shift of emission energy is not present in lead halide perovskites ($MAPbI_3$ or $FAPbI_3$) films. It is noted that HCs need to be rapidly harvested while remaining at their highest possible temperatures for

maximal efficiencies. This extended hot carrier PL emission should not be mistakenly interpreted as implications of the higher potential for application in HCSCs.

❖ Intrinsic Phonon Bottleneck in Perovskite Nanocrystals

The intrinsic phonon bottleneck effect primarily arises from energy and momentum conservation and large energy level spacing.[99, 132] Thus, it is expected to show reduced carrier–phonon coupling and HC cooling rates in quantum-confined systems. Surprisingly, strongly quantum-confined conventional II–VI and IV–VI semiconducting NCs do not show slow slow HC cooling due to other rapid relaxation pathways for HCs such as Auger-type energy transfer, atomic fluctuations and defects trapping [133-134] Recently, Sum and co-workers showed the nanoscale confinement approach to further retard the hot carrier cooling using 3D perovskite NCs.[67] They showed reduced HC cooling in weakly confined colloidal $MAPbBr_3$ NCs (average radius around 2.5–5.6 nm) compared to their bulk perovskite counterparts and conventional semiconductor NCs. It is found that the HC lifetimes in the perovskites NCs are greatly retarded, reaching ≈32 ps with increasing pump fluence ($<N_0>$ ≈2.5) (Figure 1.19).[67]

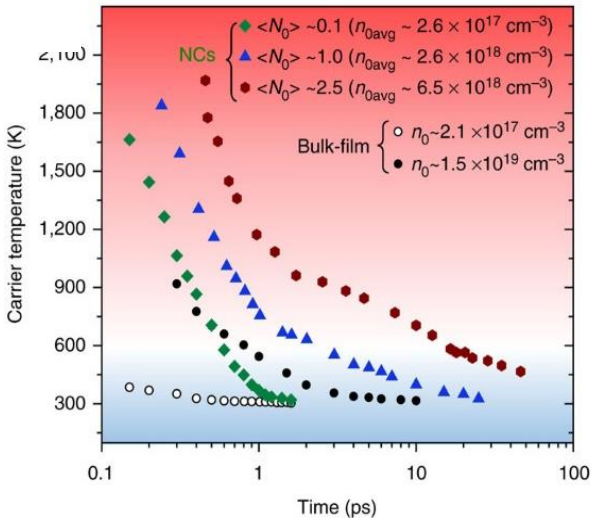

Figure 1.19. *HC temperature versus delay time for the MAPbBr3 NCs and bulk film under 3.1 eV photo-excitation with carrier densities.[67] Reproduced with permission from reference 67(Copyright 2017, Nature Publishing Group.).*

Similarly, long-lived HCs in weakly confined colloidal $FAPbI_3$ NCs (from the pump-induced lengthening of the TA band edge bleaching rise-time) were also reported by Papagiorgis *et al*. [111]The unique features of symmetric energy dispersion together with similar and small electron and effective hole masses for halide perovskites will help sustain the intrinsic

phonon bottleneck. Furthermore, the high PL quantum yield of 3D perovskite NCs (>80%) also means low defect densities, thereby mitigating hot carrier losses. These observations clearly demonstrate the much slower HC cooling time in perovskite NCs at both low and high pump intensities, thus highlighting perovskite NCs as up-and-coming candidates for HCSCs.[68]

The slow HC cooling properties of halide perovskites show great promise for developing advanced perovskite HCSCs and/or concentrator solar cells. However, further studies are required before utilization in practical HCSCs and to uncover the origin of such retarded cooling phenomena. In summary, the necessary toolbox for engineering slow HC cooling and designing efficient perovskite based HC absorbers require properties such as enlarged phononic bandgap, lower thermal conductivity, small LO phonon energy, smaller carrier effective mass, energetic molecular cations, quantum confinement etc.[71, 112]

1.3.4. Hot Carrier (HC) Extractions from Perovskite Nanocrystals

Efficient HC extraction is an important step for developing practical perovskite HCSC.[68] It is predicted that the efficiency of single-junction solar cells can be improved up to 66% by utilizing the excess non-thermalized energy of HCs.[101-102] However, HC extraction must be extremely fast because the extraction rate competes with the rate of cooling rather than the carrier recombination rate. Unlike the metal chalcogenide semiconductors, perovskites provide a much longer lifespan for hot carriers, which makes them more attractive for harvesting excess energy from hot carriers.[98] Furthermore, the thickness of the perovskite absorber must lie within the range of the HC transport distance. Notably, long-lived hot carriers of perovskite NCs are found to travel distances as long as ~600 nm overcoming obstacles like grain boundaries, which suggests that efficient transport of these carriers towards the electrode is technically feasible.[103] However, only a few studies have been made on harvesting these hot carriers.[67, 69-70, 135-137] In this section, we will summarize the recent findings of HC extractions from perovskite NCs with different acceptors via various time-resolved techniques. Li *et al.* studied the HC dynamics of $MAPbBr_3$ NCs employing ultrafast TA spectroscopy and demonstrated efficient hot electron extraction (83%) by 4,7-diphenyl-1,10- phenanthroline (Bphen).[67] The extraction of hot electrons by Bphen is evident from the rapid reduction of the high-energy tail in TA spectra, a drastic drop of carrier temperature (T_c) from 1300 to 450 K within 200 fs after photoexcitation and the observation of a new PA band in the near-IR region due to the radical anion of Bphen (Figure 1.20).[67]

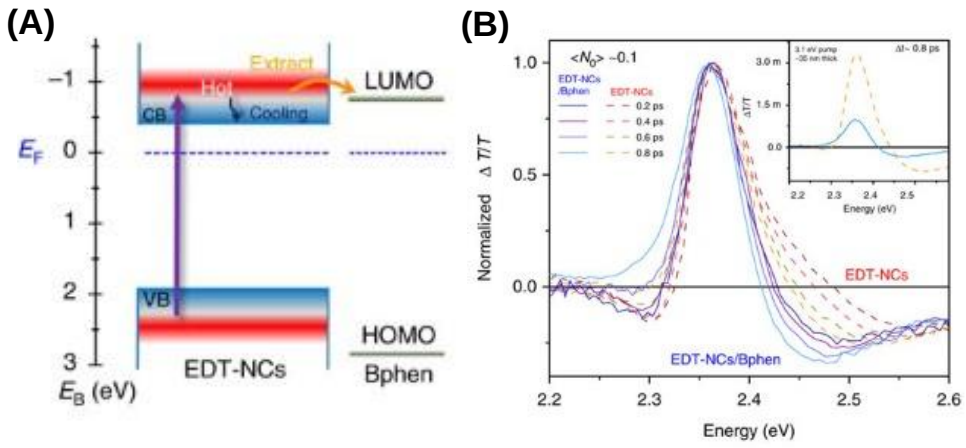

Figure 1.20. *(A) Energy level diagram for illustration of the hot-electron extraction from perovskites NCs to Bphen with competing hot-electron cooling pathways and (B) Normalized TA spectra of NCs film with (solid lines) and without (dashed lines) Bphen after 3.1 eV photoexcitation with a pump fluence of <N_0> ≈0.1. Inset shows the unnormalized TA spectra at a delay time of 0.8 ps.*[67] *Reproduced with permission from reference 67 (Copyright 2017 Nature Springer).*

The hot electron injection process is controlled by the diffusion of carriers within the NCs followed by hopping of the electrons at the NCs–Bphen interface, which is evident from the reduction of the hot ET efficiency from 72% to 10% with an increase in NC film thickness from 35 to 140 nm.[67] Also, Shen *et al.* had reported HC extraction for a $CsPbI_3$ film with P3HT as the extraction layer using the TA approach, where the near-instantaneous disappearance of the hot-energy tail (within ≈0.3 ps) and the reduction of HC temperatures in $CsPbI_3$/P3HT bilayers validate the efficient and extremely fast hot-hole injection into P3HT.[138] Dursun *et al.* have shown the hot carrier extraction from $MAPbI_3$ NCs using spiro-OMeTAD (hole transporting layer) and TiO_2 (electron transporting layer).[137] The hot carrier transfer from the higher excited state of $CH_3NH_3PbI_3$ to bathophenanthroline has been investigated by pump-push-probe spectroscopy.[139] Recently, HC transfer is observed within 300 fs in the interface of $CsPbBr_3$ and benzoquinone molecules (electron acceptor) or phenothiazine molecules (hole acceptor) by monitoring the time dependence of the THz signal.[135] Ultrafast hot hole transfer from photoexcited perovskites to MoS_2 is also monitored in a timescale of ~320 fs.[136] All of the above pioneering works provide important validation on the feasibility of HC extraction from halide perovskites, although they are primarily based on spectroscopy techniques. Hence, more direct electrical measurements on HC extraction is needed for practical development of HCSC. In addition, finding suitable candidates for

selective energy contact (SEC), appropriate device architecture (such as patterning, templating the SEC) which can protect the HCs from mixing with cold carriers in the contacts and minimize the entropy production during extraction is also essential. As halide perovskites continue to capture our imagination with their extraordinary properties, only time will tell if they can translate to disruptive technologies that transform our lives.

1.3.5. Photophysics in Perovskite Hybrid/Composite

Understanding the photophysical properties of perovskites alone is not enough to maximize their performance in real devices, as the efficiency of a photovoltaic device depends on several microscopic processes occurring at the interfaces of electron/hole transport layers and smooth arrival of the charge carriers to electrodes.[140-141] The charge transfer and separation are essential processes for light-harvesting applications. For charge separation, electron and hole acceptor molecules are coupled with LHP. LHP acts as either electron donor or hole acceptor, which depends upon the nature of perovskite and band position of both LHP foreign materials. After charge separation, the charge transport reaching the respective electrode before the charge recombination is another issue to optimize efficiency. Therefore, the overall photophysical processes at the interface can be tuned by the appropriate selection of materials with different band alignment, favorable exciton diffusion length, and suitable charge transport properties. Significant attention has recently been devoted to measuring the charge transfer rate and efficiency (including both electrons and holes) using a variety of potential acceptors. [142-143]This section highlights the recent advances and challenging issues on interfacial charge transfer and energy transfer of LHP NCs for the development of efficient light-harvesting. Lian *et al.* reported the first example of electron and hole transfer dynamics from $CsPbBr_3$ quantum dots (QDs) in 2015, wherein benzoquinone (BQ) and phenothiazine (PTZ) were used as the model electron and hole acceptor, respectively.[64] Analysis of transient absorption (TA) kinetics at the band edge of $CsPbBr_3$ QDS reveals electron and hole transfer timescales of 65 ± 5 ps and 49 ± 6 ps, respectively, whereas the half-lives of charge-separated states $CsPbBr_3^+$-BQ^- and $CsPbBr_3^-$-PTZ^+ were found 2.6 ± 0.4 and 1.0 ± 0.2 ns, respectively (Figure 1.21A).[64] Again, charge transfer (CT) dynamics of similar nano-composites were re-investigated by Mandal *et al.* using time resolved terahertz (THz) spectroscopy, where the observed electron and hole transfer was observed timescales are 20–50 ps and 137–166 ps, respectively.[135] Ahmed *et al.* studied CT dynamics between various dimensions (spherical, platelets and cubes) of $MAPbBr_3$ NCs and tetracyanoethylene (TCNE). They observed that CT rate varies in the following order: spherical (static) > platelets (static & dynamic) > cubes

(dynamic) due to the enhanced surface to volume ratio (Figure 1.21B).[144] In addition, several other molecular acceptors such as $Ti_3C_2T_x$ MXene (MXN), a few layers of black phosphorous (FLBP), Rhodamine-6G, fullerene (C_{60}), anthraquinone (AQ) and many other polycyclic aromatic hydrocarbon have been extensively studied to monitor the charge transfer processes from perovskite NCs.[140-141, 145-151]

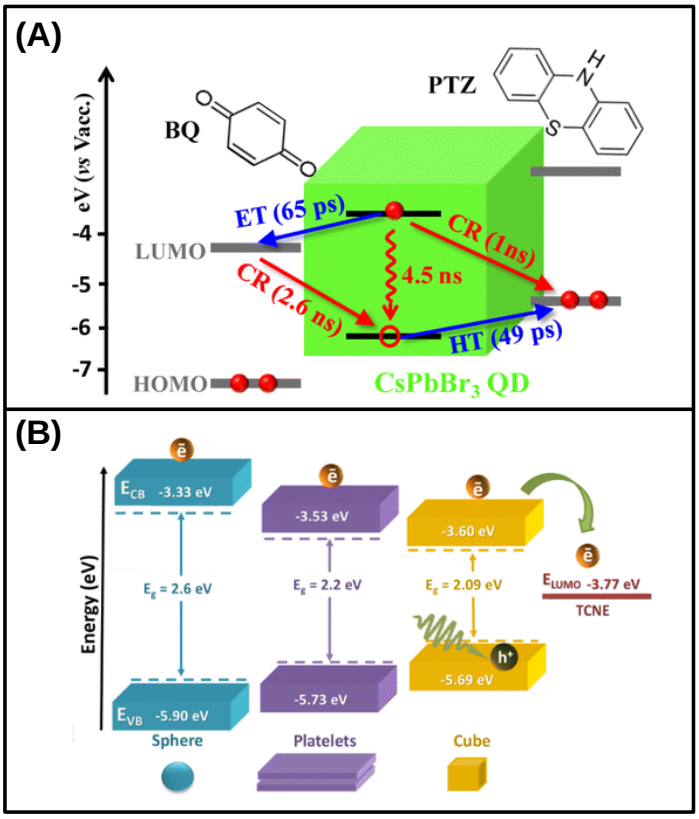

Figure 1.21. *Schematic energy level representation of (A) $CsPbBr_3$ QDs with respect to HOMO and LUMO energy levels of BQ and PTZ molecules and possible charge separation and recombination pathway.[64] Reproduced with permission from reference 64 (Copyright 2015 American Chemical Society) (B) $MAPbBr_3$ NCs of spheres, platelets, and cubes with respect to the LUMO value of TCNE.[144] Reproduced with permission from reference 144 (Copyright 2015 American Chemical Society)*

Various nanocomposites of $CsPbX_3$ NCs and inorganic semiconductors (like CdSe, CdTe, TiO_2, MoS_2/WS_2 etc) have also been studied to understand the nature of interaction and interfacial CT dynamics.[77, 136, 152-156] The simultaneous electron and hole transfer dynamics have been reported between $CsPbBr_3$ NCs and CdSe QDs. The measured electron transfer time from $CsPbBr_3$ NCs to CdSe QDs and hole-transfer time from CdSe QDs to $CsPbBr_3$ NCs were 550 and 750 fs, respectively.[152] Later, Schaller *et al.* have systematically studied

the impact of nanoparticle dimensionality on the electronic interactions between $CsPbBr_3$ and CdSe with two different morphologies, namely quantum dots (QDs) and nanoplatelets (NPLs) (Figure 1.22).[153] Although electron transfer is observed from $CsPbBr_3$ to CdSe regardless of particle dimensionality, a faster rate is found for the mixtures of two-dimensional (2D) NPLs than corresponding zero-dimensional (0D) analogs (such as QDs). It is explained that faster CT processes may arise from the extended spatial area of the 2D-2D composite system and the continuous density of acceptor states of the CdSe NPLs.[153]

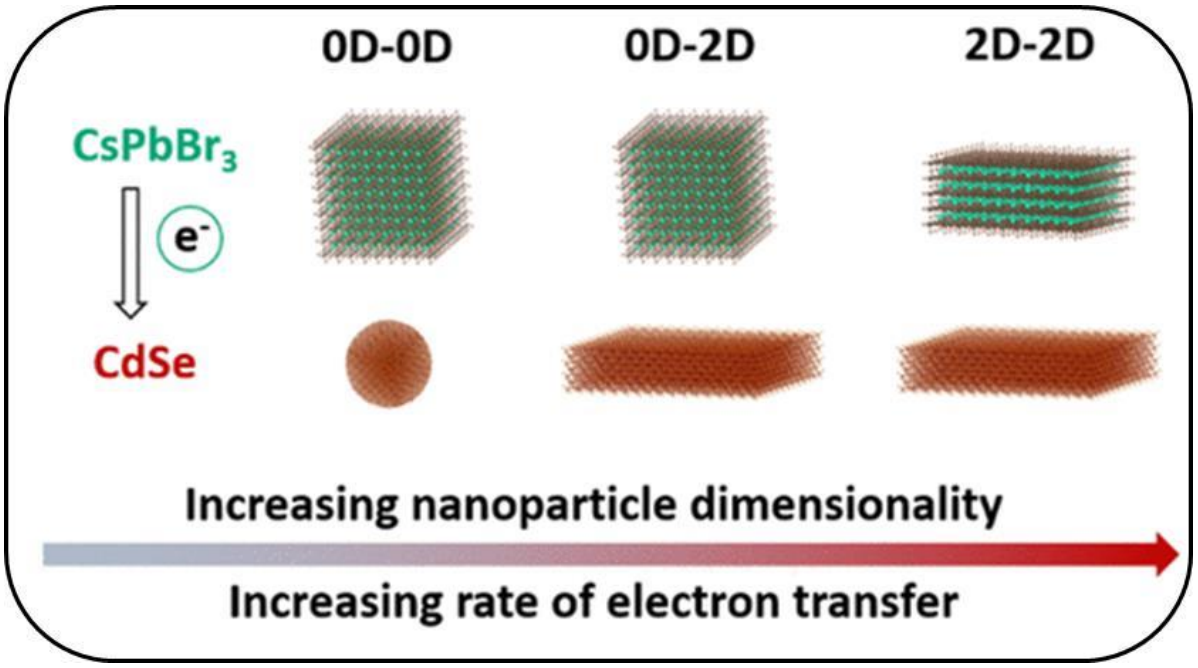

Figure 1.22. *Schematic representation of electron transfer from $CsPbBr_3$ NCs to CdSe NPLs with a variation of nanoparticle dimensionality.[153] Reproduced with permission from reference 153 (Copyright 2018 American Chemical Society)*

Liu *et al.* have recently shown that 99% of the photoexcited electron in $CsPbI_3$ QDs can be injected into TiO_2 with a size-dependent rate ranging from 1.30×10^{10} to 2.10×10^{10} S^{-1}, which is also ~2.5 times faster than that in the case of ZnO.

1.4. Applications of semiconducting perovskite nanocrystals

LHP NCs have rapidly emerged as one of the most promising materials of 21st century with many exciting properties and great potential for a broad range of applications.[19-20, 157] The certified power conversion efficiency (PCE) of single-junction perovskite-based solar cells has already exceeded 22% within a decade, left behind the conventional silicon solar cells and other related technologies due to outstanding optoelectronic properties. In addition, LHP NCs show great promise in a wide range of technological applications such as light-emitting diodes (LEDs), lasers, transistors, photo-detectors, and photocatalysis. This section will highlight the significant advancement and breakthroughs in different applications using these novel materials.

❖ Solar cells

Since Miyasaka and colleagues' first report of perovskite solar cells in 2009, perovskite-based solar cells have become one of the hottest research fields.[21] Intense research efforts have led to a rapid increase in the certified power conversion efficiencies to over 22% within a decade.[158-161] Although most of the reported efficient solar cell devices are based on perovskite films; several recent attempts have employed perovskite NCs as active materials, too. Figure 1.23 shows the typical architecture of a perovskite solar cell, where $CsPbI_3$ quantum dots (QDs) are sandwiched between an electron-accepting layer (TiO_2) and hole accepting layer (spiro-OMeTAD).[162]

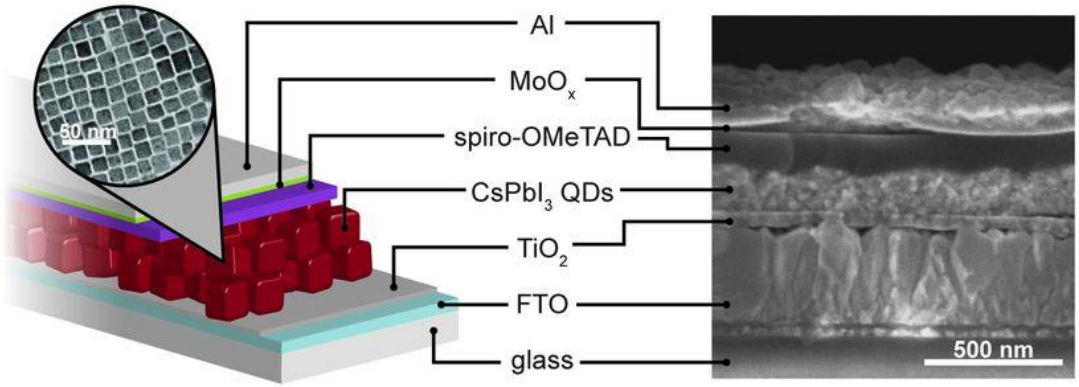

Figure 1.23. *Schematic representation of a perovskite QD solar cell with halide perovskite NCs as the light absorber and corresponding SEM image of an exposed cross-section.*[162] *Reproduced with permission from reference 162 (Copyright 2016 American Association for the Advancement of Science)*

It was found that the $CsPbI_3$ NCs-based solar cell devices showed improved operational stability and tolerance to higher relative humidity levels. Recently, Im *et al.* reported the fabrication of solar cells using $MAPbI_3$ nanowires (NWs). The maximum power conversion efficiency of these solar cells reached 14.7% using the device architecture of FTO/compact TiO_2/mesoporous TiO_2 +$MAPbI_3$ NW-$MAPbI_3$+Spiro-MeOTAD/Au (Figure 1.24).[163]

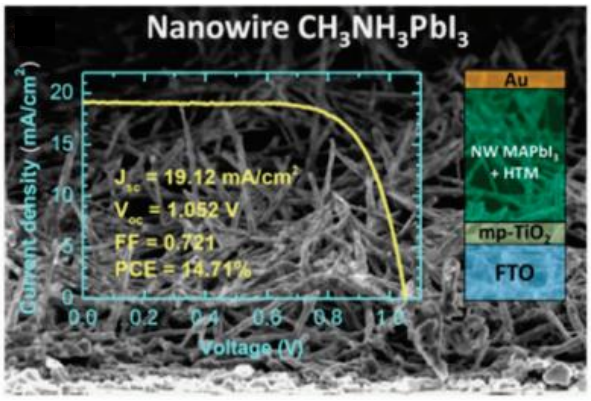

Figure 1.24. *Solar cells based on $CH_3NH_3PbI_3$ NWs showing SEM image, device architecture and the J–V curve with the corresponding performance characteristics.*[163] *Reproduced with permission from reference 163 (Copyright 2015 American American Chemical Society)*

Mali *et al.* fabricated $MAPbBr_3$ NCs-based solar cells with a power conversion efficiency of 11.4% using FTO/Bl-TiO_2/mp-TiO_2+$MAPbBr_3$ (~2nm NCs)/PTAA/Au as a device configuration.[164] Currently, a reported PCE record of QD solar cells of 16.6% was obtained with devices using $Cs_xFA_{1-x}PbI_3$ NCs as a light-harvesting material.[165] It is noted that low non-radiative recombination (ensures high V_{OC}) and good transport properties of the photogenerated charges, along with an absorber layer thick enough to harvest all available incident light, are necessary for achieving high efficiencies.[166] Although the efficiency of perovskite solar cells has shown impressive performance, the phase stability of these materials is still a concern. Hence, extensive research efforts are needed before the commercialization of these materials.

❖ Light Emitting Diodes (LED)

Tunable emission with high PLQY, low cost, and solution processability of perovskite NCs make them attractive for use in light-emitting diodes (LED).[167-170] The classification of LHP LEDs is mainly based on the colors, dimensions, film deposition technologies, and other features of LHP emitters. The typical LED structure can be classified as (a) standard structure

and (b) inverted structure (shown in Figure 1.25).[171] Tan *et al.* fabricated room temperature-working bright LEDs. A solution-processed $CH_3NH_3PbI_{3-x}Cl_x$ perovskite layer was sandwiched between TiO_2 and poly(9,9-dioctylfluorene) (F8) layers for effective radiate recombination of electrons and holes in the perovskite layer. The device produced a radiance of 13.2 W $sr^{-1}m^{-2}$ at a current density of 363 mA cm^{-2} with internal and external quantum efficiencies of 3.4% and 0.76%, respectively.[172]

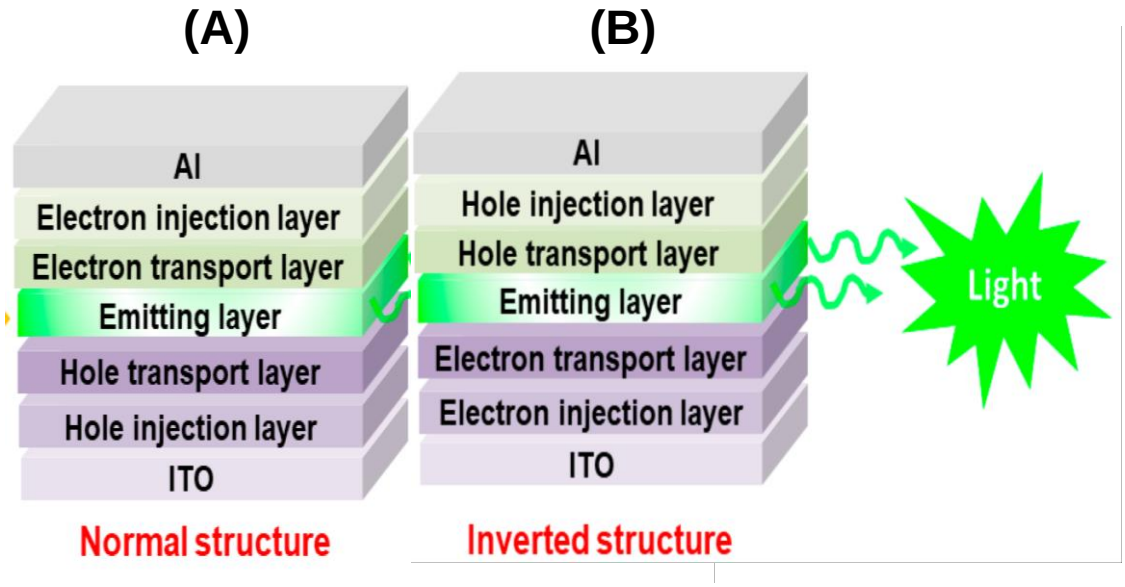

Figure 1.25. *Typical representation of perovskite LED structure (A) normal structure and (B) inverted structure.[171] Reproduced with permission from reference 171 (Copyright 2018 MDPI)*

Manna and colleagues incorporated inorganic halide perovskite NCs with varying morphology (cubes and platelets) and composition (bromide and iodide) for white-light-emitting perovskite LEDs.[173] Notably, the performance of LEDs depends on the radiative recombination of electrons and holes in the active layer, where the film morphology has a vital role. Di *et al.* had shown that incorporating perovskite NCs into a dielectric polymer matrix might help to reduce non-radiative current losses.[174] Thus far, some impressive achievements have been reported, including a high external quantum efficiency level of over 20%, ultrahigh brightness level over 100 000 cd m^{-2}, good flexibility, and facile device fabrication.[20, 175] However, more fundamental work on LHP-LEDs is required for a better understanding of the working mechanism of such contemporary LEDs, which would provide a guideline for the device to work at the technical level and trigger a breakthrough in the device performance improvement in the future.

❖ Photodetctors

Photodetectors convert light signals to electrical signals, which are critical for various applications, such as sensors and optical communication devices.[176] LHP NCs are promising materials for photodetectors with high figure-of-merit (e.g., responsivity and temporal response).[177-178]The first reported perovskite photodetectors were based on the polycrystalline film, which indicates the highest photoresponsivity of ~3.5 A W^{-1} at 365 nm in the visible range.[179] However, the performance of the photodetectors is found to be limited due to numerous crystal boundaries and defects in the perovskite films.[179] Later, low-dimensional perovskite NCs including nanocubes, nanowires, nanorods (1D), and nanosheets (2D) have recently been developed and tested for high-performance photodetectors due to lower defect density than corresponding 3D counterparts. It is noted that photodetectors based on fully inorganic $CsPbX_3$ QD have achieved high photocurrent on/off ratios of over 10^5, thereby enabling effective switching.[180] Usually, perovskite NCs have long-chain organic ligands into their surface, hindering charge transport and leading to slow photoresponses (>1 s). In this context, $CsPbBr_3$ QD/carbon nanotube (CNT) composites were used to improve charge extraction and transport, by which fast-response photodetectors with a rise time of 0.016 ms have been achieved.[181] Despite these promising results, there is a lot of scope for improving their device performances by controlling the NC morphology and device architectures.

❖ Photocatalysis

Harvesting the energy from chemical fuels (such as hydrogen, oxygen and methane) through the use of solar radiation can enable clean and efficient storage or renewable solar energy.[182] Halide perovskite NCs offers great potential for solar-driven photocatalytic applications due to the attractive optical properties like high absorption coefficients in the UV-visible region, a tunable band gap, and high PLQY. However, using perovskite NCs as a photocatalyst is exceptionally challenging due to their poor aqueous stability.[183-184] Some crucial findings are given below: Recently, $CsPbBr_3$ NCs have been used in the photocatalytic degradation of a typical organic pollutant 2-mercaptobenzothiazole (MBT).[185] Band gap funneled $MAPbBr_{3-x}I_x$ perovskite showed an impressive amount (255.3 mol/h) of photocatalytic H_2 evolution under visible light than pure $MAPbBr_3$ perovskite.[186] Again, $CsPbBr_3$ NCs anchored on porous g-C_3N_4 nanosheet heterojunctions are used for CO_2 photoreduction by Ou *et al.* (Figure 1.26).[187] In this context, Wu *et al.* had prepared Fe-based MOF-coated $MAPbI_3$ perovskites (i.e., $MAPbI_3$@PCN-221(Fex)) via a sequential deposition method, which serves

as an efficient photocatalyst for CO_2 reduction with the highest yield of 19.5 μmol g^{-1} h^{-1} for solar fuel production (CH_4 + CO).[188]

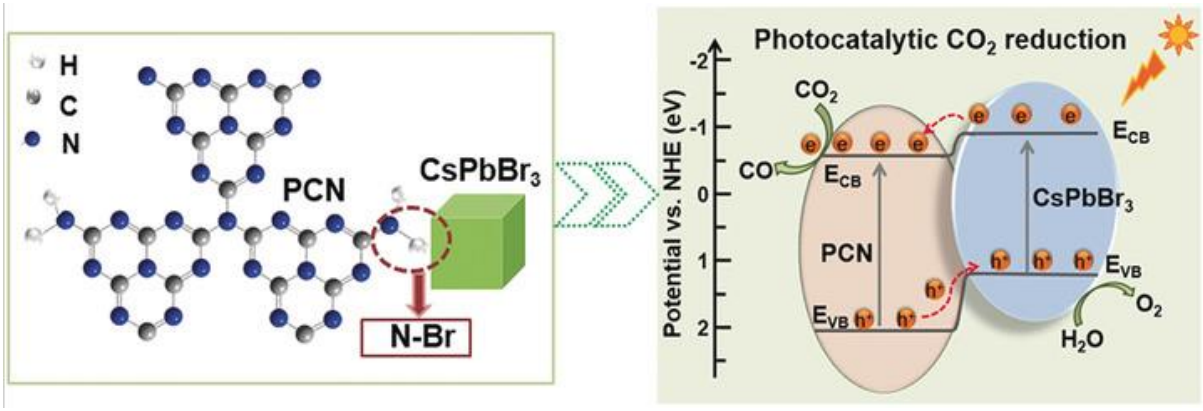

Figure 1.26. *Schematic representation for the interfacial interaction and band alignment within $CsPbBr_3$ NCs/g-C_3N_4 heterojunction.[187] Reproduced with permission from reference 187 (Copyright 2018 Wiley-VCH Verlag GmbH &Co. KGaA, Weinheim)*

It is reported that the halide perovskites NCs can catalyze a series of organic reactions, such as C-C bond formations via C-H activation C-N bond formations via N-heterocyclizations and C-O bond formations via aryl esterifications.[189] Zhu *et al.* reported the C-C bond coupling organic reactions using $APbBr_3$ (A = Cs or MA) as photocatalysts.[190] Apart from the above-discussed applications, perovskite NCs, are also used for lasing purposes, x-ray scintillators, field-effect transistors, spintronics devices, and many other applications.[191-194]

1.5. Outline of the thesis

In this thesis, emphasis has been given to designing lead halide perovskite (LHP) nanocrystals (NCs) based light-harvesting systems. Ultrafast spectroscopy and theoretical calculations are used to understand the hot carrier (HC) cooling dynamics and HC extraction. We have investigated the impact of the shape of the crystal structure of LHP on the ultrafast carrier dynamics. Then we have designed various heterostructures of LHP and studied their interfacial charge transfer dynamics using ultrafast spectroscopy. The impacts of compositions of LHP and the presence of QDs on the hot carrier dynamics have been studied, which is beneficial for efficient devices. A brief outline of the following chapters is given below.

Chapter 2:

In this chapter, the synthetic procedures of all-inorganic $CsPbBr_3$ NCs with different shape and $CsPbBr_xI_{3-x}$ (X= 0, 1 and 1.5) NCs with variable compositions, 2D CdSe NPLs, surface functionalization of $CsPbBr_3$ NCs with porphyrin ligands, $CsPbBr_3$/PbSe hetero-structures and 2D CdSe-$CsPbX_3$ hybrid systems are described. The analysis of 3D data matrices of femtosecond pump-probe data by single wavelength kinetic fitting and GLOTARAN (global and target analysis), instrumentation and working principle of photo-current measurement, theories of density functional theory (DFT) for understanding the different phonon mode and electronic interaction between porphyrin and perovskite NCs have been elaborated.

Chapter 3:

This chapter describes the influence of different shapes on the relaxation dynamics of perovskite NCs. The structural transformation of $CsPbBr_3$ NCs from cubic form to rod shape occurs with changing the solvent from toluene to dichloromethane (DCM). The time-resolved emission spectroscopy and the ultrafast transient absorption spectroscopy are used to understand the photoinduced relaxation processes. The global and target analysis of femtosecond transient absorption kinetics has been done to understand the individual excited-state species. The lifetime of the swallow trap (ST) changes from 25 ps to 45 ps and the lifetime of the deep trap (DT) state changes from 163 ps to 303 ps with changing the shape of nanocrystals from cubic to rod. Analysis reveals that trap states play an important role in the carrier relaxation dynamics of cubic and rod-shaped NCs. This work highlights the tuning of the crystal phase, shape, and exciton dynamics of $CsPbBr_3$ NCs that would be beneficial for designing efficient photovoltaic devices.

Chapter 4:

In this chapter, the hot hole cooling and transfer dynamics of $CsPbBr_3$ nanocrystals (NCs) is investigated using 5,10,15,20-Tetra(4pyridyl) porphyrin (TpyP) molecules. Density-functional theory (DFT) is used to elucidate the mechanism underlying charge extraction and the HC transfer process in the $CsPbBr_3$-TpyP system. The significant drop of initial hot carrier temperature (T_C^0) from 1140 K to 638 K at 400 nm excitation confirms the hot holes transfer from $CsPbBr_3$ NCs to TpyP molecules. It is dependent on the excitation energy, and the maximum transfer efficiency is 42% (for 0.85eV above band edge photo-excitation). Additionally, the hot hole transfer rate is almost 11 times faster than the band edge hole transfer rate. The findings will be relevant for the development of next-generation perovskite-based optoelectronic devices.

Chapter 5:

This chapter presents a new strategy to retard the HC cooling via charge localization at the $CsPbBr_3$/PbSe heterostructure interface. The transient absorption measurements reveal two times slower HC relaxation time (from 770 fs to 1.4 ps) and much higher initial HC temperature, T_C (1663 K, compared to 900 K) for the heterostructure compared to the pure $CsPbBr_3$ at 3.64 eV excitation, under 1.86×10^{17} cm^{-3} carrier density. Furthermore, a combination of an electron-phonon coupling model and first-principles calculations suggest a retarded relaxation through the Klemens channel due to an appearance of a large energy gap between the longitudinal optical (LO) and longitudinal acoustic (LA) phonon modes. The localization of charge density near the heterojunction is responsible for the up-conversion of LO modes to the higher energy and retards the HC relaxation. The findings highlight a new protocol for achieving long-lived HCs in perovskites at low carrier densities, which would benefit the future of HC photovoltaics.

Chapter 6:

This chapter describes the design of composites of 2D CdSe nanoplatelets and $CsPbX_3$ (X = mixture of Br and I or I) perovskite nanocrystals. We investigate the interfacial charge transfer dynamics with changing composition using ultrafast spectroscopy. Time-resolved fluorescence upconversion study confirms the electron transfer from CdSe NPLs to $CsPbX_3$, which varies by changing the perovskite composition. From the transient absorption spectroscopic study, the shortening of faster bleach recovery kinetics of CdSe NPLs and the enhancement of growth time of $CsPbX_3$ NCs in composites indicate the ultrafast electron transfer from CdSe NPLs to $CsPbX_3$ NCs. The ultrafast electron transfer from 2D CdSe NPLs to $CsPbX_3$ NCs enhances in following order: $CsPbI_3$> $CsPbBrI_2$> $CsPbBr_{1.5}I_{1.5}$. The high dark current and photo current are 0.04 μA and 62.4 μA in the CdSe-$CsPbI_3$ composite. The dramatically improved photocurrent response in the CdSe-$CsPbI_3$ composite confirms the enhancement of the efficient charge separation due to the ultrafast electron transfer from CdSe NPLs to perovskite NCs. The finding reveals that the heterostructure of 2D CdSe NPLs with perovskite NCs offers an opportunity to improve the efficiency of perovskite solar cells because of the interfacial charge transfer.

Chapter 7:

In this chapter, conclusive remarks of the above chapters and the scope for further research for a more efficient light-harvesting system are discussed here.

1.6. References

(1) Cao, G.; Wang, Y., *Nanostructures and Nanomaterials: Synthesis, Properties, and Applications*; World Scientific, 2011.

(2) Sze, S. M., *Physics of Semiconductor Devices*; John Wiley & Sons, 1981.

(3) Bhattacharya, S., Spectroscopic Properties of Semiconducting Polymer Nanomaterials. *PhD. Dissertation, Jadavpur University* **2013**.

(4) Pope, M.; Swenberg, C. E., *Electronic Processes in Organic Crystals and Polymers*; Oxford University Press, 1999.

(5) Gutmann, F., *Organic Semiconductors*; R. E. Krieger: Malabar, Fla., 1981.

(6) Silinsh, E. A., *Organic Molecular Crystals: Their Electronic States*; Springer-Verlag, 1980.

(7) Ekimov, A. I.; Onushchenko, A. A., Quantum Size Effect in Three-Dimensional Microscopic Semiconductor Crystals. *Soviet J. Exp. Theor. Phys* **1981**, *34*, 345.

(8) Brus, L. E., Electron–Electron and Electron-Hole Interactions in Small Semiconductor Crystallites: The Size Dependence of the Lowest Excited Electronic State. *J. Chem. Phys.* **1984**, *80*, 4403-4409.

(9) Alivisatos, A. P., Semiconductor Clusters, Nanocrystals, and Quantum Dots. *Science* **1996**, *271*, 933-937.

(10) Henglein, A., Small-Particle Research: Physicochemical Properties of Extremely Small Colloidal Metal and Semiconductor Particles. *Chem. Rev. (Washington, DC, U. S.)* **1989**, *89*, 1861-1873.

(11) Chestnoy, N.; Harris, T. D.; Hull, R.; Brus, L. E., Luminescence and Photophysics of Cadmium Sulfide Semiconductor Clusters: The Nature of the Emitting Electronic State. *J. Phys. Chem.* **1986**, *90*, 3393-3399.

(12) Steigerwald, M. L.; Brus, L. E., Semiconductor Crystallites: A Class of Large Molecules. *Acc. Chem. Res.* **1990**, *23*, 183-188.

(13) Haase, M.; Weller, H.; Henglein, A., Photochemistry of Colloidal Semiconductors. 26. Photoelectron Emission from Cadmium Sulfide Particles and Related Chemical Effects. *J. Phys. Chem.* **1988**, *92*, 4706-4712.

(14) Brus, L., Electronic Wave Functions in Semiconductor Clusters: Experiment and Theory. *J. Phys. Chem.* **1986**, *90*, 2555-2560.

(15) C. B. M.; Kagan, C. R.; Bawendi, M. G., Synthesis and Characterization of Monodisperse Nanocrystals and Close-Packed Nanocrystal Assemblies. *Annu. Rev. Mater. Sci.* **2000**, *30*, 545-610.

(16) Ithurria, S.; Dubertret, B., Quasi 2d Colloidal Cdse Platelets with Thicknesses Controlled at the Atomic Level. *Journal of the American Chemical Society* **2008**, *130*, 16504-16505.

(17) Rabouw, F. T.; de Mello Donega, C., Excited-State Dynamics in Colloidal Semiconductor Nanocrystals. *Topics in Current Chemistry* **2016**, *374*, 58.

(18) Dutta, A.; Medda, A.; Patra, A., Recent Advances and Perspectives on Colloidal Semiconductor Nanoplatelets for Optoelectronic Applications. *J. Phys. Chem. C* **2021**, *125*, 20-30.

(19) Akkerman, Q. A.; Rainò, G.; Kovalenko, M. V.; Manna, L., Genesis, Challenges and Opportunities for Colloidal Lead Halide Perovskite Nanocrystals. *Nat. Mater.* **2018**, *17*, 394-405.

(20) Dey, A.; Ye, J.; De, A.; Debroye, E.; Ha, S. K.; Bladt, E.; Kshirsagar, A. S.; Wang, Z.; Yin, J.; Wang, Y., et al., State of the Art and Prospects for Halide Perovskite Nanocrystals. *ACS Nano* **2021**, *15*, 10775-10981.

(21) Kojima, A.; Teshima, K.; Shirai, Y.; Miyasaka, T., Organometal Halide Perovskites as Visible-Light Sensitizers for Photovoltaic Cells. *J. Am. Chem. Soc.* **2009**, *131*, 6050-6051.

(22) Protesescu, L.; Yakunin, S.; Bodnarchuk, M. I.; Krieg, F.; Caputo, R.; Hendon, C. H.; Yang, R. X.; Walsh, A.; Kovalenko, M. V., Nanocrystals of Cesium Lead Halide Perovskites ($CsPbX_3$, X = Cl, Br, and I): Novel Optoelectronic Materials Showing Bright Emission with Wide Color Gamut. *Nano Lett.* **2015**, *15*, 3692-3696.

(23) Akkerman, Q. A.; Manna, L., What Defines a Halide Perovskite? *ACS Energy Lett.* **2020**, *5*, 604-610.

(24) Mitchell, R. H.; Welch, M. D.; Chakhmouradian, A. R., Nomenclature of the Perovskite Supergroup: A Hierarchical System of Classification Based on Crystal Structure and Composition. *Mineral. Mag.* **2018**, *81*, 411-461.

(25) Shamsi, J.; Urban, A. S.; Imran, M.; De Trizio, L.; Manna, L., Metal Halide Perovskite Nanocrystals: Synthesis, Post-Synthesis Modifications, and Their Optical Properties. *Chem. Rev.* **2019**, *119*, 3296-3348.

(26) Manser, J. S.; Christians, J. A.; Kamat, P. V., Intriguing Optoelectronic Properties of Metal Halide Perovskites. *Chem. Rev.* **2016**, *116*, 12956-13008.

(27) Protesescu, L.; Yakunin, S.; Kumar, S.; Bär, J.; Bertolotti, F.; Masciocchi, N.; Guagliardi, A.; Grotevent, M.; Shorubalko, I.; Bodnarchuk, M. I., et al., Dismantling the "Red Wall" of Colloidal Perovskites: Highly Luminescent Formamidinium and Formamidinium–Cesium Lead Iodide Nanocrystals. *ACS Nano* **2017**, *11*, 3119-3134.

(28) Zhang, F.; Zhong, H.; Chen, C.; Wu, X.-g.; Hu, X.; Huang, H.; Han, J.; Zou, B.; Dong, Y., Brightly Luminescent and Color-Tunable Colloidal $CH_3NH_3PbX_3$ (X = Br, I, Cl) Quantum Dots: Potential Alternatives for Display Technology. *ACS Nano* **2015**, *9*, 4533-4542.

(29) Li, X.; Wu, Y.; Zhang, S.; Cai, B.; Gu, Y.; Song, J.; Zeng, H., $CsPbX_3$ Quantum Dots for Lighting and Displays: Room-Temperature Synthesis, Photoluminescence Superiorities, Underlying Origins and White Light-Emitting Diodes. *Adv. Funct. Mater.* **2016**, *26*, 2435-2445.

(30) Akkerman, Q. A.; D'Innocenzo, V.; Accornero, S.; Scarpellini, A.; Petrozza, A.; Prato, M.; Manna, L., Tuning the Optical Properties of Cesium Lead Halide Perovskite Nanocrystals by Anion Exchange Reactions. *J. Am. Chem. Soc.* **2015**, *137*, 10276-10281.

(31) Guhrenz, C.; Benad, A.; Ziegler, C.; Haubold, D.; Gaponik, N.; Eychmüller, A., Solid-State Anion Exchange Reactions for Color Tuning of $CsPbX_3$ Perovskite Nanocrystals. *Chem. Mater.* **2016**, *28*, 9033-9040.

(32) Sichert, J. A.; Tong, Y.; Mutz, N.; Vollmer, M.; Fischer, S.; Milowska, K. Z.; García Cortadella, R.; Nickel, B.; Cardenas-Daw, C.; Stolarczyk, J. K., et al., Quantum Size Effect in Organometal Halide Perovskite Nanoplatelets. *Nano Lett.* **2015**, *15*, 6521-6527.

(33) Tyagi, P.; Arveson, S. M.; Tisdale, W. A., Colloidal Organohalide Perovskite Nanoplatelets Exhibiting Quantum Confinement. *J. Phys. Chem. Lett.* **2015**, *6*, 1911-1916.

(34) Zhang, C.; Chen, J.; Wang, S.; Kong, L.; Lewis, S. W.; Yang, X.; Rogach, A. L.; Jia, G., Metal Halide Perovskite Nanorods: Shape Matters. *Adv. Mater.* **2020**, *32*, 2002736.

(35) Chakraborty, R.; Nag, A., Dielectric Confinement for Designing Compositions and Optoelectronic Properties of 2D Layered Hybrid Perovskites. *Phys. Chem. Chem. Phys.* **2021**, *23*, 82-93.

(36) Butkus, J.; Vashishtha, P.; Chen, K.; Gallaher, J. K.; Prasad, S. K. K.; Metin, D. Z.; Laufersky, G.; Gaston, N.; Halpert, J. E.; Hodgkiss, J. M., The Evolution of Quantum Confinement in $CsPbBr_3$ Perovskite Nanocrystals. *Chem. Mater.* **2017**, *29*, 3644-3652.

(37) Rossi, D.; Parobek, D.; Dong, Y.; Son, D. H., Dynamics of Exciton–Mn Energy Transfer in Mn-Doped $CsPbCl_3$ Perovskite Nanocrystals. *J. Phys. Chem. C* **2017**, *121*, 17143-17149.

(38) Xu, K.; Vliem, J. F.; Meijerink, A., Long-Lived Dark Exciton Emission in Mn-Doped $CsPbCl_3$ Perovskite Nanocrystals. *J. Phys. Chem. C* **2019**, *123*, 979-984.

(39) Schmidt, L. C.; Pertegás, A.; González-Carrero, S.; Malinkiewicz, O.; Agouram, S.; Mínguez Espallargas, G.; Bolink, H. J.; Galian, R. E.; Pérez-Prieto, J., Nontemplate Synthesis of $CH_3NH_3PbBr_3$ Perovskite Nanoparticles. *J. Am. Chem. Soc.* **2014**, *136*, 850-853.

(40) Huang, H.; Susha, A. S.; Kershaw, S. V.; Hung, T. F.; Rogach, A. L., Control of Emission Color of High Quantum Yield $CH_3NH_3PbBr_3$ Perovskite Quantum Dots by Precipitation Temperature. *Adv. Sci.* **2015**, *2*, 1500194.

(41) Huang, H.; Bodnarchuk, M. I.; Kershaw, S. V.; Kovalenko, M. V.; Rogach, A. L., Lead Halide Perovskite Nanocrystals in the Research Spotlight: Stability and Defect Tolerance. *ACS Energy Lett.* **2017**, *2*, 2071-2083.

(42) De Roo, J.; Ibáñez, M.; Geiregat, P.; Nedelcu, G.; Walravens, W.; Maes, J.; Martins, J. C.; Van Driessche, I.; Kovalenko, M. V.; Hens, Z., Highly Dynamic Ligand Binding and Light Absorption Coefficient of Cesium Lead Bromide Perovskite Nanocrystals. *ACS Nano* **2016**, *10*, 2071-2081.

(43) Yin, W.-J.; Shi, T.; Yan, Y., Unusual Defect Physics in $CH_3NH_3PbI_3$ Perovskite Solar Cell Absorber. *Appl. Phys. Lett.* **2014**, *104*, 063903.

(44) Mondal, N.; De, A.; Das, S.; Paul, S.; Samanta, A., Ultrafast Carrier Dynamics of Metal Halide Perovskite Nanocrystals and Perovskite-Composites. *Nanoscale* **2019**, *11*, 9796-9818.

(45) Kovalenko, M. V.; Protesescu, L.; Bodnarchuk, M. I., Properties and Potential Optoelectronic Applications of Lead Halide Perovskite Nanocrystals. *Science* **2017**, *358*, 745-750.

(46) Prasad, P. N., Nanophotonics. *John Wiley & Sons, Inc* **2004**.

(47) Baranowski, M.; Plochocka, P., Excitons in Metal-Halide Perovskites. *Adv. Energy Mater.* **2020**, *10*, 1903659.

(48) Jana, B., Photophysical Studies of Π-Conjugated Organic Molecules Based Functional Nanomaterials. *PhD. Dissertation, Jadavpur University* **2019**.

(49) P. Y. Yu, C. M., Fundamentals of Semiconductors: Physics and Materials Properties, Springer, New Delhi. **2007**.

(50) D'Innocenzo, V.; Grancini, G.; Alcocer, M. J. P.; Kandada, A. R. S.; Stranks, S. D.; Lee, M. M.; Lanzani, G.; Snaith, H. J.; Petrozza, A., Excitons Versus Free Charges in Organo-Lead Tri-Halide Perovskites. *Nat. Commun.* **2014**, *5*, 3586.

(51) Sestu, N.; Cadelano, M.; Sarritzu, V.; Chen, F.; Marongiu, D.; Piras, R.; Mainas, M.; Quochi, F.; Saba, M.; Mura, A., et al., Absorption F-Sum Rule for the Exciton Binding Energy in Methylammonium Lead Halide Perovskites. *J. Phys. Chem. Lett.* **2015**, *6*, 4566-4572.

(52) Phuong, L. Q.; Nakaike, Y.; Wakamiya, A.; Kanemitsu, Y., Free Excitons and Exciton–Phonon Coupling in $CH_3NH_3PbI_3$ Single Crystals Revealed by Photocurrent and Photoluminescence Measurements at Low Temperatures. *J. Phys. Chem. Lett.* **2016**, *7*, 4905-4910.

(53) Jha, A.; Duan, H.-G.; Tiwari, V.; Nayak, P. K.; Snaith, H. J.; Thorwart, M.; Miller, R. J. D., Direct Observation of Ultrafast Exciton Dissociation in Lead Iodide Perovskite by 2d Electronic Spectroscopy. *ACS Photonics* **2018**, *5*, 852-860.

(54) Valverde-Chávez, D. A.; Ponseca, C. S.; Stoumpos, C. C.; Yartsev, A.; Kanatzidis, M. G.; Sundström, V.; Cooke, D. G., Intrinsic Femtosecond Charge Generation Dynamics in Single Crystal $CH_3NH_3PbI_3$. *Energy Environ. Sci.* **2015**, *8*, 3700-3707.

(55) Chen, X.; Lu, H.; Yang, Y.; Beard, M. C., Excitonic Effects in Methylammonium Lead Halide Perovskites. *J. Phys. Chem. Lett.* **2018**, *9*, 2595-2603.

(56) Jiang, Y.; Wang, X.; Pan, A., Properties of Excitons and Photogenerated Charge Carriers in Metal Halide Perovskites. *Adv. Mater.* **2019**, *31*, 1806671.

(57) Herz, L. M., Charge-Carrier Mobilities in Metal Halide Perovskites: Fundamental Mechanisms and Limits. *ACS Energy Lett.* **2017**, *2*, 1539-1548.

(58) Herz, L. M., Charge-Carrier Dynamics in Organic-Inorganic Metal Halide Perovskites. *Annu. Rev. Phys. Chem.* **2016**, *67*, 65-89.

(59) Rossi, D.; Wang, H.; Dong, Y.; Qiao, T.; Qian, X.; Son, D. H., Light-Induced Activation of Forbidden Exciton Transition in Strongly Confined Perovskite Quantum Dots. *ACS Nano* **2018**, *12*, 12436-12443.

(60) Ghosh, T.; Aharon, S.; Shpatz, A.; Etgar, L.; Ruhman, S., Reflectivity Effects on Pump–Probe Spectra of Lead Halide Perovskites: Comparing Thin Films Versus Nanocrystals. *ACS Nano* **2018**, *12*, 5719-5725.

(61) Ghosh, G.; Jana, B.; Sain, S.; Ghosh, A.; Patra, A., Influence of Shape on the Carrier Relaxation Dynamics of $CsPbBr_3$ Perovskite Nanocrystals. *Phys. Chem. Chem. Phys.* **2019**, *21*, 19318-19326.

(62) Yang, Y.; Ostrowski, D. P.; France, R. M.; Zhu, K.; van de Lagemaat, J.; Luther, J. M.; Beard, M. C., Observation of a Hot-Phonon Bottleneck in Lead-Iodide Perovskites. *Nat. Photonics* **2016**, *10*, 53-59.

(63) Ghosh, G.; Dutta, A.; Ghosh, A.; Ghosh, S.; Patra, A., Ultrafast Carrier Dynamics in 2D CdSe Nanoplatelets–$CsPbX_3$ Composites: Influence of the Halide Composition. *J. Phys. Chem. C* **2020**, *124*, 10252-10260.

(64) Wu, K.; Liang, G.; Shang, Q.; Ren, Y.; Kong, D.; Lian, T., Ultrafast Interfacial Electron and Hole Transfer from $CsPbBr_3$ Perovskite Quantum Dots. *J. Am. Chem. Soc.* **2015**, *137*, 12792-12795.

(65) Klimov, V. I., Spectral and Dynamical Properties of Multiexcitons in Semiconductor Nanocrystals. *Annu. Rev. Phys. Chem.* **2007**, *58*, 635-673.

(66) Yumoto, G.; Tahara, H.; Kawawaki, T.; Saruyama, M.; Sato, R.; Teranishi, T.; Kanemitsu, Y., Hot Biexciton Effect on Optical Gain in $CsPbI_3$ Perovskite Nanocrystals. *J. Phys. Chem. Lett.* **2018**, *9*, 2222-2228.

(67) Li, M.; Bhaumik, S.; Goh, T. W.; Kumar, M. S.; Yantara, N.; Grätzel, M.; Mhaisalkar, S.; Mathews, N.; Sum, T. C., Slow Cooling and Highly Efficient Extraction of Hot Carriers in Colloidal Perovskite Nanocrystals. *Nat. Commun.* **2017**, *8*, 14350.

(68) Li, M.; Fu, J.; Xu, Q.; Sum, T. C., Slow Hot-Carrier Cooling in Halide Perovskites: Prospects for Hot-Carrier Solar Cells. *Adv. Mater.* **2019**, *31*, 1802486.

(69) De, A.; Das, S.; Samanta, A., Hot Hole Transfer Dynamics from $CsPbBr_3$ Perovskite Nanocrystals. *ACS Energy Lett.* **2020**, *5*, 2246-2252.

(70) Ghosh, G.; Marjit, K.; Ghosh, S.; Ghosh, A.; Ahammed, R.; De Sarkar, A.; Patra, A., Hot Hole Cooling and Transfer Dynamics from Lead Halide Perovskite Nanocrystals Using Porphyrin Molecules. *J. Phys. Chem. C* **2021**, *125*, 5859-5869.

(71) Chen, J.; Messing, M. E.; Zheng, K.; Pullerits, T., Cation-Dependent Hot Carrier Cooling in Halide Perovskite Nanocrystals. *J. Am. Chem. Soc.* **2019**, *141*, 3532-3540.

(72) Lim, J. W. M.; Giovanni, D.; Righetto, M.; Feng, M.; Mhaisalkar, S. G.; Mathews, N.; Sum, T. C., Hot Carriers in Halide Perovskites: How Hot Truly? *J. Phys. Chem. Lett.* **2020**, *11*, 2743-2750.

(73) Mondal, N.; Samanta, A., Complete Ultrafast Charge Carrier Dynamics in Photo-Excited All-Inorganic Perovskite Nanocrystals ($CsPbX_3$). *Nanoscale* **2017**, *9*, 1878-1885.

(74) Jin, H.; Debroye, E.; Keshavarz, M.; Scheblykin, I. G.; Roeffaers, M. B. J.; Hofkens, J.; Steele, J. A., It's a Trap! On the Nature of Localised States and Charge Trapping in Lead Halide Perovskites. *Mater. Horiz.* **2020**, *7*, 397-410.

(75) deQuilettes, D. W.; Frohna, K.; Emin, D.; Kirchartz, T.; Bulovic, V.; Ginger, D. S.; Stranks, S. D., Charge-Carrier Recombination in Halide Perovskites. *Chem. Rev.* **2019**, *119*, 11007-11019.

(76) Dey, A.; Rathod, P.; Kabra, D., Role of Localized States in Photoluminescence Dynamics of High Optical Gain $CsPbBr_3$ Nanocrystals. *Adv. Opt. Mater.* **2018**, *6*, 1800109.

(77) Liu, F.; Zhang, Y.; Ding, C.; Toyoda, T.; Ogomi, Y.; Ripolles, T. S.; Hayase, S.; Minemoto, T.; Yoshino, K.; Dai, S., et al., Ultrafast Electron Injection from Photoexcited Perovskite $CsPbI_3$ Qds into Tio2 Nanoparticles with Injection Efficiency near 99%. *J. Phys. Chem. Lett.* **2018**, *9*, 294-297.

(78) Liu, F.; Zhang, Y.; Ding, C.; Kobayashi, S.; Izuishi, T.; Nakazawa, N.; Toyoda, T.; Ohta, T.; Hayase, S.; Minemoto, T., et al., Highly Luminescent Phase-Stable $CsPbI_3$ Perovskite Quantum Dots Achieving near 100% Absolute Photoluminescence Quantum Yield. *ACS Nano* **2017**, *11*, 10373-10383.

(79) Nenon, D. P.; Pressler, K.; Kang, J.; Koscher, B. A.; Olshansky, J. H.; Osowiecki, W. T.; Koc, M. A.; Wang, L.-W.; Alivisatos, A. P., Design Principles for Trap-Free $CsPbX_3$ Nanocrystals: Enumerating and Eliminating Surface Halide Vacancies with Softer Lewis Bases. *J. Am. Chem. Soc.* **2018**, *140*, 17760-17772.

(80) Yang, D.; Li, X.; Zhou, W.; Zhang, S.; Meng, C.; Wu, Y.; Wang, Y.; Zeng, H., $Cspbbr_3$ Quantum Dots 2.0: Benzenesulfonic Acid Equivalent Ligand Awakens Complete Purification. *Adv. Mater.* **2019**, *31*, 1900767.

(81) Lai, R.; Wu, K., Picosecond Electron Trapping Limits the Emissivity of $CsPbCl_3$ Perovskite Nanocrystals. *J. Chem. Phys.* **2019**, *151*, 194701.

(82) De, A.; Das, S.; Mondal, N.; Samanta, A., Highly Luminescent Violet- and Blue-Emitting Stable Perovskite Nanocrystals. *ACS Materials Lett.* **2019**, *1*, 116-122.

(83) Makarov, N. S.; Guo, S.; Isaienko, O.; Liu, W.; Robel, I.; Klimov, V. I., Spectral and Dynamical Properties of Single Excitons, Biexcitons, and Trions in Cesium–Lead-Halide Perovskite Quantum Dots. *Nano Lett.* **2016**, *16*, 2349-2362.

(84) Klimov, V. I.; Mikhailovsky, A. A.; McBranch, D. W.; Leatherdale, C. A.; Bawendi, M. G., Quantization of Multiparticle Auger Rates in Semiconductor Quantum Dots. *Science* **2000**, *287*, 1011-1013.

(85) Schaller, R. D.; Klimov, V. I., High Efficiency Carrier Multiplication in PbSe Nanocrystals: Implications for Solar Energy Conversion. *Phys. Rev. Lett.* **2004**, *92*, 186601.

(86) Kambhampati, P., Hot Exciton Relaxation Dynamics in Semiconductor Quantum Dots: Radiationless Transitions on the Nanoscale. *J. Phys. Chem. C* **2011**, *115*, 22089-22109.

(87) Aneesh, J.; Swarnkar, A.; Kumar Ravi, V.; Sharma, R.; Nag, A.; Adarsh, K. V., Ultrafast Exciton Dynamics in Colloidal $CsPbBr_3$ Perovskite Nanocrystals: Biexciton Effect and Auger Recombination. *J. Phys. Chem. C* **2017**, *121*, 4734-4739.

(88) de Jong, E. M. L. D.; Yamashita, G.; Gomez, L.; Ashida, M.; Fujiwara, Y.; Gregorkiewicz, T., Multiexciton Lifetime in All-Inorganic $CsPbBr_3$ Perovskite Nanocrystals. *J. Phys. Chem. C* **2017**, *121*, 1941-1947.

(89) Eperon, G. E.; Jedlicka, E.; Ginger, D. S., Biexciton Auger Recombination Differs in Hybrid and Inorganic Halide Perovskite Quantum Dots. *J. Phys. Chem. Lett.* **2018**, *9*, 104-109.

(90) Castañeda, J. A.; Nagamine, G.; Yassitepe, E.; Bonato, L. G.; Voznyy, O.; Hoogland, S.; Nogueira, A. F.; Sargent, E. H.; Cruz, C. H. B.; Padilha, L. A., Efficient Biexciton Interaction in Perovskite Quantum Dots under Weak and Strong Confinement. *ACS Nano* **2016**, *10*, 8603-8609.

(91) Mondal, N.; De, A.; Samanta, A., Biexciton Generation and Dissociation Dynamics in Formamidinium- and Chloride-Doped Cesium Lead Iodide Perovskite Nanocrystals. *J. Phys. Chem. Lett.* **2018**, *9*, 3673-3679.

(92) Yarita, N.; Tahara, H.; Saruyama, M.; Kawawaki, T.; Sato, R.; Teranishi, T.; Kanemitsu, Y., Impact of Postsynthetic Surface Modification on Photoluminescence Intermittency in Formamidinium Lead Bromide Perovskite Nanocrystals. *J. Phys. Chem. Lett.* **2017**, *8*, 6041-6047.

(93) Seth, S.; Ahmed, T.; Samanta, A., Photoluminescence Flickering and Blinking of Single $CsPbBr_3$ Perovskite Nanocrystals: Revealing Explicit Carrier Recombination Dynamics. *J. Phys. Chem. Lett.* **2018**, *9*, 7007-7014.

(94) Yarita, N.; Tahara, H.; Ihara, T.; Kawawaki, T.; Sato, R.; Saruyama, M.; Teranishi, T.; Kanemitsu, Y., Dynamics of Charged Excitons and Biexcitons in $CsPbBr_3$ Perovskite Nanocrystals Revealed by Femtosecond Transient-Absorption and Single-Dot Luminescence Spectroscopy. *J. Phys. Chem. Lett.* **2017**, *8*, 1413-1418.

(95) Kanemitsu, Y., Trion Dynamics in Lead Halide Perovskite Nanocrystals. *J. Chem. Phys.* **2019**, *151*, 170902.

(96) Nrel Best Research-Cell Efficiencies. https://www.nrel.gov/pv/assets/pdfs/best-research-cell-efficiencies.20200104.pdf.

(97) Kahmann, S.; Loi, M. A., Hot Carrier Solar Cells and the Potential of Perovskites for Breaking the Shockley–Queisser Limit. *J. Mater. Chem. C* **2019**, *7*, 2471-2486.

(98) Paul, K. K.; Kim, J.-H.; Lee, Y. H., Hot Carrier Photovoltaics in Van Der Waals Heterostructures. *Nat. Rev. Phys.* **2021**, *3*, 178-192.

(99) Nozik, A. J., Spectroscopy and Hot Electron Relaxation Dynamics in Semiconductor Quantum Wells and Quantum Dots. *Annu. Rev. Phys. Chem.* **2001**, *52*, 193-231.

(100) Green, M. A., Third Generation Photovoltaics: Ultra-High Conversion Efficiency at Low Cost. *Prog. Photovoltaics* **2001**, *9*, 123-135.

(101) Shockley, W.; Queisser, H. J., Detailed Balance Limit of Efficiency of P-N Junction Solar Cells. *J. Appl. Phys.* **1961**, *32*, 510-519.

(102) Ross, R. T.; Nozik, A. J., Efficiency of Hot-Carrier Solar Energy Converters. *J. Appl. Phys.* **1982**, *53*, 3813-3818.

(103) Guo, Z.; Wan, Y.; Yang, M.; Snaider, J.; Zhu, K.; Huang, L., Long-Range Hot-Carrier Transport in Hybrid Perovskites Visualized by Ultrafast Microscopy. *Science* **2017**, *356*, 59-62.

(104) Richter, J. M.; Branchi, F.; Valduga de Almeida Camargo, F.; Zhao, B.; Friend, R. H.; Cerullo, G.; Deschler, F., Ultrafast Carrier Thermalization in Lead Iodide Perovskite Probed with Two-Dimensional Electronic Spectroscopy. *Nat. Commun.* **2017**, *8*, 376.

(105) Nie, Z.; Gao, X.; Ren, Y.; Xia, S.; Wang, Y.; Shi, Y.; Zhao, J.; Wang, Y., Harnessing Hot Phonon Bottleneck in Metal Halide Perovskite Nanocrystals Via Interfacial Electron–Phonon Coupling. *Nano Lett.* **2020**, *20*, 4610-4617.

(106) Zhu, H.; Miyata, K.; Fu, Y.; Wang, J.; Joshi, P. P.; Niesner, D.; Williams, K. W.; Jin, S.; Zhu, X. Y., Screening in Crystalline Liquids Protects Energetic Carriers in Hybrid Perovskites. *Science* **2016**, *353*, 1409-1413.

(107) Xing, G.; Mathews, N.; Sun, S.; Lim, S. S.; Lam, Y. M.; Grätzel, M.; Mhaisalkar, S.; Sum, T. C., Long-Range Balanced Electron- and Hole-Transport Lengths in Organic-Inorganic $CH_3NH_3PbI_3$. *Science* **2013**, *342*, 344-347.

(108) Sum, T. C.; Mathews, N.; Xing, G.; Lim, S. S.; Chong, W. K.; Giovanni, D.; Dewi, H. A., Spectral Features and Charge Dynamics of Lead Halide Perovskites: Origins and Interpretations. *Acc. Chem. Res.* **2016**, *49*, 294-302.

(109) Yang, J.; Wen, X.; Xia, H.; Sheng, R.; Ma, Q.; Kim, J.; Tapping, P.; Harada, T.; Kee, T. W.; Huang, F., et al., Acoustic-Optical Phonon up-Conversion and Hot-Phonon Bottleneck in Lead-Halide Perovskites. *Nat. Commun.* **2017**, *8*, 14120.

(110) Price, M. B.; Butkus, J.; Jellicoe, T. C.; Sadhanala, A.; Briane, A.; Halpert, J. E.; Broch, K.; Hodgkiss, J. M.; Friend, R. H.; Deschler, F., Hot-Carrier Cooling and Photoinduced Refractive Index Changes in Organic–Inorganic Lead Halide Perovskites. *Nat. Commun.* **2015**, *6*, 8420.

(111) Papagiorgis, P.; Protesescu, L.; Kovalenko, M. V.; Othonos, A.; Itskos, G., Long-Lived Hot Carriers in Formamidinium Lead Iodide Nanocrystals. *J. Phys. Chem. C* **2017**, *121*, 12434-12440.

(112) Fu, J.; Xu, Q.; Han, G.; Wu, B.; Huan, C. H. A.; Leek, M. L.; Sum, T. C., Hot Carrier Cooling Mechanisms in Halide Perovskites. *Nat. Commun.* **2017**, *8*, 1300.

(113) Nah, S.; Spokoyny, B. M.; Soe, C. M. M.; Stoumpos, C. C.; Kanatzidis, M. G.; Harel, E., Ultrafast Imaging of Carrier Cooling in Metal Halide Perovskite Thin Films. *Nano Lett.* **2018**, *18*, 1044-1048.

(114) Chen, K.; Barker, A. J.; Morgan, F. L. C.; Halpert, J. E.; Hodgkiss, J. M., Effect of Carrier Thermalization Dynamics on Light Emission and Amplification in Organometal Halide Perovskites. *J. Phys. Chem. Lett.* **2015**, *6*, 153-158.

(115) Hopper, T. R.; Gorodetsky, A.; Frost, J. M.; Müller, C.; Lovrincic, R.; Bakulin, A. A., Ultrafast Intraband Spectroscopy of Hot-Carrier Cooling in Lead-Halide Perovskites. *ACS Energy Lett.* **2018**, *3*, 2199-2205.

(116) Madjet, M. E.; Berdiyorov, G. R.; El-Mellouhi, F.; Alharbi, F. H.; Akimov, A. V.; Kais, S., Cation Effect on Hot Carrier Cooling in Halide Perovskite Materials. *J. Phys. Chem. Lett.* **2017**, *8*, 4439-4445.

(117) Chung, H.; Jung, S. I.; Kim, H. J.; Cha, W.; Sim, E.; Kim, D.; Koh, W.-K.; Kim, J., Composition-Dependent Hot Carrier Relaxation Dynamics in Cesium Lead Halide ($CsPbX_3$, X=Br and I) Perovskite Nanocrystals. *Angew. Chem. Int. Ed.* **2017**, *56*, 4160-4164.

(118) Wei, Q.; Yin, J.; Bakr, O. M.; Wang, Z.; Wang, C.; Mohammed, O. F.; Li, M.; Xing, G., Effect of Zinc-Doping on the Reduction of the Hot-Carrier Cooling Rate in Halide Perovskites. *Angew. Chem. Int. Ed.* **2021**, *60*, 10957-10963.

(119) Mondal, A.; Aneesh, J.; Kumar Ravi, V.; Sharma, R.; Mir, W. J.; Beard, M. C.; Nag, A.; Adarsh, K. V., Ultrafast Exciton Many-Body Interactions and Hot-Phonon Bottleneck in Colloidal Cesium Lead Halide Perovskite Nanocrystals. *Phys. Rev. B* **2018**, *98*, 115418.

(120) Prabhu, S. S.; Vengurlekar, A. S., Hot-Carrier Energy-Loss Rates in Alloy Semiconductors. *Phys. Rev. B* **1996**, *53*, 7815-7818.

(121) Choi, C. K.; Kwon, Y. H.; Krasinski, J. S.; Park, G. H.; Setlur, G.; Song, J. J.; Chang, Y. C., Ultrafast Carrier Dynamics in a Highly Excited Gan Epilayer. *Phys. Rev. B* **2001**, *63*, 115315.

(122) Klimov, V.; Haring Bolivar, P.; Kurz, H., Hot-Phonon Effects in Femtosecond Luminescence Spectra of Electron-Hole Plasmas in Cds. *Phys. Rev. B: Condens. Matter Mater. Phys.* **1995**, *52*, 4728-4731.

(123) Wen, Y.-C.; Chen, C.-Y.; Shen, C.-H.; Gwo, S.; Sun, C.-K., Ultrafast Carrier Thermalization in Inn. *Appl. Phys. Lett.* **2006**, *89*, 232114.

(124) Achermann, M.; Bartko, A. P.; Hollingsworth, J. A.; Klimov, V. I., The Effect of Auger Heating on Intraband Carrier Relaxation in Semiconductor Quantum Rods. *Nat. Phys.* **2006**, *2*, 557-561.

(125) Downer, M. C.; Shank, C. V., Ultrafast Heating of Silicon on Sapphire by Femtosecond Optical Pulses. *Phys. Rev. Lett.* **1986**, *56*, 761-764.

(126) Beattie, A. R., Auger Transitions in Semiconductors and Their Computation. *J. Phys. C: Solid State Phys.* **1985**, *18*, 6501-6515.

(127) Kaur, G.; Justice Babu, K.; Ghorai, N.; Goswami, T.; Maiti, S.; Ghosh, H. N., Polaron-Mediated Slow Carrier Cooling in a Type-1 3D/0D $CsPbBr_3@Cs_4PbBr_6$ Core–Shell Perovskite System. *J. Phys. Chem. Lett.* **2019**, *10*, 5302-5311.

(128) Miyata, K.; Meggiolaro, D.; Trinh, M. T.; Joshi, P. P.; Mosconi, E.; Jones, S. C.; Angelis, F. D.; Zhu, X.-Y., Large Polarons in Lead Halide Perovskites. *Sci. Adv.* **2017**, *3*, e1701217.

(129) Savenije, T. J.; Ponseca, C. S.; Kunneman, L.; Abdellah, M.; Zheng, K.; Tian, Y.; Zhu, Q.; Canton, S. E.; Scheblykin, I. G.; Pullerits, T., et al., Thermally Activated Exciton Dissociation and Recombination Control the Carrier Dynamics in Organometal Halide Perovskite. *J. Phys. Chem. Lett.* **2014**, *5*, 2189-2194.

(130) Manser, J. S.; Kamat, P. V., Band Filling with Free Charge Carriers in Organometal Halide Perovskites. *Nat. Photonics* **2014**, *8*, 737-743.

(131) Fang, H.-H.; Adjokatse, S.; Shao, S.; Even, J.; Loi, M. A., Long-Lived Hot-Carrier Light Emission and Large Blue Shift in Formamidinium Tin Triiodide Perovskites. *Nat. Commun.* **2018**, *9*, 243.

(132) Bockelmann, U.; Bastard, G., Phonon Scattering and Energy Relaxation in Two-, One-, and Zero-Dimensional Electron Gases. *Phys. Rev. B* **1990**, *42*, 8947-8951.

(133) Kelly, K. L.; Coronado, E.; Zhao, L. L.; Schatz, G. C., The Optical Properties of Metal Nanoparticles: The Influence of Size, Shape, and Dielectric Environment. *J. Phys. Chem. B* **2003**, *107*, 668-677.

(134) Binz, B.; Vishwanath, A.; Aji, V., Theory of the Helical Spin Crystal: A Candidate for the Partially Ordered State of Mnsi. *Phys. Rev. Lett.* **2006**, *96*, 207202.

(135) Sarkar, S.; Ravi, V. K.; Banerjee, S.; Yettapu, G. R.; Markad, G. B.; Nag, A.; Mandal, P., Terahertz Spectroscopic Probe of Hot Electron and Hole Transfer from Colloidal $CsPbBr_3$ Perovskite Nanocrystals. *Nano Lett.* **2017**, *17*, 5402-5407.

(136) Peng, B.; Yu, G.; Zhao, Y.; Xu, Q.; Xing, G.; Liu, X.; Fu, D.; Liu, B.; Tan, J. R. S.; Tang, W., et al., Achieving Ultrafast Hole Transfer at the Monolayer MoS_2 and $CH_3NH_3PbI_3$ Perovskite Interface by Defect Engineering. *ACS Nano* **2016**, *10*, 6383-6391.

(137) Dursun, I.; Maity, P.; Yin, J.; Turedi, B.; Zhumekenov, A. A.; Lee, K. J.; Mohammed, O. F.; Bakr, O. M., Why Are Hot Holes Easier to Extract Than Hot Electrons from Methylammonium Lead Iodide Perovskite? *Adv. Energy Mater.* **2019**, *9*, 1900084.

(138) Shen, Q.; Ripolles, T. S.; Even, J.; Zhang, Y.; Ding, C.; Liu, F.; Izuishi, T.; Nakazawa, N.; Toyoda, T.; Ogomi, Y., et al., Ultrafast Selective Extraction of Hot Holes from Cesium Lead Iodide Perovskite Films. *J. Energy Chem.* **2018**, *27*, 1170-1174.

(139) Lim, S. S.; Giovanni, D.; Zhang, Q.; Solanki, A.; Jamaludin, N. F.; Lim, J. W. M.; Mathews, N.; Mhaisalkar, S.; Pshenichnikov, M. S.; Sum, T. C., Hot Carrier Extraction in $CH_3NH_3PbI_3$ Unveiled by Pump-Push-Probe Spectroscopy. *Sci. Adv.* **2019**, *5*, eaax3620.

(140) Kulbak, M.; Cahen, D.; Hodes, G., How Important Is the Organic Part of Lead Halide Perovskite Photovoltaic Cells? Efficient Cspbbr3 Cells. *J. Phys. Chem. Lett.* **2015**, *6*, 2452-2456.

(141) Kulbak, M.; Gupta, S.; Kedem, N.; Levine, I.; Bendikov, T.; Hodes, G.; Cahen, D., Cesium Enhances Long-Term Stability of Lead Bromide Perovskite-Based Solar Cells. *J. Phys. Chem. Lett.* **2016**, *7*, 167-172.

(142) Greenham, N. C.; Peng, X.; Alivisatos, A. P., Charge Separation and Transport in Conjugated-Polymer/Semiconductor-Nanocrystal Composites Studied by Photoluminescence Quenching and Photoconductivity. *Phys. Rev. B* **1996**, *54*, 17628-17637.

(143) Xu, Z.; Hine, C. R.; Maye, M. M.; Meng, Q.; Cotlet, M., Shell Thickness Dependent Photoinduced Hole Transfer in Hybrid Conjugated Polymer/Quantum Dot Nanocomposites: From Ensemble to Single Hybrid Level. *ACS Nano* **2012**, *6*, 4984-4992.

(144) Ahmed, G. H.; Liu, J.; Parida, M. R.; Murali, B.; Bose, R.; AlYami, N. M.; Hedhili, M. N.; Peng, W.; Pan, J.; Besong, T. M. D., et al., Shape-Tunable Charge Carrier Dynamics at the Interfaces between Perovskite Nanocrystals and Molecular Acceptors. *J. Phys. Chem. Lett.* **2016**, *7*, 3913-3919.

(145) Begum, R.; Parida, M. R.; Abdelhady, A. L.; Murali, B.; Alyami, N. M.; Ahmed, G. H.; Hedhili, M. N.; Bakr, O. M.; Mohammed, O. F., Engineering Interfacial Charge Transfer in $CsPbBr_3$ Perovskite Nanocrystals by Heterovalent Doping. *J. Am. Chem. Soc.* **2017**, *139*, 731-737.

(146) Wang, J.; Ding, T.; Leng, J.; Jin, S.; Wu, K., "Intact" Carrier Doping by Pump–Pump–Probe Spectroscopy in Combination with Interfacial Charge Transfer: A Case Study of Cspbbr3 Nanocrystals. *J. Phys. Chem. Lett.* **2018**, *9*, 3372-3377.

(147) Luo, X.; Liang, G.; Wang, J.; Liu, X.; Wu, K., Picosecond Multi-Hole Transfer and Microsecond Charge-Separated States at the Perovskite Nanocrystal/Tetracene Interface. *Chem. Sci.* **2019**, *10*, 2459-2464.

(148) Maity, P.; Dana, J.; Ghosh, H. N., Multiple Charge Transfer Dynamics in Colloidal $CsPbBr_3$ Perovskite Quantum Dots Sensitized Molecular Adsorbate. *J. Phys. Chem. C* **2016**, *120*, 18348-18354.

(149) De, A.; Mondal, N.; Samanta, A., Hole Transfer Dynamics from Photoexcited Cesium Lead Halide Perovskite Nanocrystals: 1-Aminopyrene as Hole Acceptor. *J. Phys. Chem. C* **2018**, *122*, 13617-13623.

(150) Nair, V. C.; Muthu, C.; Rogach, A. L.; Kohara, R.; Biju, V., Channeling Exciton Migration into Electron Transfer in Formamidinium Lead Bromide Perovskite Nanocrystal/Fullerene Composites. *Angew. Chem., Int. Ed.* **2017**, *56*, 1214-1218.

(151) Mandal, S.; George, L.; Tkachenko, N. V., Charge Transfer Dynamics in Cspbbr3 Perovskite Quantum Dots–Anthraquinone/Fullerene (C_{60}) Hybrids. *Nanoscale* **2019**, *11*, 862-869.

(152) Dana, J.; Maity, P.; Jana, B.; Maiti, S.; Ghosh, H. N., Concurrent Ultrafast Electron- and Hole-Transfer Dynamics in Cspbbr3 Perovskite and Quantum Dots. *ACS Omega* **2018**, *3*, 2706-2714.

(153) Brumberg, A.; Diroll, B. T.; Nedelcu, G.; Sykes, M. E.; Liu, Y.; Harvey, S. M.; Wasielewski, M. R.; Kovalenko, M. V.; Schaller, R. D., Material Dimensionality Effects on Electron Transfer Rates between $CsPbBr_3$ and CdSe Nanoparticles. *Nano Lett.* **2018**, *18*, 4771-4776.

(154) Ding, J.; Duan, J.; Guo, C.; Tang, Q., Toward Charge Extraction in All-Inorganic Perovskite Solar Cells by Interfacial Engineering. *J. Mater. Chem. A* **2018**, *6*, 21999-22004.

(155) Scheidt, R. A.; Kerns, E.; Kamat, P. V., Interfacial Charge Transfer between Excited $CsPbBr_3$ Nanocrystals and TiO_2: Charge Injection Versus Photodegradation. *J. Phys. Chem. Lett.* **2018**, *9*, 5962-5969.

(156) Najafi, L.; Taheri, B.; Martín-García, B.; Bellani, S.; Di Girolamo, D.; Agresti, A.; Oropesa-Nuñez, R.; Pescetelli, S.; Vesce, L.; Calabrò, E., et al., MoS_2 Quantum Dot/Graphene Hybrids for Advanced Interface Engineering of a $CH_3NH_3PbI_3$ Perovskite Solar Cell with an Efficiency of over 20%. *ACS Nano* **2018**, *12*, 10736-10754.

(157) Lee, M. M.; Teuscher, J.; Miyasaka, T.; Murakami, T. N.; Snaith, H. J., Efficient Hybrid Solar Cells Based on Meso-Superstructured Organometal Halide Perovskites. *Science* **2012**, *338*, 643-647.

(158) Zhou, Y.; Zhu, K., Perovskite Solar Cells Shine in the "Valley of the Sun". *ACS Energy Lett.* **2016**, *1*, 64-67.

(159) National Renewable Energy Laboratory Best Research-Cell Efficiencies. *https://www.nrel.gov/pv/assets/pdfs/best-research-cell-efficiencies.20200406.pdf*.

(160) Yao, H.; Zhou, F.; Li, Z.; Ci, Z.; Ding, L.; Jin, Z., Strategies for Improving the Stability of Tin-Based Perovskite ($ASnX_3$) Solar Cells. *Adv. Sci.* **2020**, *7*, 1903540.

(161) Liu, C.; Zeng, Q.; Zhao, Y.; Yu, Y.; Yang, M.; Gao, H.; Wei, H.; Yang, B., Surface Ligands Management for Efficient $CsPbBrI_2$ Perovskite Nanocrystal Solar Cells. *Solar RRL* **2020**, *4*, 2000102.

(162) Swarnkar, A.; Marshall, A. R.; Sanehira, E. M.; Chernomordik, B. D.; Moore, D. T.; Christians, J. A.; Chakrabarti, T.; Luther, J. M., Quantum Dot Induced Phase Stabilization of $CsPbI_3$ Perovskite for High-Efficiency Photovoltaics. *Science* **2016**, *354*, 92-95.

(163) Im, J.-H.; Luo, J.; Franckevičius, M.; Pellet, N.; Gao, P.; Moehl, T.; Zakeeruddin, S. M.; Nazeeruddin, M. K.; Grätzel, M.; Park, N.-G., Nanowire Perovskite Solar Cell. *Nano Lett.* **2015**, *15*, 2120-2126.

(164) Mali, S. S.; Shim, C. S.; Hong, C. K., Highly Stable and Efficient Solid-State Solar Cells Based on Methylammonium Lead Bromide ($CH_3NH_3PbBr_3$) Perovskite Quantum Dots. *NPG Asia Mater.* **2015**, *7*, e208-e208.

(165) Suri, M.; Hazarika, A.; Larson, B. W.; Zhao, Q.; Vallés-Pelarda, M.; Siegler, T. D.; Abney, M. K.; Ferguson, A. J.; Korgel, B. A.; Luther, J. M., Enhanced Open-Circuit Voltage of Wide-Bandgap Perovskite Photovoltaics by Using Alloyed ($FA_{1-x}Cs_x$)$Pb(I_{1-X}Br_x)_3$ Quantum Dots. *ACS Energy Lett.* **2019**, *4*, 1954-1960.

(166) Hao, M.; Bai, Y.; Zeiske, S.; Ren, L.; Liu, J.; Yuan, Y.; Zarrabi, N.; Cheng, N.; Ghasemi, M.; Chen, P., et al., Ligand-Assisted Cation-Exchange Engineering for High-Efficiency Colloidal $Cs_{1-X}FA_xPbI_3$ Quantum Dot Solar Cells with Reduced Phase Segregation. *Nat. Energy* **2020**, *5*, 79-88.

(167) Yan, F.; Demir, H. V., Leds Using Halide Perovskite Nanocrystal Emitters. *Nanoscale* **2019**, *11*, 11402-11412.

(168) Song, J.; Fang, T.; Li, J.; Xu, L.; Zhang, F.; Han, B.; Shan, Q.; Zeng, H., Organic–Inorganic Hybrid Passivation Enables Perovskite Qleds with an Eqe of 16.48%. *Adv. Mater.* **2018**, *30*, 1805409.

(169) Lin, K.; Xing, J.; Quan, L. N.; de Arquer, F. P. G.; Gong, X.; Lu, J.; Xie, L.; Zhao, W.; Zhang, D.; Yan, C., et al., Perovskite Light-Emitting Diodes with External Quantum Efficiency Exceeding 20 Per Cent. *Nature* **2018**, *562*, 245-248.

(170) Luo, J.; Wang, X.; Li, S.; Liu, J.; Guo, Y.; Niu, G.; Yao, L.; Fu, Y.; Gao, L.; Dong, Q., et al., Efficient and Stable Emission of Warm-White Light from Lead-Free Halide Double Perovskites. *Nature* **2018**, *563*, 541-545.

(171) Xiao, P.; Huang, J.; Yan, D.; Luo, D.; Yuan, J.; Liu, B.; Liang, D., Emergence of Nanoplatelet Light-Emitting Diodes. *Materials* **2018**, *11*, 1376.

(172) Tan, Z.-K.; Moghaddam, R. S.; Lai, M. L.; Docampo, P.; Higler, R.; Deschler, F.; Price, M.; Sadhanala, A.; Pazos, L. M.; Credgington, D., et al., Bright Light-Emitting Diodes Based on Organometal Halide Perovskite. *Nat. Nanotechnol.* **2014**, *9*, 687-692.

(173) Palazon, F.; Di Stasio, F.; Akkerman, Q. A.; Krahne, R.; Prato, M.; Manna, L., Polymer-Free Films of Inorganic Halide Perovskite Nanocrystals as UV-to-White Color-Conversion Layers in Leds. *Chem. Mater.* **2016**, *28*, 2902-2906.

(174) Di, D.; Musselman, K. P.; Li, G.; Sadhanala, A.; Ievskaya, Y.; Song, Q.; Tan, Z.-K.; Lai, M. L.; MacManus-Driscoll, J. L.; Greenham, N. C., et al., Size-Dependent Photon Emission from Organometal Halide Perovskite Nanocrystals Embedded in an Organic Matrix. *J. Phys. Chem. Lett.* **2015**, *6*, 446-450.

(175) Vashishtha, P.; Halpert, J. E., Field-Driven Ion Migration and Color Instability in Red-Emitting Mixed Halide Perovskite Nanocrystal Light-Emitting Diodes. *Chem. Mater.* **2017**, *29*, 5965-5973.

(176) Wang, H.; Kim, D. H., Perovskite-Based Photodetectors: Materials and Devices. *Chem. Soc. Rev.* **2017**, *46*, 5204-5236.

(177) Ahmadi, M.; Wu, T.; Hu, B., A Review on Organic–Inorganic Halide Perovskite Photodetectors: Device Engineering and Fundamental Physics. *Adv. Mater.* **2017**, *29*, 1605242.

(178) Jing, H.; Peng, R.; Ma, R.-M.; He, J.; Zhou, Y.; Yang, Z.; Li, C.-Y.; Liu, Y.; Guo, X.; Zhu, Y., et al., Flexible Ultrathin Single-Crystalline Perovskite Photodetector. *Nano Lett.* **2020**, *20*, 7144-7151.

(179) Hu, X.; Zhang, X.; Liang, L.; Bao, J.; Li, S.; Yang, W.; Xie, Y., High-Performance Flexible Broadband Photodetector Based on Organolead Halide Perovskite. *Adv. Funct. Mater.* **2014**, *24*, 7373-7380.

(180) Ramasamy, P.; Lim, D.-H.; Kim, B.; Lee, S.-H.; Lee, M.-S.; Lee, J.-S., All-Inorganic Cesium Lead Halide Perovskite Nanocrystals for Photodetector Applications. *Chem. Commun.* **2016**, *52*, 2067-2070.

(181) Li, X.; Yu, D.; Chen, J.; Wang, Y.; Cao, F.; Wei, Y.; Wu, Y.; Wang, L.; Zhu, Y.; Sun, Z., et al., Constructing Fast Carrier Tracks into Flexible Perovskite Photodetectors to Greatly Improve Responsivity. *ACS Nano* **2017**, *11*, 2015-2023.

(182) Lewis, N. S.; Nocera, D. G., Powering the Planet: Chemical Challenges in Solar Energy Utilization. *Proc. Natl. Acad. Sci. U. S. A.* **2006**, *103*, 15729-15735.

(183) Huynh, K. A.; Nguyen, D. L. T.; Nguyen, V.-H.; Vo, D.-V. N.; Trinh, Q. T.; Nguyen, T. P.; Kim, S. Y.; Le, Q. V., Halide Perovskite Photocatalysis: Progress and Perspectives. *J. Chem.Technol. Biotechnol.* **2020**, *95*, 2579-2596.

(184) Park, S.; Chang, W. J.; Lee, C. W.; Park, S.; Ahn, H.-Y.; Nam, K. T., Photocatalytic Hydrogen Generation from Hydriodic Acid Using Methylammonium Lead Iodide in Dynamic Equilibrium with Aqueous Solution. *Nat. Energy* **2016**, *2*, 16185.

(185) Cardenas-Morcoso, D.; Gualdrón-Reyes, A. F.; Ferreira Vitoreti, A. B.; García-Tecedor, M.; Yoon, S. J.; Solis de la Fuente, M.; Mora-Seró, I.; Gimenez, S., Photocatalytic and Photoelectrochemical Degradation of Organic Compounds with All-Inorganic Metal Halide Perovskite Quantum Dots. *J. Phys. Chem. Lett.* **2019**, *10*, 630-636.

(186) Wu, Y.; Wang, P.; Guan, Z.; Liu, J.; Wang, Z.; Zheng, Z.; Jin, S.; Dai, Y.; Whangbo, M.-H.; Huang, B., Enhancing the Photocatalytic Hydrogen Evolution Activity of Mixed-Halide Perovskite $CH_3NH_3PbBr_{3-X}I_x$ Achieved by Bandgap Funneling of Charge Carriers. *ACS Catal.* **2018**, *8*, 10349-10357.

(187) Ou, M.; Tu, W.; Yin, S.; Xing, W.; Wu, S.; Wang, H.; Wan, S.; Zhong, Q.; Xu, R., Amino-Assisted Anchoring of $CsPbBr_3$ Perovskite Quantum Dots on Porous G-C_3N_4 for Enhanced Photocatalytic CO_2 Reduction. *Angew. Chem., Int. Ed.* **2018**, *57*, 13570-13574.

(188) Wu, L.-Y.; Mu, Y.-F.; Guo, X.-X.; Zhang, W.; Zhang, Z.-M.; Zhang, M.; Lu, T.-B., Encapsulating Perovskite Quantum Dots in Iron-Based Metal–Organic Frameworks (Mofs) for Efficient Photocatalytic Co2 Reduction. *Angew. Chem., Int. Ed.* **2019**, *58*, 9491-9495.

(189) Zhu, X.; Lin, Y.; San Martin, J.; Sun, Y.; Zhu, D.; Yan, Y., Lead Halide Perovskites for Photocatalytic Organic Synthesis. *Nat Commun* **2019**, *10*, 2843.

(190) Zhu, X.; Lin, Y.; Sun, Y.; Beard, M. C.; Yan, Y., Lead-Halide Perovskites for Photocatalytic A-Alkylation of Aldehydes. *J. Am. Chem. Soc.* **2019**, *141*, 733-738.

(191) Wei, Q.; Ning, Z., Chiral Perovskite Spin-Optoelectronics and Spintronics: Toward Judicious Design and Application. *ACS Materials Lett.* **2021**, *3*, 1266-1275.

(192) Wang, K.; Wang, S.; Xiao, S.; Song, Q., Recent Advances in Perovskite Micro- and Nanolasers. *Adv. Opt. Mater.* **2018**, *6*, 1800278.

(193) Birowosuto, M. D.; Cortecchia, D.; Drozdowski, W.; Brylew, K.; Lachmanski, W.; Bruno, A.; Soci, C., X-Ray Scintillation in Lead Halide Perovskite Crystals. *Sci Rep* **2016**, *6*, 37254.

(194) Matsushima, T.; Hwang, S.; Sandanayaka, A. S. D.; Qin, C.; Terakawa, S.; Fujihara, T.; Yahiro, M.; Adachi, C., Solution-Processed Organic–Inorganic Perovskite Field-Effect Transistors with High Hole Mobilities. *Adv. Mat.* **2016**, *28*, 10275-10281.

Chapter 2

Methodology

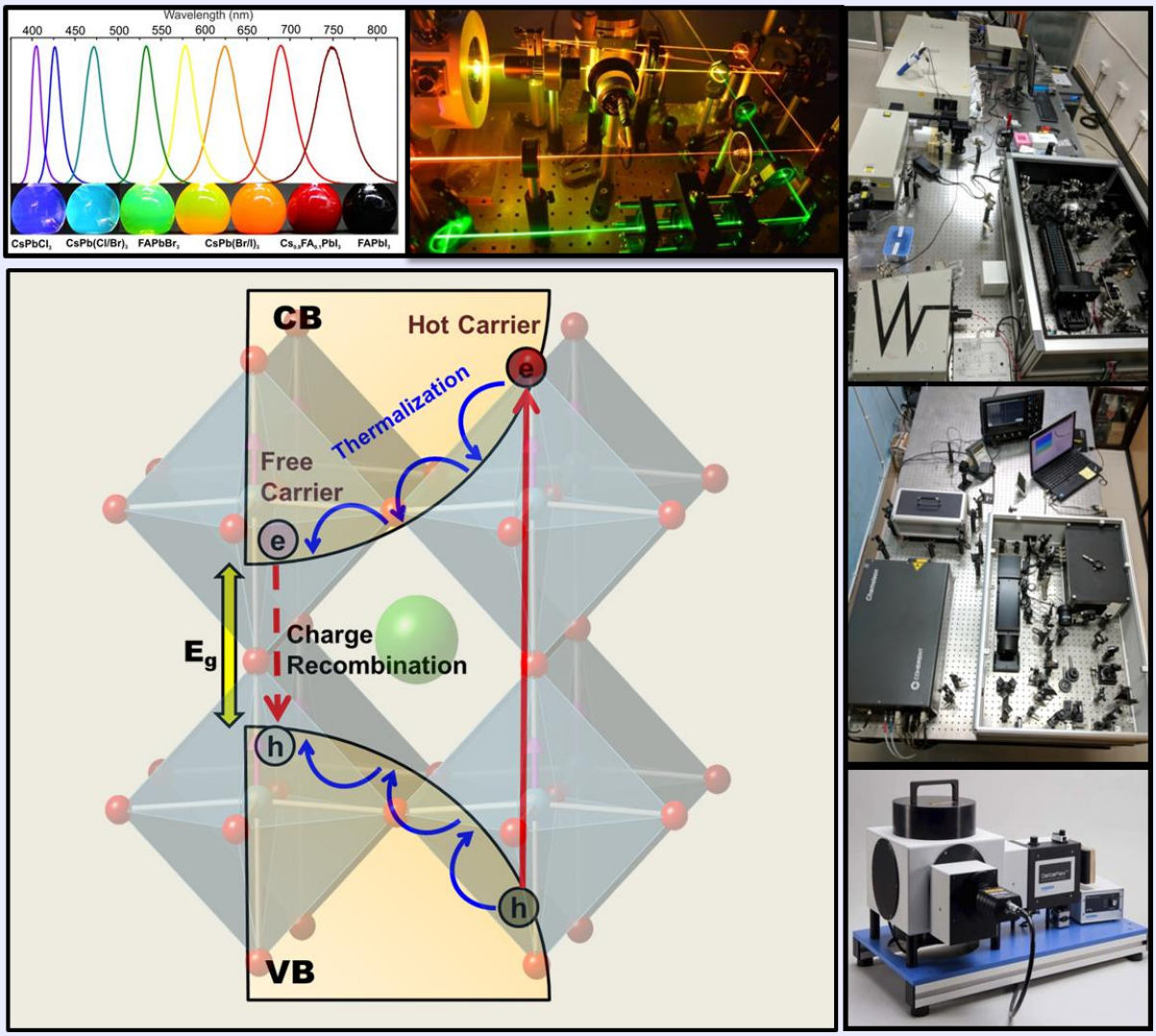

This chapter describes the general synthesis protocols of lead halide perovskite nanocrystals (NCs) which includes all-inorganic $CsPbBr_3$ NCs with different shape and variable compositions of $CsPbBr_xI_{3-x}$ (X= 0, 1 and 1.5), two dimensional (2D) cadmium selenide nanoplatelets (NPLs), porphyrin ligand modified $CsPbBr_3$ NCs, $CsPbBr_3$/PbSe heterostructures and 2D CdSe-$CsPbX_3$ hybrid systems for light-harvesting. Moreover, a brief overview of the characterization tools' basic principles and theories and the spectroscopic techniques has been demonstrated. In addition, detailed computational methodologies and photovoltaics measurement have also been elaborated.

2.1 Synthesis procedure

This chapter describes general methodologies for preparing lead halide perovskite NCs. In addition, detailed synthesis of solvent polarity dependent shape tunability of $CsPbBr_3$ NCs, different composition of $CsPbBr_xI_{3-x}$ (where, x= 0, 1, 1.5) and 2D CdSe NPLs are described. Moreover, strategies for surface modifications of $CsPbBr_3$ NCs with porphyrin ligand, $CsPbBr_3$/PbSe heterostructure, and CdSe-$CsPbBr_xI_{3-x}$ hybrid are pointed out here.

2.1.1. Synthesis of Lead Halide Perovskite Nanocrystals (LHP NCs)

Generally, metal halide perovskite NCs are synthesized by two well-known methods: (a) Hot-injection synthesis Method and (b) Ligand-assisted re-precipitation methods. Both of these techniques are schematically represented in Figure 2.1.

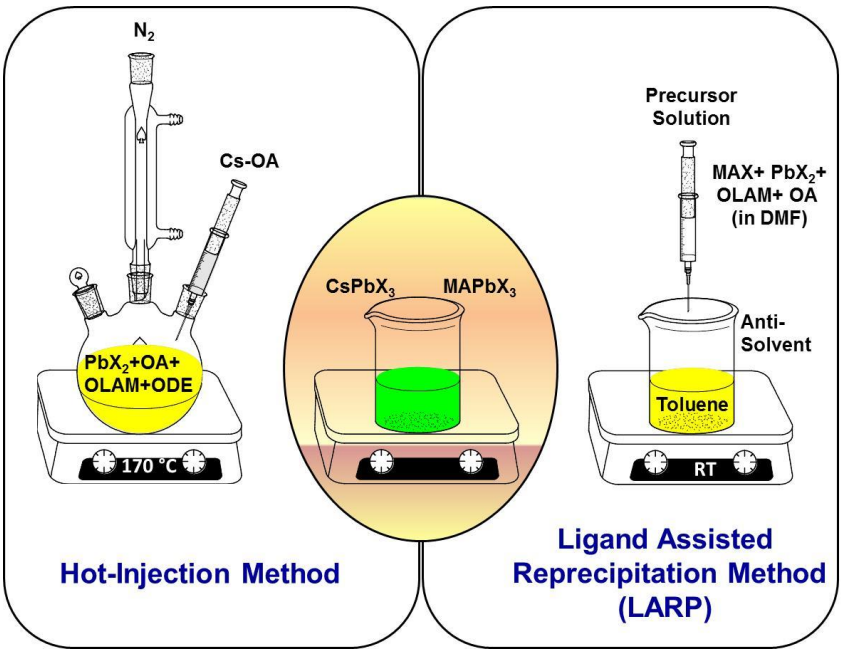

Figure 2.1. *Different protocols for the synthesis of lead halide perovskite NCs.*

In addition, anion exchange reactions and amine-free methods have been developed to synthesize lead halide perovskite NCs.

2.1.1.1. Hot-injection synthesis methods

With bandgap engineering, Kovalenko and colleagues first reported the synthesis of all-inorganic cesium lead halide perovskite NCs (CsPbX3, X= Cl, Br, and I).[1] In this method, highly mono-dispersed cubic shape NCs, having 4-15 nm edge length, can be prepared by arrested precipitation of Cs-oleate and Pb (II)-halide precursors in octadecene (see Figure 2.1). The size of the NCs decreases with the decrease of temperature (140-200 °C), and the NCs are crystallized mainly in cubic phase rather than orthorhombic or tetragonal phase. Interestingly, the emission band of the NCs tunes throughout the whole visible spectral region (400-700 nm) by varying halide precursors and the temperature of the NCs (Figure 2.2).

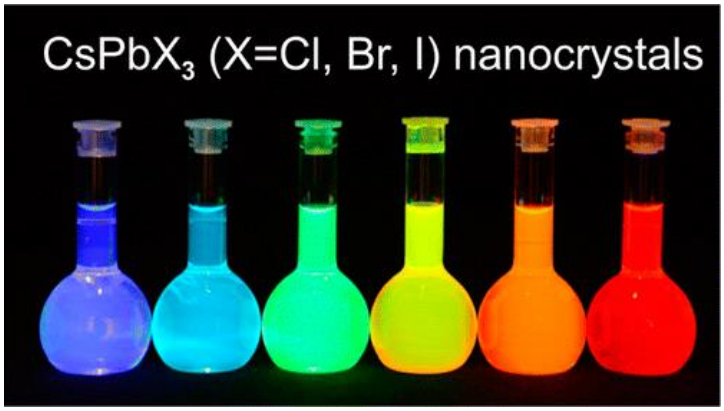

Figure 2.2. *Photograph of colloidal $CsPbX_3$ NCs (X=Cl, Br, and I) by hot-injection synthesis methods.[1] Reproduced with permission from reference 1 (Copyright 2015 American Chemical Society).*

❖ **Synthesis of different shaped $CsPbBr_3$ NCs**

$CsPbBr_3$ NCs are synthesized by the hot-injection method as described by Protesescu et al.[1]

- ***Preparation of Cs-Oleate***

Briefly, 0.163g cesium carbonate is taken into a 25 mL 2-neck flask along with 8mL octadecene and 0.5 mL oleic acid (OA). The solution is dried for 1 h at 120ºC and then heated to 150ºC under N_2 atmosphere.

In a separate 25 mL 2-neck flask, $PbBr_2$ (0.188 mmol, 0.069g) along with 1-octadecene (5 mL, ODE) are loaded and dried under vacuum for 1h at 120ºC. Dried oleic acid (0.5 mL, OA) and dried oleylamine (0.5 mL, OLAM) were injected into the solution at 120ºC under an N_2 atmosphere. After complete solubilization of $PbBr_2$ salt, the temperature is raised to 170ºC, and Cs-oleate solution (0.4 mL, 0.125 M in ODE, prepared as described above) is quickly

injected. The ice-water bath immediately cools the reaction mixture. The crude solution is precipitated out by methyl acetate (MeOAC). Aggregated NCs are divided into two equal volumes and separated by centrifuging at 7000 r.p.m. for 10 minutes. After discarding the supernatants, the residues are re-dispersed into two different solvents, namely toluene and dichloromethane (DCM), having polarity index values 2.4 and 3.1, respectively. The NCs dissolved in toluene show cubic shape and the NCs in DCM exhibit rod-shaped NCs.

❖ **Synthesis of different compositions of $CsPbBr_xI_{3-x}$ (where, x= 0, 1 and 1.5)**

Synthesis of $CsPbBr_xI_{3-x}$ (where, x= 0, 1 and 1.5) NCs with variable halide compositions are synthesized by the hot-injection method described earlier.[1-2] Briefly, a mixture of 34.49 mg $PbBr_2$ and 43.33 mg PbI_2 for $CsPbBr_{1.5}I_{1.5}$, mixture of 23 mg $PbBr_2$ and 58 mg PbI_2 for $CsPbBrI_2$ and 87 mg PbI_2 for $CsPbI_3$ are loaded in a 2 neck flask with 5 mL ODE at 120ºC under vacuum for 1 hour. Dried OA (0.5 mL) and dried OAM (0.5 mL) are injected into the flask under an N_2 atmosphere. After complete solubilization of lead halide precursors, the temperature is raised to 170ºC, and Cs-oleate solution (0.4 mL, 0.125 M in ODE, prepared as described above) is quickly injected. The ice-water bath immediately cools the reaction mixture to obtain the desired NCs. The crude solution is precipitated out by adding ethyl acetate or methyl acetate (for $CsPbI_3$) and finally separated by centrifuging at 7000 r.p.m for 10 minutes. After discarding the supernatants, the residues are re-dispersed in toluene for further characterizations.

2.1.1.2. Ligand-assisted re-precipitation methods

In 2015, Huang *et al.* initially proposed room temperature synthesis of organic-inorganic hybrid lead halide perovskite NCs by ligand assisted re-precipitation method (Figure 2.1).[3] Later on, this method was also extended for all-inorganic cesium lead halide perovskite NCs by Li *et al.*[4] Typically, a mixture of 0.16 mmol CH_3NH_3Br and 0.2 mmol $PbBr_2$ was dissolved in 5 mL of DMF with 20 µL of n-oleylamine and 0.5 mL of oleic acid to form a precursor solution. After that, 2 mL of precursor solution was injected into 10 mL of toluene with vigorous stirring. Strong green PL emission was observed along with the mixing. The solution was centrifuged at 7000 rpm for 10 min, and the precipitates were discarded. The supernatant shows a bright yellow green colloidal solution of $CH_3NH_3PbBr_3$ quantum dots (QDs).

2.1.1.3. Halide-ion exchange reactions

A unique route of preparation of perovskite NCs using post-preparative halide-ion exchange reactions was almost simultaneously discovered by Kovalenko *et al*. and Manna *et al*, where emission color of $CsPbX_3$ NCs can be tuned via their halide ion composition.[5-6]

Such anion exchange reactions are feasible in the liquid phase, although halide ion exchange reactions through solid-solid contact between NCs were also reported.[7] In the case of the liquid phase, control of emission color is done by adding a solution of a chosen halide compound to $CsPbX_3$ NCs dispersion. Anion exchanges reactions including $Cl^- \rightarrow Br^-$, $Br^- \rightarrow Cl^-$, $Br^- \rightarrow I^-$, and $I^- \rightarrow Br^-$ can be achieved using various halide compounds, such as Grignard reagents (CH_3MgX), oleyl-ammonium halides, or PbX_2 (Figure 2.3).[5] The exchange between Cl^- and I^- is difficult due to the significant difference in their ionic radii. Parobek *et al.* monitored the anion exchange reactions by light irradiation in the presence of a dihalomethane solvent.[8] Later, such anion exchange reactions were also reported for hybrid organic-inorganic $MAPbBr_3$ NCs to prepare mixed halide perovskite NCs.[9]

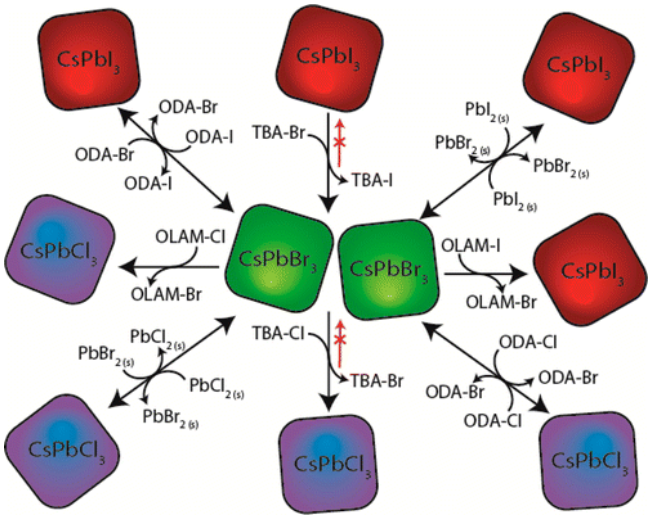

Figure 2.3. *Different routes and precursors for $CsPbX_3$ (X=Cl, Br and I) NCs by halide ion exchange reactions.[8] Reproduced with permission from reference 8 (Copyright 2017 American Chemical Society).*

2.1.1.4. Amine free methods

It is worth noting that CsPbX3 NCs capped with long chain aliphatic acids and amine like oleic acid and oleylamine show poor dispersion stability, i.e., they readily undergo aggregation and sedimentation degradation. This can be attributed to facile proton transfer from oleic acid to oleylamine, leading to detachment of oleylamine from the surface of the nanocrystals.[10]

Yassitepe *et al.* proposed an amine-free method for synthesizing CsPbX3 NCs which is different from the conventional strategy of LHP synthesis.[11] Typically, a mixture of cesium acetate, lead acetate, oleic acid, and 1-octadecene was heated to 100◦C in a vacuum to form a Cs-Pb precursor solution. Then, tetraoctylammonium bromide dissolved in anhydrous toluene

was swiftly injected into the Cs-Pb precursor solution at 75 ºC to synthesize $CsPbBr_3$ NCs. The heating source was then removed, and the sample was allowed to cool naturally.

2.1.2. Synthesis of two dimensional (2D) CdSe Nanoplatelets (NPLs)

We have synthesized 4 monolayers (ML) CdSe NPLs by following the previous solution-phase colloidal method with some modifications.[12-13]

- ***Preparation of Cadmium myristate [$Cd(Myr)_2$]***

Firstly, we have synthesized cadmium myristate [$Cd(Myr)_2$] by following previously published procedures with some modifications.[14] In brief, a solution of sodium myristate was prepared by dissolving 0.43 g of sodium hydroxide and 3.42 g of myristic acid in anhydrous methanol (300 mL). In another beaker, 1.106g of cadmium nitrate tetrahydrate was dissolved in 40 mL methanol. Then, the cadmium nitrate solution was added dropwise into the sodium myristate solution with vigorous stirring at room temperature, and a white precipitate of cadmium myristate started to appear. After the complete addition of cadmium nitrate solution, the reaction was allowed to stir for another 1 hr to complete the reaction. The residue was washed with dried methanol several times to remove unreacted precursors, followed by drying at 600C under vacuum overnight.

In a separate two-neck flask, $Cd(Myr)_2$ (170 mg), Se powder (12 mg), and 15 mL ODE are degassed at 90 ºC for 30 minutes. Then, the temperature of the flask is raised to 240 ºC under continuous argon flow. $Cd(OAc)_2$ (40 mg) are immediately added to the reaction flask when the color of the solution becomes yellowish-orange at 195 ºC. The solution temperature is maintained at 240 ºC for 10 minutes, and then the reaction is stopped. Oleic acid (2 mL) is added when the temperature is 80 ºC. Finally, the mixtures are dissolved in hexane, and quantum dots are removed from the mixture by size-selective precipitation. The precipitates contain the desired 4 ML CdSe NPLs and are re-dispersed in toluene for further characterizations.

2.1.3. Synthesis of $CsPbBr_3$-TpyP NCs by surface modifications

A simple ligand exchange procedure is used to prepare CsPbBr3-TpyP NCs.[15] Surface modified $CsPbBr_3$ NCs by porphyrin ligand (TpyP) is schematically represented in Figure 2.4. First of all, we have prepared a stock solution (2.5 mg/ 5 mL) of TpyP in chloroform. Then, we have prepared a series of set solutions by mixing fixed concentration pristine $CsPbBr_3$ NCs (100 nM) with the desired volume of TpyP from the above stock solution. The final mixture of the solution was kept under mild stirring conditions for 5 minutes.

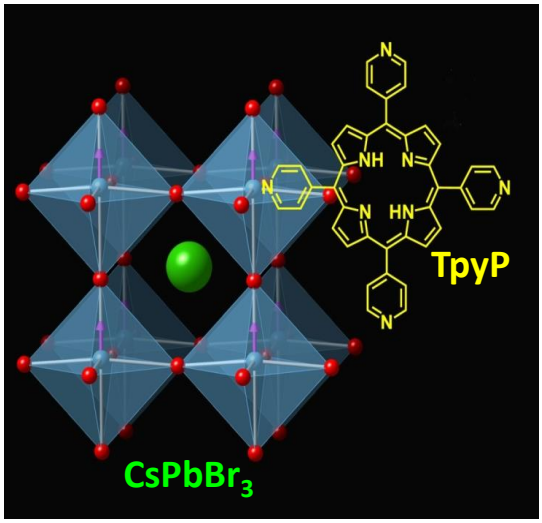

Figure 2.4. *Schematic representation of porphyrin ligand (TpyP) modified $CsPbBr_3$ NCs.[15] Reproduced with permission from reference 15 (Copyright 2021 American Chemical Society).*

2.1.4. Synthesis of CdSe-$CsPbX_3$ composites

Three different composite structures, namely CdSe-$CsPbBr_{1.5}I_{1.5}$, CdSe-$CsPbBrI_2$ and CdSe-$CsPbI_3$ are prepared by mixing fixed volume of CdSe NPLs from the stock solution with desired amount $CsPbBr_{1.5}I_{1.5}$, $CsPbBrI_2$ and $CsPbI_3$ NCs, respectively.[16] Concentration of CdSe NPLs for each composite structure is the same. All the samples are kept for at least 2 hours under mild stirring conditions before any spectroscopic investigations. Figure 2.5 shows a schematic representation of the CdSe-$CsPbX_3$ hybrid.

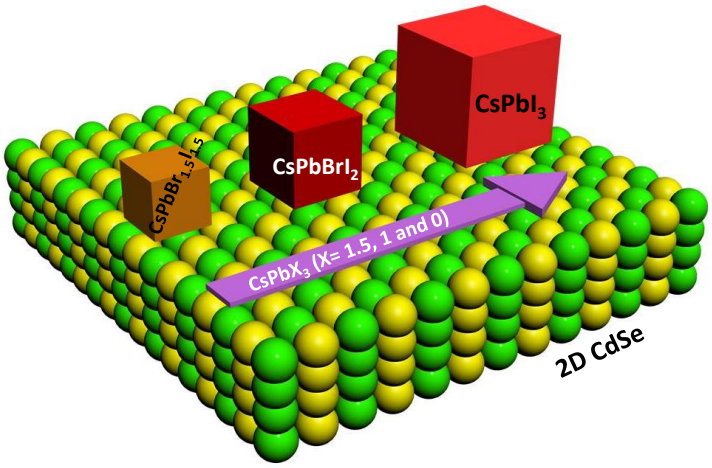

Figure 2.5. *Schematic representation of CdSe-$CsPbX_3$ composites with variable halide compositions.[16] Reproduced with permission from reference 15 (Copyright 2020 American Chemical Society).*

2.2 Characterization Techniques: Fundamentals and Instrumentation

To study the structural and spectroscopic properties of the synthesized NCs and analyze the scope of practical application, several microscopic, spectroscopic and spectrometric techniques were employed. The next section discusses the working principle and instrumentation of these techniques.

2.2.1. Transmission electron microscopy (TEM)

In transmission electron microscopy (TEM), a beam of electrons is transmitted through an ultra-thin specimen, interacting with the sample as it passes through it.[17] Image appears on an imaging screen from the collection of the magnified and focused transmitted electron through the specimen. High-resolution TEM (HRTEM) provides the size, shape, and lattice-fringes of the NCs. Often advanced techniques like the first Fourier transformation pattern (FFT), selected area electron diffraction patterns (SAED), high angle annular dark-field scanning transmission electron microscope image (HAADF-STEM), and energy-dispersive X-ray spectroscopy (EDS) provides information about crystalline phases and chemical composition of the NCs.

The basic principles are similar to the light microscope but use electrons instead of light. The wavelength of light limits a light microscope. TEM uses electrons as a "light source," and their much lower wavelength makes it possible to get a resolution of a thousand times better than with a light microscope to the order of a few angstroms. TEM instrument is composed of several components (a series of electromagnetic lenses and electrostatic plates).[18] Magnetic lenses at the microscope's top guide the emitted electrons are traveling through the vacuum system. Instead of glass lenses for focusing the light in the light microscope, magnetic lenses are also used to focus the electrons into a very thin beam. After this, the electron beam promptly passes through, observing the specimen. Depending on the density of the material present, some of the electrons are scattered and disappear from the beam. The remaining electrons hit a fluorescence screen, which gives rise to a "shadow image" of the specimen with its different parts displayed in varied darkness according to their density. The image can be studied by the operator or photographed with a camera. A schematic representation of the components of the TEM instrument is shown in Figure 2.6.

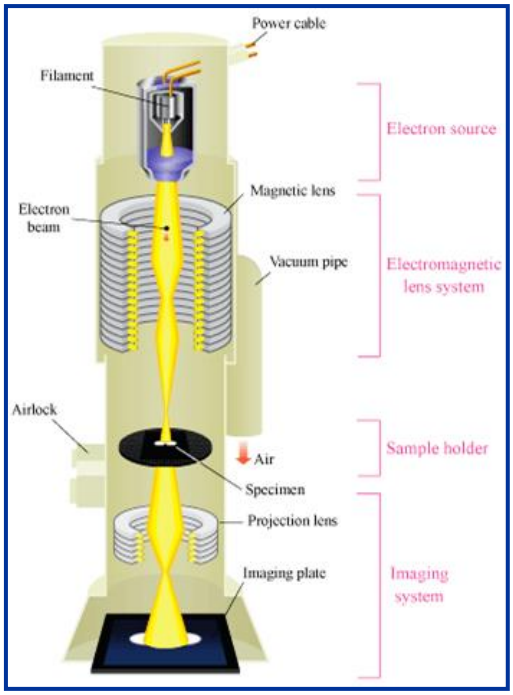

Figure 2.6. *Schematic representation of the transmission electron microscopy (the image is adapted from http://www.hk-phy.org/atomic_world/tem/tem02_e.html)*

In the present thesis, the HRTEM measurements were carried out with a JEOL model 2100 instruments operated at an accelerating voltage of 200 kV. All the TEM images (which are provided in this thesis) are taken using JEOL-JEM-2100F transmission electron microscope.

2.2.2. X-ray diffraction (XRD)

XRD is a non-destructive analytical technique that reveals information about materials and thin films' crystallographic structure, chemical composition, and physical properties.[19] This technique is based on observing the scattered intensity of an X-ray beam hitting a sample as a function of incident and scattered angle, polarization, and wavelength or energy. The intensity of diffracted X-rays is measured as a function of the diffraction angle 2θ. In the first decade of this century, it was realized that X-rays are really light waves of very short wavelength, probably 10^{-8} ~10^{-9}cm. X-rays are electromagnetic radiations with typical photon energies in the range of 100eV-100keV. For diffraction applications, only short-wavelength X-rays (hard X-rays) in the range of a few angstroms to 0.1 angstroms (1 keV-120keV) are used. As the X-ray wavelength is comparable to the size of the atoms, they are ideally suited for probing the structural arrangement of atoms and molecules in a wide range of materials. When crystals are irradiated with X-rays, crystal atoms scatter X-ray waves, primarily through the atomic electrons. Just as an ocean wave striking a lighthouse produces secondary circular waves emanating from the lighthouse, an X-ray striking an

electron produces secondary spherical waves emanating from the electron. This phenomenon is known as scattering, and the electron (or lighthouse) is known as the scatter.

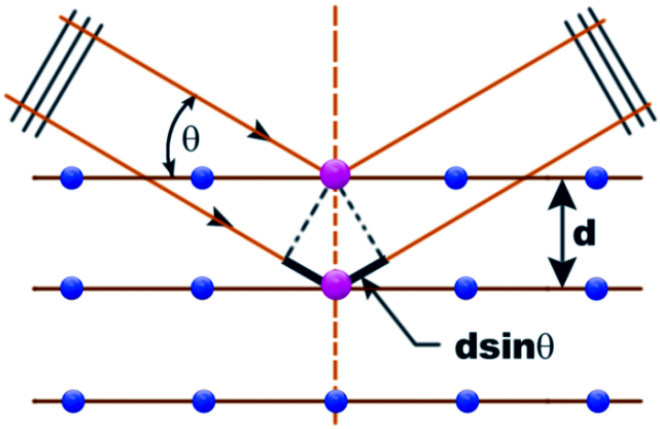

Bragg's law

Figure 2.7. *X-ray Reflections from a Crystal*

A regular array of scatters produces a regular array of spherical waves. Although these waves cancel one another out in most directions (destructive interference), they add constructively in a few specific directions, determined by Bragg's law (Figure 2.7).

$$2d \sin \theta = n\lambda \qquad (2.1)$$

where *n* is an integer representing the order of the X-ray, θ is the scattering angle, λ is the wavelength of the X-ray. These specific directions appear as diffraction patterns, often called reflections. Thus, x-ray diffraction results from an electromagnetic wave (the X-ray) impinging on a regular array of scatters (the repeating arrangement of atoms within the crystal). Generally, the broadenings of the diffraction peaks depend upon crystallite size and strain. The crystallite size of the nanoparticles is obtained from the broadened XRD pattern. The crystallite sizes are calculated using Scherrer's equation

$$D = K \lambda / \beta \cos \theta \qquad (2.2)$$

where K = 0.9 and related to shape factor, D represents crystallite size (Å), λ is the wavelength of Cu kα radiation, and β is the corrected half-width of the diffraction peak. The volume fraction of a particular crystal phase can also be obtained from the integrated peak intensity of the diffraction peak. Besides this, we can calculate the lattice parameters by putting the value of 2(and their corresponding (hkl) values. Bruker D8 advanced powder X-

ray diffractometer having CuKα source (1.5418 Å radiation) was used for XRD measurement.

2.2.2.1. Rietveld Analysis

Rietveld powder structure refinement method is globally recognized as one of the best-known methods for obtaining different (micro) structure parameters of a multiphase material.[20] The essence of this method remains in the minimization of the difference between observed (I_O) and structurally calculated (I_C) X-ray diffraction (XRD) spectra by refining different model parameters using the Marquardt least-squares procedure. The evolution of refinement is reflected by Goodness of Fit (GoF), which is the ratio of R_{wp} (weighted R-factor) to R_{exp} (expected R-factor).The pseudo-Voigt function is employed for peak shape analysis since it accounts for broadening resulting from the combined effect of crystallite size and microstrain.[21] The angular dependence of full-width-at-half-maximum (FWHM) is taken care of using the Caglioti function. Quantification of the amorphous (glassy) phase in mixed crystalline and amorphous phases is achieved by using a poorly crystalline phase in the line shape calculation. For materials possessing some geometric shape, it is often noticed that relative intensities of Bragg reflections alter due to the presence of preferred orientation (PO).[22-23] March-Dollase function is incorporated into the calculation to resolve and quantify the amount of PO in terms of texturing coefficient (r), where $r>0$ and $r=1$ signifies random orientation distribution. In the present study, Rietveld software MAUD (V. 2.80) is utilized to refine different (micro) structural parameters simultaneously.

2.2.3. Fourier Transform Infrared Spectroscopy

Fourier transforms infrared (FTIR) spectroscopy is a technique to investigate the nature of chemical bonds in any molecule or materials using absorbance or transmittance spectra. It deals with the infrared (IR) region of the electromagnetic spectrum.[24] The investigation can be carried out in liquid, powder or films of the samples. The molecules do not remain in a fixed relative position and vibrate with a particular frequency about a mean position. If there is a periodic alternation in the dipole moment due to this vibrational motion, then such a vibration mode is IR active. The IR region of the electromagnetic spectrum is 100 μm–1μm wavelengths. The IR region of the electromagnetic spectrum is divided into three regions; the near-, mid and far- IR, named for their relation to the visible spectrum. The far-IR, approximately 400–10 cm^{-1} (1000–30 μm), lying adjacent to the microwave region, has

low energy and is used for rotational spectroscopy. The mid-IR, approximately 4000–400 cm^{-1} (30–1.4 μm) is used to study the fundamental vibrations and associated rotational-vibrational structure. The higher energy near-IR, around 14000–4000 cm^{-1} (1.4–0.8 μm) can excite overtone or harmonic vibrations. However, these classifications of sub-regions are merely conventions.

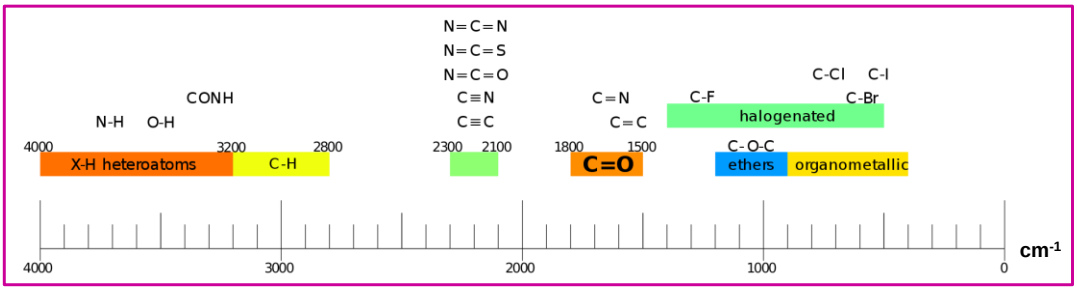

Figure 2.8. *Signature peaks in a FTIR region (The image is adapted from https://en.wikipedia.org/wiki/Infrared_spectroscopy).*

They are neither strict division nor based on exact molecular or electromagnetic properties. The classification of the IR region with signature peaks is indicative in Figure 2.8. There are several types of vibrational and rotational modes, depending upon the geometry and symmetry of molecules. The vibrational modes can be stretching (symmetric and asymmetric), scissoring, rocking, wagging, and twisting, while the rotational modes are symmetric and asymmetric rotations.

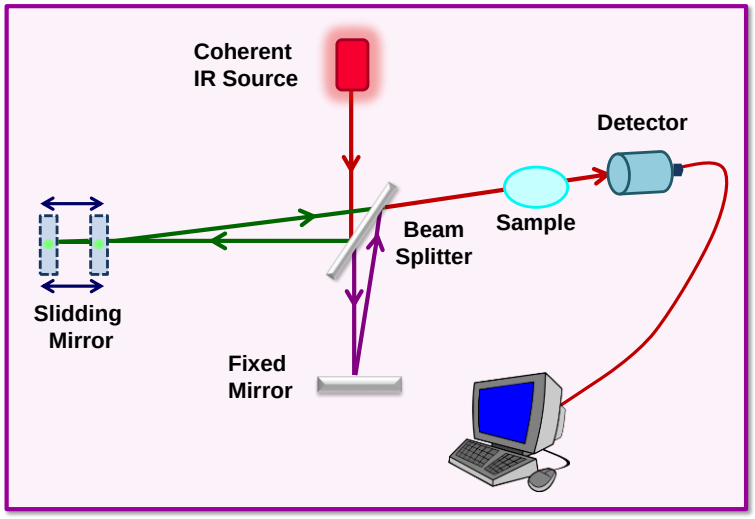

Figure 2.9. *Block diagram of FTIR spectrophotometer.*

The vibrating molecule absorbs energy only from radiation with which it can coherently interact such that the radiation of its oscillation frequency. The appearance or non-appearance

of specific vibration frequencies gives valuable information about the structure of a particular molecule. Each functional group has a specific range of vibration frequencies and is very sensitive to the chemical environment and the neighboring. It provides valuable information regarding certain functional groups in the specific sample for further characterization and identification. The relation gives the frequency of vibration,

$$\gamma = \frac{1}{2\pi}\sqrt{\frac{k}{\mu}} \qquad (2.3)$$

where, k is the force constant and μ is the reduced mass.

The collection modes associated with FTIR are transmission, diffuse reflectance IR Fourier transform (DRIFT), and attenuated total reflectance (ATR). In this thesis, all FTIR spectra were collected in transmittance mode. The detector gives the data in absorbance vs. wavenumber showing peaks at specific wavenumbers corresponding to particular bond vibrations in the sample. Figure 2.9 gives a schematic representation of the line diagram of the FTIR instrument. FTIR spectra of the powdered samples were recorded in the range of 400–4000 cm^{-1} on a Nicolet-380 FTIR spectrophotometer.

2.2.4. X-ray Photoelectron Spectroscopy

X-ray photoelectron spectroscopy (XPS) is a surface-sensitive, quantitative spectroscopic technique based on the photoelectric effect, which provides information about elemental composition, chemical states of elements and overall electronic structure of a material. The XPS signal tells which elements are present and can shed light on the binding nature of each component. XPS spectra are collected by irradiating a solid surface with a beam of X-rays and measuring the kinetic energy of electrons emitted from 1–10 nm of target material being analyzed. The experiment is carried out in a high vacuum (Residual gas pressure, p ~ 10^{-6} Pa) or ultra-high vacuum (p ~ 10^{-7} Pa) chamber. Generally, 20–500 μm diameter beam of monochromatic Al K_α X-rays or a broad 10–30 mm diameter beam of non-monochromatic (polychromatic) Al K_α X-rays or Mg K_α X-rays are used in commercial XPS instruments.[25] The working principle and instrumentation are depicted in Figure 2.10. An electron may be ejected when a molecule or material absorbs an X-ray photon of a specific frequency (Al Kα X-ray, E_{Photon} = 1486.7 eV). The ejected electron's kinetic energy ($E_{Kinetic}$) depends on the electron's photon energy and binding energy (EBinding). Measuring the $E_{Kinetic}$, electron BE is calculated by an equation based on Ernest Rutherford's work.

$$E_{Binding} = E_{Photon} - (E_{Kinetic} + \phi) \quad (2.4)$$

where ϕ is the work function depends on the spectrometer and the material.

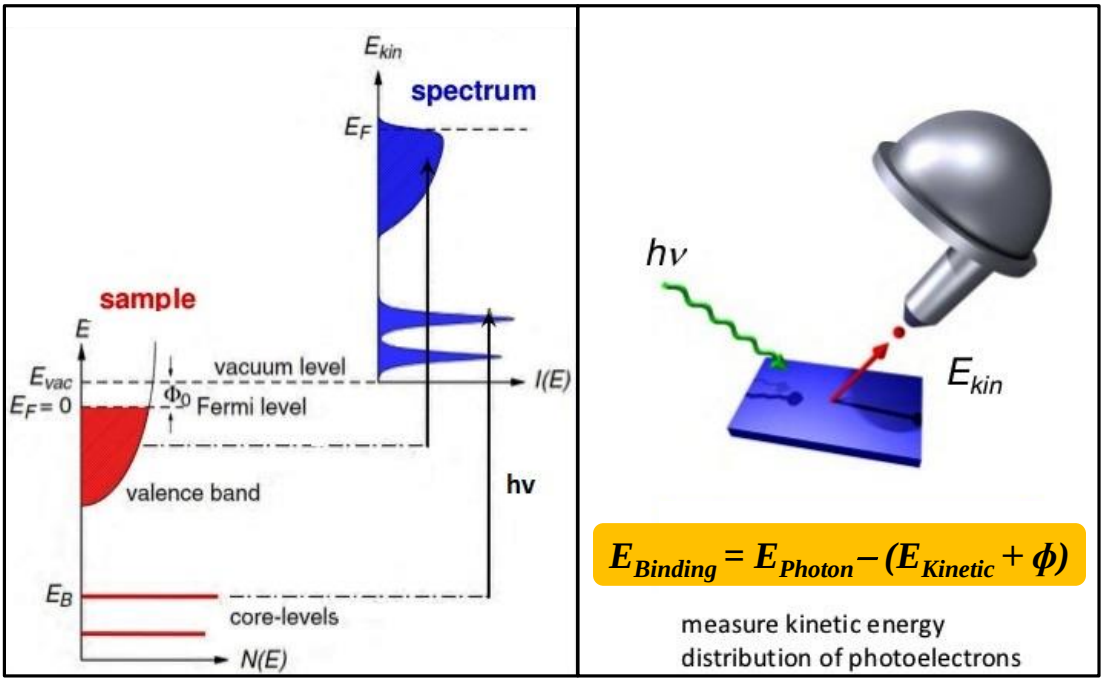

Figure 2.10. *Schematic energy level diagram of XPS working principle and instrumentation (Image is adapted from https://www.slideshare.net, photoelectron spectroscopy for functional oxides).*

This term can be described as an adjustable instrumental correction factor that accounts for the few eV of kinetic energy given up by the photoelectron as it gets emitted from the bulk and absorbed by the detector. In practice, it is a constant that rarely needs to be adjusted. The equation is essentially an energy conservation equation. By measuring the $E_{Kinetic}$ it is possible to gain information about the elements near the materials' surface. The $E_{Binding}$ depends on several factors, such as the element from which the electron is ejected, the orbital of the ejected electron and the chemical environment of the atom. The quantification of the chemical states of atoms can be possible from XPS because the cross-section of the emission of a photoelectron is independent of the chemical environment of an atom. In this thesis, XPS is employed to determine the oxidation states of metals in NCs, and an XPS survey spectrum of Cu NCs is given in Figure 2.11. The measurements were carried out with an Omicron Nanotechnology instrument.

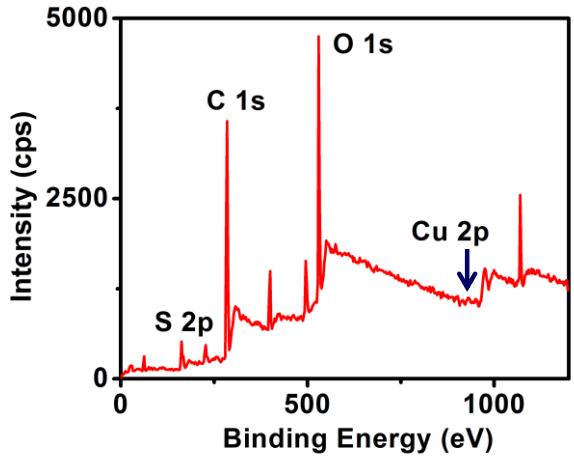

Figure 2.11. *XPS survey spectrum of a Cu NC.*

2.2.5. UV-Vis Absorption spectroscopy

The transition of a light-absorbing molecule from the ground state to the excited state can be measured by Ultraviolet-Visible (UV-Vis) spectroscopy. It fundamentally measures the amount of optical absorption/transmittance/reflectance in a material as a function of wavelength. The absorbance of a solution increases with increasing the attenuation of the incident beam. According to *Lambert-Beer* law, the absorbance of a solution is directly proportional to the concentration of the absorbing species in the solution and the path length. According to *Beer's Law*.[26]

$$A = \log_{10}\left(\frac{I_0}{I}\right) = \varepsilon.c.l \qquad (2.5)$$

where A is the measured absorbance, I_0 is the intensity of the incident light at a given wavelength, I is the transmitted intensity, l is the path length through the sample, and c is the concentration of the absorbing species. For each species and wavelength, ε is a constant known as the molar absorptivity or extinction coefficient. It defines the fundamental molecular property in a given solvent at a particular temperature and pressure and has units of $M^{-1}cm^{-1}$. The Lambert-Beer law (Equation 2.5) is helpful for quantitatively determining the absorber concentration in a solution.

A number of absorption bands can be found in an absorption spectrum corresponding to different structural groups within the molecule. After absorbing energy, electrons are promoted from their ground state to an excited state. In a molecule, the atoms can rotate and vibrate with respect to each other. The absorption spectra are relatively broad compared to the atomic and molecular spectra as in solids, large degeneracy of the atomic levels is split by

interactions into quasi-continuous conduction and valence bands. The energy difference between the highest lying valence (The highest occupied molecular orbital, HOMO) and the lowest-lying conduction (the lowest unoccupied molecular orbital, LUMO) bands can be defined as the fundamental bandgap.

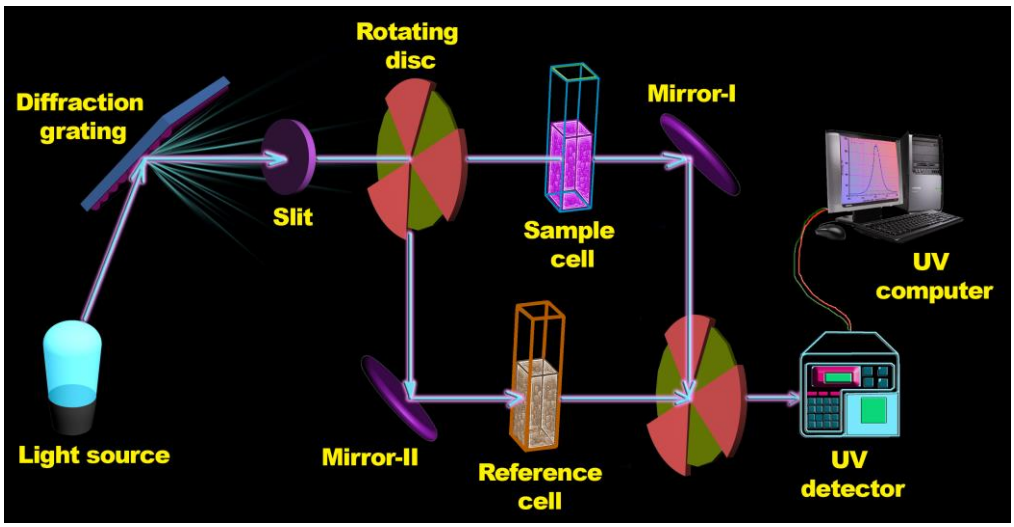

Figure 2.12. *Schematic Representation of UV-Vis Spectrophotometer*[27]

Figure 2.12 describes the working diagram of the UV-vis spectrophotometer. In this thesis, UV-visible spectroscopy is used to study the absorption spectra of different synthesized nanoparticles. The required concentrations of samples s are prepared from Lambert-Beers law (Equation 2.5) by putting the OD values obtained from UV-visible spectrophotometer. Optical spectra of the samples are recorded at room temperature using a UV-2401 PC SHIMADZU spectrophotometer.

2.2.6. Photoluminescence (PL) spectroscopy

Photoluminescence/Fluorescence spectroscopy is a dominant methodology of probing the electronic structure of materials, used extensively in biotechnology, medical diagnostics, DNA sequencing, forensics, genetic analysis, cellular imaging, and energy transfer studies. It measures the fluorescence from a sample upon excitation with a beam of light. Photoluminescence is the emission of light from any substance due to electronic transition from an excited state to a ground state. The photoluminescence intensity and their spectral signatures directly measure various important material properties. The undergoing fundamental processes are usually illustrated by the Jablonski diagram (Figure 2.13).[28] By absorbing a photon, a fluorophore molecule is excited from its ground electronic state (S_0) to one of the various vibrational states in either the first or second excited electronic states (S_1 or S_2). After a collision with other molecules, the excited molecule reaches the lowest vibration state of S_1 by releasing its vibrational energy. It is assigned as internal conversion. The

molecule then drops down to one of the various vibration levels of the ground electronic state again, emitting a photon in the process (fluorescence).

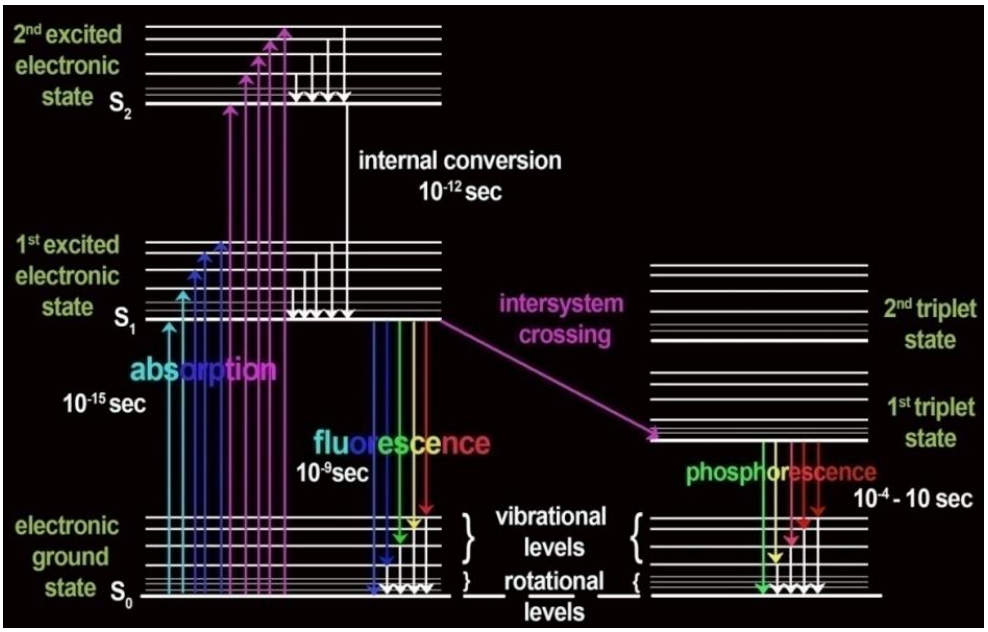

Figure 2.13. *Schematic Representation of Jablonski Diagram*[27]

As molecules drop down into several vibration levels in the ground state, the emitted photons will have different energies and thus frequencies. The emission spectrum is typically a mirror image of the absorption spectrum of the $S_0 \rightarrow S_1$ transition because electronic excitation does not significantly alter the nuclear geometry. Hence the spacing of the vibration levels of excited states is similar to that of the ground state, and identical vibration structures are seen in the absorption and emission spectra. Molecules in the S_1 state can undergo a spin conversion to the first triplet state T_1 (intersystem crossing). Emission from T_1 is termed as phosphorescence and is shifted to longer wavelengths (lower energy) relative to fluorescence. The transition from T_1 to S_0 is forbidden, and therefore, the phosphorescence (10^3-10^0 s^{-1}) rate is several orders of magnitude smaller than those for fluorescence (10^8 s^{-1}). A fluorescence spectrum represents the fluorescence intensity versus wavelength (nm) plot. Examination of the diagram reveals that the energy of the emission is less than that of absorption. Fluorescence occurs at a longer wavelength. This phenomenon is called the Stokes shift. It occurs due to the rapid decay from higher vibrational levels of S_1 to the lowest vibrational level of S_1 and from that to higher vibrational levels of S_0, resulting in further loss of excitation energy by thermalization of excess vibrational energy. Fluorophores can display additional Stokes shifts due to solvent effects, excited state reactions, complex formation, and energy transfer. Figure 2.14 describes the functional diagram of the PL spectrophotometer.

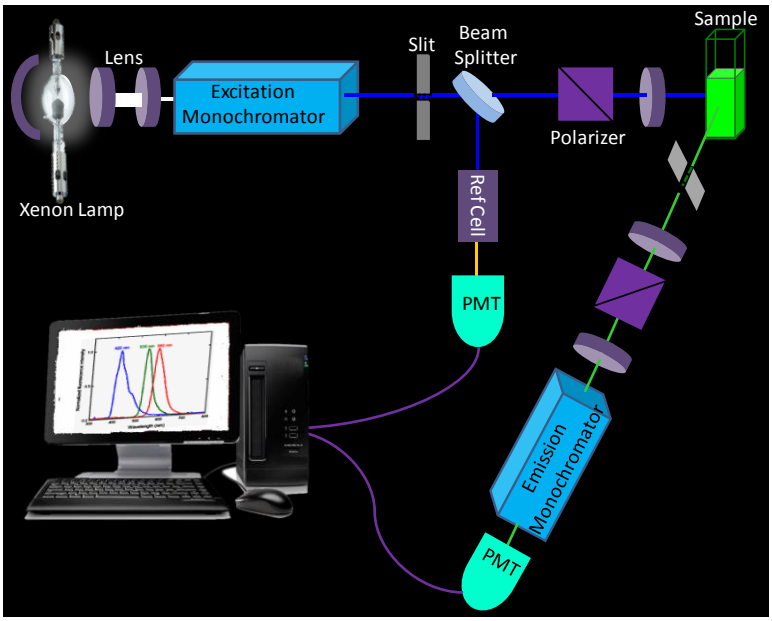

Figure 2.14. *Schematic Representation of PL Spectrophotometer* [29]

The *quantum yield (QY)* of samples are obtained by comparison with reference dye using the following equation:[28]

$$QY_s = (F_s \times A_r \times \eta_s^2 \times QY_s) / (F_r \times A_s \times \eta_r^2) \quad (2.6)$$

F_s and F_r are the integrated fluorescence emission of the sample and the reference. A_s and A_r are the absorbance at the excitation wavelength of the sample and the reference. QY_s and QY_r are the quantum yields of the sample and the reference. The refractive indices of the solvents used to prepare the sample and reference are given by n_s and n_r, respectively.[28] In this thesis, fluorescence spectroscopy has been undertaken to investigate the photophysical properties of different semiconductors and hybrids systems. All samples' emission and excitation spectra are recorded in a Fluoro-Max-P (Horiba Jobin Yvon) luminescence spectrophotometer.

2.2.7. Time correlated single photon counting (TCSPC)

Time-resolved spectroscopy is used to understand different dynamical processes, e. g. solvation dynamics, interactions of other molecules, etc., during the relaxation of an excited state fluorescent irradiation. Presently, most of the time-domain measurements are primarily performed using Time correlated single photon counting (TCSPC) measurement.[28] It fundamentally records fluorescence intensity decays with picosecond time resolution. Photon counting, which is basically a light measurement technique and it takes the advantage of the quantum nature of the light. To measure the intensity of a light source, one needs to count the number of photons emitted in a given unit of Time. The analyzed light pulse starts out bright and then rapidly decays in intensity. The working principle of TCSPC is unique. Figure 2.15 describes the working diagram of the TCSPC setup.

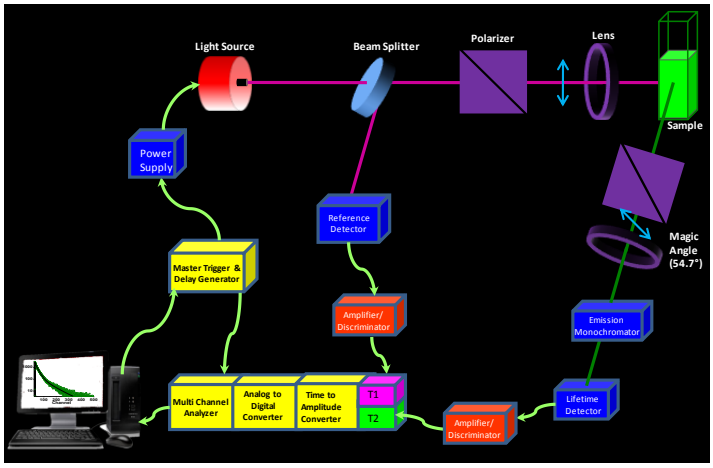

Figure 2.15. *Schematic Representation of TCSPC setup*[27]

The sample is excited with a pulse of laser light, resulting in the waveform shown at the top of Figure 2.16. TCSPC is based on detecting single photons of a periodical light signal, the measurement of the detection times of the individual photons, and the reconstruction of the waveform from the individual time measurements. The method uses the fact that for low level, high repetition rate signals, the light intensity is usually so low that the probability of detecting one photon in one signal period is much less than one. In TCSPC measurement, per laser pulse can detect less than one photon. The observed detection rate is 1 photon per 100 laser pulses. Therefore, the detection of several photons can be neglected. The detector signal consists of a train of randomly distributed pulses due to the detection of the individual photons. There are many signal periods without photons; other signal periods contain one photon pulse. Periods with more than one photon are very rare. Furthermore, all detected photons contribute to the result of the measurement. These moderately complex data obtained from TCSPC are analyzed by nonlinear least squares (NLLS). The goodness of fitting of a decay spectrum depends on the value of χ^2, which is the sum of the squares deviations between the measured and expected values, each divided by squared standard deviations expected for the number of detected photons. For a good fitting, the value of χ^2 is expected to be close to unity. Experimental time-resolved luminescence decays are analyzed by using the following equation:[28]

$$I(t) = \sum_{i=1}^{n} \alpha_i \exp\ (-t / \tau_i) \qquad (2.7)$$

Here, n is the number of discrete emissive species i.e. no. of decay components, τ_i are the excited-state fluorescence lifetimes, and α_i are the amplitudes associated with the i^{th} components. For multi-exponential decays (n), the average lifetime, $\langle\tau\rangle$, is calculated by using the equation

$$\langle \tau \rangle = \sum_{i=1}^{n} \beta_i \tau_i \qquad (2.8)$$

Where $\beta_i = \alpha_i / \sum \alpha_i$ and α_i is the contribution of the decay component.

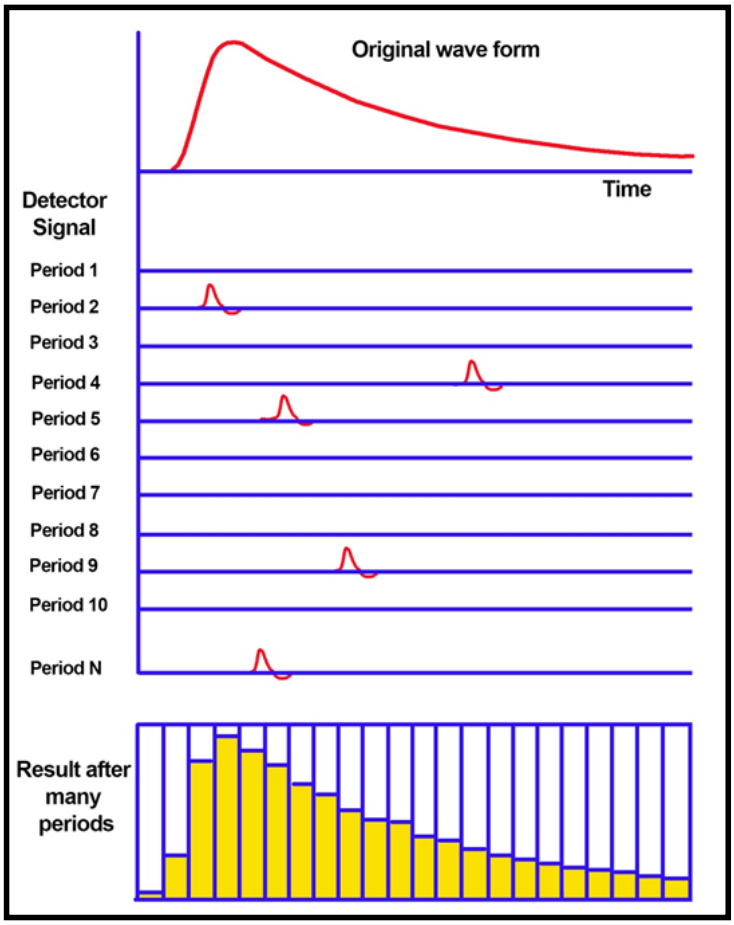

Figure 2.16. *Schematic Representation of Basic Mechanism of TCSPC*[27]

Time-resolved study gives essential information over standard steady-state photoluminescence spectroscopy. It is noteworthy that both static and dynamic quenching can be quantitatively estimated using Time-resolved spectroscopy. Furthermore, resonance energy transfer can also be well studied using lifetime measurements. The donor decays are highly informative about the purity of the sample whether the donors are completely quenched or partially quenched by the nearby acceptors and the donor to acceptor distance. In the present thesis, the Time correlated single photon counting (TCSPC) measurements are performed various times to study the decay kinetics of different semiconducting polymeric and inorganic nanomaterials and their hybrid system. The fluorescence decays are collected on a Hamamatsu MCP photomultiplier (C487802). The fluorescence decays are analyzed using IBH DAS6 software.

2.2.8. Ultrafast Spectroscopy

Ultrafast spectroscopy is being used to understand the photochemical and photophysical processes, which are accompanied during the first few picoseconds after excitation by various relaxation processes of the nuclear degrees of freedom. In most cases, these relaxation processes are much faster, which was proposed by Kasha and Vavilov. In ultrafast photochemical reactions, the reactants start to propagate along the coordinate of response before the nuclear coordinates have relaxed to the equilibrium configuration of the excited state.

For instance, measurements in nanosecond to picosecond time regime, a fast photomultiplier (PMT) or photodetector in conjunction with fast electronics, photocathode-based techniques such as time-correlated single-photon counting and streak camera give susceptible results. However, meticulous deconvolution procedures are needed to detect in picosecond time resolution using TCSPC with a fast PMT. Based on these techniques at subpicosecond resolution level, much attention should be needed because of their expensive and unstable natures. The photodetectors with quick response time (<5 ps) may also restrict their use to detect strong signals from lasers due to low sensitivity and small active area (needed to keep RC low). This problem can be avoided by using "single-shot" streak cameras having a better resolution up to 1 ps with the wide spectral response (200- 1600 nm). The new challenges are the system maintenance for day-to-day reproducibility of sensitive sample measurements and high expensiveness makes the use of streak cameras often impossible.

But in recent years, the event was deemed a great success by prospects for several advanced, stable, and commercially available ultrafast lasers (primarily Ti:sapphire-based lasers with ~ 100-fs or shorter pulse widths) and associated with optoelectronic instruments. In practice, the best choice is nonlinear optical (NLO) laser sampling techniques based on optical shutter by optical Kerr (OK) effect. An ultrafast shutter could be created by using transient birefringence (third-order nonlinear effect) induced in a nonlinear medium with high nonlinear susceptibility by an intense laser pulse (like a Pockels cell driven by light instead of high voltage). Interestingly, the demanding very narrow instrument response function as fast as ~ 200 fs was demonstrated by employing the gate with liquids (CS2, benzene, and toluene) or solid-state materials (glasses, fused silica doped with gold nanoparticles, etc.). However, the birefringence relaxation component with a long recovery time makes poor Kerr shutter contrast and needs meticulous spectral, temporal correction. Furthermore, low sensitivity and spectral restriction to a visible range limit the applications of this technique. Other

intrinsically high-resolution spectroscopic technique-based nonlinear sampling technique may be helpful to overcome this problem.

Achieving better results, many different techniques have been developed to obtain picosecond to femtosecond time resolution. Commonly used techniques to study ultrafast photochemical processes are transient absorption and fluorescence upconversion, which monitor the population of excited states and the evolution of their spectral signatures as a function of Time. However, the obtained data from fluorescence upconversion measurement are often easier to interpret as only the population of the emitting state is probed. In contrast, the sum of excited-state emission, excited-state absorption, and ground-state bleaching is recorded with transient absorption.

2.2.8.1 Ultrafast fluorescence up-conversion spectroscopy

The fluorescence upconversion method, of course, can be applied only to fluorescing species. Fluorescence is highly sensitive to small environmental changes of chromophores. Thus, fluorescence measurements can reveal spectral changes in nanomaterials, the origins of charge transfer reactions, solvent relaxation phenomena, and local photochemical changes in and around the chromophore. As most fluorescence decays occur in the time window of ~ 100 fs to nanoseconds, short light pulses and high temporal resolution instrumentation are required for measurements.

The phenomenon is based on the sum or difference frequency generation of light (second-order nonlinear effect) in a nonlinear crystal [potassium dihydrogen phosphate or KH_2PO_4, $LiNbO_3$, b-barium borate (BBO) etc.]. This technique is called fluorescence 'upconversion' or 'downconversion' for sum or difference frequency generation. The signals are generated at the emission and gate pulse's sum or difference frequencies (higher or lower photon energies). Since this mixing process takes place only during the presence of the second laser pulse, it provides time resolution comparable to the pulse width; delaying the gate pulses with a mechanical stage leads to an "optical boxcar approach." Fluorescence downconversion is less common and needs significant modification before wide use in determining ultrafast spectral signature. On the other hand, fluorescence upconversion is mainly used superior technique about time resolution, measurement sensitivity, and accuracy. This technique has been adopted for investigations in the UV, visible, and near-IR spectral regions and has been used to study many diverse phenomena, such as solvation dynamics, intramolecular coherent vibrations, ultrafast photoisomerization reaction dynamics, charge transfer reactions.

The time resolution mechanism underlying the fluorescence upconversion technique is illustrated in Figure 2.17. The upconversion is a cross-correlation between the fluorescence and a probe laser pulse. As stated earlier, the fluorescence upconversion relies on the sum frequency signal generated from the sample fluorescence and the gate pulse in a birefringent material with a non-zero second-order polarisation susceptibility. Furthermore, the phase-matching condition is necessary for sum-frequency generation. The intensity of the sum frequency signal (I_s) at some delay time (τ), is given by the convolution integral of the sample fluorescence (I_f) and the gate pulse (I_g) according to the following equation

$$I_s(\tau) = \int_{-\infty}^{+\infty} I_f(t) I_g(t-\tau)\, dt \qquad (2.9)$$

At Time t = 0, the sample is excited by second harmonics of an ultrafast laser pulse with frequency, $2\omega_p$. The collected incoherent fluorescence frequency (ω_f) and the probe laser pulse frequency, ω_p arriving at different Time are co-focused in BBO crystal oriented at an appropriate angle with respect to the fluorescence and laser beams. Sum frequency photons (Upconversion frequency, $\omega_s = \omega_f + \omega_p$) are generated only when the probe laser pulse is present in the crystal, acting as a 'gate', thus keeping the time resolution within the laser pulse width. The time evolution of the fluorescence may then be traced by varying the delay of the probe laser beam. It is easy to show that the intensity of the signal beam at sum frequency and at a given delay time is proportional to the correlation function of the fluorescence with the probe laser pulse.

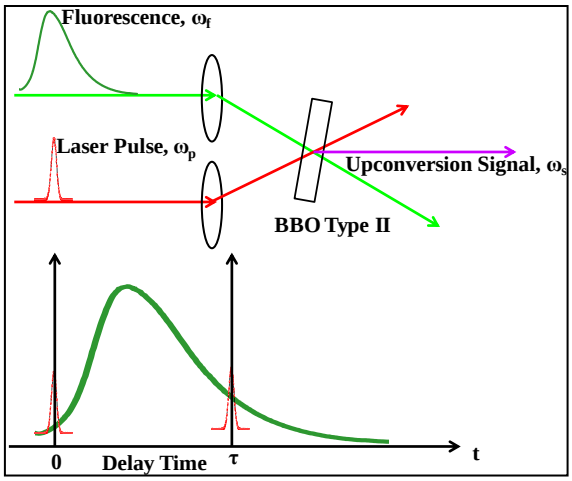

Figure 2.17. *Schematic diagram of generation of upconversion signal*[30]

Ultrafast spectroscopic data are acquired using a commercially available femtosecond fluorescence upconversion spectrophotometer with a Halcyone ultrafast setup (Figure 2.18).

A Ti:sapphire laser system (Chameleon; Coherent) is employed as a light source (140 fs, 80 MHz, at 800 nm) to pump the sample and gate excited state lifetime simultaneously. The second harmonic (at 400 nm) is generated in a thin BBO (type I) crystal and focused onto the sample containing a 2-mm light path lengths cuvette to generate the fluorescence. The fluorescence is collected with the help of a pair of parabolic mirrors and focused, together with the gate beam (at 800 nm), on a BBO type II crystal to generate the upconverted signal. After passing through a grating monochromator (CM112 Compact 1/8 Meter Double Monochromator, Spectral products), the fluorescence is detected with photosensor modules containing a metal package PMT and a high-voltage power supply circuit (Hamamatsu H10721P-110). The FWHM of the instrument response function (determined using Raman scattering in water) is about 288 fs. The femtosecond time-resolved decay traces are fitted using Surface Xplorer 4 fitting software.

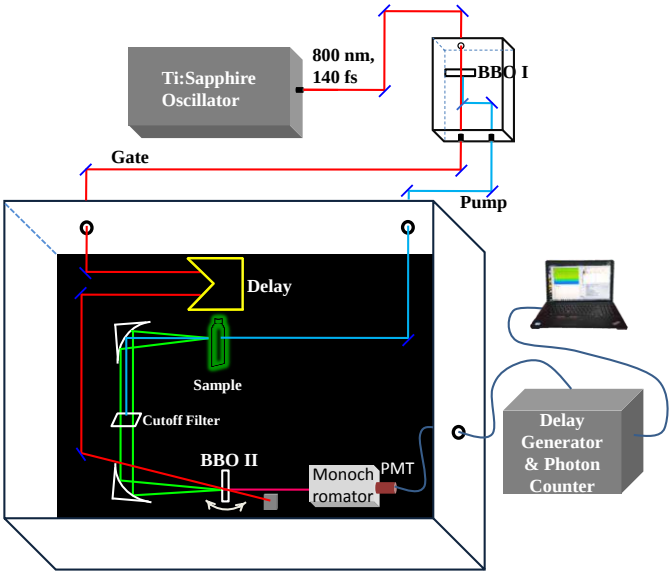

Figure 2.18. *Schematic diagram of fluorescence upconversion setup*[29]

2.2.8.2 Transient absorption spectroscopy

Transient absorption is another essential time-resolved spectroscopic technique applied in order to study energy and charge transfer processes. In transient absorption, firstly, the sample is excited by the pump pulse. Afterward, a relatively low intense (compared to the pump pulse) white-light continuum probe pulse measures the absorption of that excited sample after some delay. The pump pulse is synchronized so that every alternative pump pulse and probe pulse coincide at the sample. Therefore, the difference in the absorbance of the sample with the pump pulse ($A_{pump\ on}$) and absorbance without the pump pulse ($A_{pump\ off}$) is measured in different delay time.

$$\Delta A = A_{pump\ on} - A_{pump\ off} \quad (2.10)$$

Excitation by the pump pulse followed by absorption of white light continuum leads to different electronic transitions in the sample (Figure 2.19). The probe intensity must be low enough to inhibit further sample excitation by the probe pulse. Thus, the excited state population is not significantly altered by the probe.

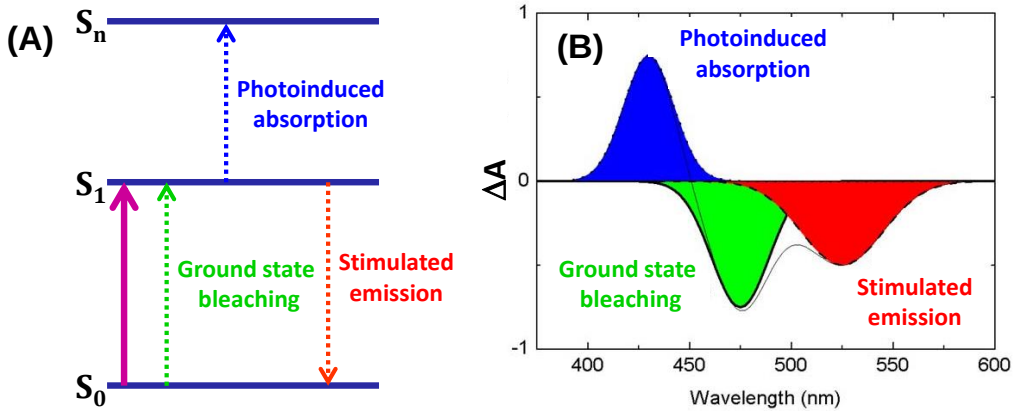

Figure 2.19. *(A) Possible quantum transitions by the probe pulse in a transient absorption measurement. The pump and probe pulses are indicated by solid and dotted line respectively.*[31] *(B) The corresponding transient absorption spectrum and with separated contributions from ground state bleaching (GSB), excited state absorption (ESA) and stimulated emission (SE) with green, blue and red-marked area respectively. (The image is adapted from http://web.vu.lt/ff/m.vengris)*

The ground state bleach has been found when the probe wavelength is resonant with the electronic transition of the sample. Thus, reducing the ground state population occurs as the fractions of the absorbing units of the samples are promoted to the excited state by the pump pulse. Consequently, a negative signal in the ΔA spectrum is observed in the wavelength region of ground-state absorption. Again, absorbing units, which reside in the sample's excited state, may further promote to the higher excited state if the probe's energy is resonant with the transition from the first excited state to a higher excited state. This photoinduced absorption leads to a positive signal in transient absorption. It is also noted that the intensity of the probe pulse is so weak that the excited-state population is not affected appreciably by the excited-state absorption process. Another transition can be induced by the probe pulse i.e., stimulated emission. In this process, a probe photon induces to return an excited state molecule to the ground state by emitting an additional photon of equal energy. The probe and emitted photons are identical and share the same direction of propagation. Both photons will be measured by the detector producing a negative transient absorption signal, as there is no

stimulated emission and therefore fewer photons detected when the pump is absent. Generally, stimulated emission mirrors the fluorescence profile and thus provides the same information as fluorescence upconversion with more fantastic practical inappropriate convenience samples when using a broadband probe.

In our experiment, shown in Figure 2.20, the output from a Ti:sapphire oscillator ~220 mW of the oscillator (Spectra Physics,Mai-Tai-HP) is used as the seed laser for the Ti: sapphire regenerative amplifier (Spectra Physics, Spitfire ACE). The amplifier is pumped with an intracavity doubled, Q-switched, diode-pumped Nd: YLF laser (Spectra-Physics, Ascend) producing 5000 ns pulses with a repetition rate of 1 kHz at 527 nm. Ultimately, amplified pulses centered at 800 nm are 100 fs in duration with a repetition rate of 1 kHz having ~5mJ energy. A portion of this output is used to generate the pump beam (285-2680 nm) using an optical parametric amplifier (Light Conversion Topas Prime).

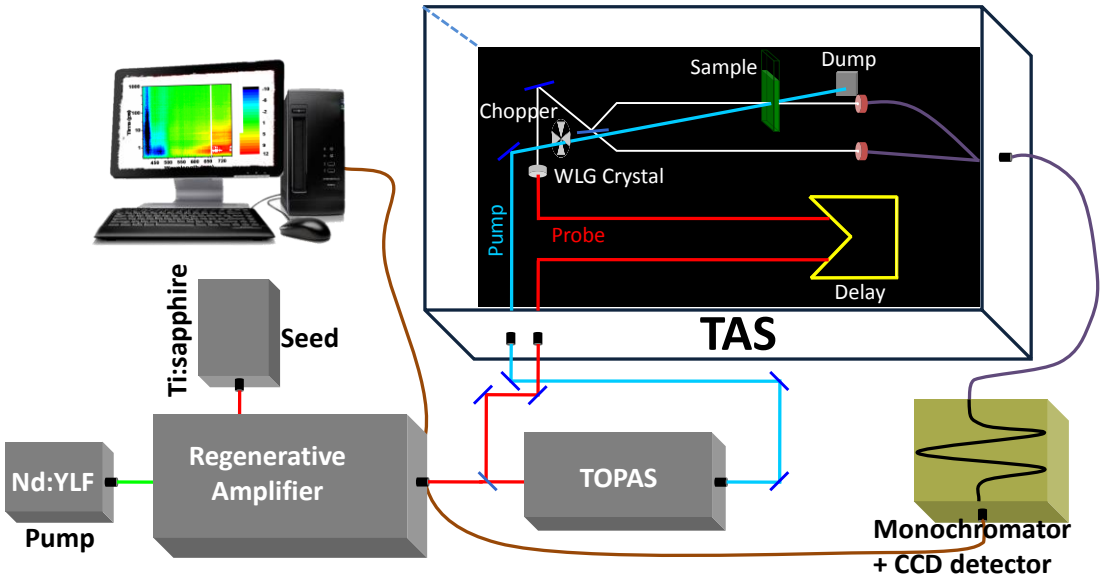

Figure 2.20. *Diagram of transient absorption setup (adapted with permission from ref* [29]

Ultrafast transient absorption data have been collected using Transient Absorption Spectrometer (TAS), Newport. Inside the spectrometer, the pump beam (coming from Topas) is mechanically chopped at 500 Hz and focussed onto the sample with pulse energy of 5μJ/cm^2. While another light beam is passing through a beam splitter from which 95% is dumped, and 5% is delayed relative to the pump pulsed using a motorized translation stage to generate probe pulse by passing through a CaF_2 crystal (330 nm – 750 nm) or Ti-Sapphire crystal (470 nm – 1000 nm).

Further, a beam splitter divides the white light continuum into sample and reference beams. The pump beam diameter is slightly larger than the probe beam size to ensure that the probe samples only within the excitation volume. The sample and reference beams are then directed into complementary CCD detectors. Surface Xplorer 4.1.0 has been used for the chirp correction of TA data before single wavelength kinetic fitting analysis.

2.2.9. Global & target analysis

The measured time-resolved spectrum ψ can be represented as a superposition of the contribution of n_{comp} different components:

$$A\psi(t,\lambda) = \sum_{l=1}^{n_{comp}} c_l(t)\varepsilon_l(\lambda) \qquad (2.11)$$

Where $c_l(t)$ and $\varepsilon_l(\lambda)$ denote, respectively, the concentration and spectrum of component *l*.

Or, in matrix notation:

$$\Psi = CE^T \qquad (2.12)$$

Here Ψ represents the *m x n* data matrix denoting the Time-resolved spectrum, measured at n time instants and m wavelengths. Each column of the $m \times n_{comp}$ matrix **C** represents a concentration profile c_l of component *l* as a function of the independent variable *t*. Likewise, each column of the $n \times n_{comp}$ matrix **E** represents a spectrum ε_l of component *l* as a function of a second independent variable like λ. Here it is assumed that the spectroscopic properties of a mixture of components are a superposition of the spectroscopic properties of the individual components, weighted by their respective concentrations.[32]

In global and target analysis, three different types of models exists: ***a)*** kinetic model [in this case, a parameterized model for the concentrations of the components ($c_l(t)$) is used]; ***b)*** spectral model [in this case a parameterized model for the spectra of the components ($\varepsilon_l(\lambda)$) is used] and ***c)*** spectrotemporal model [in this case knowledge about kinetic and spectral properties of the components is combined].

2.2.9.1 Kinetic models

A kinetic model describes the concentrations of components in measurement over time. It directly models the dynamics of the sample. Typically, first-order kinetics describe measures, meaning that linear first-order differential equations describe the concentrations.[32] The solution for a system of linear differential equations is given by a sum of exponentially decaying functions convolved with the function describing the initial condition, which in spectroscopy termed as Instrument Response Function. The basic form of a kinetic model describing the measured data Ψ as a function of Time and the independent spectral variable λ can then be represented as

$$\psi(t,\lambda) = \sum_{l=1}^{n_{comp}} (exp\ (-\mathrm{k_1 t}) \circ i(t))\ \varepsilon_l(\lambda) \quad (2.13)$$

Where k_l is the exponential decay rate of component *l* and the symbol '∘' indicates the convolution with the IRF *i(t)*. The amplitudes of the concentration profiles are described by the spectra $\varepsilon_l(\lambda)$. In matrix notation, Equation 2.13 can be formulated as follows:

$$\Psi = \mathrm{C}(\theta_l)\mathrm{E}^{\mathrm{T}} \quad (2.14)$$

Here $C(\theta_l)$ is the matrix of concentration profiles as determined by the vector of nonlinear parameters θ_l. **E** is the matrix of spectral amplitudes for which the entries are estimated as so-called conditionally linear parameters.

2.2.9.2 Global analysis

A unified separable nonlinear model describes all measurements collected over multiple independent variables in global analysis. Kinetic models fit the data with a sufficient number of exponential decays and their amplitudes (i.e. the lifetimes of the components). The number of components can be estimated based on the data matrix's singular value decomposition (SVD). The SVD theorem states that any *m x n* matrix has a singular value decomposition of the form:

$$\Psi_{\mathrm{m\times n}} = \mathrm{U_{m\times m} S_{m\times n} W^{T}_{n\times n}} \quad (2.15)$$

Where U and W are orthogonal matrices, containing respectively the left and the right singular vectors and S is a matrix which is zero expect for its diagonal, which holds the singular values or eigenvalues. The singular values indicate the number of components in the data. This is best visualized in the form of a screeplot where the singular values are plotted on a logarithmic range axis, see Figure 2.21.

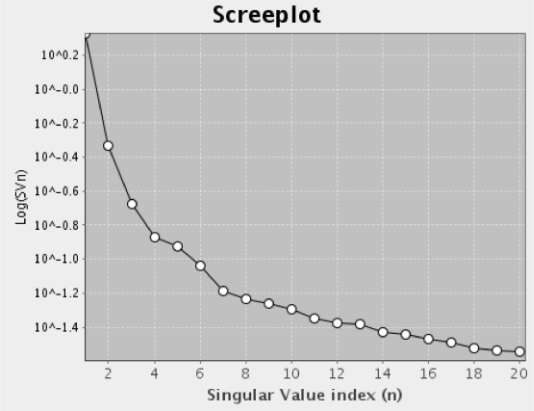

Figure 2.21. *Screeplot of the first 20 singular values of the SVD of typical data with noise* [33]

We start with as little components as possible and then look at the SVD of the residual matrix for more significant values. The structure of the left and right singular vectors reflects the physical aspects of a particular component. In this case the matrix of left singular vectors

represents the time-dependence of the particular components, (see Figure 2.22A). Inspection of the right singular vectors can also be helpful; here they represent the particular components' spectral dependence (see Figure 2.22B). By visualizing only the first few components it is easier to qualitatively evaluate the individual contribution of the components to the dataset as a whole. Usually the number of visualized traces is incremented by one until the structure is no longer clearly distinct from noise. Typically this value is plus or minus one around the value estimated from the screeplot.

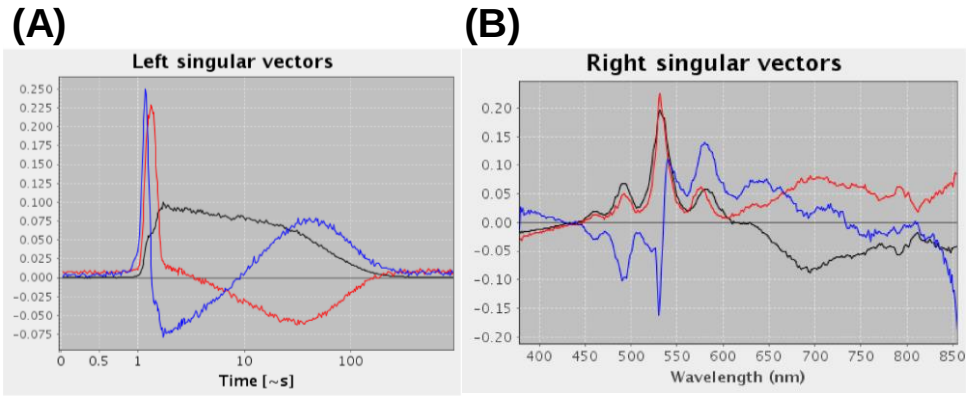

Figure 2.22. *The first three (A) left singular vectors representing the time dependence and (B) right singular vectors representing the spectral dependence of the components*[33]

2.2.9.2.1 Parallel model

As mentioned before, the first part of global analysis using a kinetic scheme is to fit the data with a sufficient number of exponential decays and amplitudes. This is the most straightforward kinetic scheme where every component decays independently (or in parallel), resulting in decay-associated spectra, one for every component, the collection of which is referred to as the Decay Associated Spectra (DAS). In the case of difference absorption spectroscopy, the amplitudes associated with the exponential decays are termed Decay Associated Difference Spectra (DADS).

2.2.9.2.2 Sequential model

Apart from global analysis with independent decays, the simplest analysis uses a kinetic scheme where the components decay sequentially (most often with increasing lifetimes), this is termed the unbranched, unidirectional model ($1 \rightarrow 2 \rightarrow \ldots \rightarrow n_{comp}$). The individual components are referred to as compartments. In this scenario the first compartment gets populated by an input excitation pulse and subsequently forms the second component. The second component decays into the third compartment and so on until finally, the nth component decays to the ground state. The unbranched, unidirectional model is also termed a sequential model. The estimated spectra are called Evolution Associated Spectra (EAS) or

Evolution Associated Difference Spectra (EADS) in the case of difference absorption spectroscopy; the spectra reflect the spectral evolution, e.g. the third EAS or EADS rises with the lifetime of the second component and decays with the third lifetime. In the sequential model, any back-reactions are ignored on the assumption that the energy losses are large enough that the reverse reaction rates are negligible. In the same way, it is assumed that there are no losses in the chain $1 \rightarrow 2 \rightarrow \ldots \rightarrow n_{comp}$ to the ground state.

2.2.9.3 Target analysis

Combining global analysis with testing a specific photophysical or photochemical model is called target analysis. For target analysis, a more complicated scheme can be used that is a combination of the parallel and sequential model and involves branching, back-reaction or multiple compartment excitations. In target analysis linear time-invariant compartmental model is used, where transitions between compartments are described by microscopic rate constants, which constitute the off-diagonal elements of the transfer matrix K. Each compartment is represented by a column in this K-matrix. The lifetimes of the components are the reciprocals of the eigenvalues of this matrix. The concentration of each compartment is described by a vector $c(t) = [c_1(t) \ldots c_{ncomp}(t)]^T$. Thus a linear compartmental model with n_{comp} compartments is described by a differential equation for these concentrations:

$$\frac{d}{dt}C(t)=Kc(t)+j(t) \qquad (2.16)$$

Where the input to the system is described by a vector $j(t) = i(t) [1\ x_2 \ldots x_l]^T$, where the IRF and xl describe me (t) represent possible extra input to compartment *l*. The solution for Equation 2.16 is an exponential function convolved with the IRF, which can be used to calculate the concentration matrix.

Figure 2.23 shows a diagram in which the dynamics are more easily represented. In this compartmental model the first compartment is populated as a direct result excitation, as represented by the IRF multiplied with j_1. This compartment then evolves into the second and third compartment, with kinetic rate k_1 multiplied by branching ratios b_1 and b_2, respectively. The second and third component shares the same spectrum from 10 nm to 1000 nm. Both compartment then evolves into the final compartment with rates k_2 and k_3. This compartment then finally decays to the ground state with rate k_4.

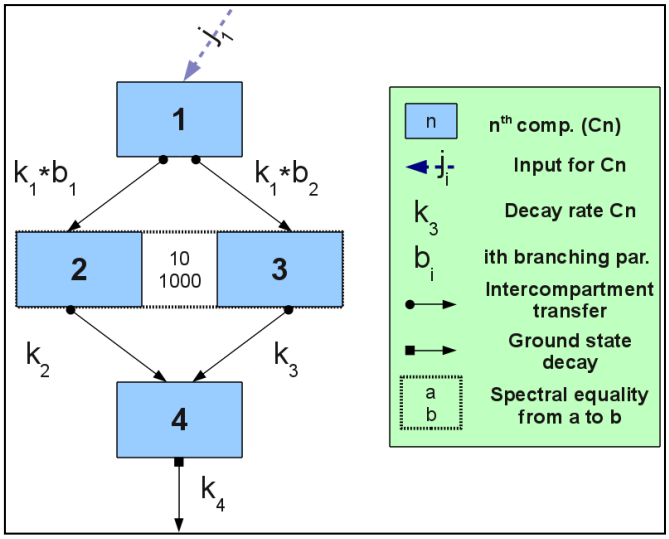

Figure 2.23. *Example of compartmental model* [33]

In this thesis, pump-probe spectroscopic data were globally analyzed[32, 34-35] by using a kinetic model consisting of sequentially interconverting EADS, e.g., 1 → 2 → 3 → 4 → 5→ ….. in which the arrows indicate successive monoexponential decays of increasing time constants, which can be regarded as the lifetime of each EADS. The minimum required numbers of kinetic components signify the elimination of extra correlated structures in the residuals. This procedure enables a clear depiction of the evolution of the (excited) states of the system. To obtain the contributions from these molecular species (because the EADS may reflect mixtures of molecular species), a target analysis was performed in which a specific kinetic scheme was applied. We obtained the spectrum signature of the "pure" excited and the product state intermediates (the so-called species-associated difference spectra, SADS). Each of these states can be ascribed to a distinct intermediate of the relaxation process. Ultrafast processes (energy and electron transfer) are assessed based on these species, along with a specific assignment of time scale for each process.

2.2.10. Computational Methodology

In this thesis, the state-of-the-art first-principles calculations have been carried out using density-functional theory (DFT)[36-37] as encoded in the Vienna *Ab-initio* Simulation Package (VASP).[38-40] The interaction among electrons and nuclei has been accounted for using the plane-wave projector augmented-wave (PAW)[41-42] method. The Perdew has parameterized the exchange-correlation functional within generalized gradient approximation (GGA)–Burke–Ernzerhof (PBE)[43] formalism. To investigate the electronic interaction between the porphyrin molecule and the perovskite $CsPbBr_3$, the system has been modeled by interfacing (001) surface of 3×3×5 supercell of $CsPbBr_3$ slab with the porphyrin molecule.

Structural relaxation for this designed structure was performed at first to obtain the optimized geometry. Structural optimizations were continued until the forces on the atoms had converged to less than 0.01 eV/Å. A vacuum spacing larger than 15 Å along the z-direction was used to decouple the adjacent periodic images to avoid spurious interactions. For the interlayer vdW interactions, the DFT-D3 method[44] of Grimme has been employed. For structural optimization, electronic density of states (DOS), and charge density calculations, a kinetic energy cutoff of 500 eV was used, and the Brillouin zone was sampled with a 6×6×1 **k**-point mesh[45] of Monkhorst-Pack and an energy cutoff of 500 eV. To calculate the partial charge density of a specific energy state, previously converged wave function file has been used.

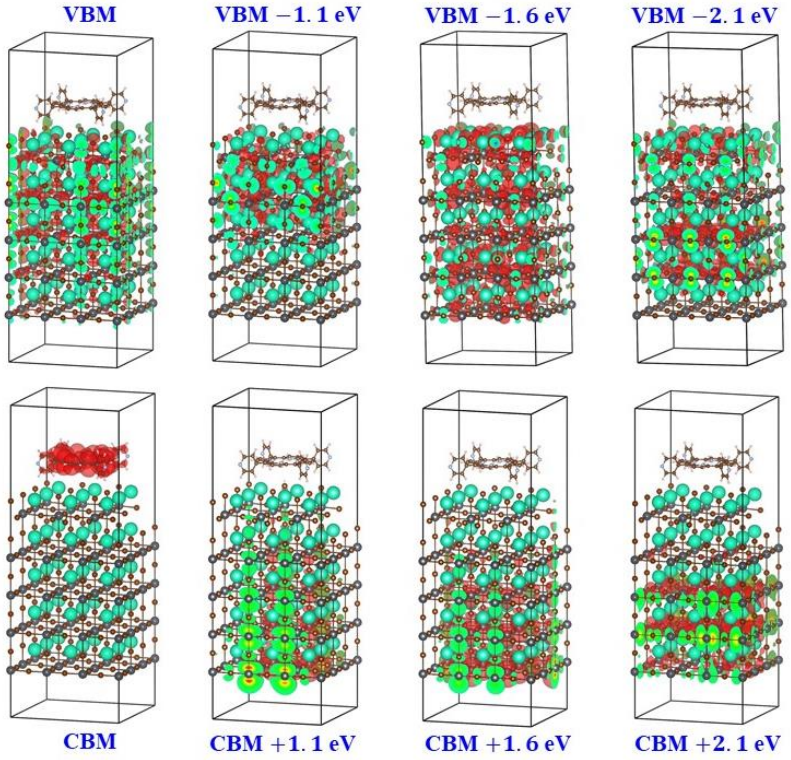

Figure 2.24. *Partial charge density at different energy states in $CsPbBr_3$@TpyP system[15]. Reproduced with permission from reference 15 (Copyright 2021 American Chemical Society).*

Moreover, the computational studies of $CsPbBr_3$, $CsPbBr_3$/PbSe heterostructure were conducted considering all-electron projector augmented plane wave (PAW) method[42] in conjunction with the Perdew-Burke-Ernserhof (PBE)[43, 46] and generalized gradient approximation (GGA)[47] for the exchange-correlation functional, as implemented in the Quantum Espresso package. Initially, we consider the cubic phase of $CsPbBr_3$ and PbSe cubic lattice with space groups Pm-3m and Fm-3m, respectively (Figure 2.24).

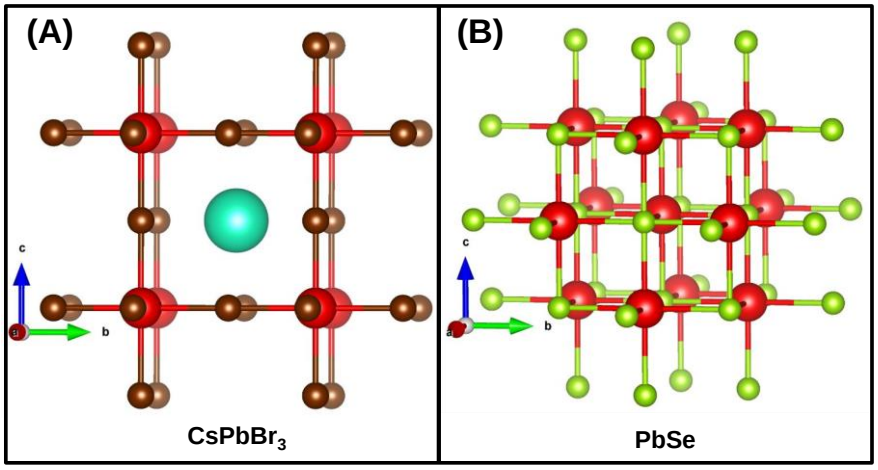

Figure 2.25. *The optimized crystal structure of (A) $CsPbBr_3$ (Space group: Pm-3m). (B) PbSe (Space group: Fm-3m). Here, Cs, Pb, Br, Se atoms are shown by cyan, red, brown and green, respectively.*

Calculations for structure optimizations were carried out by using the 8 × 8 × 8 Monkhorst−Pack grid of k-points for Brillouin zone integrations. Due to the cubic symmetry of the crystal structure, the optimized unit cell of $CsPbBr_3$ is found to be 5.9 Å 5.9 Å × 5.9 Å.[47] While performing optimizations of these cubic systems, we consider electronic wave function and charge density cutoff on a plane-wave basis to be 70 R_y and 280 R_y, respectively. Brillouin zone integration of cubic crystal structure is sampled on the uniform grid of 8 × 8 × 8 k-points. The sharp discontinuity of the electronic states near the bandgap is smeared out with the Fermi-Dirac distribution function with a broadening of 0.003 Ry. After the crystal structure optimization, we used the density functional perturbation theory (DFPT) approach to obtain phonon dispersion spectra of $CsPbBr_3$, which agrees well with previously reported results.[48-50] The force constants were constructed based on the density functional perturbation theory methods. Using those force constants, we obtained a phonon band structure along the high-symmetry direction (R→ M→ Γ→ X→ M) over the Brillouin zone (BZ) for $CsPbBr_3$.

2.2.10.1. Formation of $CsPbBr_3$/PbSe heterostructures

We considered a cubic crystal structure consisting of $CsPbBr_3$ (Pm-3m) with the optimized lattice parameter a=b=c=5.9 Å[51] and PbSe with the space group, Fm-3m (see Figure 2.25). To construct the heterostructure, we created a cell where the $CsPbBr_3$ cubic lattice was placed on top of the PbSe cubic lattice. To incorporate inter-layer interaction between the $CsPbBr_3$ and PbSe cubic lattice, we considered PBE-D2(3) van der Waal (vdW) corrections along the stacking direction. Structure optimization calculations were carried out by using the 8 × 8 × 4

Monkhorst–Pack grid of k-points for Brillouin zone integration of the heterostructure. The optimized lattice parameter of the $CsPbBr_3$-PbSe heterostructure was calculated to be a=b=5.96 Å in the in-plane direction, and the inter-layer distance between $CsPbBr_3$ and PbSe lattice turns out to be around 3.05 Å. This distance essentially signifies van der Waals scale interactions as the dominating interactions within the interface region of the heterostructure. Phonon dispersion spectra for heterostructure are plotted along the high-symmetry direction (R→ X→ Γ→ M→ X) over the Brillouin zone (Table 2.1).

***Table 2.1**. Coordinate of high symmetry q-points for phonons over the Brillouin zone.*

Γ	0.0	0.0	0.0
R	0.5	0.5	0.5
X	0.5	0.0	0.0
Γ	0.0	0.0	0.0
M	0.5	0.5	0.0
X	0.5	0.0	0.0

2.2.11. Photovoltaics measurement

2.2.11.1. Device fabrication

For device fabrication: First, the ITO coated glass was washed by soap solution and then ethanol (3 times) and 2-butanol (3 times) alternatively step by step and dried at 100˚C under vacuum. A very thin layer of PEDOT: PSS was given on this dried ITO glass by spin coating at 2000 rpm and dried at 120˚ C under vacuum for 2 hours. Here PEDOT: PSS acts as a hole acceptor and ensures a good interface between the active layer and electrode. Then, a layer of pure or composite systems that is photoactive layer was spin-coated on this modified ITO surface at 2500 rpm for 30 seconds. Then this ITO carefully was baked at 90˚ C under Ar atmosphere for 5 min. The completion of device fabrication was done by depositing Al on the active layer of ITO, which acts as a cathode. This fabricated device was used for photocurrent measurement.[52-53]

2.2.11.2. Photocurrent measurement

Photovoltaics is the process of converting sunlight directly into electricity using solar cells devices.[54] In solar cell devices, the generation of current is known as the light-generated current. It involves two key processes during light irradiation. The first process is the

absorption of incident photons to create electron-hole pairs. Electron-hole pairs will be generated in the solar cell provided that the incident photon has energy greater than that of the band gap. However, on average, electrons and holes will only exist for a length of time equal to the minority carrier lifetime before they recombine. If the carrier recombines, then the light-generated electron-hole pair is lost, and no current can be generated. Secondly, the collection of these carriers by the *p*-*n* junction which prevents this recombination process by using a *p* type and *n* type materials junction to separate the electron and the hole. The carriers are separated by the action of the electric field existing at the *p*-*n* junction. Suppose the light-generated minority carrier reaches the p-n junction. In that case, it is swept across the junction by the electric field at the junction, where it is now a majority carrier. If the emitter and base of the solar cell are connected, the light-generated carriers flow through the external circuit.

For carrying out the experiments of this thesis, we have used Newport solar simulator and Keithley electrometer (6517B). The Electrometer has the capabilities to measure DC voltage from 1μV to 210 V, and DC current from 10 aA to 21 mA. A solar simulator is a device that provides us with natural sunlight illumination using 1.5 G air mass filter. The sample layers were deposited on ITO glass using a spin coater. Then counter electrode such as 'Ag' or 'Al' was deposited on the device using a high vacuum depositor (Hind High Vacuum CO. (P) Ltd., Model: 12A4D). In this thesis, we have measured the photocurrent i.e. current-voltage characteristic curve of our sample using the system above. The schematic diagram of the instruments is given in Figure 2.26.

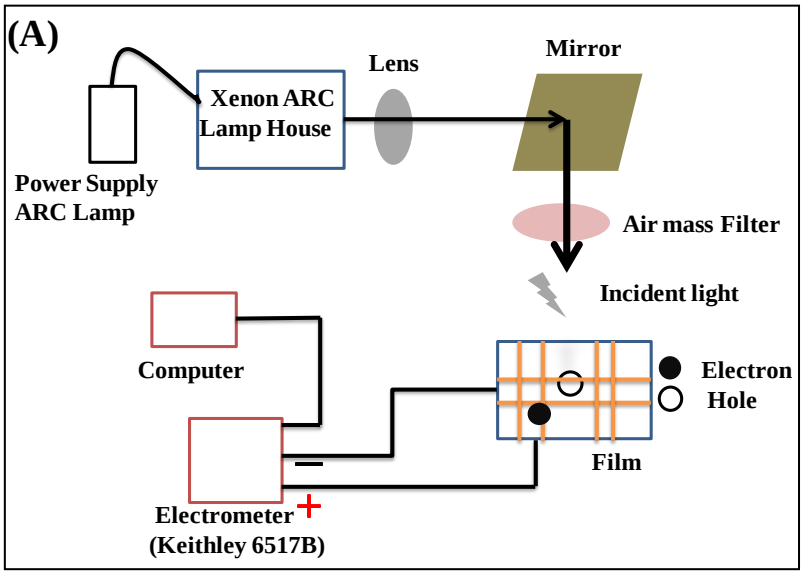

Figure 2.26. *Schematic Representation of I-V Measurement setup* [55]

2.3. References

(1) Protesescu, L.; Yakunin, S.; Bodnarchuk, M. I.; Krieg, F.; Caputo, R.; Hendon, C. H.; Yang, R. X.; Walsh, A.; Kovalenko, M. V., Nanocrystals of Cesium Lead Halide Perovskites ($CsPbX_3$, X = Cl, Br, and I): Novel Optoelectronic Materials Showing Bright Emission with Wide Color Gamut. *Nano Lett.* **2015**, *15*, 3692-3696.

(2) Krieg, F.; Ochsenbein, S. T.; Yakunin, S.; ten Brinck, S.; Aellen, P.; Süess, A.; Clerc, B.; Guggisberg, D.; Nazarenko, O.; Shynkarenko, Y., et al., Colloidal $CsPbX_3$ (X = Cl, Br, I) Nanocrystals 2.0: Zwitterionic Capping Ligands for Improved Durability and Stability. *ACS Energy Lett.* **2018**, *3*, 641-646.

(3) Zhang, F.; Zhong, H.; Chen, C.; Wu, X.-g.; Hu, X.; Huang, H.; Han, J.; Zou, B.; Dong, Y., Brightly Luminescent and Color-Tunable Colloidal $CH_3NH_3PbX_3$ (X = Br, I, Cl) Quantum Dots: Potential Alternatives for Display Technology. *ACS Nano* **2015**, *9*, 4533-4542.

(4) Li, X.; Wu, Y.; Zhang, S.; Cai, B.; Gu, Y.; Song, J.; Zeng, H., $CsPbX_3$ Quantum Dots for Lighting and Displays: Room-Temperature Synthesis, Photoluminescence Superiorities, Underlying Origins and White Light-Emitting Diodes. *Adv. Funct. Mater.* **2016**, *26*, 2435-2445.

(5) Nedelcu, G.; Protesescu, L.; Yakunin, S.; Bodnarchuk, M. I.; Grotevent, M. J.; Kovalenko, M. V., Fast Anion-Exchange in Highly Luminescent Nanocrystals of Cesium Lead Halide Perovskites ($CsPbX_3$, X = Cl, Br, I). *Nano Lett.* **2015**, *15*, 5635-5640.

(6) Akkerman, Q. A.; D'Innocenzo, V.; Accornero, S.; Scarpellini, A.; Petrozza, A.; Prato, M.; Manna, L., Tuning the Optical Properties of Cesium Lead Halide Perovskite Nanocrystals by Anion Exchange Reactions. *J. Am. Chem. Soc.* **2015**, *137*, 10276-10281.

(7) Palazon, F.; Di Stasio, F.; Akkerman, Q. A.; Krahne, R.; Prato, M.; Manna, L., Polymer-Free Films of Inorganic Halide Perovskite Nanocrystals as UV-to-White Color-Conversion Layers in Leds. *Chem. Mater.* **2016**, *28*, 2902-2906.

(8) Parobek, D.; Dong, Y.; Qiao, T.; Rossi, D.; Son, D. H., Photoinduced Anion Exchange in Cesium Lead Halide Perovskite Nanocrystals. *J. Am. Chem. Soc.* **2017**, *139*, 4358-4361.

(9) Jang, D. M.; Park, K.; Kim, D. H.; Park, J.; Shojaei, F.; Kang, H. S.; Ahn, J.-P.; Lee, J. W.; Song, J. K., Reversible Halide Exchange Reaction of Organometal Trihalide Perovskite Colloidal Nanocrystals for Full-Range Band Gap Tuning. *Nano Lett.* **2015**, *15*, 5191-5199.

(10) De Roo, J.; Ibáñez, M.; Geiregat, P.; Nedelcu, G.; Walravens, W.; Maes, J.; Martins, J. C.; Van Driessche, I.; Kovalenko, M. V.; Hens, Z., Highly Dynamic Ligand Binding and Light Absorption Coefficient of Cesium Lead Bromide Perovskite Nanocrystals. *ACS Nano* **2016**, *10*, 2071-2081.

(11) Yassitepe, E.; Yang, Z.; Voznyy, O.; Kim, Y.; Walters, G.; Castañeda, J. A.; Kanjanaboos, P.; Yuan, M.; Gong, X.; Fan, F., et al., Amine-Free Synthesis of Cesium Lead Halide Perovskite Quantum Dots for Efficient Light-Emitting Diodes. *Adv. Funct. Mater.* **2016**, *26*, 8757-8763.

(12) Ithurria, S.; Dubertret, B., Quasi 2d Colloidal Cdse Platelets with Thicknesses Controlled at the Atomic Level. *J. Am. Chem. Soc.* **2008**, *130*, 16504-16505.

(13) Das, S.; Dutta, A.; Bera, R.; Patra, A., Ultrafast Carrier Dynamics in 2D–2D Hybrid Structures of Functionalized Go and Cdse Nanoplatelets. *Phys. Chem. Chem. Phys.* **2019**, *21*, 15568-15575.

(14) Tessier, M. D.; Spinicelli, P.; Dupont, D.; Patriarche, G.; Ithurria, S.; Dubertret, B., Efficient Exciton Concentrators Built from Colloidal Core/Crown CdSe/CdS Semiconductor Nanoplatelets. *Nano Lett.* **2014**, *14*, 207-213.

(15) Ghosh, G.; Marjit, K.; Ghosh, S.; Ghosh, A.; Ahammed, R.; De Sarkar, A.; Patra, A., Hot Hole Cooling and Transfer Dynamics from Lead Halide Perovskite Nanocrystals Using Porphyrin Molecules. *J. Phys. Chem. C* **2021**, *125*, 5859-5869.

(16) Ghosh, G.; Dutta, A.; Ghosh, A.; Ghosh, S.; Patra, A., Ultrafast Carrier Dynamics in 2D CdSe Nanoplatelets–$CsPbX_3$ Composites: Influence of the Halide Composition. *J. Phys. Chem. C* **2020**, *124*, 10252-10260.

(17) Kittel, C., Introduction to Solid State Physics,. *Wiley New York,* **1976**, *8*.

(18) Carter, D. B. W. a. C. B., The Transmission Electron Microscope. *Springer* **1996**.

(19) Klug, H. P.; Alexander, L. E., X-Ray Diffraction Procedures: For Polycrystalline and Amorphous Materials. *X-Ray Diffraction Procedures: For Polycrystalline and Amorphous Materials, 2nd Edition, by Harold P. Klug, Leroy E. Alexander, pp. 992. ISBN 0-471-49369-4. Wiley-VCH, May 1974.* **1974**, *1*.

(20) Rietveld, H. M., A Profile Refinement Method for Nuclear and Magnetic Structures. *J. Appl. Crystallogr.* **1969**, *2*, 65-71.

(21) Young, R. A.; Wiles, D. B., Profile Shape Functions in Rietveld Refinements. *J. Appl. Crystallogr.* **1982**, *15*, 430-438.

(22) Sain, S.; Kar, A.; Patra, A.; Pradhan, S. K., Structural Interpretation of SnO_2 Nanocrystals of Different Morphologies Synthesized by Microwave Irradiation and Hydrothermal Methods. *CrystEngComm* **2014**, *16*, 1079-1090.

(23) Bhattacharyya, S.; Jana, B.; Sain, S.; Barman, M. K.; Pradhan, S. K.; Patra, A., Photoswitching and Thermoresponsive Properties of Conjugated Multi-Chromophore Nanostructured Materials. *Small* **2015**, *11*, 6317-6324.

(24) Ferrando, R.; Jellinek, J.; Johnston, R. L., Nanoalloys: From Theory to Applications of Alloy Clusters and Nanoparticles. *Chem. Rev.* **2008**, *108*, 845-910.

(25) Ray, S.; Shard, A. G., Quantitative Analysis of Adsorbed Proteins by X-Ray Photoelectron Spectroscopy. *Anal. Chem.* **2011**, *83*, 8659-8666.

(26) D. Ingle and S. R. Crouch, Englewood Cliffs, Nj,. **1988**, *106*, 206-226.

(27) Lakowicz, J. R., *Principles of Fluoresence Spectroscopy, 3rd ed., Springer, Berlin* **2006**.

(28) Lakowicz, J. R., *Principles of Fluorescence Spectroscopy*; Springer: New York, 2006.

(29) Jana, B., Photophysical Studies of Π-Conjugated Organic Molecules Based Functional Nanomaterials. *PhD. Dissertation, Jadavpur University* **2019**.

(30) Chosrowjan, H.; Taniguchi, S.; Tanaka, F., Ultrafast Fluorescence Upconversion Technique and Its Applications to Proteins. *FEBS J.* **2015**, *282*, 3003-3015.

(31) Clafton, S. N., *Photophysics and Photochemistry of Conjugated Polymer Nanoparticles*; University of Adelaide, School of Chemistry and Physics, 2014.

(32) van Stokkum, I. H. M.; Larsen, D. S.; van Grondelle, R., Global and Target Analysis of Time-Resolved Spectra. *Biochim. Biophys. Acta* **2004**, *1657*, 82-104.

(33) Snellenburg, J., J., Glotaran a Tool for Interactive Global and Target Analysis of Time-Resolved Spectroscopy and Microscopy Data. *Master's Dissertation, VU University Amsterdem* **2010**.

(34) Mullen, K. M.; Van Stokkum, I. H. M., An Introduction to the "Special Volume Spectroscopy and Chemometrics in R". *J. Stat. Softw.* **2007**, *18*, 1-5.

(35) Snellenburg, J., J.; Laptenok, S.; Seger, R.; Mullen, K., M.; Van Stokkum, I., H.M., Glotaran: A Java-Based Graphical User Interface for the R Package Timp. *J. Stat. Softw.* **2012**, *49*, 1-22.

(36) Kohn, W.; Sham, L. J., Self-Consistent Equations Including Exchange and Correlation Effects. *Phys. Rev.* **1965**, *140*, A1133-A1138.

(37) Hohenberg, P.; Kohn, W., Inhomogeneous Electron Gas. *Phys. Rev.* **1964**, *136*, B864-B871.

(38) Kresse, G.; Furthmüller, J., Efficient Iterative Schemes for Ab Initio Total-Energy Calculations Using a Plane-Wave Basis Set. *Phys. Rev. B* **1996**, *54*, 11169-11186.

(39) Kresse, G.; Hafner, J., Ab Initio Molecular-Dynamics Simulation of the Liquid-Metal--Amorphous-Semiconductor Transition in Germanium. *Phys. Rev. B* **1994**, *49*, 14251-14269.

(40) Kresse, G.; Furthmüller, J., Efficiency of Ab-Initio Total Energy Calculations for Metals and Semiconductors Using a Plane-Wave Basis Set. *Comput. Mater. Sci.* **1996**, *6*, 15-50.

(41) Kresse, G.; Joubert, D., From Ultrasoft Pseudopotentials to the Projector Augmented-Wave Method. *Phys. Rev. B* **1999**, *59*, 1758-1775.

(42) Blöchl, P. E., Projector Augmented-Wave Method. *Phys. Rev. B* **1994**, *50*, 17953-17979.

(43) Perdew, J. P.; Burke, K.; Ernzerhof, M., Generalized Gradient Approximation Made Simple. *Phys. Rev. Lett.* **1996**, *77*, 3865-3868.

(44) Grimme, S.; Antony, J.; Ehrlich, S.; Krieg, H., A Consistent and Accurate Ab Initio Parametrization of Density Functional Dispersion Correction (Dft-D) for the 94 Elements H-Pu. *J. Chem. Phys.* **2010**, *132*, 154104.

(45) Pack, J. D.; Monkhorst, H. J., "Special Points for Brillouin-Zone Integrations"---a Reply. *Phys. Rev. B* **1977**, *16*, 1748-1749.

(46) Perdew, J. P.; Ruzsinszky, A.; Csonka, G. I.; Vydrov, O. A.; Scuseria, G. E.; Constantin, L. A.; Zhou, X.; Burke, K., Restoring the Density-Gradient Expansion for Exchange in Solids and Surfaces. *Phys. Rev. Lett.* **2008**, *100*, 136406.

(47) Perdew, J. P.; Burke, K.; Wang, Y., Generalized Gradient Approximation for the Exchange-Correlation Hole of a Many-Electron System. *Phys. Rev. B* **1996**, *54*, 16533-16539.

(48) Lee, W.; Li, H.; Wong, A. B.; Zhang, D.; Lai, M.; Yu, Y.; Kong, Q.; Lin, E.; Urban, J. J.; Grossman, J. C., et al., Ultralow Thermal Conductivity in All-Inorganic Halide Perovskites. *Proc. Natl. Acad. Sci. U.S.A.* **2017**, *114*, 8693-8697.

(49) Lanigan-Atkins, T.; He, X.; Krogstad, M. J.; Pajerowski, D. M.; Abernathy, D. L.; Xu, G. N. M. N.; Xu, Z.; Chung, D. Y.; Kanatzidis, M. G.; Rosenkranz, S., et al., Two-Dimensional Overdamped Fluctuations of the Soft Perovskite Lattice in $CsPbBr_3$. *Nat. Mater.* **2021**, *20*, 977-983.

(50) Guo, P.; Xia, Y.; Gong, J.; Stoumpos, C. C.; McCall, K. M.; Alexander, G. C. B.; Ma, Z.; Zhou, H.; Gosztola, D. J.; Ketterson, J. B., et al., Polar Fluctuations in Metal Halide Perovskites Uncovered by Acoustic Phonon Anomalies. *ACS Energy Lett.* **2017**, *2*, 2463-2469.

(51) López, C. A.; Abia, C.; Alvarez-Galván, M. C.; Hong, B.-K.; Martínez-Huerta, M. V.; Serrano-Sánchez, F.; Carrascoso, F.; Castellanos-Gómez, A.; Fernández-Díaz, M. T.; Alonso, J. A., Crystal Structure Features of $CsPbBr_3$ Perovskite Prepared by Mechanochemical Synthesis. *ACS Omega* **2020**, *5*, 5931-5938.

(52) Kundu, S.; Sadhu, S.; Bera, R.; Paramanik, B.; Patra, A., Fluorescence Dynamics and Stochastic Model for Electronic Interaction of Graphene Oxide with CdTe Qd in Graphene Oxide-CdTe Qd Composite. *J. Phys. Chem. C* **2013**, *117*, 23987-23995.

(53) Bera, R.; Mandal, S.; Mondal, B.; Jana, B.; Nayak, S. K.; Patra, A., Graphene–Porphyrin Nanorod Composites for Solar Light Harvesting. *ACS Sustainable Chem. Eng.* **2016**.

(54) Pearce, J. M., Photovoltaics — a Path to Sustainable Futures. *Futures* **2002**, *34*, 663-674.

(55) Bera, R., Design of Graphene Based Nanostructures and Their Photophysical Properties. *PhD. Dissertation, Jadavpur University* **2018**.

Chapter 3

Ultrafast Carrier Relaxation Dynamics of $CsPbBr_3$ Perovskite Nanocrystals: Influence of Shape

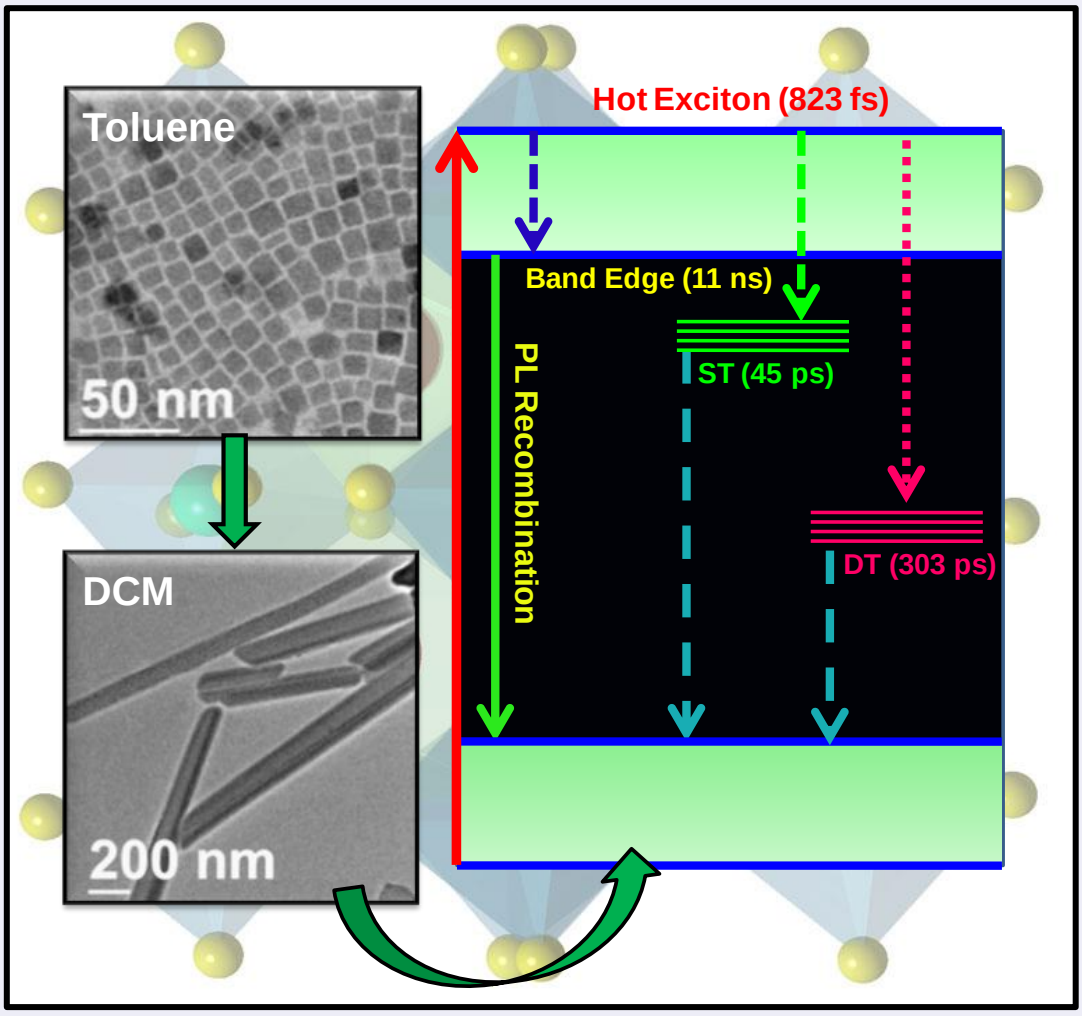

3.1. Introduction

Lead halide perovskite (LHP) nanocrystals (NCs) have emerged as an important class of nanomaterials for light-harvesting applications for photovoltaics, light-emitting diodes (LED), lasers, photodetector, and white phosphors. They exhibit extraordinary absorption coefficients, narrow full width at half maximum (FWHM), high photoluminescence quantum yield (PLQY), and defect tolerant nature, etc.[1-6] Several strategies have been used for designing various morphologies such as nanoparticles, nano-sheets, nano-wires (NWs), nano-platelets (NPLs) by altering the compositions (the ligand ratio and the anion/cation ratio) to control the photophysical properties of LHP NCs.[7-11] Usually, the tuning of photophysical properties of LHP NCs is done either changing halide precursors or anion exchange reactions.[12] The tuning of photophysical properties of LHP NCs in the presence of different solvents has been often overlooked. Less importance has been given to tuning of structural and optical properties of LHP NCs by changing solvent.[13-14]

On the other hand, the crystal phase and hot carrier cooling dynamics of perovskite NCs are critical for designing efficient photo-driven devices. The orthorhombic, tetragonal, and cubic crystal phases are found in $CsPbBr_3$ perovskites NCs, which influence the optical properties.[15-16] Minor crystal phases are sometimes missing in regular XRD analysis because most of the Bragg reflections from each polymorph overlap in the nano-regime, which are difficult to distinguish without Rietveld analysis.[17] Therefore, analysis of the actual crystal phase of LHP NCs by the Rietveld method is a very prudent choice.[18]

It is reported that the charge recombination and charge separation of perovskites NCs are essential steps for developing efficient photovoltaic devices.[19-23] Kim et al. have studied the hot carrier dynamics from $CsPbBr_3$ to $CsPbI_3$, which varies from 310 fs to 580 fs with changing the halide composition.[24] Fu et al. have studied the fluence-dependent hot carrier cooling mechanism of $MAPbI_3$ NCs.[25] Analysis of TA data by global and target kinetic models is fundamental to understand the complex carrier relaxation pathways of LHP NCs thoroughly. However, most studies regarding carrier relaxation dynamics of LHP NCs are based on single wavelength kinetics analysis. Here, we analyze TA data globally by target kinetics model to understand the complex carrier relaxation process. In the proposed model, it is assumed that the generated hot excitons will simultaneously decay to the swallow trap state (ST), deep trap state (DT), and band edge state after photoexcitation. To the best of our knowledge, less emphasis has been given on the carrier relaxation dynamics of $CsPbBr_3$ NCs

with changing the solvent polarity and shape of the NCs, which is an essential aspect for light-harvesting devices.

Here, we highlight the preparation of different shapes of $CsPbBr_3$ NCs by changing the solvent polarity and understanding their structural transformation and carrier relaxation processes. Changing the solvent polarity from toluene to dichloromethane, the structural transformation from cubic-shaped NCs to rod-shaped NCs is obtained. Rietveld analysis suggests that the preferred orientation (PO) along<202> orthorhombic phase is responsible for rod-shaped morphology. Furthermore, the influence of shape on carrier relaxation dynamics of $CsPbBr_3$ NCs by transient absorption spectroscopy is investigated. The fundamental studies of the role of solvent for changing shape and exciton dynamics of $CsPbBr_3$ NCs will be beneficial for device fabrication.

3.2. Results and Discussion

3.2.1. Structural Analysis

Morphological characterizations of the as-synthesized $CsPbBr_3$ NCs are done by Transmission electron microscopy (TEM). Figure 3.1A represents TEM image of $CsPbBr_3$ NCs in toluene. A highly monodispersed cubic shape with an average edge length of 10±0.5 nm is obtained. The high-resolution transmission electron microscopy (HRTEM) image confirms the lattice spacing of 0.291 nm (inset of Figure 3.1A).

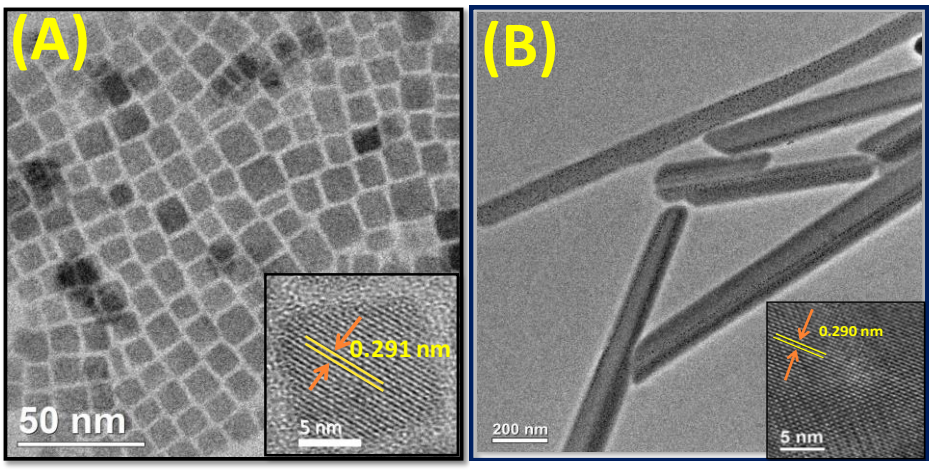

Figure 3.1. *TEM images of $CsPbBr_3$ NCs in (A) toluene, and (B) DCM. Insets show the HRTEM images.*[26] *Reproduced with permission from reference 26 (Copyright 2019 Royal Society of Chemistry).*

Analysis reveals that this lattice spacing corresponds to (200) plane formation of cubic $CsPbBr_3$ NCs. Furthermore, (200) plane from the selected area diffraction (SAED) pattern

(Figure 3.2A) confirms the appearance of the cubic phase. We have noticed a structural transformation from cubic shape to rod shape with changing the solvent from toluene to DCM. Figure 3.1B represents the TEM image of $CsPbBr_3$ NCs in DCM, which shows rod shape morphology having a width of 110±5 nm. The HRTEM image (inset of Figure 3.1B) and SAED pattern (Figure 3.2B) confirm the lattice spacing of 0.290 nm due to (202) plane of orthorhombic $CsPbBr_3$ NCs.

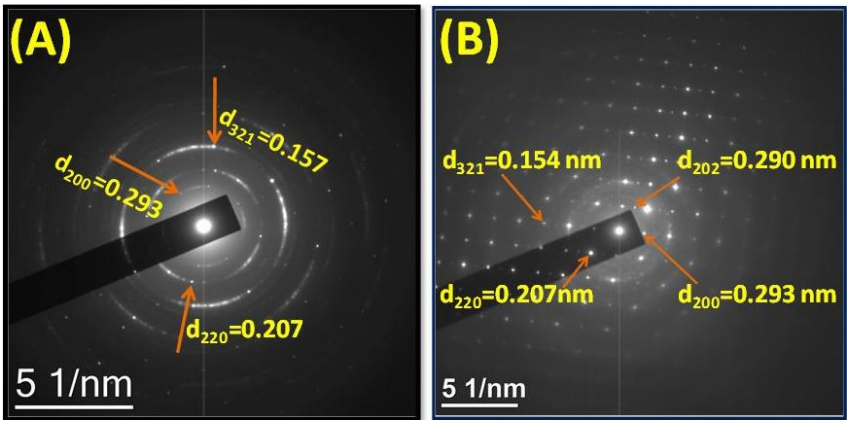

Figure 3.2. *SAED patterns of $CsPbBr_3$ NCs. (A) in toluene, (B) in DCM.[26] Reproduced with permission from reference 26 (Copyright 2019 Royal Society of Chemistry).*

Again, we have investigated the influence of various solvents on the morphology of the $CsPbBr_3$ NCs. Here, we have used THF (polarity index- 4.0), $CHCl_3$ (polarity index- 4.1) and ethyl acetate (polarity index- 4.4) also. The TEM images of $CsPbBr_3$ NCs for different solvents are given in Figure 3.3.

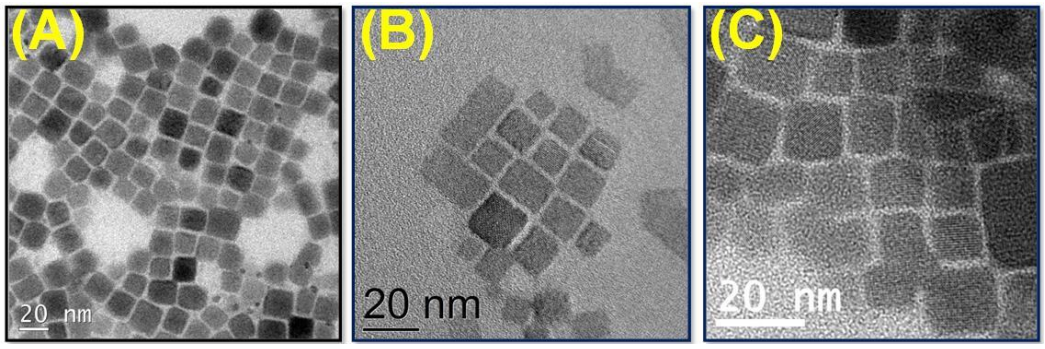

Figure 3.3. *TEM images of $CsPbBr_3$ NCs in (A) THF, (C) $CHCl_3$ and (E) ethyl acetate.[26] Reproduced with permission from reference 26 (Copyright 2019 Royal Society of Chemistry).*

Here, we discuss the probable mechanism for the structural transformation of $CsPbBr_3$ NCs from cubic to rod shape with changing the solvent from toluene to DCM (Scheme 3.1). A further detailed investigation is required to understand the mechanism for the formation of

rod shape NCs from cubic-shaped NCs. Here, $CsPbBr_3$ NCs are tightly coordinated with polar carboxylic (-COOH) and amino ($-NH_2$) head groups of oleic acid and oleyl amine capping ligands, and they are highly stable in non-polar toluene solvent.[27] After adding polar solvent (DCM), the polar head group (-COOH/$-NH_2$) of capping ligands shows a strong affinity towards the solvent and tends to come out from the surface of NCs. It results in the diffusion of a few capping ligands from the surface of NCs to solvent and causes bare NCs to surface. Thus, in a polar solvent (DCM), bare NCs facilitate to form of rod-shaped NCs by attachment of neighboring cubic NCs with each other.[28] It may be due to the less free energy on (202) plane of the cubic phase, which facilities the unidirectional growth of crystals to form rod shapes. This proposed mechanism is also supported by our Rietveld analysis which shows the unidirectional growth of rod-like morphology in DCM.

Scheme 3.1. *Schematic representation of the shape change mechanism from cubic $CsPbBr_3$ NCs to rod-shaped NCs in DCM solvent.*[26]

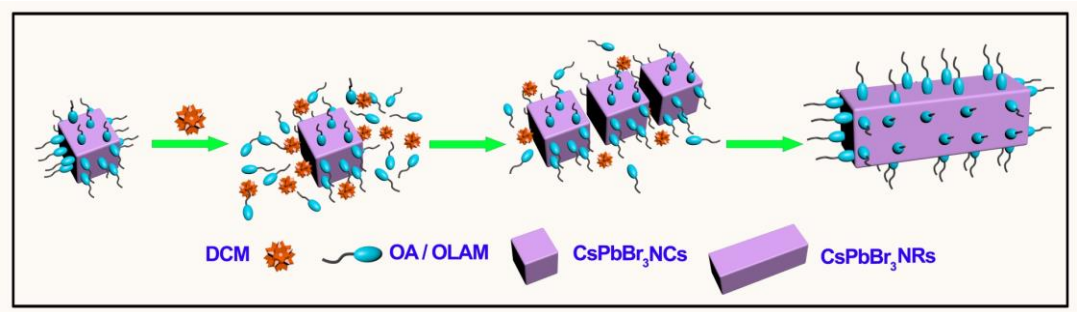

Rietveld powder structure refinement method is employed to analyze the XRD patterns of $CsPbBr_3$ NCs in two different solvents (i.e. in toluene and DCM). Figure 3.4(A-B) represents Rietveld profiles of the XRD patterns of NCs in toluene and DCM, respectively. Rietveld analysis of the XRD patterns of the $CsPbBr_3$ NCs in both toluene and DCM confirm the simultaneous presence of (i) cubic (COD# 1533063, Sp. Gr. $Pm\bar{3}m$) and (ii) orthorhombic (COD# 4510745, Sp. Gr. Pnma) $CsPbBr_3$ in different forms and ratios. All the major reflections from (100), (110), and (200) planes of cubic phase are severely overlapped with that of (101), (002), and (202) planes of orthorhombic phase owing to similar d_{hkl} (inter-planar spacing) values. This facilitates a coherent growth of the orthorhombic phase on the cubic lattice. The fitted XRD pattern of $CsPbBr_3$ NCs in toluene is displayed in Figure 3.4 A. Here, the primary (75 wt %) cubic phase remains well crystalline, whereas the minor (25 wt.%) orthorhombic phase remains in amorphous form. Interestingly, the intensity along <200> direction of cubic CsPbBr3 is more significant than its bulk counterpart (shown inset).

It signifies that (200) facet of the cube-shaped $CsPbBr_3$ is exposed more compared to the other facets along the direction of the incident beam of X-rays. However, the presence of the amorphous orthorhombic phase does not affect the gross cubic morphology. The simultaneous presence of crystalline cubic and orthorhombic phases is noticed for the XRD pattern of $CsPbBr_3$ NCs in DCM (inset of Figure 3.4 B).

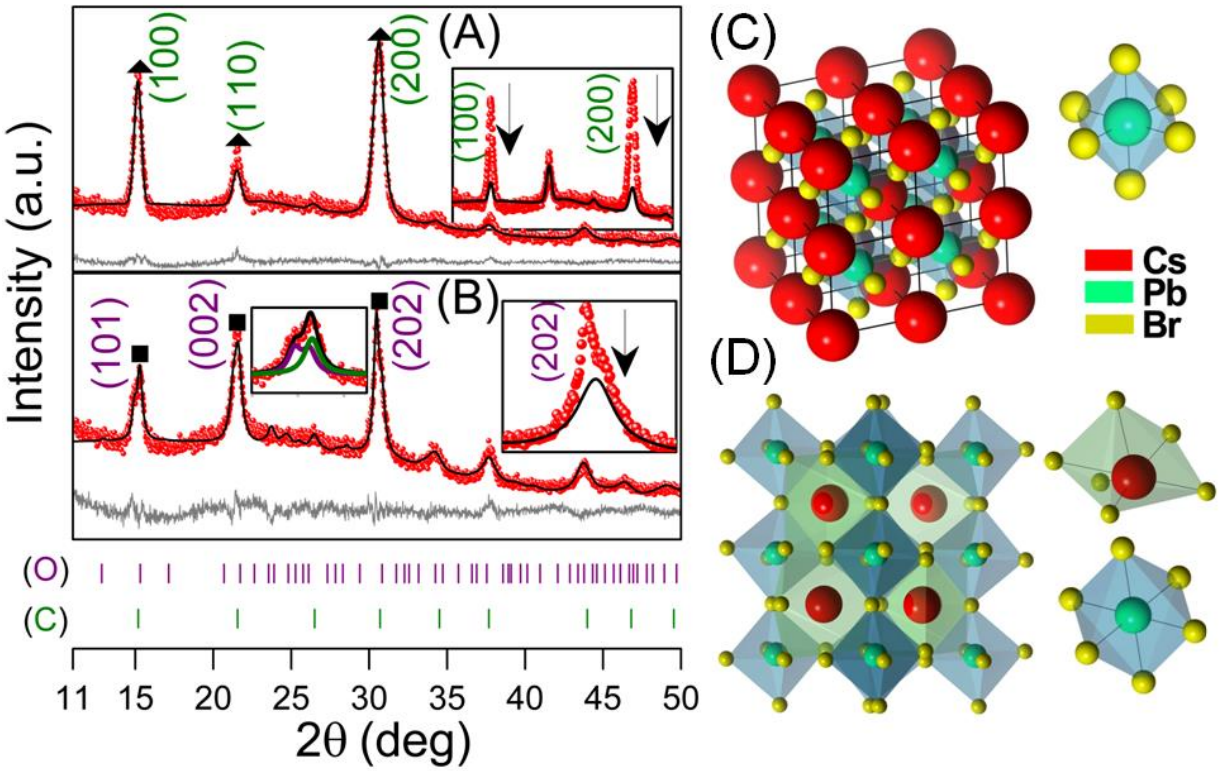

Figure 3.4. *Observed (red points) and calculated (black line) XRD patterns of $CsPbBr_3$ NCs in (A) toluene and (B) DCM. Green and purple represent cubic (C), orthorhombic (O) $CsPbBr_3$, respectively. ($I_O - I_C$), representing residue of Rietveld refinement is plotted (grey colored line) below each fitted pattern. Bar sequences, denoting the peak positions of individual phases, are plotted at the bottom. Modeling the atomic structures of (C) cubic and (D) orthorhombic $CsPbBr_3$. Different polyhedra formed by the constituent atoms of each structure are displayed at the right hand side of each corresponding structure.*[26] *Reproduced with permission from reference 26 (Copyright 2019 Royal Society of Chemistry).*

Detailed **(**micro) structural parameters obtained by refining the XRD patterns using Rietveld are given in Table 3.1. Rietveld's analysis confirms that the XRD pattern is completely devoid of any preferential growth for the cubic phase except for orthorhombic $CsPbBr_3$ along <202> (shown inset). The coherent growth of the orthorhombic (202) plane on cubic (200) lattice having preferential growth along <202> direction initiates the formation of rod shape

morphology towards $(202)_{orthorhombic}||(200)_{cubic}$ direction. Therefore, the cubic phase with preferred orientation (PO) is responsible for the cubic morphology of $CsPbBr_3$ NCs in toluene. In contrast, the crystallinity and PO of the orthorhombic phase play a pivotal role in providing the unidirectional growth of rod-shaped $CsPbBr_3$ NCs in DCM. Atomic arrangements of constituent Cs, Pb, and Br atoms in cubic and orthorhombic $CsPbBr_3$ perovskites are displayed in Figure 3.4 (C-D). In cubic $CsPbBr_3$ Cs, Pb, and Br atoms occupy corner (0,0,0), body centred (1/2,1/2,1/2), and face centred (0,1/2,1/2) positions respectively.

Table 3.1. *(Micro) structure parameters obtained by refining the XRD patterns using Rietveld fitting method.*[26]

$CsPbBr_3$	Phase(s) present			Wt. (%)	Lattice parameters (Å)			PO	
	Chemical formula	Crystal system	Sp. Gr.		*a*	*b*	*c*	Dir.	Coef.(r)
Toluene	$CsPbBr_3$	Cubic	$Pm\bar{3}m$	75	5.8308 (6)			<200>	0.33
	$CsPbBr_3$	Ortho	Pnma	25					
DCM	$CsPbBr_3$	Cubic	$Pm\bar{3}m$	60	5.8839 (8)				
	$CsPbBr_3$	Ortho	Pnma	40	8.1652 (7)	12.0673 (11)	8.5522 (16)	<202>	0.40

Here, each Pb atom remains entirely inside a regular octahedron constituted by six surrounded Br atoms (forming $PbBr_6$ octahedron), where each Pb-Br bond's bond length (BL) is 2.94 Å. In orthorhombic $CsPbBr_3$, two different types of octahedra are noticed, (i) regular $PbBr_6$ octahedron (Pb−Br, BL of 2.96 Å), and (ii) irregular $CsBr_6$ octahedron where Cs atom remains partially within the void. The XRD pattern of the residue of $CsPbBr_3$ NCs before redisperse is provided in Figure 3.5.

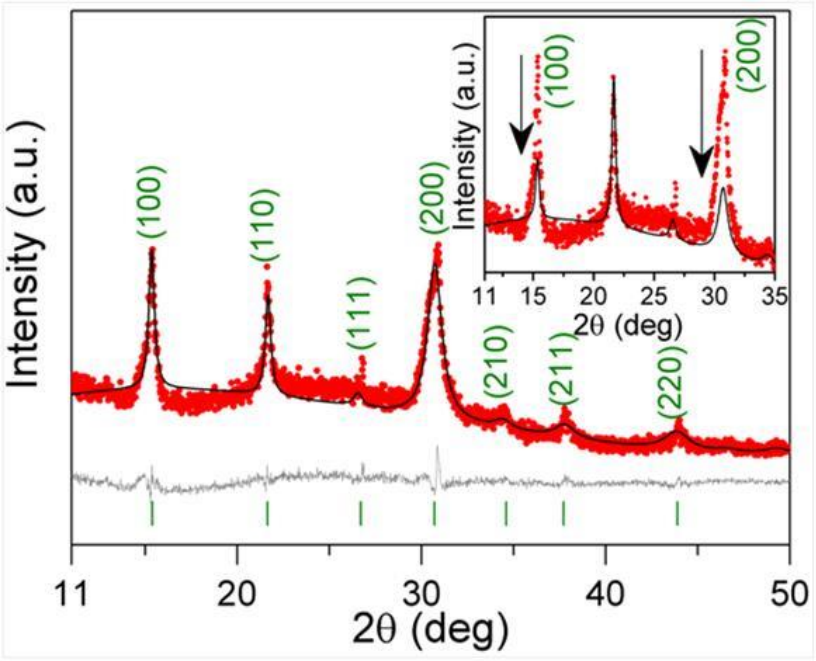

Figure 3.5. *The profile of the Rietveld analysis (black line) of the XRD pattern (red points) of the residue of the sample before redispersing in toluene and DCM. The inset of the pattern shows the presence of preferred orientation along <200>. ($I_O - I_C$), representing residue of Rietveld refinement is plotted (grey colored line) below the fitted pattern. Bar sequence, denoting the peak positions of cubic $CsPbBr_3$, is plotted at the bottom.*[26] *Reproduced with permission from reference 26 (Copyright 2019 Royal Society of Chemistry).*

3.2.2. Steady-state and time-resolved spectroscopy

Figure 3.6A represents the UV-Vis absorption (solid balls) of $CsPbBr_3$ NCs along with PL spectra (solid line) in toluene (a) and DCM (b), respectively. The emission of both the NCs shows the green color under UV excitation (λ_{ex}=365 nm). For the NCs in toluene, the absorption and PL bands are observed at 502 nm and 515 nm, respectively (Figure 3.6A, a). In the case of the NCs in DCM, absorption and PL maxima are found at 507 nm and 521 nm, respectively (Figure 3.6A, b). It is to be noticed that a small change in PL band is observed with changing the shape from cubic to rod shape. The FWHM of the PL band decreases from 21 nm to 17 nm with changing the solvent from toluene to DCM. The PLQY of $CsPbBr_3$ NCs is found to be decreased from 65% to 58% with changing the solvent from toluene to DCM. This clearly indicates the modification of radiative relaxation with the transformation from cubic-shaped (in toluene) to rod-shaped NCs (in DCM).

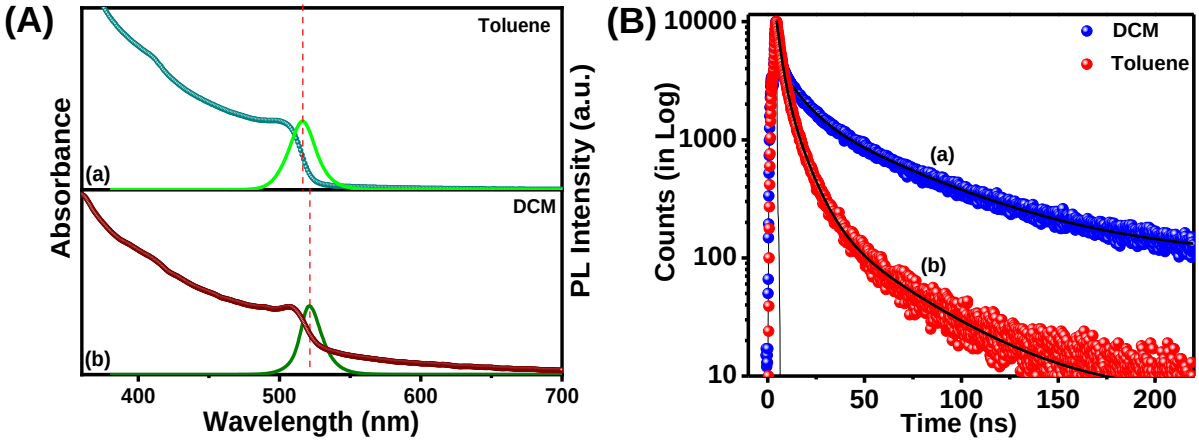

Figure 3.6. *(A) UV-Vis absorption (solid balls) and PL spectra (solid line) of $CsPbBr_3$ NCs in toluene (a), in DCM (b); (B) Time-resolved PL decay time of $CsPbBr_3$ NCs in DCM (a), in toluene (b). In Fig. B, λ_{ex}=375 nm and λ_{em}= 521 nm (a) and 515 nm (b). All the decay curves are fitted in tri-exponential function.*[26] *Reproduced with permission from reference 26 (Copyright 2019 Royal Society of Chemistry).*

Time-resolved spectroscopic studies are performed to investigate the relaxation dynamics of $CsPbBr_3$ NCs. Figure 3.6B shows the PL decay profile of $CsPbBr_3$ NCs in DCM (a) and toluene (b), respectively. It is seen that the lifetime of $CsPbBr_3$ NCs in DCM is longer than that of NCs in toluene. All the samples are excited at 375 nm, and the emission decays are monitored at 515 nm and 521 nm for $CsPbBr_3$ NCs in toluene and DCM, respectively. All the decay curves are fitted well with the tri-exponential function. For $CsPbBr_3$ NCs in toluene (cubic shape), the values for τ_1, τ_2, and τ_3 with their contributions are 2.0 ± 0.4 (63.4 ± 3.5%), 9.3 ± 0.3 (33.7 ± 1.3%), 39.2 ± 0.6 (2.9 ± 0.8%), respectively and the average value of lifetime is 5.6 ± 0.15 ns. In case of $CsPbBr_3$ NCs in DCM (rod shape), the corresponding values for τ_1, τ_2, and τ_3 with their contributions are 1.2 ± 0.2 ns (54.6 ± 2.5%), 11.0 ± 0.2 ns (28.5 ± 1.2%), 61.9 ± 0.7 ns (16.9 ± 1%) respectively and the average decay time is 14.3± 0.5 ns. The multi-exponential decay of perovskite NCs is due to excitonic recombination and radiative recombination associated with trap states.[29-30] Interpretation of multi-exponential PL decay kinetics is difficult without a well-defined kinetic model.[29] Here, τ_2 is assigned due to excitonic recombination. The other two components are due to trap state mediated radiative recombination.[16, 29] The charge trapping of the perovskite NCs is due to a halide deficient surface. Alivisatos and coworkers have demonstrated that the surface halide vacancies of perovskite NCs are responsible for charge trapping.[31] Zeng and coworkers have developed a new strategy to reduce the nonradiative recombination by an equivalent ligand to eliminate the probability of charge trapping due to bromide vacancies.[32-33] The radiative rate constants

are found to be 0.116 ns^{-1} and 0.040 ns^{-1} for cubic and rod-shaped NCs, respectively. Hence, the analysis of decay kinetics suggests that the shape has an important role that eventually controls the relaxation dynamics of the LHP NCs.

3.2.3 Ultrafast transient absorption spectroscopy

Femtosecond transient absorption spectroscopy (fs-TAS) is employed to study the carrier relaxation dynamics of $CsPbBr_3$ NCs with changing the solvent polarity. The ultrafast measurement is important to unfold the carrier relaxation processes.[34] Less emphasis has been given on the exciton dynamics of LHP NCs by using global and targeted analysis.[35-38] All the samples are excited at 375 nm pump pulse with low pump power (< 5 μJ/cm^2) to avoid multi-exciton generation. The fs-TAS data are fitted with a targeted kinetic scheme to estimate the individual rate constant and lifetime of respective relaxation channels of the NCs. Figure 3.7(A, B) represents the conventional profile pictures of fs-TAS data for cubic shaped $CsPbBr_3$ NCs (in toluene) and rod-shaped $CsPbBr_3$ NCs (in DCM), composed of TA contour plots (Ai, Bi), Time-gated spectra at short (50-800 fs) delay time (Aii, Bii), long (5-1000 ps) delay time (Aiii, Biii) and time traces at selected probe wavelengths (Aiv, Biv). Interestingly, TA spectra of both cubic and rod-shaped NCs show derivative-like spectral features, which consist of a short-lived (<700 fs) and a long-lived (>1 ns) PIA (named as PIA_1 and PIA_2, respectively) along with a strong negative exciton bleach (EB).

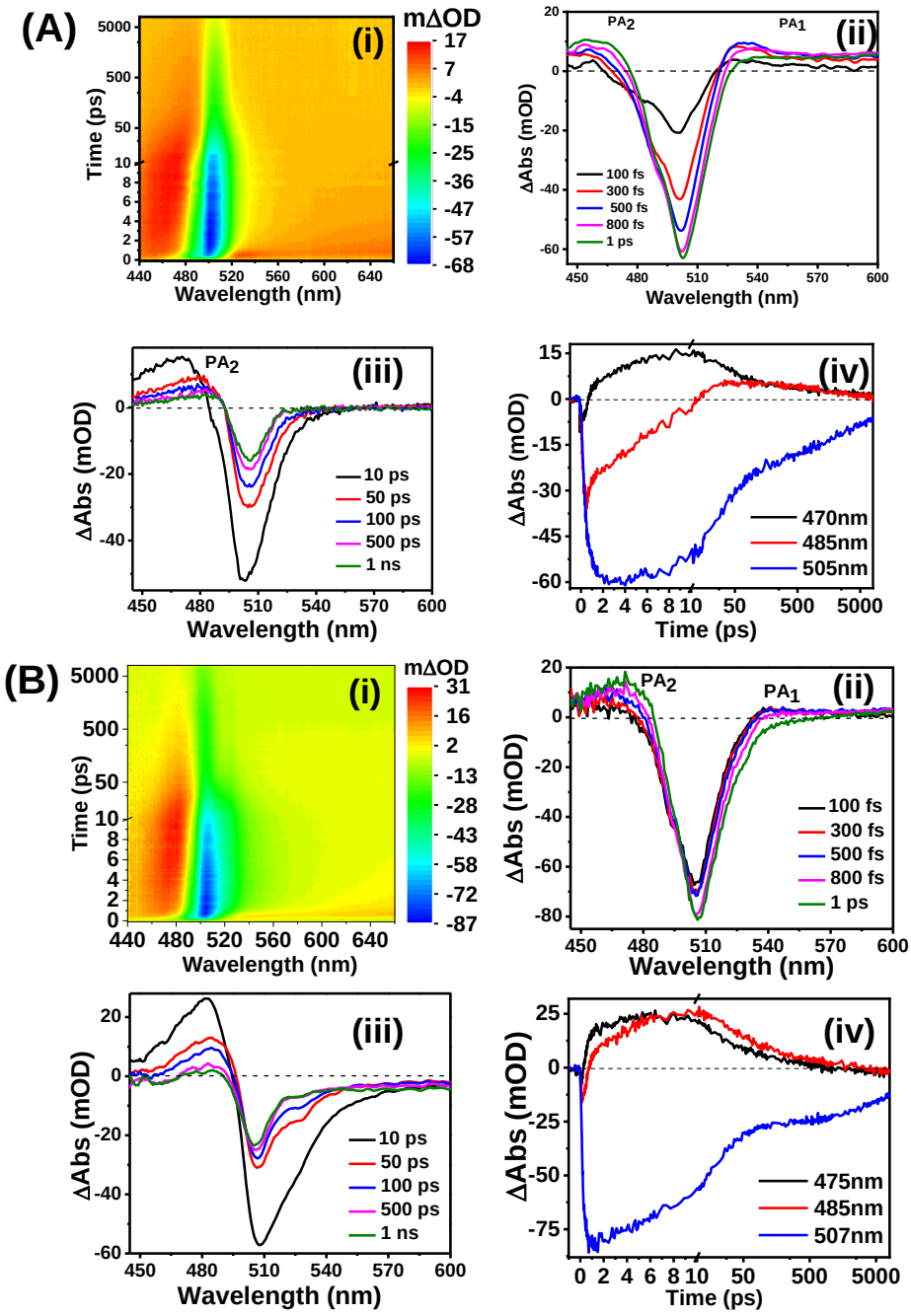

Figure 3.7. *TA profile pictures of $CsPbBr_3$ NCs (A) in toluene and (B) in DCM after exciting at 375 nm. Typical TA contour plots (Ai, Bi), Time-gated spectra at short (50-800 fs) delay time (Aii, Bii), long (5-1000 ps) delay time (Aii, Bii) and time traces (Aiii, Biii) at selected probe wavelength for NCs in toluene and DCM, respectively. The time axis is linear up to 10 ps and logarithmic thereafter.[26] Reproduced with permission from reference 26 (Copyright 2019 Royal Society of Chemistry).*

Short-lived PIA_1 vanishes after 600 fs and is dominated by strong exciton bleach (EB). EB for $CsPbBr_3$ NCs is attributed for state-filling. In contrast, derivative like TA feature is due to coulombic interaction between the hot-exciton and band edge exciton produced by the pump

and probe laser, respectively (commonly known as biexciton effect).[23-24, 39] To understand the ongoing photoinduced processes, we first analyzed the time information at all wavelengths by applying global analysis (parallel kinetic model). This procedure gives decay-associated difference spectra (DADS), the spectra of the individual excited-state species with corresponding lifetime. We observed that the four components are required for both the NCs to describe the TA data adequately during the investigation. All species with their respective decay-associated difference spectra (DADS) are shown in Figure 3.8 (as DADS1, DADS2, DADS3, and DADS4).

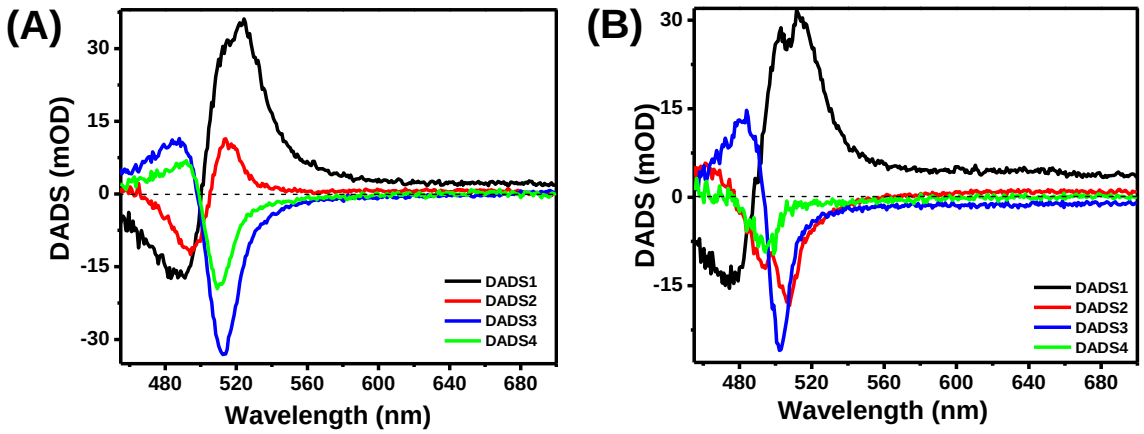

Figure 3.8. *Decay-associated difference spectra (DADS) after performing global Analysis of TA data of (A) cubic shaped $CsPbBr_3$ NCs in toluene and (B) rod-shaped $CsPbBr_3$ NCs in DCM, respectively, after using 375 nm excitation pulses.[26] Reproduced with permission from reference 26 (Copyright 2019 Royal Society of Chemistry).*

The DADS1 is short-lived (838±0.05 fs and 823 ±0.04 fs for NCs in toluene and DCM, respectively), and it is due to the initial excitation to the hot exciton state. This consists of exciton bleach (EB) nearly at 490 nm and photoinduced absorption (PIA) at 524 nm for cubic-shaped NCs (in toluene). For rod-shaped NCs (in DCM) EB and PIA are found at 475 nm and at 512nm, respectively. DADS2 (shallow trap state) has a lifetime of 25±0.3 ps for cubic-shaped NCs (in toluene) and 45±0.25 ps for rod-shaped NCs (in DCM). For DADS2, EB peak and PIA are observed at around 493 nm, and 514 nm for cubic shaped NCs in toluene, whereas corresponding EB and PIA are found at 505 nm and 468 nm, respectively for rod-shaped NCs in DCM. Similarly, DADS 3 (deep trap state) has a lifetime of 163±0.4 ps for cubic shaped NCs and 303±0.34 ps for rod shaped NCs. For DADS3, EB and PIA are observed at around 513 nm and 487 nm for cubic-shaped NCs, whereas EB and PIA are at 501 nm and 483 nm, respectively for rod-shaped NCs. DADS4 (band-edge state) has a lifetime of 5±0.5 ns for cubic-shaped NCs and 11±0.56 ns for rod-shaped NCs. For DADS4

EB and PIA are monitored at around 509 nm and 491 nm, respectively, for cubic-shaped NCs. For rod-shaped NCs, EB is observed at 495 nm, but PIA shows very negligible intensity. It is worth noting that the measurement of the slowest nanosecond time component is beyond our limitation since the maximum delay time available in our instrument is 8 ns. In the global analysis, we have performed a kinetic target model with spectro-temporal parameters on TA data to get a clear physical insight of various processes through which photogenerated excitons decay. Upon target analysis of TA data, we obtain individual excited-state (compartment) species (species associated difference spectra, SADS), their lifetimes, and decay rate constants. A four-state kinetics model is proposed to satisfy the fitting of TA data for both cubic and rod-shaped NCs along with their global lifetime (Figure 3.9 A, C).

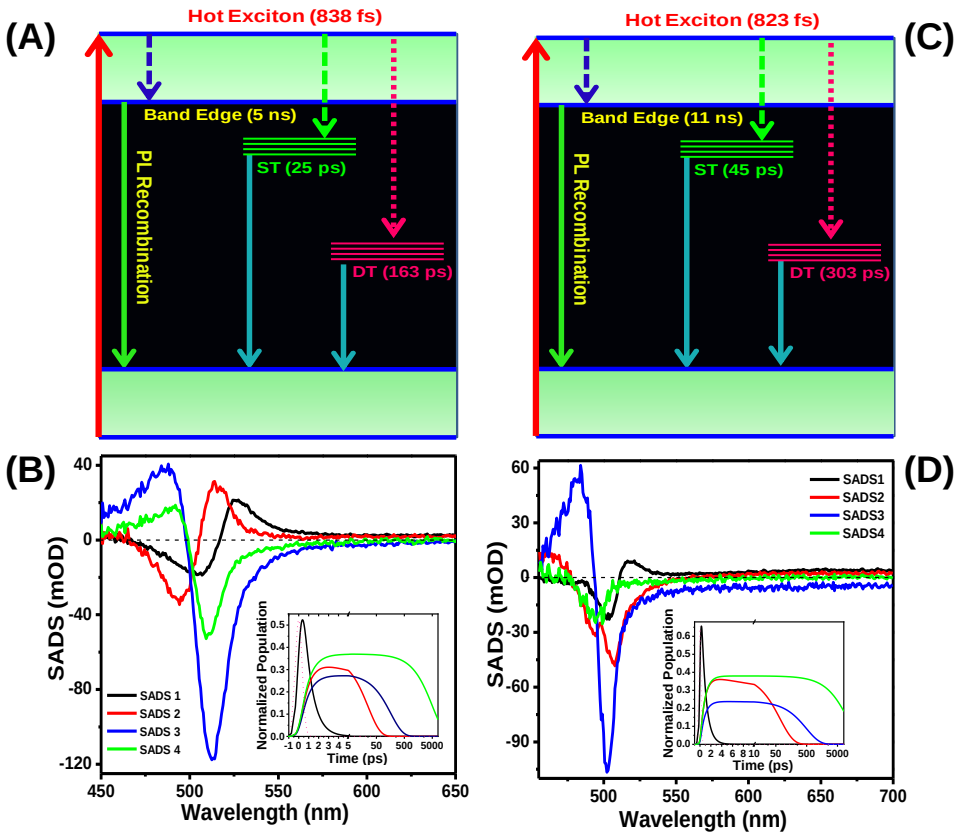

Figure 3.9. *The kinetic scheme used for target analysis of TA data and obtained species-associated difference spectra (SADS) of $CsPbBr_3$ NCs in toluene (A, B) and DCM (C D), respectively after excitation at 375 nm. Inset shows population profiles of the corresponding SADSs.*[26] *Reproduced with permission from reference 26 (Copyright 2019 Royal Society of Chemistry).*

The model assumes the presence of hot exciton, shallow trap (ST), deep trap (DT), and band edge states for relaxation processes. Here, we assume that the generated hot excitons will simultaneously decay to the ST state, DT state, and the band edge state after photoexcitation. Figure 3.9 (B, D) describes the obtained SADSs and the corresponding estimated population time (shown in the insets of Figure 3.9 B, D) for cubic and rod-shaped NCs, respectively. It is worth noting that the lifetime values associated with the four states (SADSs) are found to be same as those obtained from DADSs. The goodness of TA data for corresponding cubic and rod-shaped NCs are shown in Figure 3.10.

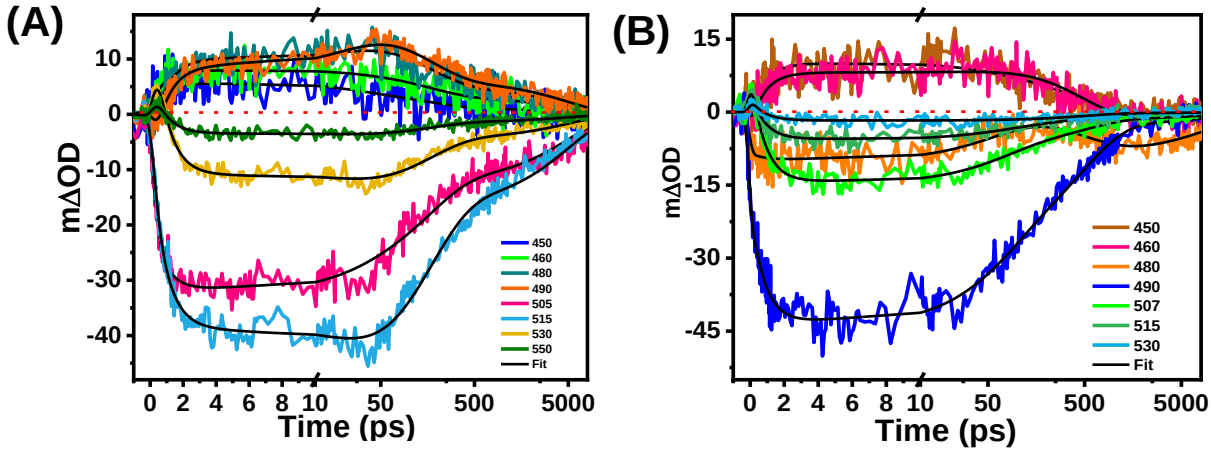

Figure 3.10. *The goodness of fit TA data based on global and target analysis for (A) cubic shaped (in toluene) and (B) rod-shaped (in DCM) NCs.[26] Reproduced with permission from reference 26 (Copyright 2019 Royal Society of Chemistry).*

The SADS1 is short-lived for both the NCs (838±0.04 fs and 823±0.05 fs for cubic and rod shaped NCs, respectively) and is due to the initial excitation of the hot exciton state. The SADS1 has a broad EB at 505 nm and PIA at 524 nm for cubic-shaped NCs, whereas the EB and PIA are around at 503 nm and 517 nm, respectively for rod-shaped NCs. SADS2 with the comparatively narrow profile is responsible for shallow trap (ST) states, having a lifetime of 25±0.25 ps and 45±0.31 ps for cubic and rod-shaped NCs, respectively. For SADS2, EB and PIA peaks are at around 494 nm, and 513 nm, respectively for cubic shaped NCs, whereas EB and PIA are observed at 507 nm, and 470 nm, respectively for rod-shaped NCs. Similarly, the spectral signature of SADS3 arises due to the deep trap state, which has a lifetime of 163 ps±0.36 with EB and PIA at 512 nm and 486 nm, respectively for cubic shaped NCs.

In contrast, for rod-shaped NCs, SADS3 has a lifetime of 303±0.27 ps with EB and PIA at 502 nm and 483 nm, respectively. The evolution of SADS4 is assigned for the band-edge state, which has a lifetime of 5±0.5 ns and 11± 0.4 ns for cubic and rod-shaped NCs,

respectively. For cubic-shaped NCs, the SADS4 has an EB and PIA at 510 nm and 491nm, respectively, whereas the SADS4 has an EB at 495 nm and very weak PIA for rod-shaped NCs. The obtained band edge lifetime (5 ns and 11 ns for cubic and rod-shaped NCs, respectively) matches the TCSPC results. It is to be mentioned that measurement of the slowest nanosecond time component is beyond our instrumental limitation since the maximum delay time available in our instrument is 8 ns. analysis reveals that trap states play a major role in determining the carrier relaxation pathways for cubic and rod-shaped NCs. The significant increase of the lifetime of ST states from 25 ps (for cubic shaped NCs) to 45 ps (for cubic shaped NCs) and DT states from 163 ps (for cubic shaped NCs) to 303 ps (for cubic shaped NCs) are responsible for the enhanced average lifetime from 5.6 ns (cubic shaped) to 14.3 ns (rod-shaped) with changing the solvent from toluene to DCM. Interestingly, we have observed the same relaxation pathways for both cubic and rod-shaped NCs upon excitation at 400 nm pulse. However, the obtained lifetime of the corresponding state (hot exciton state, ST state, DT state) differs slightly.

3.3. Conclusions

In summary, we describe the influence of the shape on carrier relaxation dynamics of $CsPbBr_3$ NCs. We have shown structural transformation from cubic form to rod shape by changing the solvent from toluene to DCM. The detailed crystal phase analysis has been done by Rietveld full profile method. The drastic increase in a lifetime (5.6 ns to 14.3 ns) is observed with changing the solvent from toluene to DCM. Furthermore, the global target kinetics model investigates the spectral signature of individual excited state species (i.e. species associated difference spectra, SADS). Femtosecond transient absorption study reveals that trap states play a vital role in the carrier relaxation dynamics of cubic and rod-shaped NCs. The lifetime of deep trap (DT) states changed drastically from 163 ps to 303 ps, respectively, changing the solvent from toluene to DCM. This solvent-controlled morphology and photophysical properties of $CsPbBr_3$ NCs may be beneficial for designing efficient light-harvesting systems.

3.4. References

(1) Stranks, S. D.; Eperon, G. E.; Grancini, G.; Menelaou, C.; Alcocer, M. J. P.; Leijtens, T.; Herz, L. M.; Petrozza, A.; Snaith, H. J., Electron-Hole Diffusion Lengths Exceeding 1 Micrometer in an Organometal Trihalide Perovskite Absorber. *Science* **2013**, *342*, 341-344.

(2) Dursun, I.; Shen, C.; Parida, M. R.; Pan, J.; Sarmah, S. P.; Priante, D.; Alyami, N.; Liu, J.; Saidaminov, M. I.; Alias, M. S., et al., Perovskite Nanocrystals as a Color Converter for Visible Light Communication. *ACS Photonics* **2016**, *3*, 1150-1156.

(3) Kundu, S.; Patra, A., Nanoscale Strategies for Light Harvesting. *Chem. Rev.* **2017**, *117*, 712-757.

(4) Chen, S.; Roh, K.; Lee, J.; Chong, W. K.; Lu, Y.; Mathews, N.; Sum, T. C.; Nurmikko, A., A Photonic Crystal Laser from Solution Based Organo-Lead Iodide Perovskite Thin Films. *ACS Nano* **2016**, *10*, 3959-3967.

(5) De Roo, J.; Ibáñez, M.; Geiregat, P.; Nedelcu, G.; Walravens, W.; Maes, J.; Martins, J. C.; Van Driessche, I.; Kovalenko, M. V.; Hens, Z., Highly Dynamic Ligand Binding and Light Absorption Coefficient of Cesium Lead Bromide Perovskite Nanocrystals. *ACS Nano* **2016**, *10*, 2071-2081.

(6) Huang, H.; Bodnarchuk, M. I.; Kershaw, S. V.; Kovalenko, M. V.; Rogach, A. L., Lead Halide Perovskite Nanocrystals in the Research Spotlight: Stability and Defect Tolerance. *ACS Energy Lett.* **2017**, *2*, 2071-2083.

(7) Shamsi, J.; Dang, Z.; Bianchini, P.; Canale, C.; Di Stasio, F.; Brescia, R.; Prato, M.; Manna, L., Colloidal Synthesis of Quantum Confined Single Crystal $CsPbBr_3$ Nanosheets with Lateral Size Control up to the Micrometer Range. *J. Am. Chem. Soc.* **2016**, *138*, 7240-7243.

(8) Zhang, D.; Yu, Y.; Bekenstein, Y.; Wong, A. B.; Alivisatos, A. P.; Yang, P., Ultrathin Colloidal Cesium Lead Halide Perovskite Nanowires. *J. Am. Chem. Soc.* **2016**, *138*, 13155-13158.

(9) Mir, W. J.; Jagadeeswararao, M.; Das, S.; Nag, A., Colloidal Mn-Doped Cesium Lead Halide Perovskite Nanoplatelets. *ACS Energy Lett.* **2017**, *2*, 537-543.

(10) Zhu, Z.-Y.; Yang, Q.-Q.; Gao, L.-F.; Zhang, L.; Shi, A.-Y.; Sun, C.-L.; Wang, Q.; Zhang, H.-L., Solvent-Free Mechanosynthesis of Composition-Tunable Cesium Lead Halide Perovskite Quantum Dots. *J. Phys. Chem. Lett.* **2017**, *8*, 1610-1614.

(11) Brennan, M. C.; Herr, J. E.; Nguyen-Beck, T. S.; Zinna, J.; Draguta, S.; Rouvimov, S.; Parkhill, J.; Kuno, M., Origin of the Size-Dependent Stokes Shift in $CsPbBr_3$ Perovskite Nanocrystals. *J. Am. Chem. Soc.* **2017**, *139*, 12201-12208.

(12) Nedelcu, G.; Protesescu, L.; Yakunin, S.; Bodnarchuk, M. I.; Grotevent, M. J.; Kovalenko, M. V., Fast Anion-Exchange in Highly Luminescent Nanocrystals of Cesium Lead Halide Perovskites ($CsPbX_3$, X = Cl, Br, I). *Nano Lett.* **2015**, *15*, 5635-5640.

(13) Ramadan, A. J.; Rochford, L. A.; Fearn, S.; Snaith, H. J., Processing Solvent-Dependent Electronic and Structural Properties of Cesium Lead Triiodide Thin Films. *J. Phys. Chem. Lett.* **2017**, *8*, 4172-4176.

(14) Park, G.; Oh, I.-H.; Park, J. M. S.; Jung, J.; You, C.-Y.; Kim, J.-S.; Kim, Y.; Jung, J. H.; Hur, N.; Kim, Y., et al., Solvent-Dependent Self-Assembly of Two Dimensional Layered Perovskite $(C_6H_5CH_2CH_2NH_3)_2MCl_4$ (M = Cu, Mn) Thin Films in Ambient Humidity. *Sci. Rep.* **2018**, *8*, 4661.

(15) Protesescu, L.; Yakunin, S.; Bodnarchuk, M. I.; Krieg, F.; Caputo, R.; Hendon, C. H.; Yang, R. X.; Walsh, A.; Kovalenko, M. V., Nanocrystals of Cesium Lead Halide Perovskites ($CsPbX_3$, X = Cl, Br, and I): Novel Optoelectronic Materials Showing Bright Emission with Wide Color Gamut. *Nano Lett.* **2015**, *15*, 3692-3696.

(16) Swarnkar, A.; Chulliyil, R.; Ravi, V. K.; Irfanullah, M.; Chowdhury, A.; Nag, A., Colloidal $CsPbBr_3$ Perovskite Nanocrystals: Luminescence Beyond Traditional Quantum Dots. *Angew. Chem. Int. Ed.* **2015**, *54*, 15424-15428.

(17) Rietveld, H. M., A Profile Refinement Method for Nuclear and Magnetic Structures. *J. Appl. Crystallogr.* **1969**, *2*, 65-71.

(18) Akkerman, Q. A.; Rainò, G.; Kovalenko, M. V.; Manna, L., Genesis, Challenges and Opportunities for Colloidal Lead Halide Perovskite Nanocrystals. *Nat. Mater.* **2018**, *17*, 394-405.

(19) Bretschneider, S. A.; Laquai, F.; Bonn, M., Trap-Free Hot Carrier Relaxation in Lead–Halide Perovskite Films. *J. Phys. Chem. C* **2017**, *121*, 11201-11206.

(20) Yumoto, G.; Tahara, H.; Kawawaki, T.; Saruyama, M.; Sato, R.; Teranishi, T.; Kanemitsu, Y., Hot Biexciton Effect on Optical Gain in $CsPbI_3$ Perovskite Nanocrystals. *J. Phys. Chem. Lett.* **2018**, *9*, 2222-2228.

(21) Begum, R.; Parida, M. R.; Abdelhady, A. L.; Murali, B.; Alyami, N. M.; Ahmed, G. H.; Hedhili, M. N.; Bakr, O. M.; Mohammed, O. F., Engineering Interfacial Charge Transfer in $CsPbBr_3$ Perovskite Nanocrystals by Heterovalent Doping. *J. Am. Chem. Soc.* **2017**, *139*, 731-737.

(22) Aneesh, J.; Swarnkar, A.; Kumar Ravi, V.; Sharma, R.; Nag, A.; Adarsh, K. V., Ultrafast Exciton Dynamics in Colloidal $CsPbBr_3$ Perovskite Nanocrystals: Biexciton Effect and Auger Recombination. *J. Phys. Chem. C* **2017**, *121*, 4734-4739.

(23) Wu, K.; Liang, G.; Shang, Q.; Ren, Y.; Kong, D.; Lian, T., Ultrafast Interfacial Electron and Hole Transfer from $CsPbBr_3$ Perovskite Quantum Dots. *J. Am. Chem. Soc.* **2015**, *137*, 12792-12795.

(24) Chung, H.; Jung, S. I.; Kim, H. J.; Cha, W.; Sim, E.; Kim, D.; Koh, W.-K.; Kim, J., Composition-Dependent Hot Carrier Relaxation Dynamics in Cesium Lead Halide ($CsPbX_3$, X=Br and I) Perovskite Nanocrystals. *Angew. Chem. Int. Ed.* **2017**, *56*, 4160-4164.

(25) Fu, J.; Xu, Q.; Han, G.; Wu, B.; Huan, C. H. A.; Leek, M. L.; Sum, T. C., Hot Carrier Cooling Mechanisms in Halide Perovskites. *Nat. Commun.* **2017**, *8*, 1300.

(26) Ghosh, G.; Jana, B.; Sain, S.; Ghosh, A.; Patra, A., Influence of Shape on the Carrier Relaxation Dynamics of $CsPbBr_3$ Perovskite Nanocrystals. *Phys. Chem. Chem. Phys.* **2019**, *21*, 19318-19326.

(27) Huang, H.; Raith, J.; Kershaw, S. V.; Kalytchuk, S.; Tomanec, O.; Jing, L.; Susha, A. S.; Zboril, R.; Rogach, A. L., Growth Mechanism of Strongly Emitting $CH_3NH_3PbBr_3$ Perovskite Nanocrystals with a Tunable Bandgap. *Nature Communications* **2017**, *8*, 996.

(28) Jing, Q.; Su, Y.; Xing, X.; Lu, Z., Highly Luminescent Cspbbr3 Nanorods Synthesized by a Ligand-Regulated Reaction at the Water–Oil Interface. *J. Mater. Chem. C*, **2019**, *7*, 1854-1858.

(29) Koscher, B. A.; Swabeck, J. K.; Bronstein, N. D.; Alivisatos, A. P., Essentially Trap-Free $CsPbBr_3$ Colloidal Nanocrystals by Postsynthetic Thiocyanate Surface Treatment. *J. Am. Chem. Soc.* **2017**, *139*, 6566-6569.

(30) Li, X.; Wu, Y.; Zhang, S.; Cai, B.; Gu, Y.; Song, J.; Zeng, H., $CsPbX_3$ Quantum Dots for Lighting and Displays: Room-Temperature Synthesis, Photoluminescence Superiorities, Underlying Origins and White Light-Emitting Diodes. *Adv. Funct. Mater.* **2016**, *26*, 2435-2445.

(31) Nenon, D. P.; Pressler, K.; Kang, J.; Koscher, B. A.; Olshansky, J. H.; Osowiecki, W. T.; Koc, M. A.; Wang, L.-W.; Alivisatos, A. P., Design Principles for Trap-Free $CsPbX_3$ Nanocrystals: Enumerating and Eliminating Surface Halide Vacancies with Softer Lewis Bases. *J. Am. Chem. Soc.* **2018**, *140*, 17760-17772.

(32) Yang, D.; Li, X.; Zhou, W.; Zhang, S.; Meng, C.; Wu, Y.; Wang, Y.; Zeng, H., $CsPbBr_3$ Quantum Dots 2.0: Benzenesulfonic Acid Equivalent Ligand Awakens Complete Purification. *Adv. Mater.* **2019**, *31*, 1900767.

(33) Wu, Y.; Wei, C.; Li, X.; Li, Y.; Qiu, S.; Shen, W.; Cai, B.; Sun, Z.; Yang, D.; Deng, Z., et al., In Situ Passivation of $Pbbr6^{4-}$ Octahedra toward Blue Luminescent $CsPbBr_3$ Nanoplatelets with near 100% Absolute Quantum Yield. *ACS Energy Lett.* **2018**, *3*, 2030-2037.

(34) Cooper, J. K.; Reyes-Lillo, S. E.; Hess, L. H.; Jiang, C.-M.; Neaton, J. B.; Sharp, I. D., Physical Origins of the Transient Absorption Spectra and Dynamics in Thin-Film Semiconductors: The Case of $BiVO_4$. *J. Phys. Chem. C* **2018**, *122*, 20642-20652.

(35) Chirvony, V. S.; Martínez-Pastor, J. P., Trap-Limited Dynamics of Excited Carriers and Interpretation of the Photoluminescence Decay Kinetics in Metal Halide Perovskites. *J. Phys. Chem. Lett.* **2018**, *9*, 4955-4962.

(36) Bakthavatsalam, R.; Biswas, A.; Chakali, M.; Bangal, P. R.; Kore, B. P.; Kundu, J., Temperature-Dependent Photoluminescence and Energy-Transfer Dynamics in Mn^{2+}-Doped $(C_4H_9NH_3)_2PbBr_4$ Two-Dimensional (2D) Layered perovskite. *J. Phys. Chem. C* **2019**, *123*, 4739-4748.

(37) Luo, B.; Pu, Y.-C.; Yang, Y.; Lindley, S. A.; Abdelmageed, G.; Ashry, H.; Li, Y.; Li, X.; Zhang, J. Z., Synthesis, Optical Properties, and Exciton Dynamics of Organolead Bromide Perovskite Nanocrystals. *J. Phys. Chem. C* **2015**, *119*, 26672-26682.

(38) Zheng, K.; Žídek, K.; Abdellah, M.; Chen, J.; Chábera, P.; Zhang, W.; Al-Marri, M. J.; Pullerits, T., High Excitation Intensity Opens a New Trapping Channel in Organic–Inorganic Hybrid Perovskite Nanoparticles. *ACS Energy Lett.* **2016**, *1*, 1154-1161.

(39) Makarov, N. S.; Guo, S.; Isaienko, O.; Liu, W.; Robel, I.; Klimov, V. I., Spectral and Dynamical Properties of Single Excitons, Biexcitons, and Trions in Cesium–Lead-Halide Perovskite Quantum Dots. *Nano Lett.* **2016**, *16*, 2349-2362.

Chapter 4

Hot Hole Transfer Dynamics from $CsPbBr_3$ Perovskite Nanocrystals

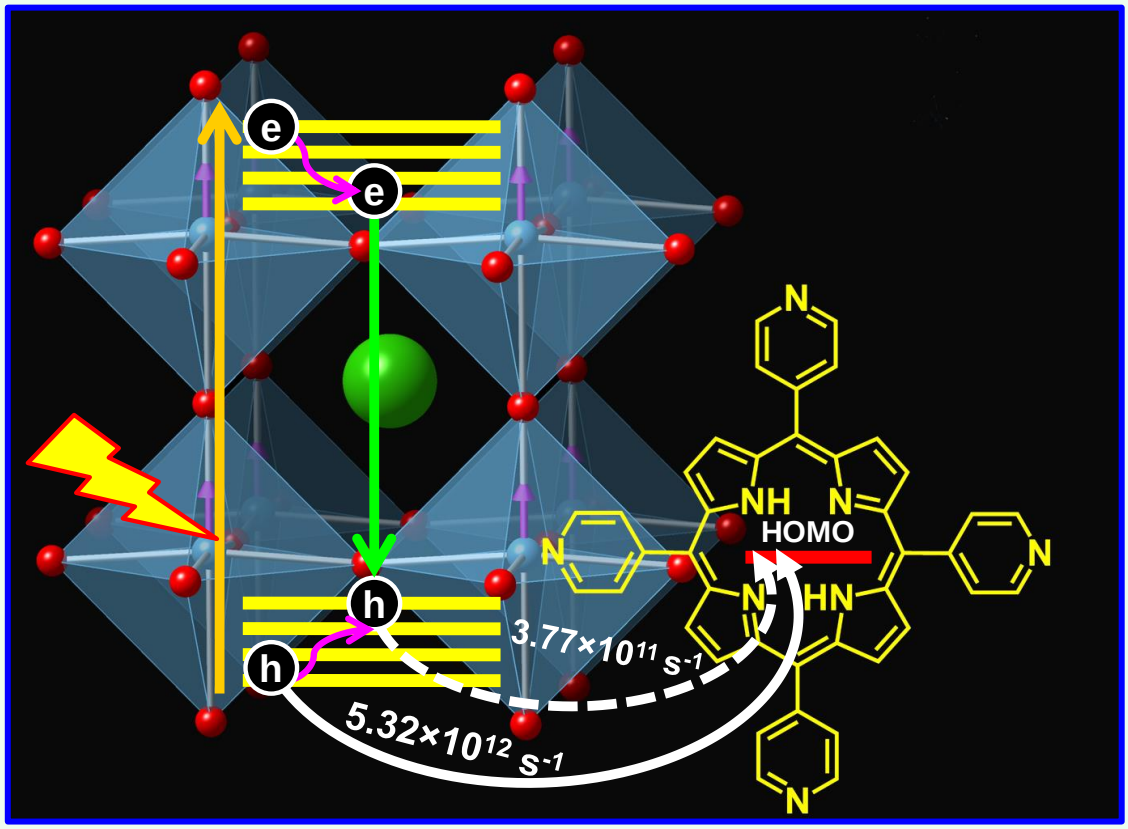

4.1. Introduction

The recent emergence of lead-based halide perovskite (LHP) materials has shown great promise hot carrier solar cells (HCSCs),[1-3] light-emitting diode (LED),[4-6] photo-detectors,[7-8] scintillators,[9] and lasing devices[10-11] because of their exceptional photophysical properties such as high absorption coefficient,[12] long carrier diffusion length,[13] and defect tolerant nature.[14] A clear understanding of the hot carrier cooling dynamics is of fundamental importance for enhancing the functionalities of optoelectronic devices. Photoexcitation with excess energy than the bandgap of the semiconductor creates carriers above the conduction band (CB) (for electrons) and below the valence band (VB) (for holes) and subsequent formation of hot carriers (HCs), which have a temperature higher than the lattice temperature. These HCs rapidly relax to the band edge by losing their excess energies to phonons via carrier-phonon scattering.[15-16] This rapid cooling of HCs is the major energy loss channel of semiconductor materials that limits the efficiency of any single-junction solar cell.[17] Theoretical calculation shows that using the excess energy of non-thermalized photo-excited HCs can extend the solar conversion efficiency up to 66% under one sun illumination, beyond the Shockley-Queisser (SQ) limit 33%.[18-19] Thus, the efficient extraction of HCs is significantly valuable for advancing next-generation optoelectronic devices and breaking the so-called SQ limit.

However, HC cooling occurs very rapidly (typically within hundreds of femtoseconds) for most semiconductor nano-materials, which makes the extraction of HCs very difficult. A slow HC cooling is a key to the successful utilization of excess energy of HCs. LHP NCs are suitable for slow hot-carrier cooling properties, which are essential for enhancing the performance of optoelectronic devices.[15, 20-21] Thus, significant emphasis has been given to explaining the origins and the mechanism of HC cooling for LHP NCs, after the first report of slow HC cooling (0.4 ps) in $MAPbI_3$ polycrystalline thin films.[13] The HC cooling dynamics depend on several factors like the initial HC excess energy,[21-23] photoexcited carrier density,[24] cation species,[25-27] morphology[28], and quantum confinement effects.[20, 29] Niesner et al. have described hot fluorescence emission of 100 ps lifetime for $CH_3NH_3PbBr_3$,[30]. In contrast, Huang et al. have shown the long-range transport of HCs up to 600 nm in methylammonium lead iodide (MAPI) thin films by direct visualization of HC migration.[31] Most of the previous reports reveal that hot-phonon bottleneck [21, 32] and Auger heating effects[22, 33] are primarily responsible for the slow HC cooling of these NCs. At the same time, some crucial factors are large polaron formation,[34]band-filling effects,[35-36], and

dielectric screening[37]. So far, investigations have been made on the hot carrier cooling dynamics of LHP NCs, and less emphasis has been given on the extraction of hot carriers from LHP NCs. Li et al. have reported the efficient extraction of hot electrons from $MAPbBr_3$ NCs at room temperature using energy selective molecular semiconductor 4,7-diphenyl-1,10-phenanthroline (Bphen),[20].

In contrast, Dursun et al. have shown the hot carrier extraction from $MAPbI_3$ NCs using spiro-OMeTAD (hole transporting layer) and TiO_2 (electron transporting layer).[38] The hot carrier transfer from the higher excited state of $CH_3NH_3PbI_3$ to bathophenanthroline has been investigated by pump-push-probe spectroscopy.[39]Shen et al. have shown the hot holes transfer from $CsPbI_3$ to conjugated polymer (P3HT) within a few 100 fs.[40] Suitable acceptor molecules are required to extract the hot carriers from the photo-excited perovskite NCs.

The significant developments of perovskite solar cells (PSCs) are evident due to the high power conversion efficiency (PCE). The primary issue for the commercialization of PSCs is the lack of stability due to the hygroscopic nature of dopants in hole transport materials (HTMs).[41] Therefore, primary emphasis is given to the development of dopant-free HTMs, and porphyrin derivatives are found to be the alternative HTMs that are extensively used to overcome this issue in recent times.[42-45] The significant reasons to choose porphyrin-based derivatives as HTMs are suitable energy-level alignment with perovskite materials for efficient extraction of holes and effective blocking of electrons. High mobility, good solubility in a common solvent, and strong light-harvesting ability are other essential properties.[43] Therefore, a systematic study is required to understand the hot carrier extraction from colloidal $CsPbBr_3$ NCs to porphyrin molecules. This has benefits for artificial light-harvesting systems by exploiting the charge-transfer interactions.

In this study, we explicate the hot carrier dynamics of $CsPbBr_3$ NCs in the presence of energetically aligned porphyrin molecules, namely 5,10,15,20- Tetra(4pyridyl)porphyrin (TpyP) using transient absorption spectroscopy (TAS). Furthermore, we investigate the carrier cooling kinetics and the carrier temperature (T_c) of $CsPbBr_3$ NCs in the presence of TpyP molecule to provide fundamental insight into the carrier extraction ability of TpyP molecules. Additionally, computational modeling using density-functional theory (DFT) is used to understand their electronic interactions, further supporting the transfer of hot holes from $CsPbBr_3$ NCs.

4.2. Results and Discussion

4.2.1. Steady-State and Time-Resolved Spectroscopy

Pristine $CsPbBr_3$ NCs are prepared by previously reported hot-injection method[46] with slight modifications. Transmission electron microscopy (TEM) images of pristine NCs show a highly mono-dispersed cubic shape (Figure 4.1A) with an average edge length of 12±0.4 nm which is larger than the exciton Bohr radii of $CsPbBr_3$ NCs.[29] Figure 4.1B shows the UV-Visible absorption (Red balls) and photoluminescence (PL) spectra (Green balls) of the pristine NCs in $CHCl_3$. The excitonic absorption band and the PL maxima are at 496 nm and 505 nm. The photoluminescence quantum yield (PLQY) is 72%, and the corresponding digital image of the solution under UV light (λ_{ex}=365 nm) is shown in the inset of Figure 4.1B. A simple ligand exchange procedure modifies the surface of pristine CsPbBr3 NCs in the presence of 5,10,15,20-Tetra(4pyridyl)porphyrin (TpyP) which is confirmed by FTIR spectroscopy (Figure 4.2A) and NMR spectroscopy (Figure 4.2B).

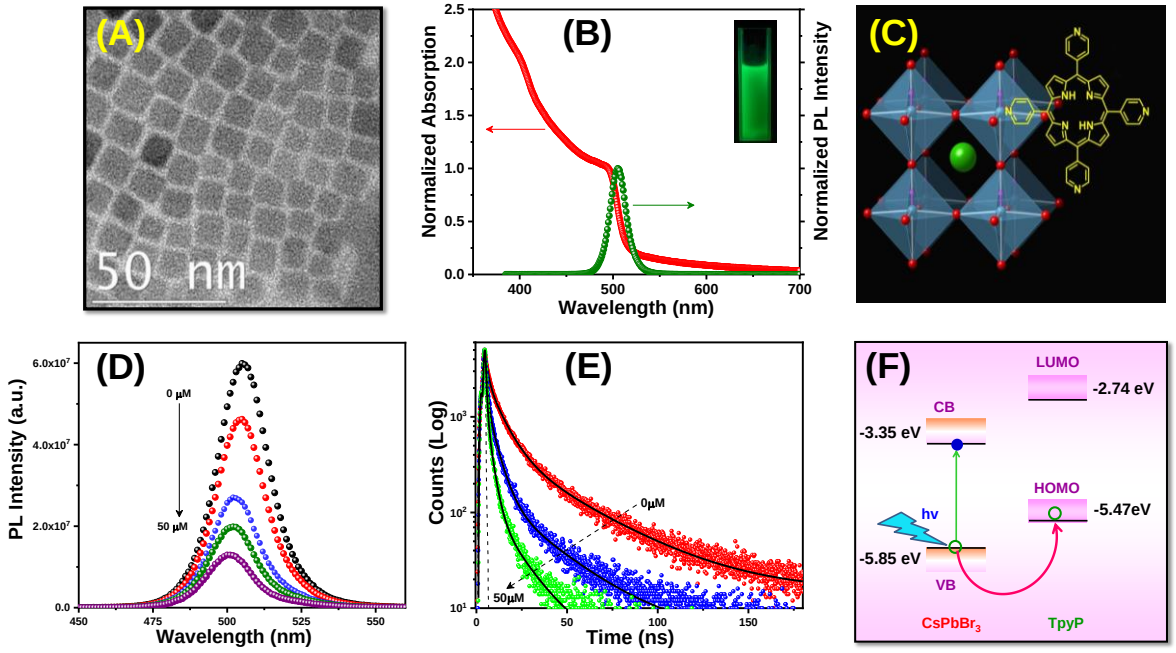

Figure 4.1. *(A) TEM image and (B) Normalized UV-Visible absorption (Red Balls) and PL spectra (Green Balls) of pristine $CsPbBr_3$ NCs, (C) Schematic representation of the TpyP modified $CsPbBr_3$ NCs, (D) PL quenching and (E) TCSPC decay profiles of pristine $CsPbBr_3$ NCs with increasing concentration (up to 50 μM) of TpyP molecules, (F) Schematic of the energy level alignment of $CsPbBr_3$ NCs and TpyP molecules. Inset of B shows a digital image*

of the solution under UV light excitation (λ_{ex}=365 nm and λ_{em}=505 nm.)[47] Reproduced with permission from reference 47 (Copyright 2021 American Chemical Society)

Figure 4.2A shows the ATR-FTIR spectra of pristine $CsPbBr_3$ NCs with original surface ligands (oleic acid/oleyl amine), $CsPbBr_3$ NCs after ligand exchange with TpyP ($CsPbBr_3$-TpyP) and pure TpyP. Reduction of CH_2 stretching peaks (at 2926 and 2856 cm^{-1}) in $CsPbBr_3$-TpyP suggests the efficient removal of oleic acid and oleyl amine from the surface of pristine NCs.[20, 48-50] Also, $CsPbBr_3$-TpyP, which are partially ligand exchanged with pyridine functionalized TpyP, has shown distinct peaks compared to that of pristine NCs. Completely new peaks at 1732 cm^{-1} and 1220-1400 cm^{-1} arise due to C=N stretching, aromatic C-C, and C=C vibration, respectively, consistent with the reference spectrum of pure TpyP.[48] Additionally, the disappearance of the wagging vibration of N-H at 780 cm^{-1} supports the ligand exchange of TpyP with oleic acid and oleyl amine.

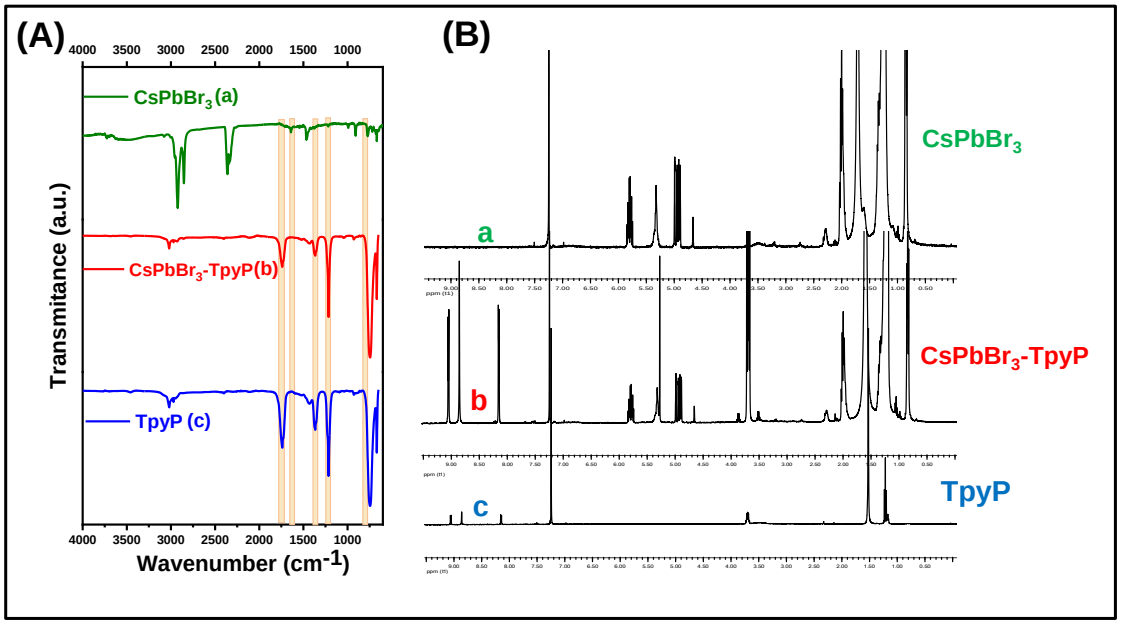

Figure 4.2. *(A) ATR-FTIR spectra (spectral window 650 to 4000 cm^{-1}) and (B) NMR spectra of (a)pristine $CsPbBr_3$ NCs, (b) $CsPbBr_3$-TpyP and (c) TpyP.[47] Reproduced with permission from reference 47 (Copyright 2021 American Chemical Society)*

Figure 4.2B shows ^{1}H NMR spectra of pristine $CsPbBr_3$, $CsPbBr_3$-TpyP, and pure TpyP in $CDCl_3$ solvent. For pristine $CsPbBr_3$ NCs, the peaks with a chemical shift of lower than 2.2 ppm are difficult to distinguish because there is an overlap of peaks arising from both oleic acid (OA) and oleyl amine (OAm). However, the slightly shifted and broadened resonance typically suggests a bounded ligand. Broad peaks at 7.0 and 3.5 ppm are corresponding to alpha proton (of NH^{3+}) and beta proton (of CH-2-N) of OAm^+ (oleyl ammonium),

respectively. It suggests binding of OAM+ ion in the surface of $CsPbBr_3$.[12, 51] It is interesting to note that the broadness of characteristic oleylammonium peaks at 3.5 and 7.0 ppm are reduced in $CsPbBr_3$-TpyP, indicating removal of OAm ligand from the surface.[51] Again, the characteristic peaks of pure TpyP at chemical shift value 3.65 ppm and above 8 ppm are slightly shifted in $CsPbBr_3$-TpyP, indicating the attachment of TpyP at the surface of $CsPbBr_3$ NCs. Figure 4.1C schematically represents the adsorption of the TpyP molecules on the surface of the pristine $CsPbBr_3$ crystal structure. The TEM image of $CsPbBr_3$-TpyP NCs and the UV-Visible absorption spectra of $CsPbBr_3$ NCs with changing the concentration of TpyP (0-50 µM) are shown in Figure 4.3.

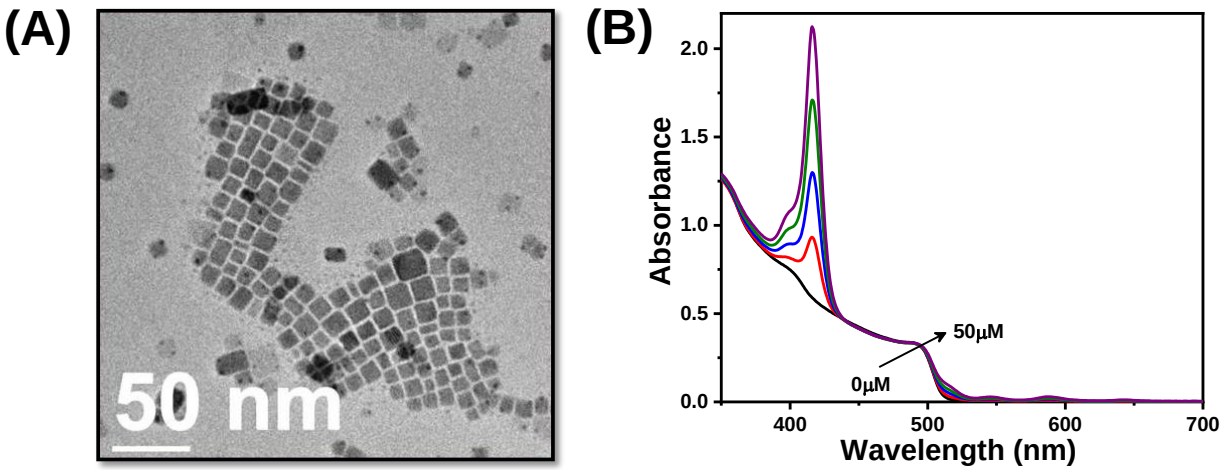

Figure 4.3. *(A)TEM image $CsPbBr_3$-TpyP NCs and (B) UV-Visible absorption spectra of $CsPbBr_3$ NCs with increasing concentration TpyP molecules (0-50 µM) in chloroform.[47] Reproduced with permission from reference 47 (Copyright 2021 American Chemical Society)*

The absorption spectrum of only TpyP molecule in $CHCl_3$ shows a characteristics Soret band (or B band) at around 416 nm with a shoulder at 400 nm due to $S_0 \rightarrow S_2$ transitions and two components Q bands (Q_x and Q_y) due to $S_o \rightarrow S_1$ transitions with four clear peaks at 512 nm, 545 nm, 587 nm, and 643 nm, respectively (Figure 4.4).

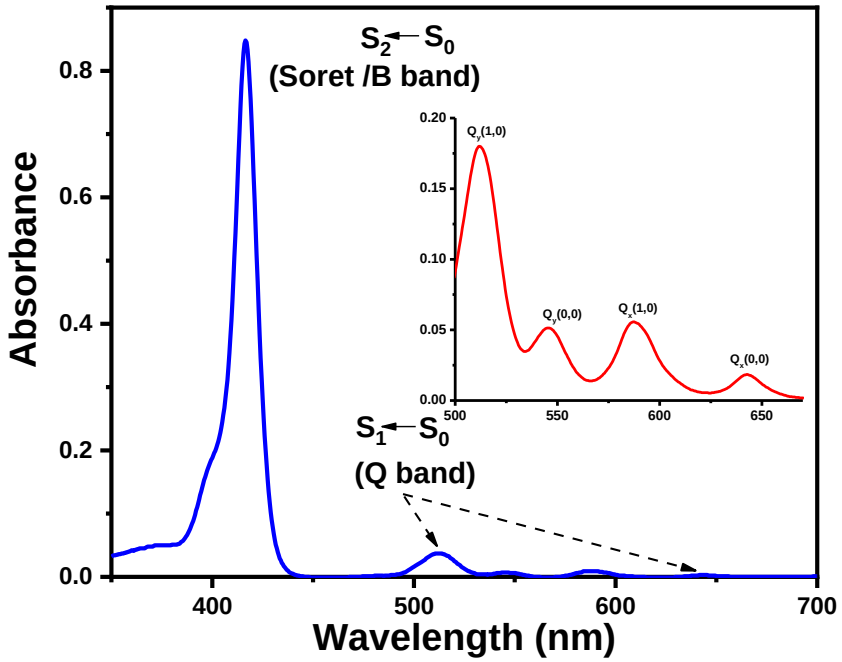

Figure 4.4. *UV-Visible absorption of pure TpyP molecules in $CHCl_3$. Inset shows a magnified view of Q_x bands from 500-700 nm.[47] Reproduced with permission from reference 47 (Copyright 2021 American Chemical Society).*

Interestingly, the PL intensity of pristine $CsPbBr_3$ NCs is drastically quenched with increasing concentration (0-50 µM) of TpyP molecules (Figure 4.1D) and the maximum PL quenching is 79% for the highest concentration of TpyP molecules (i.e. 50 µM). A Time-resolved fluorescence study (TCSPC) reveals that the PL decay time of pristine $CsPbBr_3$ NCs becomes faster with increasing concentration of TpyP molecules (Figure 4.1E). The fitted decay components of pristine NCs are (τ_1) 1.5 ns (63%), (τ_2) 8.0 ns (31%), and (τ_3) 36.5 ns (6%) with an average lifetime of 5.6±0.30 ns (Table 4.1). The τ_2 is due to excitonic recombination, and the other two components are radiative recombination processes associated with trap states.[52-53] The decay components of pristine $CsPbBr_3$ NCs in presence of TpyP molecules (50 µM) are (τ_1) 0.5 ns (90%), (τ_2) 2.7 ns (9%) and (τ_3) 14.7 ns (1%) with an average lifetime of 0.89±0.12 ns (Table 4.1). Analysis reveals that faster component decreases rapidly along with enhanced contribution with increasing the concentration of TpyP molecules, suggesting additional deactivation pathways due to electronic interaction between pristine $CsPbBr_3$ NCs and TpyP molecules. The band alignment of $CsPbBr_3$ NCs and HOMO/LUMO positions of TpyP molecules suggest the hole transfer from photoexcited $CsPbBr_3$ NCs to TpyP molecules (shown in Figure 4.1F).[54-55]

Table 4.1. *Fitted decay parameters of the PL decay curve of $CsPbBr_3$ NCs and $CsPbBr_3$-TpyP NCs with different concentrations.*[47]

Systems	**τ_1[a] (ns) (a_1)[b]**	**τ_2[a](ns) (a_2)[b]**	**τ_3[a] (ns) (a_3)[b]**	**<τ> (ns)**
Pristine $CsPbBr_3$	1.5 (63%)	8.0 (31%)	36.5 (6%)	5.6±0.30
$CsPbBr_3$-TpyP (25μM)	0.88 (84%)	4.9 (14%)	27.5 (2%)	1.9±0.21
$CsPbBr_3$-TpyP (50μM)	0.56 (90%)	2.7 (9%)	14.79 (1%)	0.89±0.12

[a]±4% and [b]±5%

4.2.2 Fluorescence Up-conversion Spectroscopy

Fluorescence up-conversion measurements have been employed to unravel the ultrafast carrier dynamics of pristine $CsPbBr_3$ NCs in the presence of TpyP molecules. We used 400 nm laser pulses to generate HCs and examined the up-converted PL decay at band edge emission of $CsPbBr_3$ NCs (505 nm). Figure 4.5A shows the decay kinetics of band-edge PL for $CsPbBr_3$ NCs in the absence and presence of TpyP molecules on a short time scale.

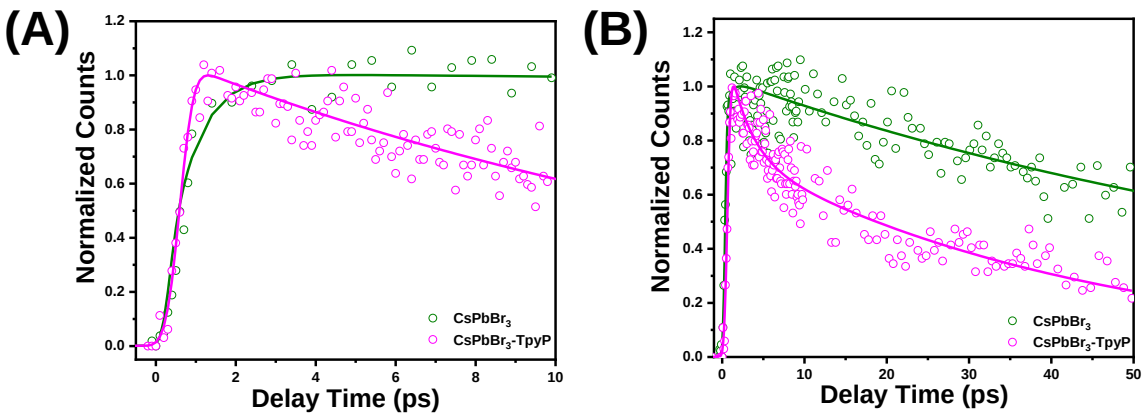

Figure 4.5. *Comparison of decay kinetics of band-edge PL (at 505 nm) for $CsPbBr_3$ NCs and $CsPbBr_3$-TpyP NCs in a short time scale (A) and long time scale (B) at 400 nm excitation.*[47] *Reproduced with permission from reference 47 (Copyright 2021 American Chemical Society).*

The fitted time constant is 740 ± 30 fs for pristine $CsPbBr_3$ NCs, whereas a much shorter time constant of 195± 20 fs is obtained in the presence of TpyP (Table 4.2). The shortening of time in the presence of TpyP indicates the ultrafast carrier transfer from pristine $CsPbBr_3$ NCs to TpyP molecules.

Table 4.2. *Fitted parameters of up-converted PL signal for $CsPbBr_3$ NCs and $CsPbBr_3$-TpyP NCs measured at corresponding band-edge emission (at 505 nm). λ_{ex}= 400 nm.*[47]

Systems	**τ_{growth} (a_{growth}) (fs)**	**τ_1 (a_1) (ps)**	**τ_2 (a_2) (ps)**
Pristine $CsPbBr_3$	740±30 fs (100%)	--------	>50 ps (100%)
$CsPbBr_3$-TpyP (50µM)	195±20 fs (100%)	2.7±0.4ps (33.3%)	45±5 ps (11.6%)

Figure 4.5 B shows the upconverted decay traces of $CsPbBr_3$ NCs in the absence and presence of TpyP molecules on a long time scale. The decay traces of pristine $CsPbBr_3$ NCs is fitted mono-exponentially with time constants τ_1> 50 ps (100%), whereas the decay is fitted bi-exponentially with time constants τ_1=2.7±0.4 ps (33.3%) and τ_2> 50 ps (66.7%) for $CsPbBr_3$-TpyP NCs (Table 4.2). The longer component is due to the band-edge recombination, consistent with previous reports.[56] Analysis suggests that the additional component of 2.7± 0.4 ps is due to the ultrafast carrier transfer from $CsPbBr_3$ NCs to TpyP molecules which is comparable with previous reports of band edge hole transfer from $CsPbBr_3$ NCs.[57]

4.2.3 Computational Modelling

First-principles calculations have been carried out based on state-of-the-art density-functional theory (DFT) to elucidate the underlying mechanism of charge extraction and the HC transfer process in the $CsPbBr_3$-TpyP system. A 3×3×5 slab of the perovskite cubic phase of $CsPbBr_3$ followed by a vacuum spacing larger than 15 Å along the *z*-direction constitutes the supercell used in our systematic investigations. The electronic interaction between the TpyP molecule and the pristine $CsPbBr_3$ NCs has been modeled by interfacing the (001) surface of the $CsPbBr_3$ slab with the TpyP molecule depicted in Figure 4.6.

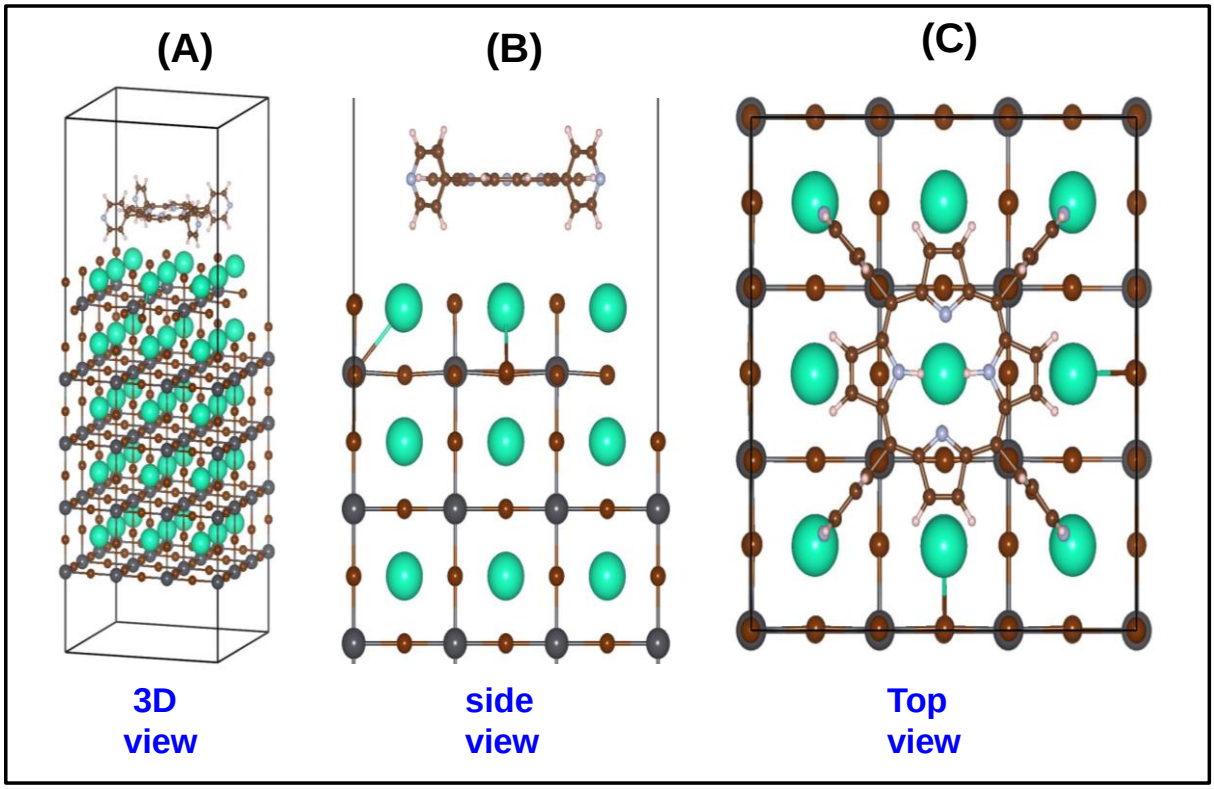

Figure 4.6. *Super-cell of modelled $CsPbBr_3$@TpyP system (A) 3D view, (B) side view, and (C) top view.[47] Reproduced with permission from reference 47 (Copyright 2021 American Chemical Society).*

Charge density (ρ) distributions of the geometrically optimized structure, the $CsPbBr_3$ slab, TpyP molecule, and $CsPbBr_3$-TpyP system are shown in Figure 4.7 (A-C), respectively. Charge transfer distribution of the $CsPbBr_3$-TpyP system as shown in Figure 4.7 (D-G) is calculated using the following formula:

$$\Delta\rho = \rho_{\mathrm{CsPbBr3@TpyP}} - \rho_{\mathrm{CsPbBr3}} - \rho_{\mathrm{Tpyp}} \quad (4.1)$$

The electronic charge is found to be transferred from the surface of $CsPbBr_3$ to the TpyP molecule based on the electronic charge density difference plots, as shown in Figure 4.7. In Figure 4.7 (D-F), the red (green) color represents spatial regions of charge accumulation (depletion). In Figure 4.7G; charge accumulation (depletion) is indicated by a negative (positive) sign on the color scale bar.

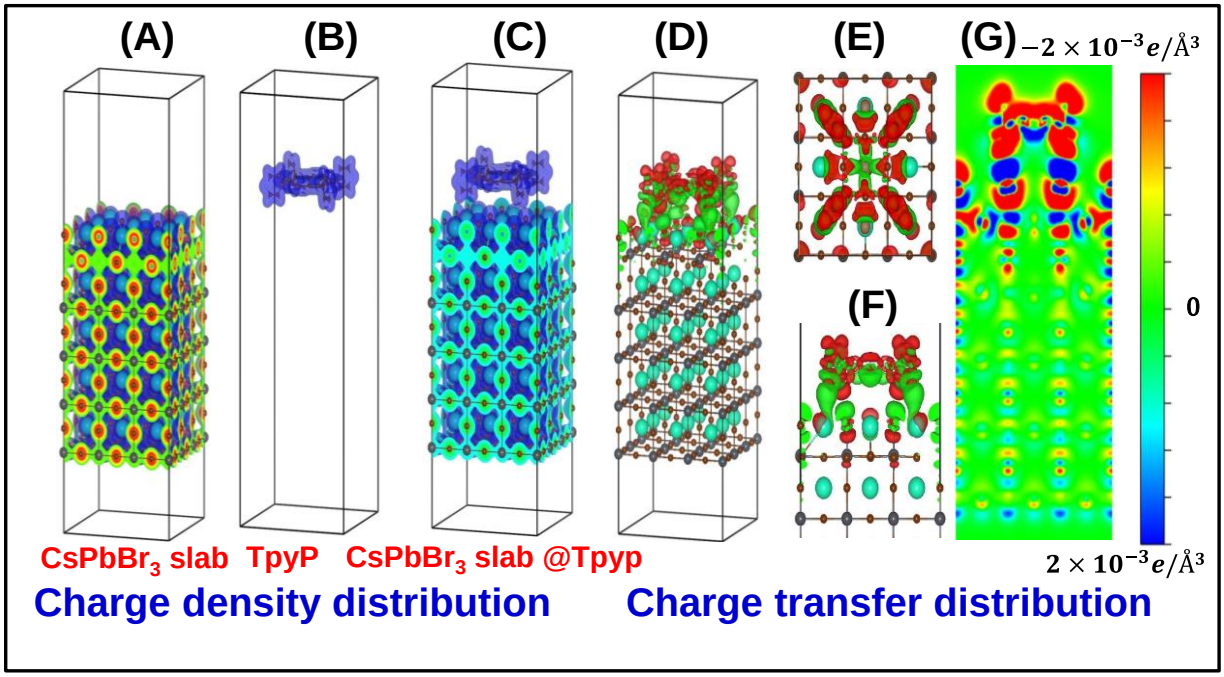

Figure 4.7. *Charge density distribution on (A) $CsPbBr_3$, (B) isolated TpyP molecule and (C) $CsPbBr_3$ slab/TpyP supercell. Distribution of charge transferred between $CsPbBr_3$ slab and TpyP molecule: (D) 3D view, (E) top view, and (F) side view. Red (green) color represents spatial regions of charge accumulation (depletion). (G) Charge transfer distribution projected on (100) plane. The color map shows the magnitude of charge transfer and the charge accumulation (depletion) is indicated by a negative (positive) sign.[47] Reproduced with permission from reference 47 (Copyright 2021 American Chemical Society).*

To gain a deeper insight into the process of charge-carrier extraction in the $CsPbBr_3$-TpyP system, the electronic density of states (DOS) and partial charge density at a specific energy state have been calculated as shown in Figure 4.8 (A-C) and Figure 4.8 (D-M), respectively.

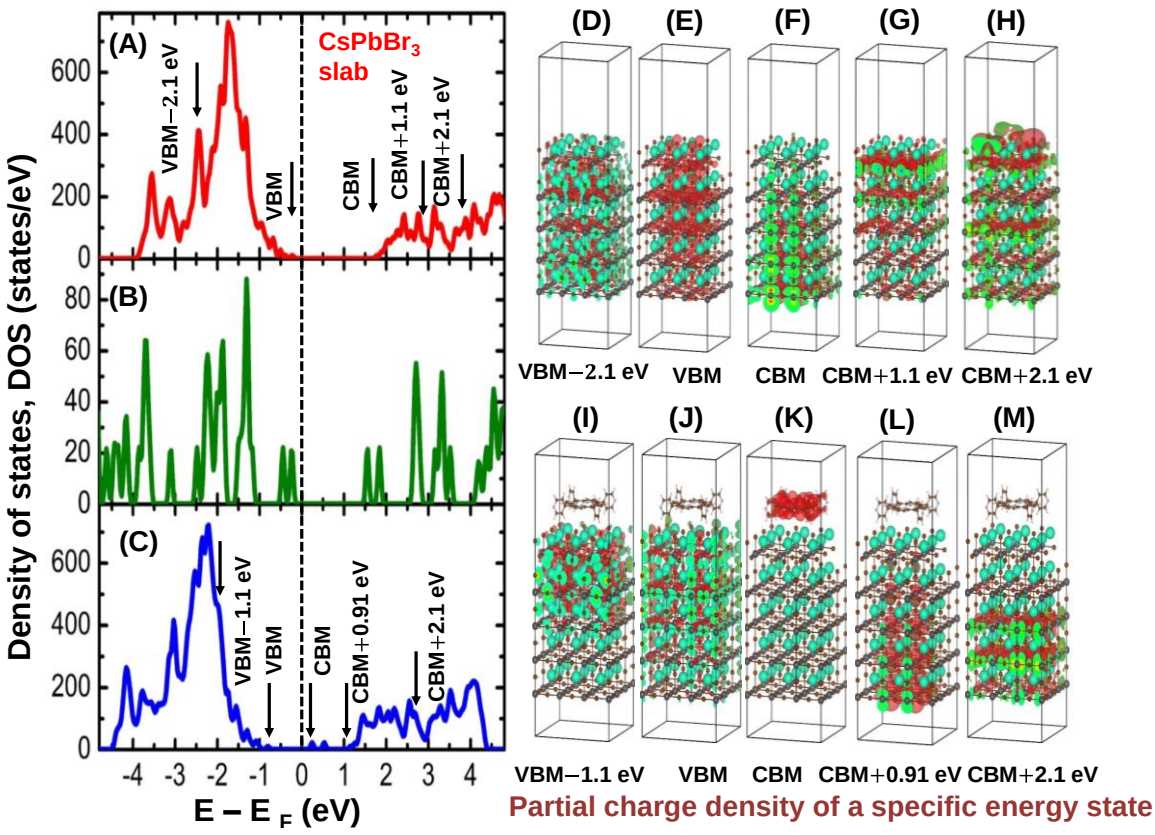

Figure 4.8. *Electronic density of states of (A) $CsPbBr_3$ slab, (B) TpyP molecule and (C) $CsPbBr_3$/TpyP supercell. Fermi level has been set to zero. (D-M): Partial charge density at a specific energy state is indicated.*[47] *Reproduced with permission from reference 47 (Copyright 2021 American Chemical Society).*

Figure 4.9 shows the partial charge density at different energy states for the $CsPbBr_3$/TpyP system. The holes in the perovskite $CsPbBr_3$ NCs are delocalized through the whole slab along with the top surface, as shown in Figure 4.8E. Figure 4F reveals that the electrons are delocalized away from the top surface. Figure 4.8K indicates that the conduction band minimum (CBM) state in the $CsPbBr_3$-TpyP system is localized on the TpyP molecule. In contrast, the valence band maximum (VBM) state is delocalized/ distributed over the whole $CsPbBr_3$ slab, as evident from Figure 4.8J. Furthermore, the position of band edges calculated using GGA-PBE exchange-correlation functional shows type-II band alignment (Figure 4.9).

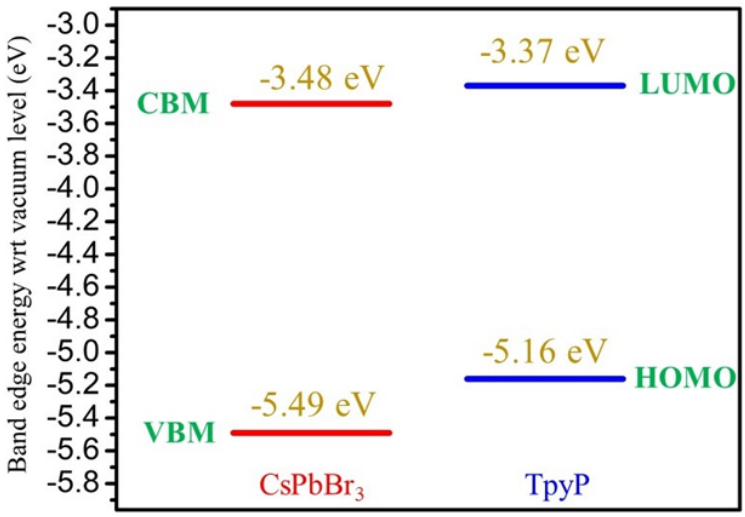

Figure 4.9. *Band edges (valence band maximum (VBM), conduction band minimum (CBM)) in an absolute vacuum scale, i.e., renormalized with respect to the absolute vacuum level of independent $CsPbBr_3$ slab and TpyP molecule, in the Anderson limit, using GGA-PBE functional. It shows type-II band alignment in agreement with experimental results.*[47] *Reproduced with permission from reference 47 (Copyright 2021 American Chemical Society).*

It may be noted that the hot hole state at (VBM-1.1) eV as depicted in Figure 4.8I is localized around the top surface of $CsPbBr_3$, while the hot electron state at (CBM+2.1) eV is delocalized away from its top surface, as shown by Figure 4.8M. As the hot holes are localized around the top surface of the perovskite, they can be easily extracted from the $CsPbBr_3$ by TpyP molecules compared to the hot electrons.

4.2.4. Ultrafast Transient Absorption Spectroscopy

Femtosecond broadband transient absorption spectroscopy (TAS) was employed to study the hot carriers cooling dynamics of $CsPbBr_3$ NCs in the presence of TpyP molecules. We have performed the TA experiment with varying the excitation wavelength (at 370 nm, 400 nm, and 450 nm). In the TA study, all the measurements were carried out with sufficiently low pump fluence (average number of excitons per NCs ~ 0.15) to avoid multi-excitonic processes. Figure 4.10(A, B) represents a 2D pseudo-color TA spectrogram of pristine $CsPbBr_3$ and $CsPbBr_3$-TpyP NCs at 400 nm. A strong negative ground state bleach (GSB) signal at around 496 nm (2.49 eV) is observed for the state filling effect.[56, 58] A short-lived (<2.5 ps) positive photo-induced absorption (PIA) at the lower energy side of the first excitonic band (521-575 nm) and a long-lived (>400 ps) PIA at the higher energy side of the bleach (420-470 nm) are obtained. At early delay time, the initial intensity of the GSB signal

increases and reaches a maximum (shown by the arrow in Figures 4.10A, B) because a short-lived positive PIA signal is replaced by a strong GSB signal after the relaxation of hot carriers to the lowest energy band edge states.[25]

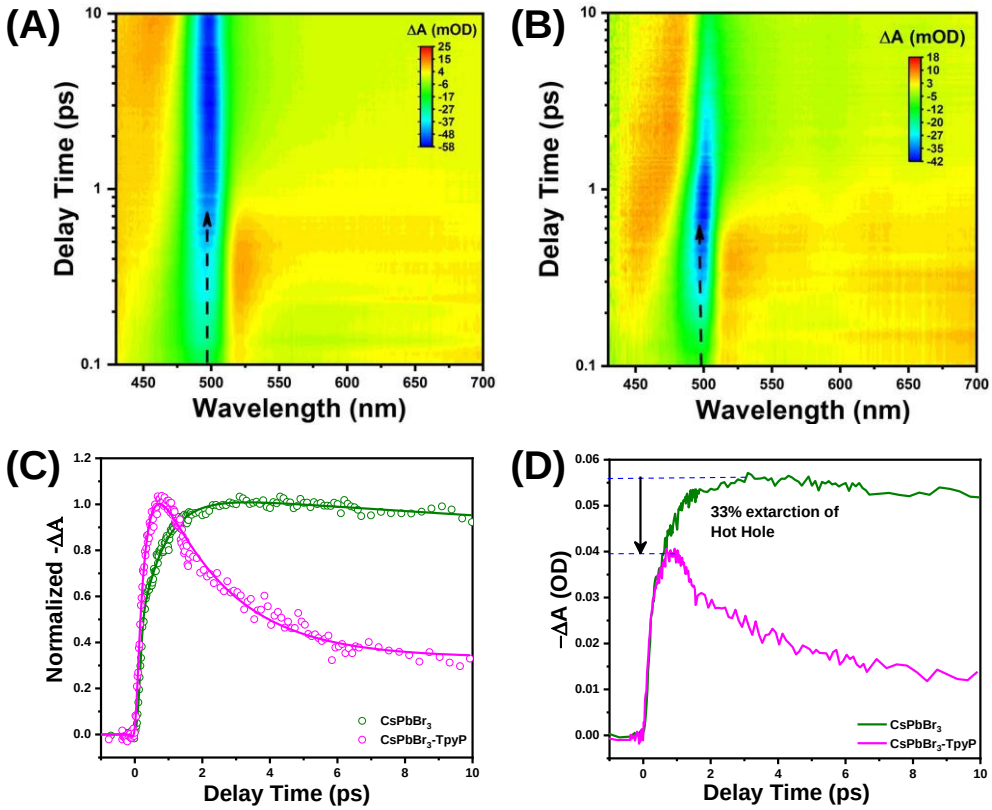

Figure 4.10. *2D Pseudo-color TA plots (A, B), of $CsPbBr_3$ NCs and $CsPbBr_3$-TpyP NCs and their bleach formation kinetics (C) and absolute bleach amplitude at early delay time (D) at 400 nm excitation.[47] Reproduced with permission from reference 47 (Copyright 2021 American Chemical Society).*

The derivative-like spectral feature at early delay time (shift of GSB signal to PIA signal) arises due to the columbic interaction between hot exciton and the band edge exciton, also known as bi-exciton induced stark-effect.[58-59] The long-lived PIA appears due to the absorption of carriers from band edge states.[59-60] 2D pseudo-color TA plots of $CsPbBr_3$ and $CsPbBr_3$-TpyP NCs at 370 nm and 450 nm are given in Figure 4.11. It is to be noted that we have used a very low concentration of TpyP molecules at which TA signals for TpyP is negligible. Thus, we can eliminate the influence of Tpyp. Figure 4.12 shows the TA signal for pure TpyP (the same concentration of TpyP used for $CsPbBr_3$-TpyP NCs) at 370 nm and 400 nm excitation, respectively.

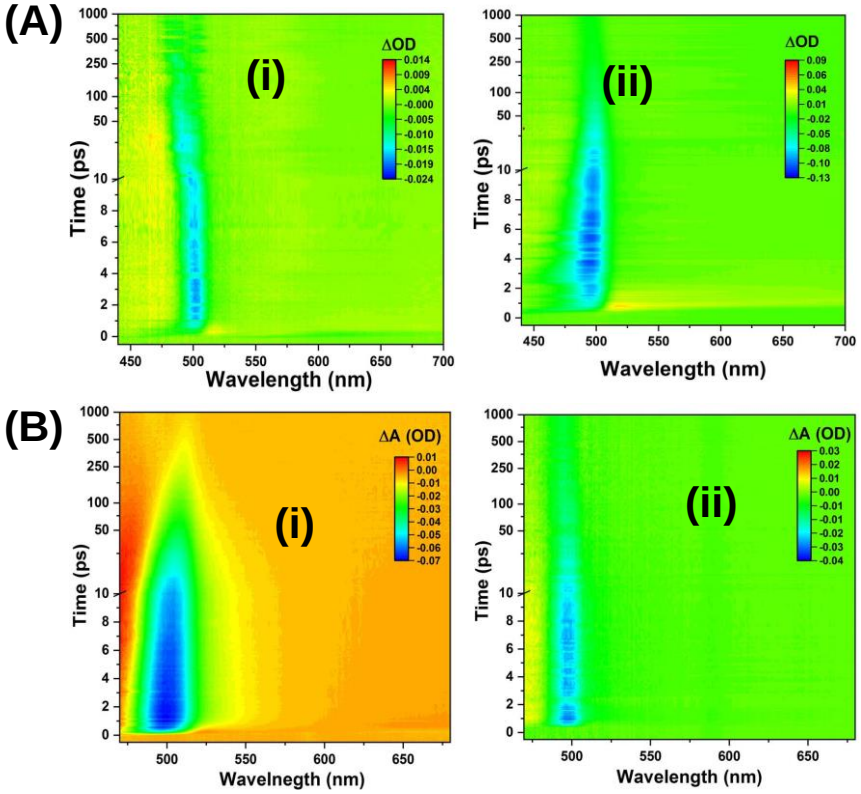

Figure 4.11. *2D pseudo-color TA plots at (A) 370 nm and (B) 450 nm excitation for (i) $CsPbBr_3$ NCs and (ii) $CsPbBr_3$-TpyP NCs.*[47] *Reproduced with permission from reference 47 (Copyright 2021 American Chemical Society).*

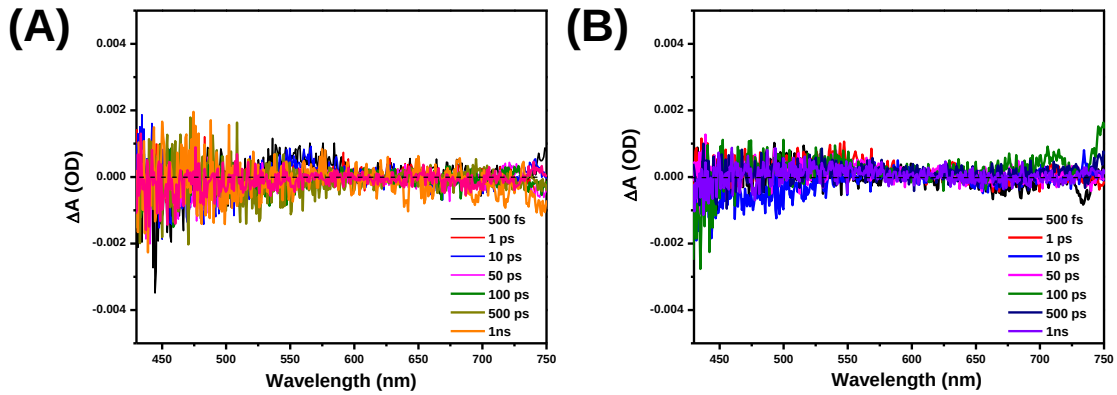

Figure 4.12. *TA profiles of pure TpyP at excitation (A) 370 nm and (B) 400 nm, the same concentration of TpyP is used for $CsPbBr_3$-TpyP NCs.*[47] *Reproduced with permission from reference 47 (Copyright 2021 American Chemical Society).*

It is found that the PIA decay overlaps with GSB growth of pristine $CsPbBr_3$ NCs, suggesting the carriers returning to band edge during initial thermalization (Figure 4.13).[59]

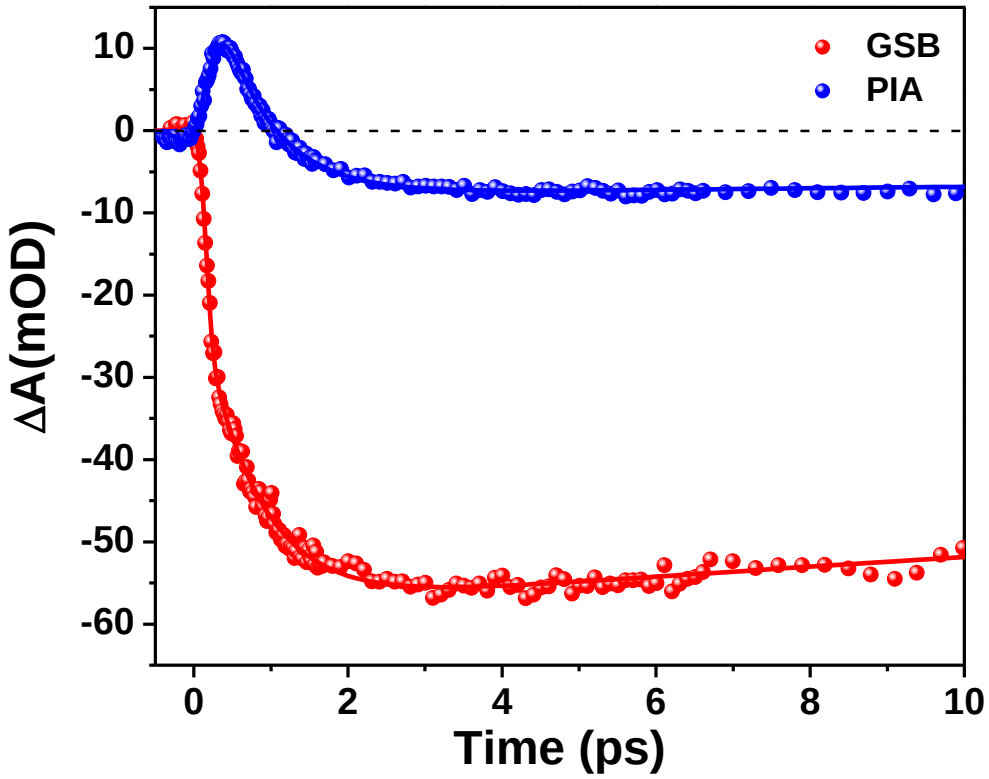

Figure 4.13. *Early time TA dynamics at the position of GSB (at 496 nm) and PIA (at 525 nm) for pristine $CsPbBr_3$ NCs at 400 nm.[47] Reproduced with permission from reference 47 (Copyright 2021 American Chemical Society).*

Hence, the HC cooling time is determined by global analysis (two-component sequential decay model) of the TA spectra at early delay times, giving a more accurate fit of time constants.[25, 53, 61] Global fitting produces the spectra of individual excited state species with their corresponding lifetime, evolution associated difference spectra (EADS). TA spectra with evolution-associated spectral (EAS) components at 400 nm are shown in Figure 4.14. From the analysis, we have obtained a fast component (EADS1) and a slow component (EADS2) for both pristine $CsPbBr_3$ and $CsPbBr_3$-TpyP NCs and the lifetime values are 736 fs and >> 10 ps for $CsPbBr_3$ NCs and 188 fs and >> 10 ps for $CsPbBr_3$-TpyP NCs.

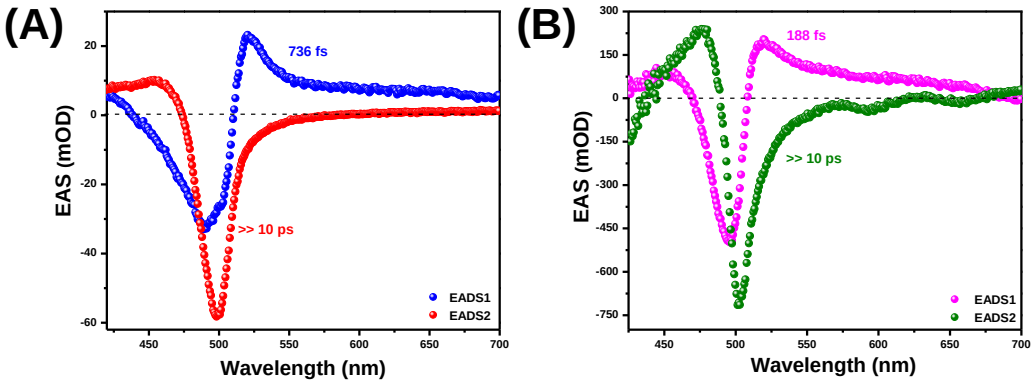

Figure 4.14. *TA spectra with evolution associated spectral (EAS) component derived from singular value decomposition (SVD) based global fitting for (A) $CsPbBr_3$ NCs and (B) $CsPbBr_3$-TpyP NCs at 400 nm excitation.[47] Reproduced with permission from reference 47 (Copyright 2021 American Chemical Society).*

The corresponding EAS spectra at 370 nm and 400 nm are given in Figure 4.15. At 370 nm excitation, the obtained lifetime values are 900 fs (for pristine $CsPbBr_3$) and 210 fs (for $CsPbBr_3$-TpyP NCs), whereas the lifetime values are 300 fs (for pristine $CsPbBr_3$) and 180 fs (for $CsPbBr_3$-TpyP NCs) at 450 nm excitation.

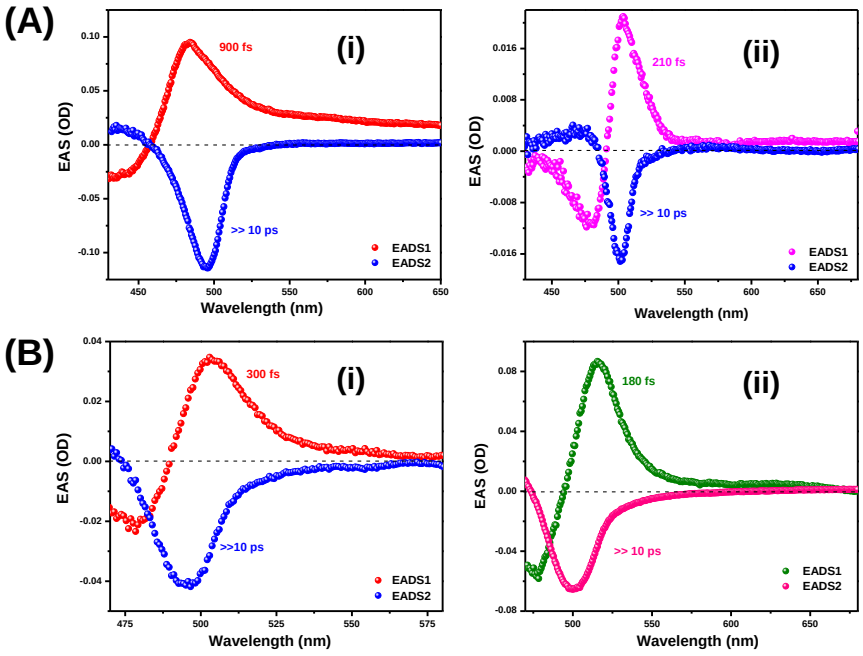

Figure 4.15. *TA spectra with evolution associated spectral (EAS) component derived from singular value decomposition (SVD) based global fitting at (A) 350 nm and (B) 450 excitation for (i) $CsPbBr_3$ NCs and (ii) $CsPbBr_3$-TpyP NCs at 370 nm excitation.[47] Reproduced with permission from reference 47 (Copyright 2021 American Chemical Society).*

Here, the slow component (EADS2) is assigned to the band edge carrier.[25, 58] The fast component (EADS1, several hundred femtoseconds), with blue-shifted GSB, is due to the hot-carrier relaxation, which is consistent with previous reports.[25, 59] HC cooling times are measured from the growth time of the GSB signal of TA spectra which exactly matches with the global analysis. The estimated HC cooling times with varying excitation wavelengths are summarized in Table 4.3.

Table 4.3. *Bleach formation time for $CsPbBr_3$ NCs and $CsPbBr_3$-TpyP NCs at different excitation wavelength.*[47]

Excitation	$CsPbBr_3$	$CsPbBr_3$-TpyP
370 nm	900±35 fs	210±25 fs
400 nm	736±30 fs	188±20 fs
450 nm	300±20 fs	180±15 fs

The growth time of the bleach signal at 400 nm (Figure 4.10C), 370 nm (Figure 4.16A) and 450 nm (Figure 4.16B) clearly shows a faster HC cooling for $CsPbBr_3$-TpyP NCs, suggesting a competitive hot-carrier transfer process.

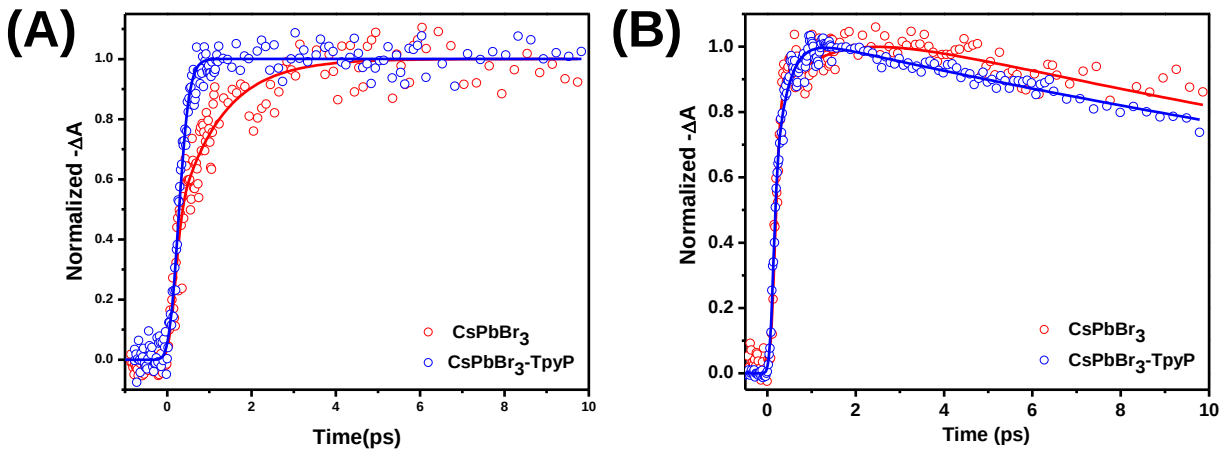

Figure 4.16. *Bleach formation kinetics for $CsPbBr_3$ and $CsPbBr_3$-TpyP NCs at (A) 370 nm and (B) 450 nm excitation.*[47] *Reproduced with permission from reference 47 (Copyright 2021 American Chemical Society).*

Thus, both hot electron and hot hole are generated with equal probability after the photoexcitation. Considering the DFT calculation and the band alignment of the $CsPbBr_3$ NCs and TpyP molecules, only hot hole transfer is thermodynamically feasible in the present case. The drops of HC cooling time in the presence of porphyrin are due to hot hole transfer from $CsPbBr_3$ NCs to TpyP molecules and fast heat dissipation through the ligand. We have investigated the efficiency of hot hole transfer from $CsPbBr_3$ NCs to TpyP molecules by monitoring the absolute bleach amplitude at early delay times. Figure 4.10D compares absolute bleach amplitude at 400 nm, and Figure 4.17 (A, B) indicates the bleach amplitude at 370 nm and 450 nm, respectively.

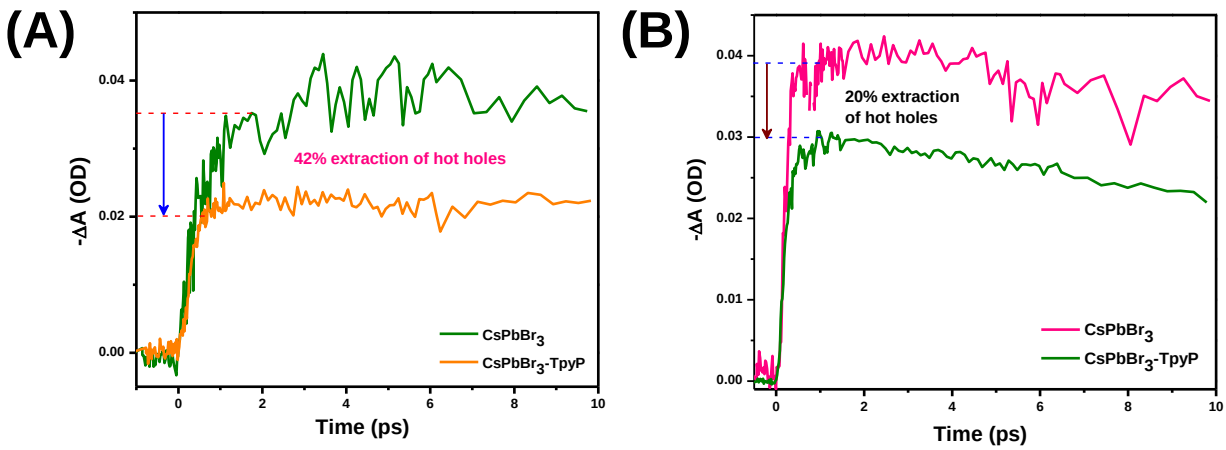

Figure 4.17. *Comparison of absolute bleach amplitude for $CsPbBr_3$ and $CsPbBr_3$-TpyP NCs at (A) 370 nm and (B) 450 nm excitation.[47] Reproduced with permission from reference 47 (Copyright 2021 American Chemical Society).*

The considerably lower amplitude for $CsPbBr_3$-TpyP NCs compared to pristine $CsPbBr_3$ NCs confirms the transfer of hot holes to TpyP molecules. The efficiency of hot hole transfer is excitation wavelength-dependent (Figure 4.18), and the measured efficiencies are 42 %, 33 %, and 20% at 370 nm (0.85 eV above band edge), 400 nm (0.6 eV above band edge) and 450 nm (0.25 eV above band edge), respectively.

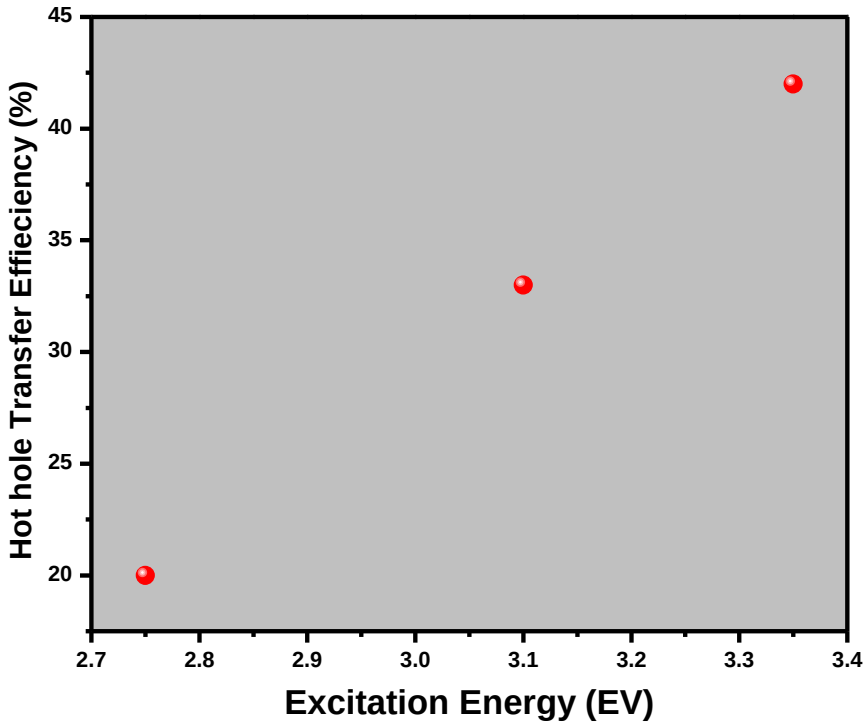

Figure 4.18. *Variation of hot hole transfer efficiency with excitation energy.[47] Reproduced with permission from reference 47 (Copyright 2021 American Chemical Society).*

The rate of hot hole transfer is calculated using equation (4.2):

$$k_{Hot\ hole} = \frac{1}{\tau^{growth}_{CsPbBr3-TpyP}} - \frac{1}{\tau^{growth}_{CsPbBr3}} \quad (4.2)$$

The rate of hot hole transfer is 4.76 x 10^{12} S^{-1}, 3.96 x 10^{12} S^{-1}, and 2.22 x 10^{12} S^{-1} for 370 nm, 400 nm, and 450 nm, respectively. The dynamics of the band edge ('cold' hole) carrier transfer from pristine $CsPbBr_3$ NCs to TpyP molecules are analyzed from the bleach recovery dynamics of pristine $CsPbBr_3$ NCs and $CsPbBr_3$-TpyP NCs. Figure 4.19(A, B) compares bleach recovery for $CsPbBr_3$ NCs and $CsPbBr_3$-TpyP NCs upon 400 nm excitation, where the faster recovery is observed for $CsPbBr_3$-TpyP NCs. For pristine $CsPbBr_3$ NCs, the kinetics is fitted with two components with time constants 58.4±7 ps (42%) and >1 ns (36%), whereas the kinetics of $CsPbBr_3$-TpyP NCs is fitted with time constants 2.65± 0.3 ps (75.7%), 45±5 ps (11.6%) and >1 ns (12.7%) (Table 4.3).

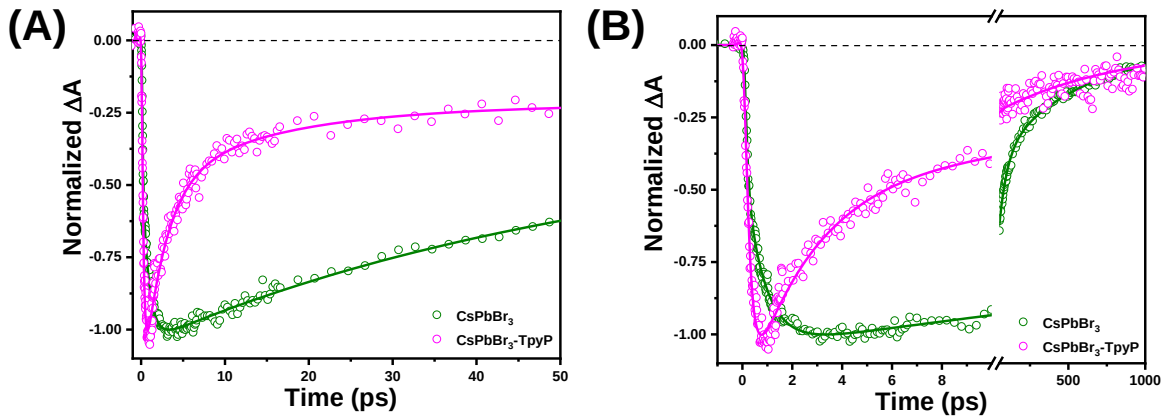

Figure 4.19. *Bleach recovery dynamics (A) at shorter delay time (up to 50 ps), (B) at longer delay time (up to1 ns) for $CsPbBr_3$ NCs and $CsPbBr_3$-TpyP NCs at 400 nm. Bleach recovery dynamics are measured at corresponding excitonic absorption (at 496 nm) of the NCs.*[47] *Reproduced with permission from reference 47 (Copyright 2021 American Chemical Society).*

The longer component is attributed to the radiative recombination process of electron and hole while the intermediate component is due to trapping state mediated process.[56, 58] Our analysis tells that the additional faster component for $CsPbBr_3$-TpyP NCs arises due to the band edge carrier ('cold' hole) transfer which matches with the up-conversion data (2.7±0.4 ps).

Table 4.4. *Fitted parameters of bleach recovery kinetics for $CsPbBr_3$ NCs and $CsPbBr_3$-TpyP NCs measured at corresponding bleach position (at 496 nm).*[47] *λ_{ex}= 400 nm*

Systems	**τ_{growth} (a_{growth})** **fs**	**τ_1 (a_1)** **ps**	**τ_2 (a_1)** **ps**	**τ_3 (a_3)** **ns**
Pristine $CsPbBr_3$	736±30 (100%)	--------	58.4±7 (42%)	>1 (36%)
$CsPbBr_3$-TpyP	188±20 (100%)	2.65±0.3 (75.7%)	45±5 (11.6%)	>1 (12.7%)

We have analyzed the bleach recovery dynamics at 450 nm excitation, where the absorption of TpyP is minimal (Figure 4.20).

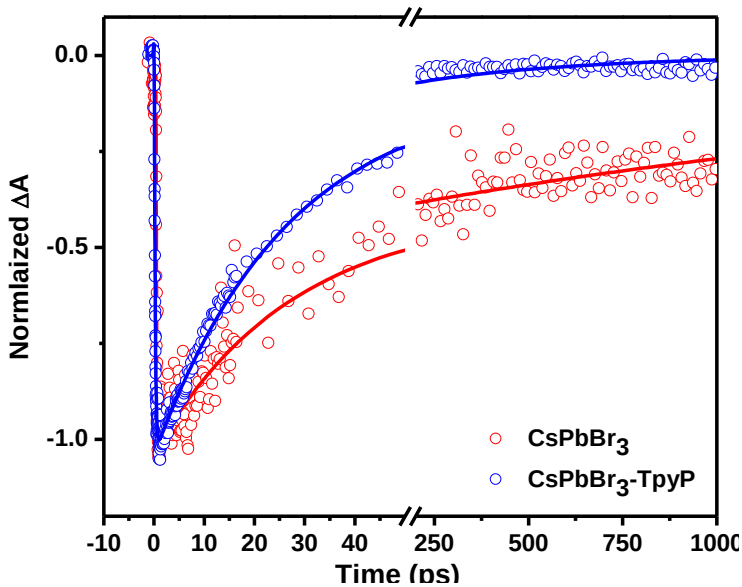

Figure 4.20. *Bleach recovery kinetics of $CsPbBr_3$ NCs and $CsPbBr_3$-TpyP at 450 nm excitation.[47] Reproduced with permission from reference 47 (Copyright 2021 American Chemical Society).*

The kinetics of pristine $CsPbBr_3$ NCs are fitted with time constants 26.8 ± 5 ps (59%) and >1 ns (41%), whereas the kinetics of $CsPbBr_3$-TpyP NCs is fitted with time constants 2.5 ± 0.4 ps (89 %) and >1 ns (11%) (Table 4.5).

Table 4.5. *Fitted parameters of bleach recovery kinetics for $CsPbBr_3$ NCs and $CsPbBr_3$-TpyP NCs measured at corresponding bleach position (at 496 nm). [47] λ_{ex}= 450 nm*

Systems	**τ_{growth} (a_{growth}) fs**	**τ_1 (a_1) ps**	**τ_2 (a_1) ps**
Pristine $CsPbBr_3$	300±20 (100%)	26.8±5 (59%)	>1 (41%)
$CsPbBr_3$-TpyP	180±15 (100%)	2.5±0.4 (89%)	>1 (11%)

This faster component (2.5 ± 0.4 ps) with a more significant contribution is due to the band edge carrier ('cold' hole) transfer from $CsPbBr_3$ NCs to TpyP. The band edge carrier ('cold' hole) transfer rate at 400 nm is 3.77×10^{11} s^{-1}. It is interesting to note that the rate of hot hole transfer is 11 times faster than the rate of the band edge carrier transfer at 400 nm excitation. The dynamics of hot hole transfer and the band edge carrier transfer at 400 nm from photo-excited $CsPbBr_3$ NCs to the surface attached TpyP molecules are schematically illustrated in Scheme 4.1.

Scheme 4.1. *Schematic representation of photo-induced hot hole and the band edge carrier transfer from $CsPbBr_3$ NCs to TpyP molecules at 400 nm excitation.*[47]

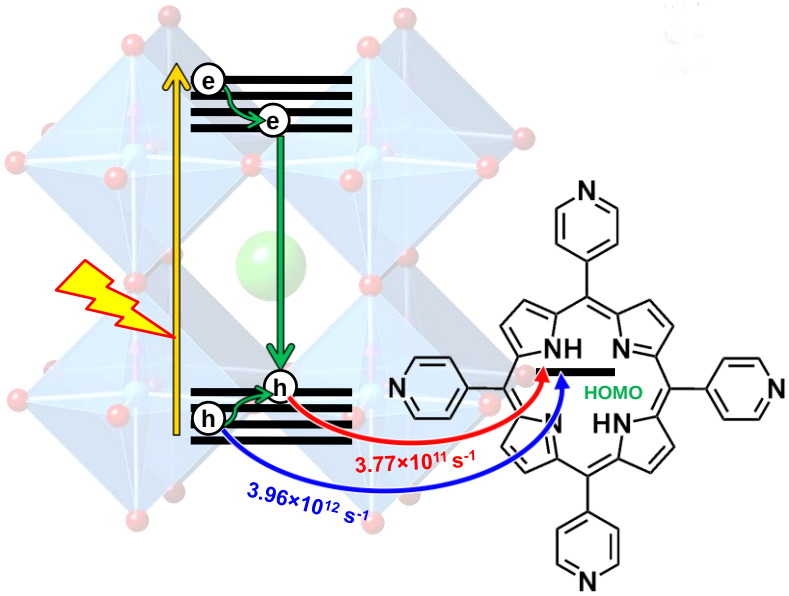

4.2.5. Hot-Carrier (HC) Temperature Calculation

The cooling dynamics and extraction of HC at the interface before complete cooling is significant for designing efficient perovskite solar cells by utilizing the excess energy of HC. Hence, we have evaluated the temporal evolution of HC temperature (T_c) for both $CsPbBr_3$ and $CsPbBr_3$-TpyP NCs from the respective TA spectra to understand HC cooling dynamics. According to previous studies, HC temperature (T_c) can be calculated from the fitting of the high energy tail of the GSB signal by Maxwell-Boltzmann (MB) distribution function that can be generalized as:[20, 23, 25, 36, 62]

$$\Delta T(\hbar\omega) = -T_0 \exp\left(-\frac{\hbar\omega}{k_B T_C}\right) \quad (4.3)$$

Where ΔT stands for the amplitude of bleach at a particular probe wavelength, k_B is the Boltzmann constant, and T_C is the HC temperature. It is worth noting that carrier temperature (T_C) of the lead halide perovskite (LHP) NCs signifies the average temperature of electrons and holes because of equal effective mass for electrons and holes.[20, 25] Again, the high energy tail of the GSB signal originates from the rapid distribution of initially created non-equilibrium carriers into quasi-equilibrium Fermi-Dirac distribution via carrier-carrier scattering within 100 fs.[23, 25] This Fermi-Dirac distribution can be approximated to MB distribution because the excess energy of HC is much greater than the quasi-Fermi energy of the NCs.[21] Figures 4.21 A, D show the normalized TA spectra for $CsPbBr_3$ and $CsPbBr_3$-TpyP NCs, respectively, at 400 nm.

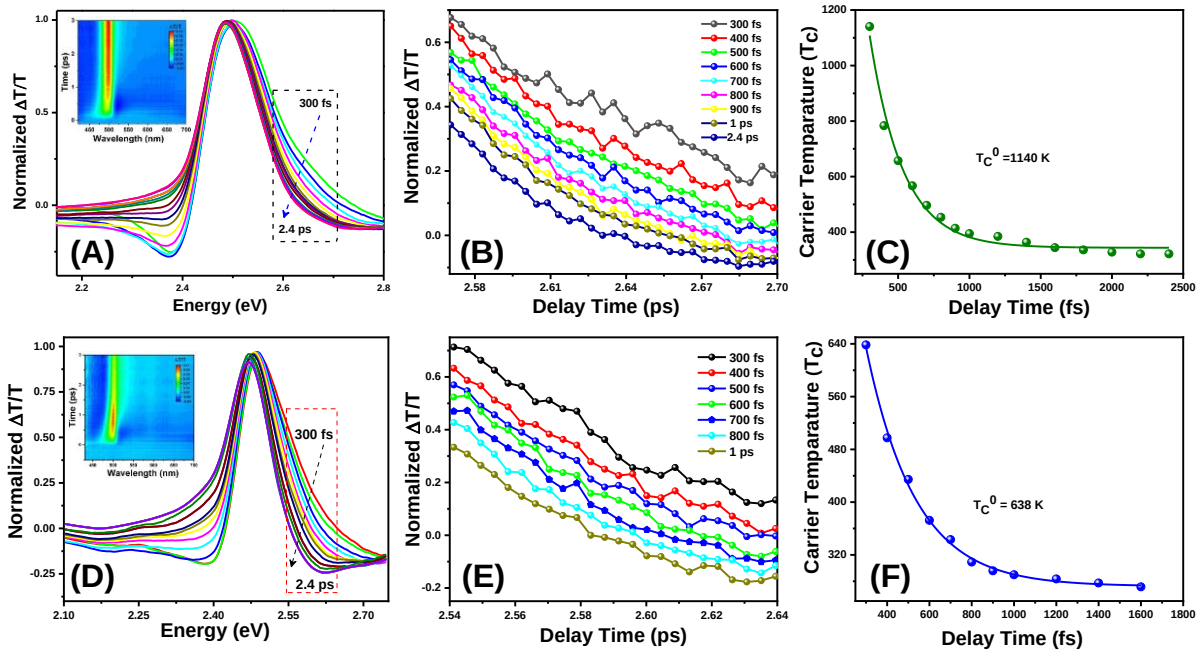

Figure 4.21. *Normalized TA spectra with varying delay times (from 300 fs to 2.4 ps) (A, D), Magnified view of high energy tail of GSB signal used for MB fitting for extraction of T_C (B, E), and Time-dependent carrier temperature profiles (C, F) for $CsPbBr_3$ NCs and $CsPbBr_3$-TpyP NCs, respectively at 400 nm. The inset of (A, D) shows the corresponding 2D pseudo-color plot, and the dashed boxes represent the region of high-energy tail used for MB fitting*[47]*. Reproduced with permission from reference 47 (Copyright 2021 American Chemical Society).*

We have calculated the HC temperature by MB fitting of the high-energy tail of the GSB signal (marked by dotted area). Due to changes in carrier concentration, the difference in the broadening of the high-energy tail of $CsPbBr_3$ NCs is evident in the presence of TpyP molecules. For MB distribution function to extract the HC temperature (shown in Figures 4.21 B, E), we consider the high energy tail (2.57-2.70 eV) for $CsPbBr_3$ NCs and (2.54-2.64 eV) for $CsPbBr_3$-TpyP NCs. In the present study, the hot carrier cooling dynamics are examined only after 300 fs to ensure that the quasi-equilibrium state has been reached. Figure 4.21 (C, F) shows the time-dependent carrier temperature (T_C) profile for $CsPbBr_3$ and $CsPbBr_3$-TpyP NCs, respectively under similar experimental conditions. The initial carrier temperature (T_C^0) for pristine $CsPbBr_3$ NCs is 1140 K which significantly drops to 300 K within 2.4 ps, suggesting that the excess energy of HCs is dissipated to crystal lattice through non-radiative pathways. The cooling of HCs in LHP NCs occurs through the emission of phonons.[15, 25] The initial carrier temperature (T_C^0) of $CsPbBr_3$-TpyP NCs is 638 K which decreases to 300 K within 800 fs, indicating that the excess energy of hot holes is efficiently

transferred to TpyP molecules before relaxing to the crystal lattice. Moreover, the broadening of the quasi-equilibrium distribution of $CsPbBr_3$ NCs decreases in the presence of TpyP molecules, which further confirms the extraction of hot holes from $CsPbBr_3$ NCs. It is noted that HC cooling rates are dependent on initial HC excess energy, photoexcited carrier density, the resolution of the instrument, and many other factors.[15] We consider the high energy tail (2.64 - 2.85 eV) for $CsPbBr_3$ NCs and (2.52 - 2.76 eV) for $CsPbBr_3$-TpyP NCs to calculate HC temperature at 370 nm and 450 nm excitation. At 370 nm, T_C^0 drops from 1202 K to 300 K after 2.6 ps for $CsPbBr_3$ NCs. In the case of $CsPbBr_3$-TpyP NCs, T_C^0 drops from 451 K to 300 K after 800 fs, suggesting the efficient transfer of excess energy of hot holes to TpyP molecules. At 450 nm, T_C^0 drops from 885 K to 330 K in 1.8 ps for pristine $CsPbBr_3$ NCs. For $CsPbBr_3$-TpyP NCs, T_C^0 drops from 682 K to 330 K in 700fs, indicating that the excess energy of hot holes is efficiently transferred to TpyP molecules before relaxing to the crystal lattice. The variation of carrier temperature with varying excitation energy is shown in Figure 4.22. Li et al. have reported that the initial carrier temperature (T_C^0) of EDT treated $MAPbBr_3$ NCs drops from 1300 K to 450 K after 200 fs under low pump excitation (2.1×10^{17} cm^{-3}) when Bphen is used as a hot-electron extracting material.[20] Shen et al. have demonstrated a significant decrease of T_C^0 of $CsPbI_3/Al_2O_3$ from over 2000 K to 500 K after 0.3 ps under excitation density of 1.3×10^{18} cm^{-3} by P3HT (hot hole extracting material).[40] Dursun et al. have reported that T_C^0 of $MAPbI_3$ films drops from 1500 K to 600 K within 2 ps, in the presence of spiro-OMeTAD (hot hole extracting layer) and to 300k within 1 ps at 370 nm excitation under the fluence of $3\mu J/cm^2$.[38] These findings confirm that porphyrin (TpyP) molecules are extracted hot hole efficiently from $CsPbBr_3$ NCs.

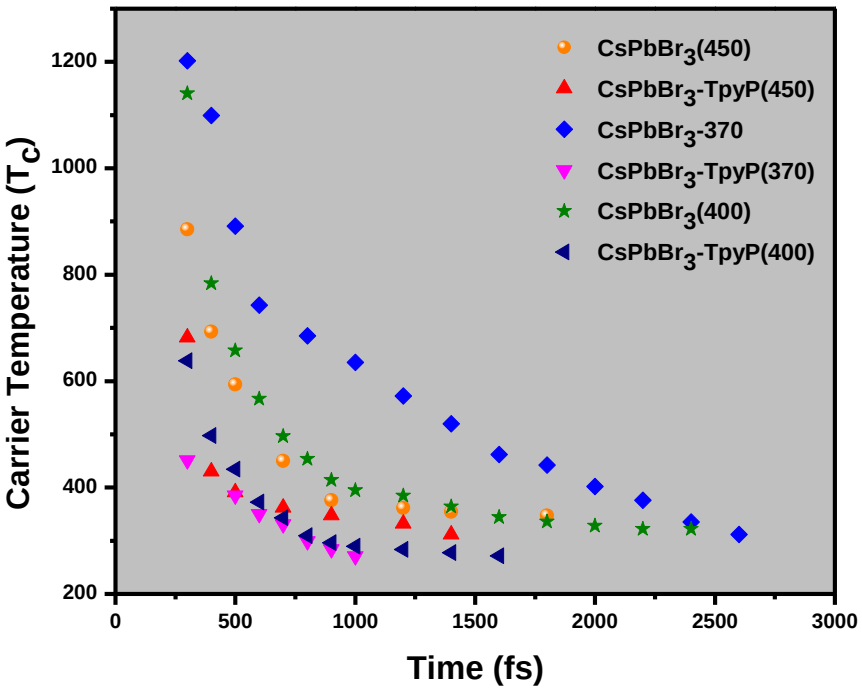

Figure 4.22. *Variation of carrier temperature for $CsPbBr_3$ and $CsPbBr_3$-TpyP NCs with excitation energy.[47] Reproduced with permission from reference 47 (Copyright 2021 American Chemical Society).*

4.3. Conclusions

In summary, we investigate the hot hole cooling dynamics of $CsPbBr_3$ NCs and their transfer dynamics to porphyrin molecules using ultrafast transient absorption and fluorescence up-conversion spectroscopy. The significant change in initial carrier temperature (T_C^0) reveals the efficient transfer of hot holes from $CsPbBr_3$ NCs to TpyP molecules. The maximum hot hole transfer efficiency is 42% at 370 nm excitation. The experimental findings have been well supported by DFT analysis. These findings not only pave the way for fundamental understanding of HC cooling dynamics of perovskite NCs but also offer the possibility for utilizing porphyrin molecules as an alternative source of hole-transporting materials for next-generation optoelectronic devices.

4.4 References

(1) Zhou, H.; Chen, Q.; Li, G.; Luo, S.; Song, T.-b.; Duan, H.-S.; Hong, Z.; You, J.; Liu, Y.; Yang, Y., Interface Engineering of Highly Efficient Perovskite Solar Cells. *Science* **2014**, *345*, 542-546.

(2) Kojima, A.; Teshima, K.; Shirai, Y.; Miyasaka, T., Organometal Halide Perovskites as Visible-Light Sensitizers for Photovoltaic Cells. *J. Am. Chem. Soc.* **2009**, *131*, 6050-6051.

(3) Kahmann, S.; Loi, M. A., Hot Carrier Solar Cells and the Potential of Perovskites for Breaking the Shockley–Queisser Limit. *J. Mater. Chem. C* **2019**, *7*, 2471-2486.

(4) Li, G.; Tan, Z.-K.; Di, D.; Lai, M. L.; Jiang, L.; Lim, J. H.-W.; Friend, R. H.; Greenham, N. C., Efficient Light-Emitting Diodes Based on Nanocrystalline Perovskite in a Dielectric Polymer Matrix. *Nano Lett.* **2015**, *15*, 2640-2644.

(5) Xiao, Z.; Kerner, R. A.; Zhao, L.; Tran, N. L.; Lee, K. M.; Koh, T.-W.; Scholes, G. D.; Rand, B. P., Efficient Perovskite Light-Emitting Diodes Featuring Nanometre-Sized Crystallites. *Nat. Photonics* **2017**, *11*, 108-115.

(6) Park, Y.-S.; Guo, S.; Makarov, N. S.; Klimov, V. I., Room Temperature Single-Photon Emission from Individual Perovskite Quantum Dots. *ACS Nano* **2015**, *9*, 10386-10393.

(7) Li, X.; Yu, D.; Chen, J.; Wang, Y.; Cao, F.; Wei, Y.; Wu, Y.; Wang, L.; Zhu, Y.; Sun, Z., et al., Constructing Fast Carrier Tracks into Flexible Perovskite Photodetectors to Greatly Improve Responsivity. *ACS Nano* **2017**, *11*, 2015-2023.

(8) Saidaminov, M. I.; Adinolfi, V.; Comin, R.; Abdelhady, A. L.; Peng, W.; Dursun, I.; Yuan, M.; Hoogland, S.; Sargent, E. H.; Bakr, O. M., Planar-Integrated Single-Crystalline Perovskite Photodetectors. *Nat. Commun.* **2015**, *6*, 8724.

(9) Chen, Q.; Wu, J.; Ou, X.; Huang, B.; Almutlaq, J.; Zhumekenov, A. A.; Guan, X.; Han, S.; Liang, L.; Yi, Z., et al., All-Inorganic Perovskite Nanocrystal Scintillators. *Nature* **2018**, *561*, 88-93.

(10) Chen, S.; Roh, K.; Lee, J.; Chong, W. K.; Lu, Y.; Mathews, N.; Sum, T. C.; Nurmikko, A., A Photonic Crystal Laser from Solution Based Organo-Lead Iodide Perovskite Thin Films. *ACS Nano* **2016**, *10*, 3959-3967.

(11) Deschler, F.; Price, M.; Pathak, S.; Klintberg, L. E.; Jarausch, D.-D.; Higler, R.; Hüttner, S.; Leijtens, T.; Stranks, S. D.; Snaith, H. J., et al., High Photoluminescence Efficiency and Optically Pumped Lasing in Solution-Processed Mixed Halide Perovskite Semiconductors. *J. Phys. Chem. Lett.* **2014**, *5*, 1421-1426.

(12) De Roo, J.; Ibáñez, M.; Geiregat, P.; Nedelcu, G.; Walravens, W.; Maes, J.; Martins, J. C.; Van Driessche, I.; Kovalenko, M. V.; Hens, Z., Highly Dynamic Ligand Binding and Light Absorption Coefficient of Cesium Lead Bromide Perovskite Nanocrystals. *ACS Nano* **2016**, *10*, 2071-2081.

(13) Stranks, S. D.; Eperon, G. E.; Grancini, G.; Menelaou, C.; Alcocer, M. J. P.; Leijtens, T.; Herz, L. M.; Petrozza, A.; Snaith, H. J., Electron-Hole Diffusion Lengths Exceeding 1 Micrometer in an Organometal Trihalide Perovskite Absorber. *Science* **2013**, *342*, 341-344.

(14) Huang, H.; Bodnarchuk, M. I.; Kershaw, S. V.; Kovalenko, M. V.; Rogach, A. L., Lead Halide Perovskite Nanocrystals in the Research Spotlight: Stability and Defect Tolerance. *ACS Energy Lett.* **2017**, *2*, 2071-2083.

(15) Li, M.; Fu, J.; Xu, Q.; Sum, T. C., Slow Hot-Carrier Cooling in Halide Perovskites: Prospects for Hot-Carrier Solar Cells. *Adv. Mater.* **2019**, *31*, 1802486.

(16) Manley, M. E.; Hong, K.; Yin, P.; Chi, S.; Cai, Y.; Hua, C.; Daemen, L. L.; Hermann, R. P.; Wang, H.; May, A. F., et al., Giant Isotope Effect on Phonon Dispersion and Thermal Conductivity in Methylammonium Lead Iodide. *Sci. Adv.* **2020**, *6*, eaaz1842.

(17) Tisdale, W. A.; Williams, K. J.; Timp, B. A.; Norris, D. J.; Aydil, E. S.; Zhu, X.-Y., Hot-Electron Transfer from Semiconductor Nanocrystals. *Science* **2010**, *328*, 1543-1547.

(18) Ross, R. T.; Nozik, A. J., Efficiency of Hot-Carrier Solar Energy Converters. *J. Appl. Phys.* **1982**, *53*, 3813-3818.

(19) Shockley, W.; Queisser, H. J., Detailed Balance Limit of Efficiency of P-N Junction Solar Cells. *J. Appl. Phys.* **1961**, *32*, 510-519.

(20) Li, M.; Bhaumik, S.; Goh, T. W.; Kumar, M. S.; Yantara, N.; Grätzel, M.; Mhaisalkar, S.; Mathews, N.; Sum, T. C., Slow Cooling and Highly Efficient Extraction of Hot Carriers in Colloidal Perovskite Nanocrystals. *Nat. Commun.* **2017**, *8*, 14350.

(21) Yang, Y.; Ostrowski, D. P.; France, R. M.; Zhu, K.; van de Lagemaat, J.; Luther, J. M.; Beard, M. C., Observation of a Hot-Phonon Bottleneck in Lead-Iodide Perovskites. *Nat. Photonics* **2016**, *10*, 53-59.

(22) Fu, J.; Xu, Q.; Han, G.; Wu, B.; Huan, C. H. A.; Leek, M. L.; Sum, T. C., Hot Carrier Cooling Mechanisms in Halide Perovskites. *Nat. Commun.* **2017**, *8*, 1300.

(23) Price, M. B.; Butkus, J.; Jellicoe, T. C.; Sadhanala, A.; Briane, A.; Halpert, J. E.; Broch, K.; Hodgkiss, J. M.; Friend, R. H.; Deschler, F., Hot-Carrier Cooling and Photoinduced Refractive Index Changes in Organic–Inorganic Lead Halide Perovskites. *Nat. Commun.* **2015**, *6*, 8420.

(24) Papagiorgis, P.; Protesescu, L.; Kovalenko, M. V.; Othonos, A.; Itskos, G., Long-Lived Hot Carriers in Formamidinium Lead Iodide Nanocrystals. *J. Phys. Chem. C* **2017**, *121*, 12434-12440.

(25) Chen, J.; Messing, M. E.; Zheng, K.; Pullerits, T., Cation-Dependent Hot Carrier Cooling in Halide Perovskite Nanocrystals. *J. Am. Chem. Soc.* **2019**, *141*, 3532-3540.

(26) Madjet, M. E.; Berdiyorov, G. R.; El-Mellouhi, F.; Alharbi, F. H.; Akimov, A. V.; Kais, S., Cation Effect on Hot Carrier Cooling in Halide Perovskite Materials. *J. Phys. Chem. Lett.* **2017**, *8*, 4439-4445.

(27) Zhu, H.; Miyata, K.; Fu, Y.; Wang, J.; Joshi, P. P.; Niesner, D.; Williams, K. W.; Jin, S.; Zhu, X. Y., Screening in Crystalline Liquids Protects Energetic Carriers in Hybrid Perovskites. *Science* **2016**, *353*, 1409-1413.

(28) Nah, S.; Spokoyny, B. M.; Soe, C. M. M.; Stoumpos, C. C.; Kanatzidis, M. G.; Harel, E., Ultrafast Imaging of Carrier Cooling in Metal Halide Perovskite Thin Films. *Nano Lett.* **2018**, *18*, 1044-1048.

(29) Butkus, J.; Vashishtha, P.; Chen, K.; Gallaher, J. K.; Prasad, S. K. K.; Metin, D. Z.; Laufersky, G.; Gaston, N.; Halpert, J. E.; Hodgkiss, J. M., The Evolution of Quantum Confinement in $CsPbBr_3$ Perovskite Nanocrystals. *Chem. Mater.* **2017**, *29*, 3644-3652.

(30) Niesner, D.; Zhu, H.; Miyata, K.; Joshi, P. P.; Evans, T. J. S.; Kudisch, B. J.; Trinh, M. T.; Marks, M.; Zhu, X. Y., Persistent Energetic Electrons in Methylammonium Lead Iodide Perovskite Thin Films. *J. Am. Chem. Soc.* **2016**, *138*, 15717-15726.

(31) Guo, Z.; Wan, Y.; Yang, M.; Snaider, J.; Zhu, K.; Huang, L., Long-Range Hot-Carrier Transport in Hybrid Perovskites Visualized by Ultrafast Microscopy. *Science* **2017**, *356*, 59-62.

(32) Prabhu, S. S.; Vengurlekar, A. S., Hot-Carrier Energy-Loss Rates in Alloy Semiconductors. *Phys. Rev. B* **1996**, *53*, 7815-7818.

(33) Klimov, V. I.; Mikhailovsky, A. A.; McBranch, D. W.; Leatherdale, C. A.; Bawendi, M. G., Quantization of Multiparticle Auger Rates in Semiconductor Quantum Dots. *Science* **2000**, *287*, 1011-1013.

(34) Fabini, D. H.; Siaw, T. A.; Stoumpos, C. C.; Laurita, G.; Olds, D.; Page, K.; Hu, J. G.; Kanatzidis, M. G.; Han, S.; Seshadri, R., Universal Dynamics of Molecular Reorientation in Hybrid Lead Iodide Perovskites. *J. Am. Chem. Soc.* **2017**, *139*, 16875-16884.

(35) Fang, H.-H.; Adjokatse, S.; Shao, S.; Even, J.; Loi, M. A., Long-Lived Hot-Carrier Light Emission and Large Blue Shift in Formamidinium Tin Triiodide Perovskites. *Nat. Commun.* **2018**, *9*, 243.

(36) Manser, J. S.; Kamat, P. V., Band Filling with Free Charge Carriers in Organometal Halide Perovskites. *Nat. Photonics* **2014**, *8*, 737-743.

(37) Hintermayr, V. A.; Polavarapu, L.; Urban, A. S.; Feldmann, J., Accelerated Carrier Relaxation through Reduced Coulomb Screening in Two-Dimensional Halide Perovskite Nanoplatelets. *ACS Nano* **2018**, *12*, 10151-10158.

(38) Dursun, I.; Maity, P.; Yin, J.; Turedi, B.; Zhumekenov, A. A.; Lee, K. J.; Mohammed, O. F.; Bakr, O. M., Why Are Hot Holes Easier to Extract Than Hot Electrons from Methylammonium Lead Iodide Perovskite? *Adv. Energy Mater.* **2019**, *9*, 1900084.

(39) Lim, S. S.; Giovanni, D.; Zhang, Q.; Solanki, A.; Jamaludin, N. F.; Lim, J. W. M.; Mathews, N.; Mhaisalkar, S.; Pshenichnikov, M. S.; Sum, T. C., Hot Carrier Extraction in $CH_3NH_3PbI_3$ Unveiled by Pump-Push-Probe Spectroscopy. *Sci. Adv.* **2019**, *5*, eaax3620.

(40) Shen, Q.; Ripolles, T. S.; Even, J.; Zhang, Y.; Ding, C.; Liu, F.; Izuishi, T.; Nakazawa, N.; Toyoda, T.; Ogomi, Y., et al., Ultrafast Selective Extraction of Hot Holes from Cesium Lead Iodide Perovskite Films. *J. Energy Chem.* **2018**, *27*, 1170-1174.

(41) Rong, Y.; Hu, Y.; Mei, A.; Tan, H.; Saidaminov, M. I.; Seok, S. I.; McGehee, M. D.; Sargent, E. H.; Han, H., Challenges for Commercializing Perovskite Solar Cells. *Science* **2018**, *361*, eaat8235.

(42) Urbani, M.; de la Torre, G.; Nazeeruddin, M. K.; Torres, T., Phthalocyanines and Porphyrinoid Analogues as Hole- and Electron-Transporting Materials for Perovskite Solar Cells. *Chem. Soc. Rev.* **2019**, *48*, 2738-2766.

(43) Yin, X.; Song, Z.; Li, Z.; Tang, W., Toward Ideal Hole Transport Materials: A Review on Recent Progress in Dopant-Free Hole Transport Materials for Fabricating Efficient and Stable Perovskite Solar Cells. *Energy Environ. Sci.* **2020**, *13*, 4057-4086.

(44) Chou, H.-H.; Chiang, Y.-H.; Li, M.-H.; Shen, P.-S.; Wei, H.-J.; Mai, C.-L.; Chen, P.; Yeh, C.-Y., Zinc Porphyrin–Ethynylaniline Conjugates as Novel Hole-Transporting Materials for Perovskite Solar Cells with Power Conversion Efficiency of 16.6%. *ACS Energy Lett.* **2016**, *1*, 956-962.

(45) Kundu, S.; Patra, A., Nanoscale Strategies for Light Harvesting. *Chem. Rev.* **2017**, *117*, 712-757.

(46) Protesescu, L.; Yakunin, S.; Bodnarchuk, M. I.; Krieg, F.; Caputo, R.; Hendon, C. H.; Yang, R. X.; Walsh, A.; Kovalenko, M. V., Nanocrystals of Cesium Lead Halide Perovskites ($CsPbX_3$, X = Cl, Br, and I): Novel Optoelectronic Materials Showing Bright Emission with Wide Color Gamut. *Nano Lett.* **2015**, *15*, 3692-3696.

(47) Ghosh, G.; Marjit, K.; Ghosh, S.; Ghosh, A.; Ahammed, R.; De Sarkar, A.; Patra, A., Hot Hole Cooling and Transfer Dynamics from Lead Halide Perovskite Nanocrystals Using Porphyrin Molecules. *J. Phys. Chem. C* **2021**, *125*, 5859-5869.

(48) Choi, S.; Moon, J.; Cho, H.; Kwon, B.-H.; Cho, N. S.; Lee, H., Partially Pyridine-Functionalized Quantum Dots for Efficient Red, Green, and Blue Light-Emitting Diodes. *J. Mater. Chem. C* **2019**, *7*, 3429-3435.

(49) Pan, A.; He, B.; Fan, X.; Liu, Z.; Urban, J. J.; Alivisatos, A. P.; He, L.; Liu, Y., Insight into the Ligand-Mediated Synthesis of Colloidal $CsPbBr_3$ Perovskite Nanocrystals: The Role of Organic Acid, Base, and Cesium Precursors. *ACS Nano* **2016**, *10*, 7943-7954.

(50) Yang, H.; Zhang, Y.; Pan, J.; Yin, J.; Bakr, O. M.; Mohammed, O. F., Room-Temperature Engineering of All-Inorganic Perovskite Nanocrsytals with Different Dimensionalities. *Chem. Mater.* **2017**, *29*, 8978-8982.

(51) Ravi, V. K.; Santra, P. K.; Joshi, N.; Chugh, J.; Singh, S. K.; Rensmo, H.; Ghosh, P.; Nag, A., Origin of the Substitution Mechanism for the Binding of Organic Ligands on the Surface of $CsPbBr_3$ Perovskite Nanocubes. *J. Phys. Chem. Lett.* **2017**, *8*, 4988-4994.

(52) Koscher, B. A.; Swabeck, J. K.; Bronstein, N. D.; Alivisatos, A. P., Essentially Trap-Free $CsPbBr_3$ Colloidal Nanocrystals by Postsynthetic Thiocyanate Surface Treatment. *J. Am. Chem. Soc.* **2017**, *139*, 6566-6569.

(53) Ghosh, G.; Jana, B.; Sain, S.; Ghosh, A.; Patra, A., Influence of Shape on the Carrier Relaxation Dynamics of $CsPbBr_3$ Perovskite Nanocrystals. *Phys. Chem. Chem. Phys.* **2019**, *21*, 19318-19326.

(54) Ravi, V. K.; Markad, G. B.; Nag, A., Band Edge Energies and Excitonic Transition Probabilities of Colloidal $CsPbX_3$ (X = Cl, Br, I) Perovskite Nanocrystals. *ACS Energy Lett.* **2016**, *1*, 665-671.

(55) Singh, A.; Lin, Y.; Quraishi, M. A.; Olasunkanmi, L. O.; Fayemi, O. E.; Sasikumar, Y.; Ramaganthan, B.; Bahadur, I.; Obot, I. B.; Adekunle, A. S., et al., Porphyrins as Corrosion Inhibitors for N80 Steel in 3.5% Nacl Solution: Electrochemical, Quantum Chemical, Qsar and Monte Carlo Simulations Studies. *Molecules* **2015**, *20*, 15122-15146.

(56) Ghosh, G.; Dutta, A.; Ghosh, A.; Ghosh, S.; Patra, A., Ultrafast Carrier Dynamics in 2D CdSe Nanoplatelets–$CsPbX_3$ Composites: Influence of the Halide Composition. *J. Phys. Chem. C* **2020**, *124*, 10252-10260.

(57) Luo, X.; Liang, G.; Wang, J.; Liu, X.; Wu, K., Picosecond Multi-Hole Transfer and Microsecond Charge-Separated States at the Perovskite Nanocrystal/Tetracene Interface. *Chem. Sci.* **2019**, *10*, 2459-2464.

(58) Wu, K.; Liang, G.; Shang, Q.; Ren, Y.; Kong, D.; Lian, T., Ultrafast Interfacial Electron and Hole Transfer from $CsPbBr_3$ Perovskite Quantum Dots. *J. Am. Chem. Soc.* **2015**, *137*, 12792-12795.

(59) Chung, H.; Jung, S. I.; Kim, H. J.; Cha, W.; Sim, E.; Kim, D.; Koh, W.-K.; Kim, J., Composition-Dependent Hot Carrier Relaxation Dynamics in Cesium Lead Halide ($CsPbX_3$, X=Br and I) Perovskite Nanocrystals. *Angew. Chem. Int. Ed.* **2017**, *56*, 4160-4164.

(60) Mondal, N.; De, A.; Das, S.; Paul, S.; Samanta, A., Ultrafast Carrier Dynamics of Metal Halide Perovskite Nanocrystals and Perovskite-Composites. *Nanoscale* **2019**, *11*, 9796-9818.

(61) Van Stokkum, I. H. M.; Larsen, D. S.; van Grondelle, R., Global and Target Analysis of Time-Resolved Spectra. *Biochim. Biophys. Acta* **2004**, *1657*, 82-104.

(62) Lim, J. W. M.; Giovanni, D.; Righetto, M.; Feng, M.; Mhaisalkar, S. G.; Mathews, N.; Sum, T. C., Hot Carriers in Halide Perovskites: How Hot Truly? *J. Phys. Chem. Lett.* **2020**, *11*, 2743-2750.

Chapter 5

Revealing Slow Hot-Carrier Cooling Dynamics in $CsPbBr_3/PbSe$ Heterostructures

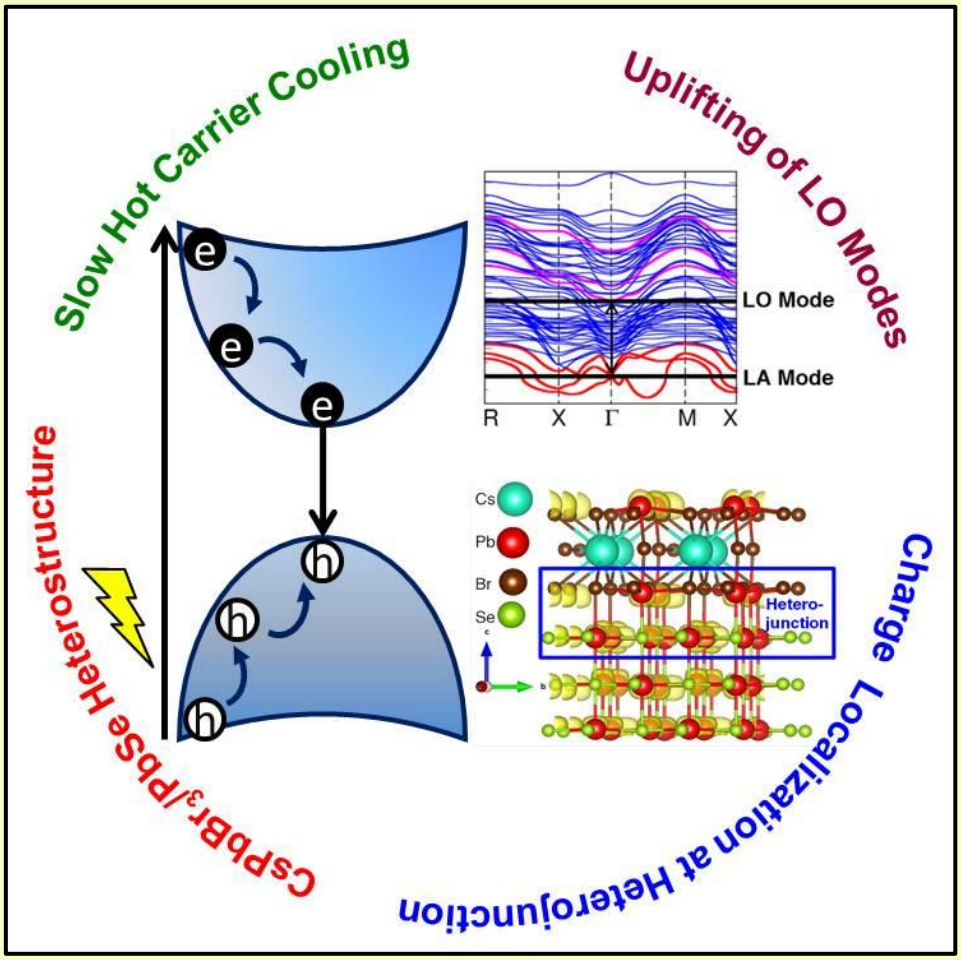

5.1 Introduction

Understanding the fundamental physics of photoexcited hot carriers (HCs) in semiconductors is essential for designing efficient next-generation photovoltaic devices.[1] HCs are the high-energy charge carriers (electrons and holes) above the semiconductor bandgap (s), not in thermal equilibrium with the lattice.[2] Thermalization of photogenerated HCs occurs by dissipating their excess energy as heat energy through phonons, and it is the major intrinsic loss channel for solar cell devices. [3] Harnessing the excess energy of photoexcited HCs will allow us to achieve maximum power conversion efficiency (PCE) up to 67% for a single-junction solar cell under one sun illumination,[4] breaking the so-called Shockley-Queisser (SQ) limit of 34%.[5] In addition, HCs can be used for photo-catalysis, photodetection, and high-power optoelectronic devices to improve efficiency.[6, 7] However, HCs loss their additional energy in sub-picosecond timescale for the conventional semiconductor nanomaterials (e.g., GaAs, PbSe, InN, and CdSe) which restrict the utilization of non-thermalized excess energy of photo-excited HCs.[8-11] Therefore, it is essential to develop a solar absorber with retarded HC cooling rate.[12]

Metal halide perovskite nanocrystals (NCs) have recently emerged as front-runner materials [13, 14] and understanding the HC cooling dynamics of lead halide perovskite is essential for low-cost, high-performance solar cells.[15-19] Slow HC relaxation mechanisms in perovskite materials are reported due to the hot-phonon bottleneck effect,[20] Auger-heating effect,[21] band-filling effects,[22] dielectric screening,[23] and large polaron screening effects.[24] However, such slow HC cooling rate is achieved at high pump fluence with photo-excited carrier densities of 10^{18}-10^{19} cm^{-3}, which is not convenient for practical use.[20, 25] It is worth noting that HC relaxation of lead halide perovskite occurs very rapidly (within hundreds of femtoseconds) under weak carrier densities (comparable to sun illumination level,10^{17} cm^{-3}).[26, 27] Thus, slowing down the HC relaxation rate of halide-based perovskite materials under low excitation power densities is a challenge for hot-carrier-based optoelectronic applications. Tuning the HC cooling dynamics of metal halide perovskite is mainly limited to reduction of dimensionality,[28] changing cation/ halide ions,[29-31] and doping impurity ions.[32] Therefore, significant efforts are needed to be put in to develop new strategies for modulating the HC cooling dynamics of lead halide perovskite NCs.

The ionic nature of the lead halide perovskite (LHP) NCs and the defect states generated due to halide vacancies have severe detrimental effects on the device functionality

and optical properties.[33, 34] Surface modifications by silica, alumina, titanium dioxide, polyhedral oligomeric silsesquioxane, and polymers are used to enhance the stability of such materials.[35-38] Most of these reported methods exhibit improved stability of perovskite NCs but at the expense of their superior charge separation and charge transport properties. The perovskite/lead chalcogenide heterojunction provided excellent stability and passivated the trap states and efficient charges separation.[39-41] In this context, Rogach *et al.* have reported the improvement of solar cell efficiency of $CsPbI_3$/PbSe heterostructure due to the enhancement of the carrier mobility and the extended excitons lifetime in the presence of the PbSe component.[39] Sargent *et al.* have reported enhancing the external quantum efficiency up to 8.1% in perovskite/PbS heterostructures.[42] However, a clear picture of the HCs and their subsequent relaxation dynamics at these heterojunctions is still lacking in the literature, which is essential to improve the efficiency of such heterostructures-based devices. Now, it is time to assess whether this type of hetero-structured material can be employed to slow down the HC relaxation rate(s). Moreover, establishing a general mechanism of slow carrier cooling in these hetero-structured materials is fundamentally exciting and essential for practical purposes. To the best of our knowledge, there is no report on the HC cooling properties of $CsPbBr_3$/PbSe heterostructures.

This work aims to slow down the HC cooling rate of $CsPbBr_3$ perovskite NCs at a low carrier density of 10^{17} cm^{-3} in the presence of PbSe. Ultrafast transient absorption (TA) spectroscopic study has been carried out for a deep understanding of HC relaxation dynamics. The HC lifetime of $CsPbBr_3$ NCs enhances up to 2 times upon forming the heterostructure with PbSe. Moreover, the electron-phonon coupling model unveils the reduced decay of LO phonons in the heterostructure. The first-principles calculations suggest that the finite energy gap between longitudinal optical (LO) phonon and longitudinal acoustic (LA) phonon mode in the $CsPbBr_3$/PbSe heterostructure prohibits the decay of LO phonon through an efficient Klemens's channel. The charge localization near the heterojunction leads to up-conversion of LO modes to the higher energy scale, attributed to the retarded HC cooling in the heterostructure. Our study will pave a new way for developing new generation photovoltaic materials by controlling the HC cooling.

5.2. Results and Discussion

5.2.1. Structural and Optical Characterizations of the $CsPbBr_3$/PbSe Heterostructure

Hot-injection methods have synthesized the pure CsPbBr3 NCs and $CsPbBr_3$/PbSe heterostructure.[39, 43] We have characterized the samples by a combination of transmission

electron microscopy (TEM), X-ray diffraction (XRD), X-ray photoelectron spectroscopy (XPS), optical absorption, and PL spectroscopy. The TEM images of the as-synthesized pure $CsPbBr_3$ NCs and $CsPbBr_3$/PbSe heterostructure are shown in Figure 5.1**.** The pure $CsPbBr_3$ NCs show a highly mono-dispersed cubic shape with an average edge length of 12±0.3 nm.

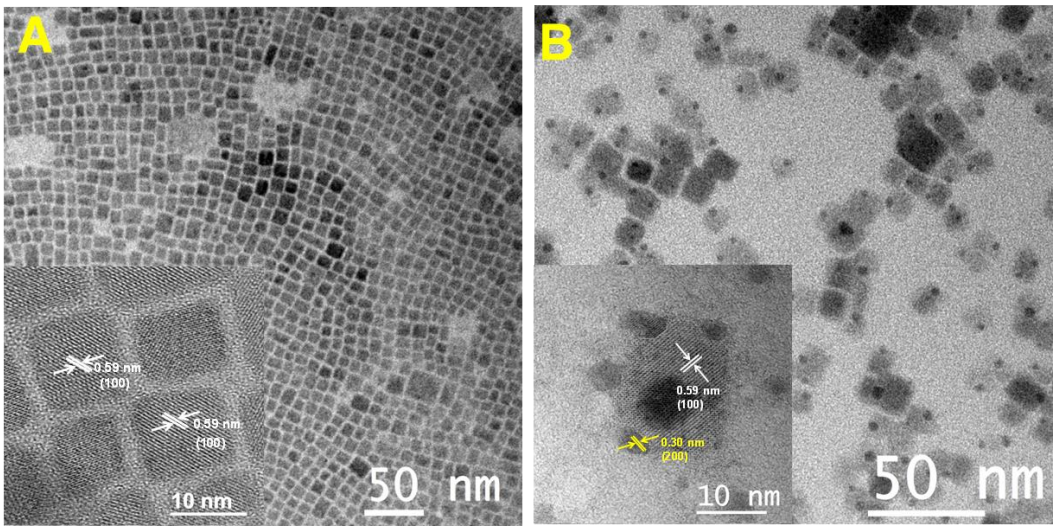

Figure 5.1*. TEM images of (A) pure $CsPbBr_3$ NCs and (B) $CsPbBr_3$/PbSe heterostructure. Inset shows HRTEM images.*

In contrast, the $CsPbBr_3$/PbSe heterostructure exhibits a cubic shape with an additional dot near the edge of every cube due to nucleation of PbSe, with an average edge length of 13±0.5 nm. The high-resolution transmission electron microscopy (HRTEM) for both the samples is depicted in the inset of Figure 5.1. For pure $CsPbBr_3$ NCs, an inter-planar distance (d-value) of 0.59 nm is observed corresponding to (100) plane of cubic $CsPbBr_3$ NCs. Interestingly, a d-value of 0.59 nm due to (100) plane of cubic $CsPbBr_3$ NCs in the central region and d-value of 0.30 nm corresponding to (200) plane of PbSe component at the surface region is observed for $CsPbBr_3$/PbSe NCs, suggesting the formation of hetero-structured NCs. Additionally, energy dispersive spectroscopy (EDS) data shows the elemental composition of Cs:Pb:Br: Se is 1:1.02:2.21:0.12 and 1:1.10:2.48:0, for $CsPbBr_3$/PbSe heterostructure and pure $CsPbBr_3$ NCs, respectively, which indicate the passivation of undesired surface dangling bond of lead by PbSe (Figure 5.2).

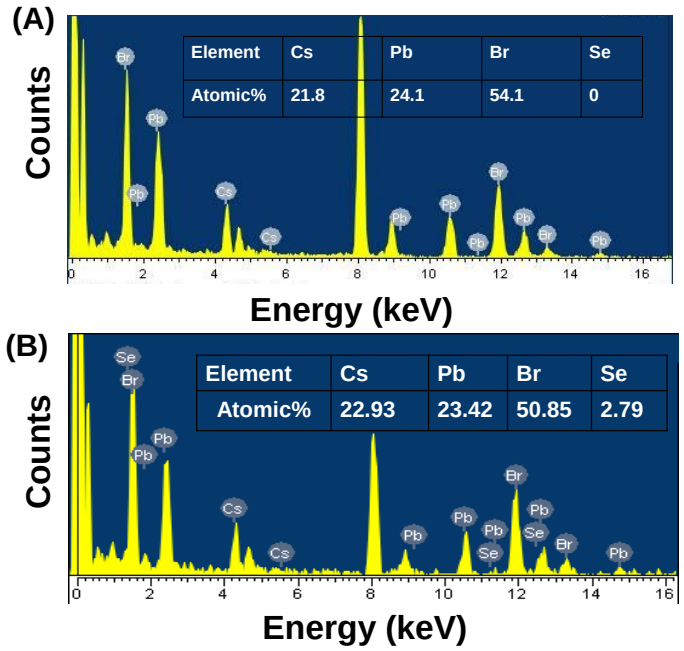

Figure 5.2. *EDS spectra of (A) pure $CsPbBr_3$ NCs and (B) $CsPbBr_3$/PbSe heterostructure. Inset shows corresponding elemental analysis.*

XRD patterns for both the samples are shown in Figure 5.3, where strong peaks around the 2θ value of 15° and 30° correspond to (100) and (200) planes of cubic $CsPbBr_3$ NCs, respectively. The overlap between $CsPbBr_3$ and PbSe is confirmed from the enlarged XRD pattern where the strongest peak corresponding to the (200) plane of $CsPbBr_3$ NCs is shifted by 0.12° towards a higher 2θ angle for $CsPbBr_3$/PbSe heterostructure (see right panel of Figure 5.3).

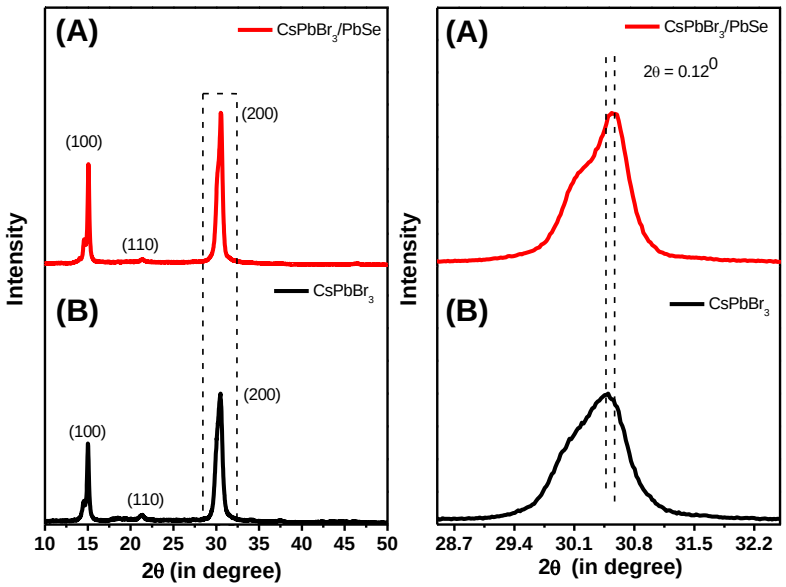

Figure 5.3. *XRD patterns of (a) pure $CsPbBr_3$ NCs and (b) $CsPbBr_3$/PbSe heterostructure. The right panel shows the enlarged XRD patterns of the (200) planes.*

In the XPS study, we observed two additional peaks for Se-3d of the heterostructure, and no Se peaks for pure NCs, suggesting the presence of Se^{2-} in these heterostructures (Figure 5.4). Interestingly, the peaks for Cs 3d, Pb 4f, and Br 3d are shifted towards lower binding energy in the heterostructure than pure NCs. This observation is found due to the strong interaction between PbSe and $CsPbBr_3$ NCs.[39, 41]

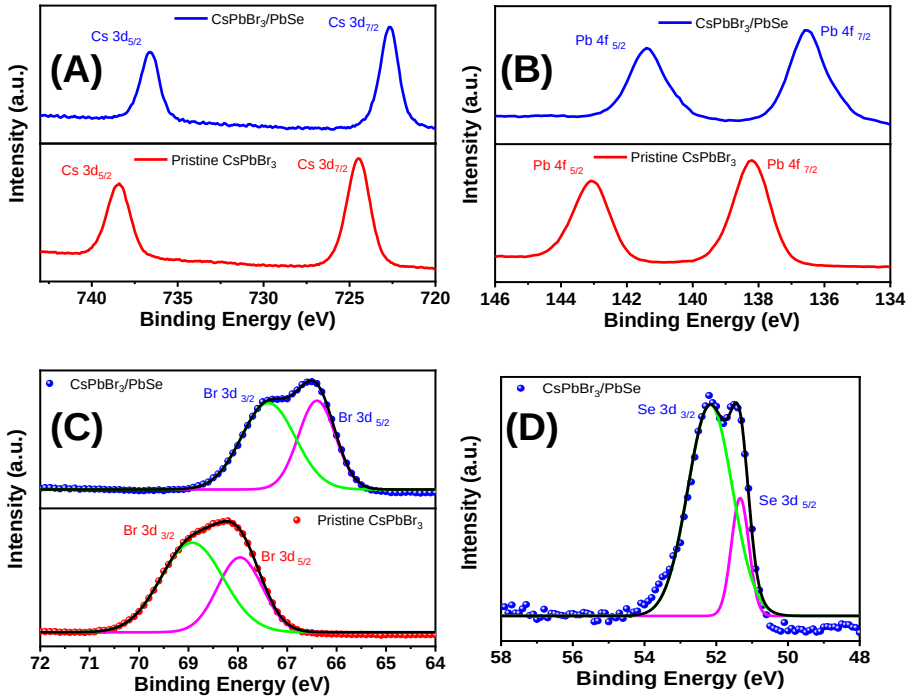

Figure 5.4. *High-resolution XPS spectrum of (a) Cs 3d, (b) Pb 4f, (c) Br 3d and (d) Se 3d for the pure $CsPbBr_3$ NCs and $CsPbBr_3$/PbSe heterostructure.*

The first excitonic absorption band is observed at 505 nm (2.45 eV) for both $CsPbBr_3$/PbSe heterostructure and $CsPbBr_3$ NCs, and the PL maxima arise at 515 nm (Figure 5.5 A, B). Interestingly, The PLQY is 87 % for $CsPbBr_3$/PbSe hetero-structure, much higher than pure $CsPbBr_3$ NCs (65%). It suggests the reduction of the surface defects of the pure perovskite NCs in the presence of the PbSe. The average PL lifetime of pure $CsPbBr_3$ NCs enhances from 5.0 ns to 8.5 ns due to heterostructure formation (Figure 5.5C). The fitted decay components associated with pure $CsPbBr_3$ NCs are τ_1 (1.0 ns, 55%) τ_2 (6.0 ns, 38%) and τ_3 (3.2 ns, 7%), while the decay components for the hetero-structure are τ_1 (1.8 ns, 20%) and τ_2 (10.8 ns, 80%). According to previous literature, τ_2 is due to excitonic recombination, and the other two components arise due to trap state mediated processes.[44] Our analysis shows that longer components due to trap states are completely absent for $CsPbBr_3$/PbSe heterostructure. This observation indicates that surface passivation by the PbSe layer helps to reduce the non-radiative channels and enhance the exciton lifetime.

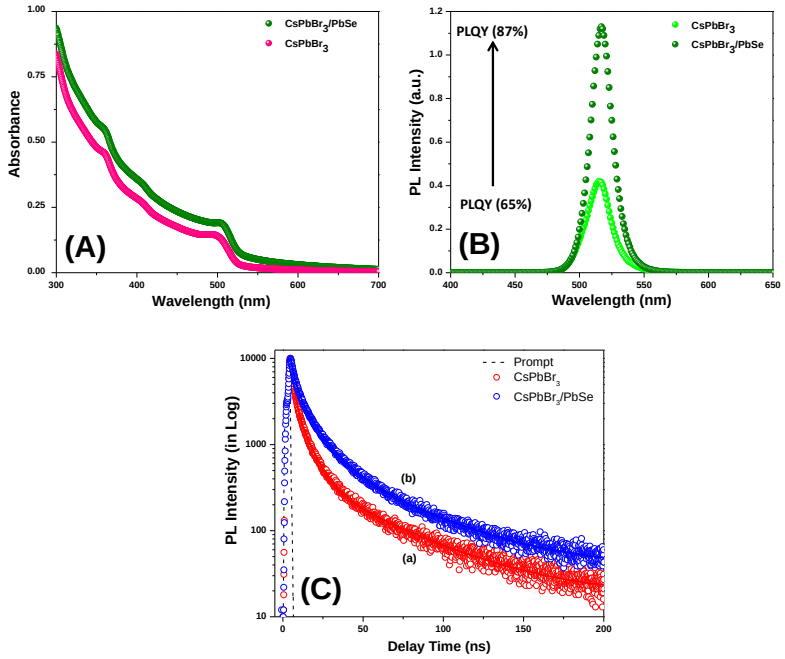

Figure 5.5. *(A) Normalized UV-visible absorption,(B) PL spectra and (C) TCSPC decay curves of pure $CsPbBr_3$ NCs and $CsPbBr_3$/PbSe heterostructure. λ_{ex}=375 nm and λ_{em}=515 nm.*

5.2.2. Slow HC cooling dynamics in $CsPbBr_3$/PbSe heterostructure

We have employed femtosecond (fs) transient absorption (TA) spectroscopy to investigate the HC cooling dynamics of pure $CsPbBr_3$ NCs and $CsPbBr_3$/PbSe heterostructure. Here, we have used three different laser pulses [i.e., 3.64 eV (340 nm); 3.10 eV (400 nm); 2.75 eV (450 nm)] as excitation sources and a white-light supercontinuum to probe the ultrafast behavior of photogenerated carriers. The pump fluence varied from 5μJ/cm^2 to 35μJ/cm^2 and the average number of excitons per NCs, $\langle N_0 \rangle$, changes from 0.3 to 2.2, calculated from the equation, $\langle N_0 \rangle = j.\sigma$, where j is the photon fluence per pulse and σ is the absorption cross-section of the NCs. The absorption cross-section (σ) value is 3.1×10^{-14} cm^2, which is consistent with the previous literature. The calculated average carrier density per volume of the NCs (n_0) varies from 1.79×10^{17} cm^{-3} to 1.27×10^{18} cm^{-3} using the equation $n_0 = \langle N_0 \rangle / V_{NC}$, where V_{NC} is the volume of the NCs. Figure 5.6 (A, D) and Figure 5.6(B, E) show the pseudo-color TA plots and normalized TA spectra of pure $CsPbBr_3$ NCs and $CsPbBr_3$/PbSe heterostructure, respectively, excited at 3.10 eV (400 nm) with an initial average carrier density, $n_0 \sim 1.79 \times 10^{17}$ cm^{-3}, corresponding to the average number of excitation per NCs, $\langle N_0 \rangle \sim 0.3$. We observed a strong negative ground state bleach (GSB) signal at the band gap (2.45 eV) with a short-lived positive photo-induced absorption (PIA) at the lower energy side (<2.40 eV) and a long-lived positive PIA signal at the higher energy side (>2.60 eV).

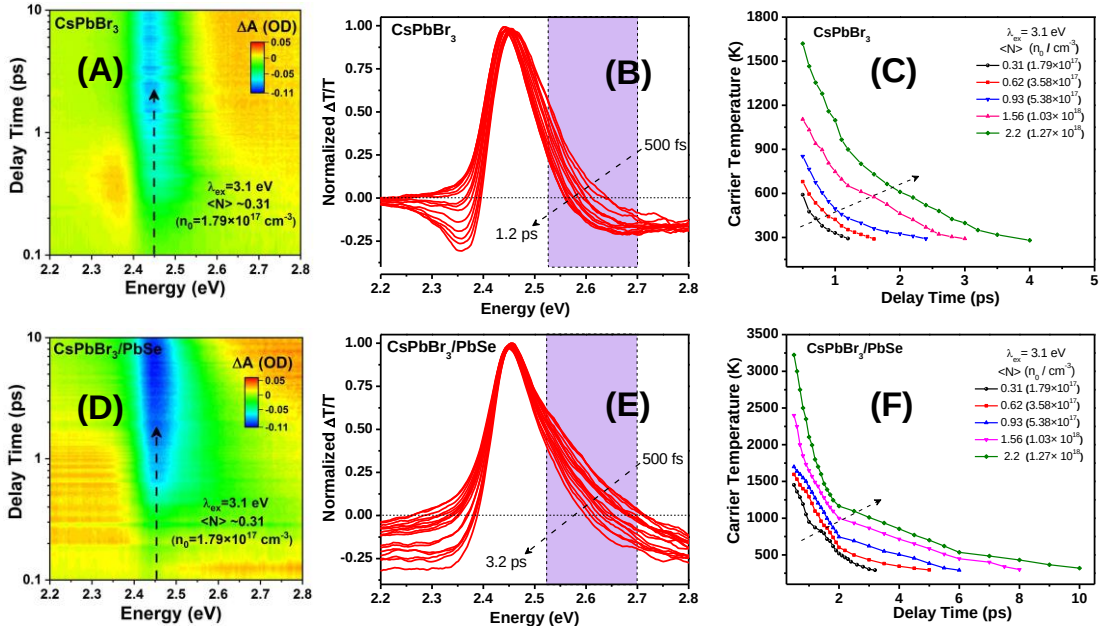

Figure 5.6. *(A, D) Pseudo-color TA spectra and (B, E) normalized TA spectra at carrier density, n_0~1.79×10^{17} cm^{-3} (<N_0>~0.3) for pure $CsPbBr_3$ NCs and $CsPbBr_3$/PbSe heterostructure, respectively. The shaded area in b and e represents the data used for the extraction of HC temperature. (C, F) HC temperature as a function of delay time under different excitation fluences for both the samples. The samples are excited using a 3.1 eV pump pulse.*

The GSB signal appears due to the state filling effect of the photogenerated carriers to the band-edge.[45, 46] The short-lived PIA arises due to the bandgap renormalization. The long-lived PIA originates due to the band edge states.[22, 47, 48] The shift of GSB signal with that of PIA signal (derivative like a spectral signature) is mainly due to the exciton-exciton interactions, which is also known as the bi-exciton induced stark effect.[30, 45] It is noted that a strong GSB signal replaces the short-lived positive PIA signal during the relaxation of HC to the lowest-energy band-edge states. Thus, the initial negative GSB intensity increases and reaches a maximum at early delay time [shown by the arrow in Figure 5.6(A, D)]. Compared to pure $CsPbBr_3$ NCs, we observed an additional high energy tail of GSB signal (at 2.5-2.7 eV) for $CsPbBr_3$/PbSe heterostructure, representing the energy distribution of state fillings by HC (shown in Figure 5.6 B, E). The high energy tail of the GSB signal originates due to the rapid distribution of the initially created non-equilibrium carriers into quasi-equilibrium Fermi-Dirac distribution via elastic scattering.[29]

Such quasi-thermal Fermi-Dirac distribution is characterized by hot carrier temperature (T_C). It can be approximated to Maxwell-Boltzmann (MB) distribution for excess energy of HC

greater than quasi-Fermi energy (E_F). Thus, as soon as HC reaches the quasi-equilibrium state, T_C is extracted by fitting the high energy tail of the GSB signal with the following MB distribution function:[22, 28, 29, 48]

$$\Delta T(\hbar\omega) = -T_0 exp\left(\frac{E_F - \hbar\omega}{k_B T_C}\right) \quad (5.1)$$

Where ΔT stands for the amplitude of bleach at a particular probe wavelength, E_F is the quasi-Fermi energy level, K_B is the Boltzmann constant, and T_C is the HC temperature (see supplementary note 3 for detailed fitting procedure). We extracted T_C from the TA spectra after 400 fs time delay to ensure a quasi-equilibrium state has been reached by HCs, after the initial fs-pulse excitation. T_C represents the average temperature of electron and hole since the average effective mass of electron and hole are almost equal in LHP NCs.[29, 45] We investigated the HC cooling dynamics by monitoring the relaxation dynamics of hot carrier temperature (T_C), which signifies the cooling process of HCs. Figure 5.6(C, F) shows the time-dependent relaxation of T_C for pure $CsPbBr_3$ and $CsPbBr_3$/PbSe hetero-structure, respectively, with increasing the carrier densities (n_0) from 1.79×10^{17} cm^{-3} to 1.27×10^{18} cm^{-3} at 3.10 eV excitation. It is interesting to note that the evolution of initial T_C and the relaxation time of T_C strongly depend on carrier density; i.e., the decay time of T_C is enhanced significantly with the increase of excitation fluence. Notably, initial hot T_C (3223 K) for $CsPbBr_3$/PbSe heterostructure is much higher than that of pure $CsPbBr_3$ NCs (1620 K) at the highest used carrier density (i.e., 1.27×10^{18} cm^{-3}). The decay time of hot T_C at this carrier density is found (up to 10 ps) for $CsPbBr_3$/PbSe heterostructure than pure $CsPbBr_3$ NCs (up to 4ps), which is much longer than the conventional semiconductor NCs (i.e., CdSe, PbSe, GaAs, etc.). Interestingly, a second slow decay component increases the excitation fluence, which de-accelerates the cooling process of HCs for the heterostructure. According to previous reports, slow HC cooling of LHP NCs at higher carrier densities is due to the hot phonon bottleneck and Auger heating effect.[20, 21] It is noted that the presence of a non-equilibrium population of Longitudinal optical (LO) phonon and their slow conversion into longitudinal acoustic (LA) phonon leads to a hot-phonon bottleneck at high carrier density.[20] Again, the interplay of hot-phonon with Auger heating effect where the recombination energy of electron-hole will transfer to another electron and re-heat HCs, further retard the HC cooling at high carrier density.[49]

Further, we study the relaxation behavior of HC at low carrier density (~10^{17} cm^{-3}) to neglect the effect of hot-phonon bottleneck, Auger heating, and State-filling, which play a

major role at higher carrier density. For comparison, we plotted the transient evolution of T_C for both the samples, excited at 3.10 eV with initial carrier density (n_0~1.79×10^{17} cm^{-3} and <N_0> ~ 0.31) in Figure 5.7A.

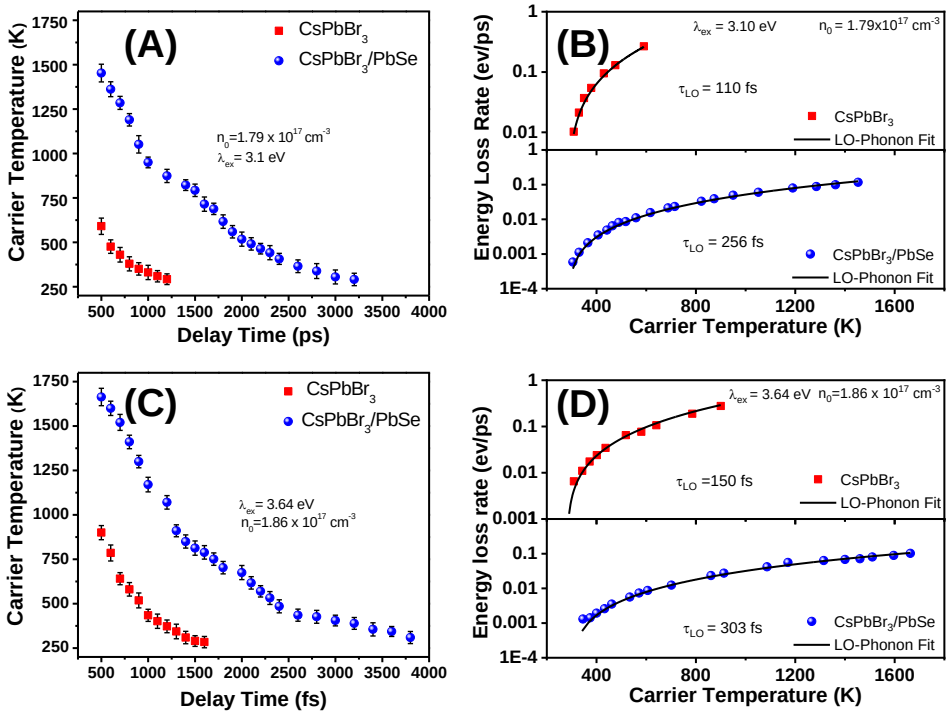

Figure 5.7. *Plots of carrier temperature with delay time (A, C) and energy loss rate as a function of carrier temperature (B, D) for pure $CsPbBr_3$ NCs and $CsPbBr_3$/PbSe heterostructure at 3.10 eV and 3.64 eV excitation, respectively. The error bar in A and C indicate the standard deviation. The solid lines in b and d represent the fitting using the LO-phonon model.*

The initial hot carrier temperature (corresponding to 0.65 eV excess energy of photo-excited HC) reduces significantly for pure $CsPbBr_3$ NCs (~590 K after 400 fs delay time) compared to $CsPbBr_3$/PbSe heterostructure (~1452 K after 400 fs delay time) under 3.1 eV photoexcitation with same initial carrier density (n_0~1.79×10^{17} cm^{-3}). Additionally, the hot T_C cools down to lattice temperature (i.e., 300 K) within 1.2 ps for pure $CsPbBr_3$ NCs. In contrast, the relaxation time of hot T_C for heterostructure is 3.2 ps, indicating the HC cooling process is substantially slower for $CsPbBr_3$/PbSe heterostructure.

To further understand the cooling dynamics of HC, we have calculated the energy loss rate per carrier (J_r) from the extracted T_C by the following equation:[19, 50]

$$J_r = -\frac{3}{2} K_B \frac{dT_C}{dt} \qquad (5.2)$$

Figure 5.7B represents the energy loss rate per carrier (J_r) as a function of carrier temperature (solid balls). The calculated J_r for the pure $CsPbBr_3$ NCs is higher (from 0.26 to 0.01 eV ps^{-1}) than $CsPbBr_3$/PbSe heterostructure (from 0.11 to 0.0006 eV ps^{-1}) until T_C reaches 300 K. It is seen that the J_r decreases more slowly in the $CsPbBr_3$/PbSe heterostructure than pure $CsPbBr_3$ NCs as the T_C approaches lattice temperature. This observation suggests that the relaxation channel for HCs is significantly modified in the heterostructure.

5.2.3. Electron-phonon coupling model of HC cooling

To obtain a clear understanding of the HC relaxation mechanism in the heterostructure, we have first revisited the well-accepted three distinct carrier relaxation stages of typical polar semiconductor,[19, 20, 25], which includes: (a) scattering between charge carriers with optical modes through dominant Fröhlich interactions, (b) optical phonon thermalization to acoustic modes, and finally (c) acoustic phonons release their energy to heat the semiconducting system. The first mechanism is unlikely in most cases as the spontaneous interaction of the charge carriers with LO phonons controls the charge carrier relaxation processes. Notably, the Fröhlich interaction in LHP NCs mainly occurs between the charge carriers and lead-halide bonds, controlling the HC relaxation pathways.[18, 51] Recently, it has been reported in several inorganic semiconductor systems that the LO phonon mode decays to LA modes through dominating symmetric Klemens channel and anti-symmetric Ridley channel.[52] The significant atomic mass differences in such complex systems and localized asymmetric charge distribution lead to a large bandgap opening between optical and acoustic branches.

Interestingly, such a bandgap formation does not allow LO phonons to decay to LA phonons, which eventually enhances the HC relaxation time. In the third stage of scattering processes, acoustic phonon thermalization occurs when the phonon dissipates heat energy to the surroundings. Now, we have modeled the above method using electron-phonon interactions.

Notably, the energy loss rate (J_r) can be modeled by the following equation in the absence of the hot-phonon bottleneck effect:[19, 28, 32, 50]

$$J_r = \frac{3}{2}\frac{\hbar\omega}{\tau_{LO}}\left(e^{\frac{\hbar\omega}{K_B T_a}} - e^{\frac{\hbar\omega}{K_B T_c}}\right)\frac{N_{LO}(T_a)}{N_{LO}(T_c)}\left(\frac{K_B T_c}{\hbar\omega}\right)^2 e^{\frac{-\hbar\omega}{K_B T_c}} \quad (5.3)$$

where $\hbar\omega$ is the LO-phonon energy, τ_{LO} is the characteristics LO-phonon time, T_a is the temperature of acoustics phonon and $N_{LO}(T)$ is the LO-phonon occupation number for specific temperature T. According to previous reports, the available LO-phonon energy for

$CsPbBr_3$ NCs, corresponding to stretching of Pb-Br bonds, is 9 meV.[53] The solid black curve in Figure 5.7B displays the fitting (LO-phonon model) of the experimentally observed J_r (solid balls) for both the samples, where reasonably good fitting with experimental data suggests the absence of hot-phonon bottleneck in the present case. We obtained characteristic LO-phonon lifetime (τ_{LO}) of 110±10 fs and acoustic phonon temperature (T_a) of 290±5 K for pure $CsPbBr_3$ NCs, which is in good agreement with the reported values for LHP NCs.[19] Interestingly, a much greater τ_{LO} of 256±10 fs and the corresponding T_a of 305± 5 K is found for $CsPbBr_3$/PbSe heterostructure. In the present case, T_a for both samples is close to lattice temperature, indicating the absence of the hot-phonon bottleneck effect at such low carrier density. Moreover, the enhancement of lifetime of the LO-phonon (almost 2.3 fold) for the heterostructure than that of pure $CsPbBr_3$ NCs, implies the retarded decay of hot LO-phonon, which is also responsible for the observed slow J_r and retarded relaxation of T_C. Our results indicate the decrease of decay channel for hot phonons or the variation of LO-phonon modes responsible for HC cooling in case $CsPbBr_3$/PbSe heterostructure, which will be corroborated through first principle calculations of phonon band structure in the subsequent section.

To see the effect of higher excitation energy on the HC cooling dynamics, we examined the transient evolution of T_C and J_r for both the samples under photoexcitation of 3.64 eV with initial n_0~ 1.86×10^{17} cm^{-3}. Figure 5.7C represents the time-dependent relaxation dynamics of extracted hot carrier temperature (at 3.64 eV excitation), which clearly shows much slower decay dynamics of T_C for $CsPbBr_3$/PbSe heterostructure than pure $CsPbBr_3$ NCs. The observed initial hot T_C after 400 fs delay time is 900 K for pure $CsPbBr_3$ NCs, whereas the corresponding initial hot T_C is 1663 K for the heterostructure. It takes almost 2.3 times much longer time for cooling down the initial hot T_C to lattice temperature for $CsPbBr_3$/PbSe heterostructure (relaxation time ~3.8 ps) than pure $CsPbBr_3$ NCs (relaxation time ~1.6 ps). Figure 5.7D displays the carrier temperature-dependent J_r (solid balls) for both the samples at this higher excitation energy. It is seen that energy loss rate (J_r) is much slower (from 0.10 to 0.001 eV ps^{-1}) for $CsPbBr_3$/PbSe hetero-structure than pure $CsPbBr_3$ NCs (from 0.24 to 0.009 eV ps^{-1}) until T_C reaches 300 K. The LO-phonon fit (black line) of the observed J_r gives τ_{LO} of 150±5 fs and 303±10 fs for $CsPbBr_3$ and $CsPbBr_3$/PbSe hetero-structure, respectively. It is noted that the excess energy will lead to a larger population build of non-equilibrium LO-phonons, which eventually increase the decay time of LO-phonons as compared to the lower photoexcitation energy.[21, 32] Thus, our results suggest that the HC relaxation dynamics become substantially slower in the heterostructure of $CsPbBr_3$/PbSe NCs

compared to pure $CsPbBr_3$ NCs, which eventually increase the hot carrier temperature, the relaxation time of HCs, and the decay time of LO-phonons compared.

Furthermore, we have plotted the HC energy loss rate of $CsPbBr_3$/Pbse heterostructure with the other relevant systems to get a quantitative picture of HC cooling properties (Figure 5.8). Notably, HC cooling strongly depends on the initial excess energies above the bandgap (ΔE), where ΔE can be calculated from the difference of pump energy and the bandgap of the materials. We have calculated the HC energy loss rate (*dE/dt*) for different systems using the following equation:[54]

$$\frac{dE}{dt} = \Delta E/\tau \qquad (5.4)$$

where τ is the HC relaxation time under very weak excitation fluence, we have taken the data reported in refs[26, 29, 32, 54] to calculate HC energy loss rate. Interestingly, it is seen that *dE/dt* for $CsPbBr_3$/PbSe heterostructure is much slower than the other systems.

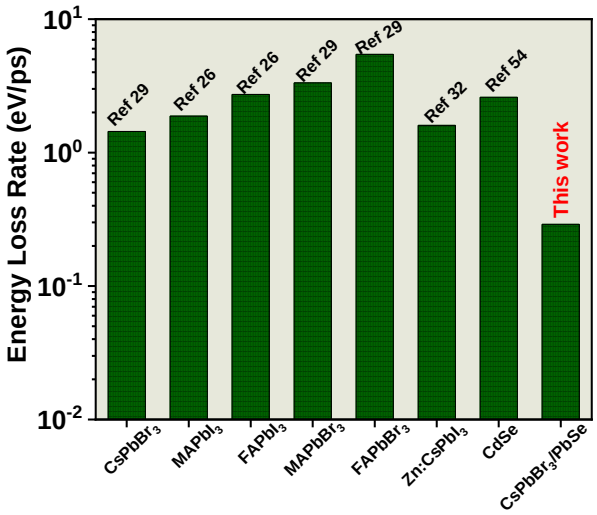

Figure 5.8. *Comparison of hot carrier energy loss rates for different perovskite systems and CdSe quantum dot with $CsPbBr_3$/PbSe heterostructure. The data for other systems are adapted from refs 26, 29, 32, and 54.*

5.2.4. Theoretical understanding of slow HC cooling

We performed a comprehensive theoretical study using first-principles-based density functional theory to understand the underlying effect of the observed slow HC cooling in the heterostructure. Here, we have considered crystal structures of $CsPbBr_3$ with space group Pm-3m and PbSe with space group Fm-3m. With this, we carefully constructed a supercell, where the $CsPbBr_3$ cubic lattice was placed on top of the PbSe cubic lattice (Figure 5.9A).

The subsequent van der Waals interactions between the $CsPbBr_3$ and PbSe lattice was incorporated via PBE-D2(3) van der Waal (vdW) corrections along the stacking direction. The density functional theory (DFT) predicted inter-layer distance around 3.05 Å (Figure 5.9B), which came under the vdW regime. In this study, our main focus was to examine the role of long-range interlayer interaction(s) on the lattice dynamics and phonon relaxations, especially in the interface region.

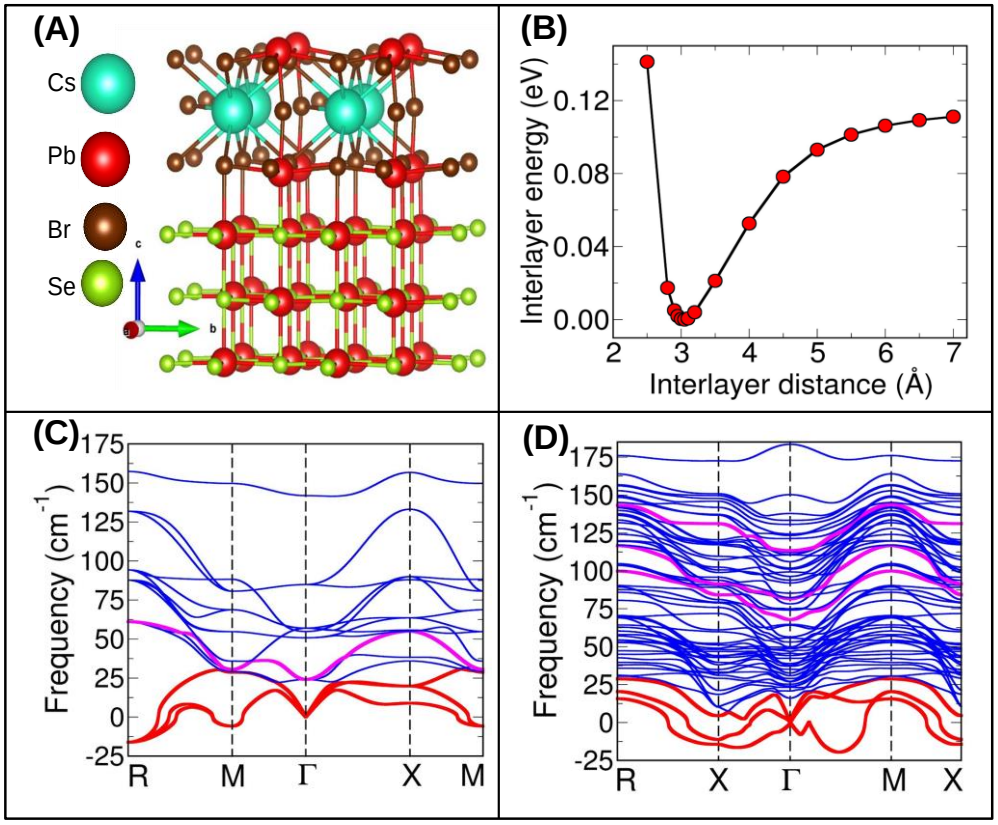

Figure 5.9. *(A) The optimized structure of the $CsPbBr_3$/PbSe heterostructure, (B) Inter-layer energy as a function of the interlayer distance between $CsPbBr_3$ and PbSe cubic lattice, (C) Phonon dispersion spectra of $CsPbBr_3$ and (D) Phonon dispersion spectra of $CsPbBr_3$/PbSe heterostructure along R→ M→ Γ→ X→ M over the Brillouin zone. All phonon modes are blue, whereas longitudinal optical (LO) and acoustic (LA) phonon modes are highlighted in magenta and red colors. Cs, Pb, Br, Se atoms are shown by cyan, red, brown, and green, respectively.*

Accordingly, we used first-principles-based density functional perturbation theory (DFPT) to obtain the phonon dispersion of the $CsPbBr_3$/PbSe heterostructure. The phonon dispersion spectra for both $CsPbBr_3$ and the $CsPbBr_3$/PbSe heterostructure have been plotted along the high-symmetry direction over the Brillouin zone and shown in Figure 5.9(C, D). All phonon

modes are blue, whereas longitudinal optical (LO) and longitudinal acoustics (LA) phonon modes are highlighted in magenta and red colors. From the phonon band dispersion of $CsPbBr_3$, we found that the low energy LO phonon mode (at ~27 cm^{-1}) has a significant band overlapping with the LA phonon modes at the high symmetry M-point. Such a finite band overlapping of the low energetic LO mode with especially LA phonon modes would undoubtedly help to decay HC significantly and reduce the HC lifetime. Thus, this kind of phonon band crossing between LO and LA modes, specifically at the high symmetry points, would eventually be detrimental for solar cell applications. In contrast to phonon spectra of $CsPbBr_3$, we find an exciting feature in the phonon dispersion spectra of the heterostructure. In this case, we observe the opening up of a large energy gap (ΔE_{gap}) between the LO and LA modes near the zone-center Γ-point (Figure 5.9D). We notice three high energetic LO modes appearing at the energy level around 68 cm^{-1} (LO_1), 81 cm^{-1} (LO_2), and 113 cm^{-1} (LO_3), respectively, in the zone-center Γ-point. Although we encounter the up-lifting of LO modes in the phonon dispersion, the maximum of LA mode remains still unaltered in the case of heterostructure and appears at ~ 27 cm^{-1}. As a result, the overall energy gap between the LO and LA modes widens up to a greater extent. This fascinating hallmark in the phonon band spectra certainly limits the HC decay and thus enhances the carrier lifetime. It is further necessary to note here that the presence of the finite energy gap between the LO and LA branches prohibits Klemens's channel for LO phonon decay ($\Delta E_{gap} > 2E_{max}(LA)$) where LO phonon transfers their energy to a pair of acoustic modes (LO→ LA+LA). This inhibition of Klemens-type phonon decay through an efficient channel gives rise to the retarded HC cooling mechanism in the heterostructure.

To understand the origin of such a high energy gap between LO and LA modes in the case of the heterostructure, we have carefully analyzed the phonon eigenvectors associated with three LO phonon at the particular high symmetry Γ-point (Figure 5.10 A-C). Our analysis exclusively reveals that the three LO phonon modes have significant contributions from the Pb and Se atomic vibrations of the PbSe sublattice. However, the atomic vibration associated with the $CsPbBr_3$ sublattice within the heterostructure is almost frozen.

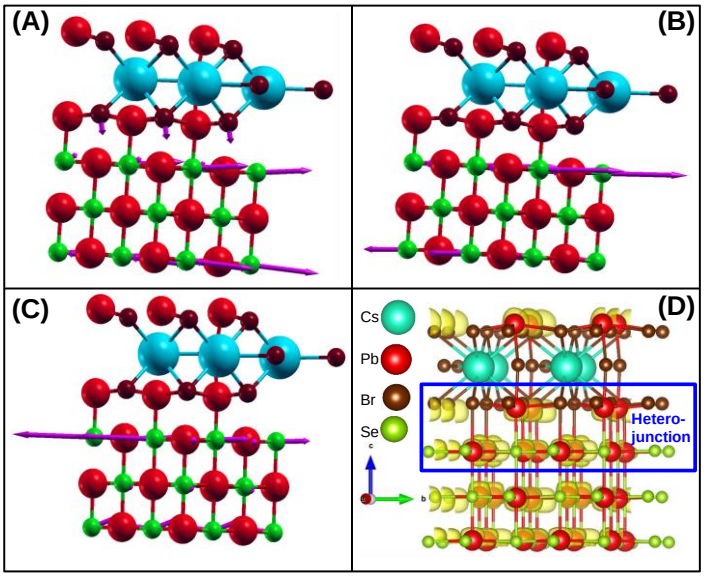

Figure 5.10. *Phonon eigenvectors at Γ point for (a) LO_1 mode, (b) LO_2 mode, (c) LO_3 mode; and (d) electron localization function (ELF) of $CsPbBr_3$/PbSe hetero-structure. Here, Cs, Pb, Br, Se atoms are indicated by cyan, red, brown, and green colors, respectively, while dark magenta arrows represent the atomic vibration direction.*

In contrast, it has been observed that the atoms vibrating in the phonon propagation direction signify LA phonon mode. The LO phonon mode is mainly contributed by the Cs and Pb-Br in-plane atomic vibrations in the opposite direction pure $CsPbBr_3$ NCs (Figure 5.11).

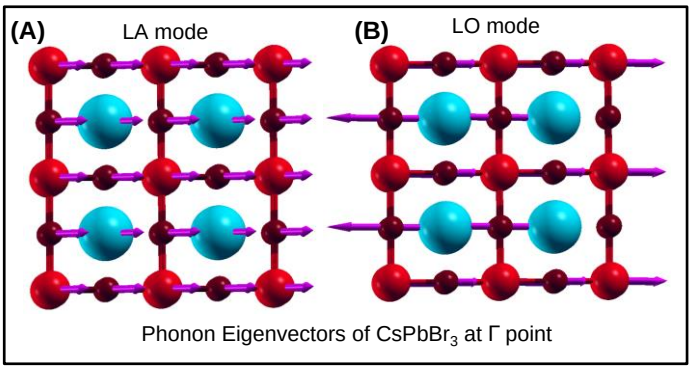

Figure 5.11. *Phonon Eigenvectors of $CsPbBr_3$ at Γ-point are represented for (A) LA mode (B) LO mode. Here, Cs, Pb, Br atoms are shown by cyan, red and brown colors. All the atoms vibrate along the phonon propagation direction in LA phonon mode, while Cs & Pb-Br vibrate along the opposite direction for LO mode at Γ-point. Dark magenta arrows represent the atomic vibration direction.*

Here, the important point to notice is that on one side, the LO phonon mode is mainly originating from Cs & Pb-Br vibration(s) for $CsPbBr_3$ NC. In contrast, the LO phonon modes

in the heterostructure have a significant contribution arising only from the PbSe sublattice. Notably, the difference in the LO phonon eigenvectors is solely responsible for creating the energy gap in the phonon spectra of the $CsPbBr_3$/PbSe heterojunctions. We have investigated the electron localization function (ELF) near the heterojunction regime to understand further the reason behind the immense up-lifting of LO phonon mode. The ELF with the iso-surface value ~ 0.9 has been demonstrated for heterostructure in Figure 5.10 D, where yellow lobes represent the localization of charges. We observe that the spherically symmetric lone-pair ($6s^2$) associated with Pb atoms is asymmetrically shifted and oriented towards the junction from both $CsPbBr_3$ and PbSe sub-lattices (Figure 5.10 D).

Moreover, the ELF plot in the same figure also shows that the Se-p_z orbital gets localized and forms a dumbbell shape structure in the heterojunction (indicated by the box in blue color), which helps to accumulate higher electronic charge density. Furthermore, we also analyzed the charge density plot quite closely and found an appearance of weak bonding between Pb from $CsPbBr_3$ and Se from PbSe in the interface region (Figure 5.12). Due to these weak bonding effects and the redistribution of charge density near the heterojunction, the LO phonon modes get perturbed in the heterostructure through increased values of the Born effective charge and dielectric constant. This manifestation essentially leads to the up-conversion of LO modes to the higher energy in the phonon dispersion spectra in the heterostructure. In this way, we achieve a feasible mechanism to harness retarded HC cooling via localizing charge density near the interfaces.

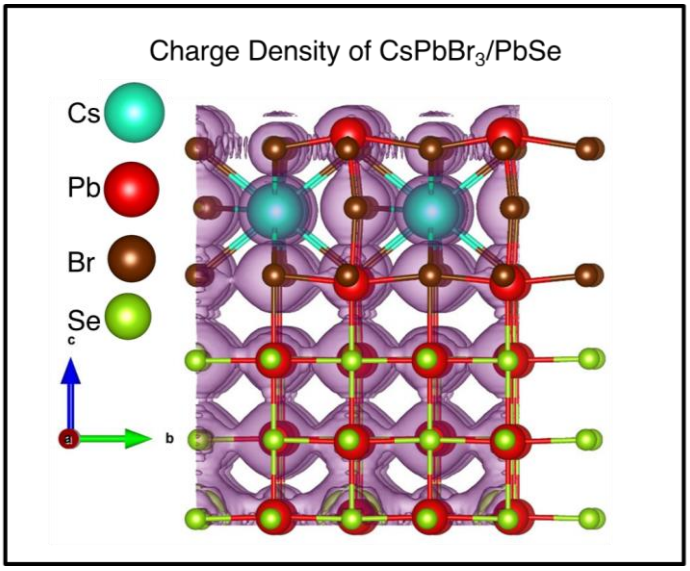

Figure 5.12. *Charge density plot of $CsPbBr_3$/PbSe heterostructure (isosurface value ~ 0.028).*

5.2.5. Extraction of HC relaxation time by Global fitting of TA spectra

Finally, we have measured the HC cooling lifetime of the samples to further confirm the slow relaxation rate in the case of the heterostructure. Generally, the HC cooling time of semiconductor NCs has measured from the rise time of GSB signal probed at the band edge position.[30] The buildup (rise time) of the GSB signal and the PIA decay indicates the average relaxation time of photo-excited HCs from the high energy level to the band-edge.[29, 45, 48] The PIA decay overlaps with GSB growth dynamics for $CsPbBr_3$ and $CsPbBr_3$/PbSe heterostructure. We thus determine the time constants of the HC cooling process via global fitting of the TA spectra using a two-component sequential decay model (where lifetimes are set as global variables), yielding a more accurate fit of time constants.[29, 44, 55, 56] This process generates the spectra of individual excited-state species (so-called evolution-associated difference spectra, EADS) with their corresponding lifetime. Figure 5.13 A shows the Global fitting of TA spectra produces a fast component (EADS1) and a slow component (EADS2) for both the samples at 3.10 eV excitation (n_0~1.79 ×10^{17} cm^{-3}).

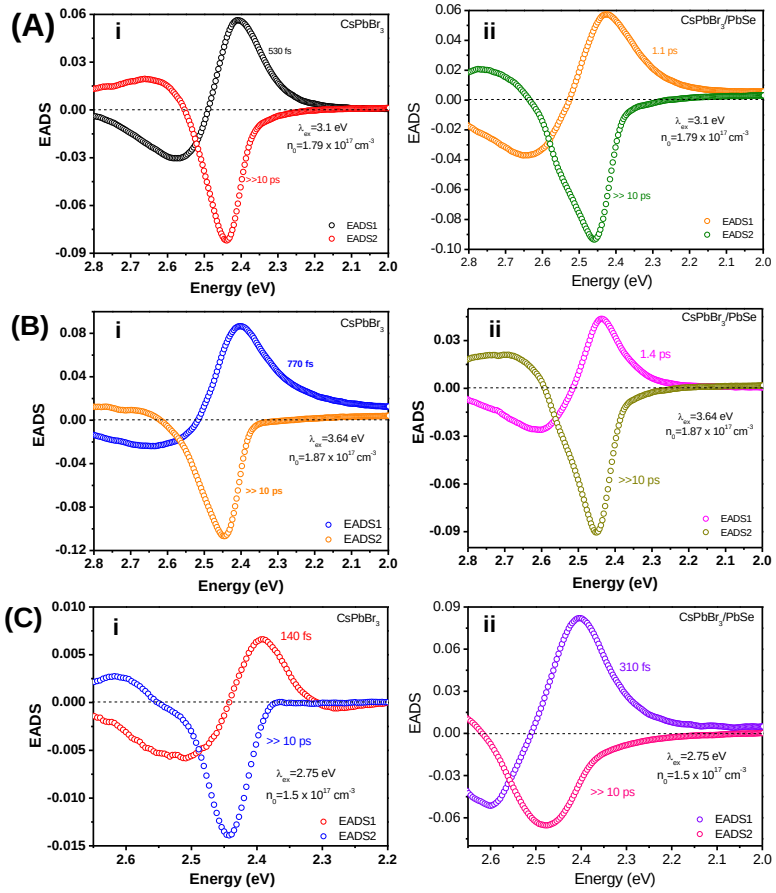

Figure 5.13. *TA spectra with evolution associated spectral (EAS) component derived from singular value decomposition (SVD) based global fitting at excitation (A) 3.1 eV, (B) 3.64 eV and (C) 2.75 ev for (i) $CsPbBr_3$ NCs and (ii) $CsPbBr_3$/PbSe NCs, respectively.*

The slow component (EADS2) arises due to the band edge-related spectral signature. In contrast, the fast component (EADS1) with slightly blue-shifted GSB has been ascribed to the relaxation of HCs.[29, 30] Figure 5.13 (B-C) shows the global fitting of TA spectra with corresponding evolution associated spectral (EAS) signature and their associated lifetimes at 3.64 and 2.75 eV excitation, respectively. The normalized GSB growth dynamics for both the samples at 3.10 eV excitation shows faster rise time faster rise time for pure $CsPbBr_3$ NCs (530±20 fs) as compared to $CsPbBr_3$/PbSe heterostructure (1.1±0.03 ps), suggesting slow HC cooling occurs upon formation of the heterostructure (Figure 5.14 A).

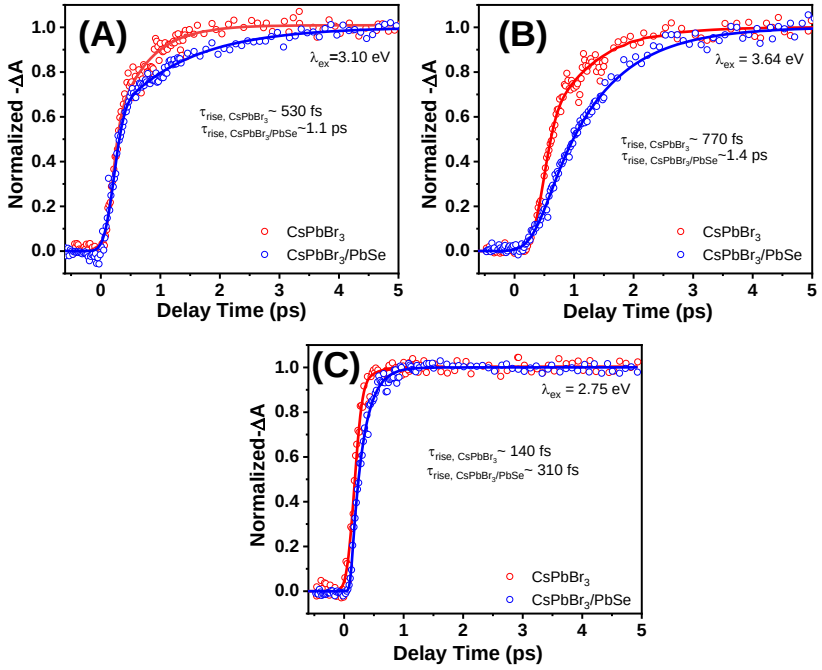

Figure 5.14. *Bleach formation kinetics of TA signal for $CsPbBr_3$ and $CsPbBr_3$/PbSe Heteo-structure at the band edge positions (i.e. 505 nm) upon excitation of (a) 3.10 eV (n_0~ 1.79×10^{17} cm^{-3}), (b) 3.64 eV (n_0~ 1.86×10^{17} cm^{-3}) and (c) 2.75 eV (n_0~ 1.5×10^{17} cm^{-3}), respectively.*

It is known that HC relaxation time strongly influences the initial excitation energy and carrier density.[29] We thus examined the HC cooling dynamics at 3.64 eV (corresponding to excess energy of 1.19 eV) and 2.75 eV photoexcitation (corresponding to excess energy of 0.3 eV) with initial n_0 of 1.86×10^{17} and 1.5×10^{17} cm^{-3}, respectively, to study the effect of the initial excess energy of HCs (Figure 5.14 B, C). Interestingly HC lifetime increases from 770±40 fs (for pure $CsPbBr_3$ NCs) to 1.4±0.06 (for $CsPbBr_3$/PbSe heterostructure) at 3.64 eV excitation (Figure 5.14 B). Also, the HC lifetime is slower for the heterostructure (310±30 fs) than pure perovskite NCs (140±20 fs) at 2.75 eV excitation (Figure 5.14 C). Notably, The

enhancement of HC cooling time with increasing the excess energy of HCs is consistent with the previous reports for other LHP NCs.[29, 30] Figure 5.15 shows the effect of pump fluence (from 3.58×10^{17} to 1.27×10^{18} cm^{-3}) on the HC relaxation time at 3.10 eV excitation.

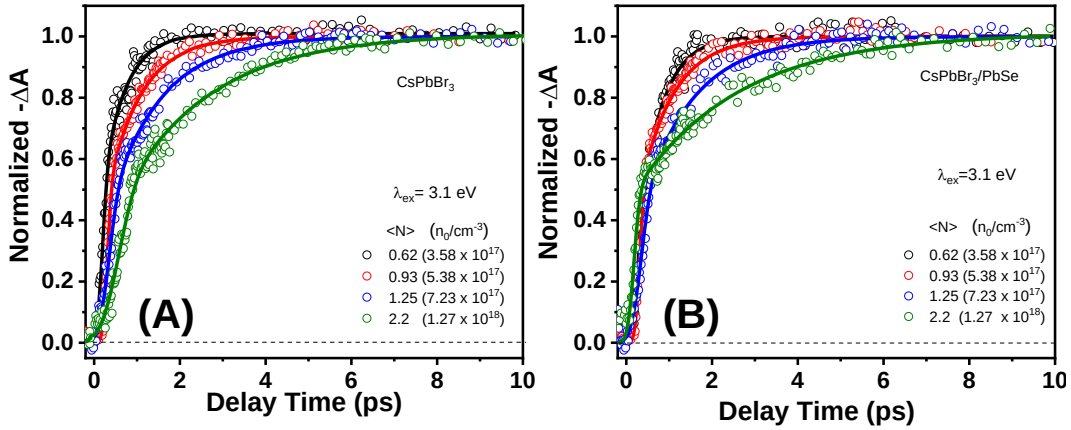

Figure 5.15. *Normalized GSB dynamics probed at band edge (2.45 eV) for (a) $CsPbBr_3$ NCs and (B) $CsPbBr_3$/PbSe NCs with excitation 3.10 eV (400 nm) with varying the carrier density from 3.58×10^{17} cm^{-3} to 1.27×10^{18} cm^{-3}*

Interestingly, HC cooling time is significantly enhanced with increasing the exciton fluence for both the NCs (Table 5.1).

Table 5.1. *Variation of HC cooling time of $CsPbBr_3$ NCs and $CsPbBr_3$/PbSe heterostructures with an increase of pump fluence*

Carrier Density (n_0)	$CsPbBr_3$	$CsPbBr_3$/PbSe
1.79×10^{17} cm^{-3}	530±20 fs	1100±30 fs
3.58×10^{17} cm^{-3}	750± 35 fs	1280±20 fs
5.38×10^{17} cm^{-3}	1120± 40 fs	1670±40 fs
7.23×10^{17} cm^{-3}	1400± 50 fs	1930±60 fs
1.27×10^{18} cm^{-3}	1750±50 fs	2650±50 fs

However, HC relaxation time is much slower for $CsPbBr_3$/PbSe heterostructure than pure $CsPbBr_3$ NCs at comparable pump fluence. The above discussions reveal that the HC cooling time of $CsPbBr_3$ NCs can be substantially retarded by the formation of $CsPbBr_3$/PbSe heterostructure.

5.3. Conclusions

In conclusion, this study presents a deep understanding of ultrafast HC cooling dynamics of metal halide perovskite using ultrafast transient absorption spectroscopy, carrier-phonon scattering model, and the first-principles calculations. We have synthesized $CsPbBr_3$/PbSe heterostructure with the motive of tuning the HC cooling dynamics at low carrier density. The transient absorption measurements reveal two times slower HC relaxation (from 770 fs to 1.4 ps) and much higher initial HC temperature, T_C (1663 K, compared to 900 K) for the heterostructure compared to pure $CsPbBr_3$ at 3.64 eV excitation, under 1.86×10^{17} cm^{-3} carrier density. The fitting of HC energy loss rate in an electron- LO phonon coupling model also suggests a much slower decay time of LO phonon through the Klemens channel after heterostructure formation. The first-principles calculation confirms a large energy gap between the LO and LA phonon modes in the heterostructure due to the localization of charge density near the heterojunction. It is the main reason behind such retardation of HC cooling. Our findings provide a new and logical insight to a relatively less explored way-out to slow down the HC cooling in perovskites which will be helpful to boost the efficiency of HC solar cells.

5.4. References

(1) Paul, K. K.; Kim, J.-H.; Lee, Y. H., Hot Carrier Photovoltaics in van der Waals Heterostructures. *Nat. Rev. Phys.* **2021,** *3* (3), 178-192.

(2) Nozik, A. J., Spectroscopy and Hot Electron Relaxation Dynamics in Semiconductor Quantum Wells and Quantum Dots. *Annu. Rev. Phys. Chem.* **2001,** *52* (1), 193-231.

(3) Tisdale, W. A.; Williams, K. J.; Timp, B. A.; Norris, D. J.; Aydil, E. S.; Zhu, X.-Y., Hot-Electron Transfer from Semiconductor Nanocrystals. *Science* **2010,** *328* (5985), 1543-1547.

(4) Ross, R. T.; Nozik, A. J., Efficiency of Hot-Carrier Solar Energy Converters. *J. Appl. Phys.* **1982,** *53* (5), 3813-3818.

(5) Shockley, W.; Queisser, H. J., Detailed Balance Limit of Efficiency of p-n Junction Solar Cells. *J. Appl. Phys.* **1961,** *32* (3), 510-519.

(6) Knight, M. W.; Sobhani, H.; Nordlander, P.; Halas, N. J., Photodetection with Active Optical Antennas. *Science* **2011,** *332* (6030), 702-704.

(7) Lao, Y.-F.; Perera, A. G. U.; Li, L. H.; Khanna, S. P.; Linfield, E. H.; Liu, H. C., Tunable Hot-Carrier Photodetection beyond the Bandgap Spectral Limit. *Nat. Photonics* **2014,** *8* (5), 412-418.

(8) Wen, Y.-C.; Chen, C.-Y.; Shen, C.-H.; Gwo, S.; Sun, C.-K., Ultrafast Carrier Thermalization in InN. *Appl. Phys. Lett.* **2006,** *89* (23), 232114.

(9) Cooney, R. R.; Sewall, S. L.; Anderson, K. E. H.; Dias, E. A.; Kambhampati, P., Breaking the Phonon Bottleneck for Holes in Semiconductor Quantum Dots. *Phys. Rev. Lett.* **2007,** *98* (17), 177403.

(10) Suntrup, D. J.; Gupta, G.; Li, H.; Keller, S.; Mishra, U. K., Measurement of the Hot Electron Mean Free Path and the Momentum Relaxation Rate in GaN. *Appl. Phys. Lett.* **2014,** *105* (26), 263506.

(11) Rosenwaks, Y.; Hanna, M. C.; Levi, D. H.; Szmyd, D. M.; Ahrenkiel, R. K.; Nozik, A. J., Hot-Carrier Cooling in GaAs: Quantum Wells Versus Bulk. *Phys. Rev. B: Condens. Matter Mater. Phys.* **1993,** *48* (19), 14675-14678.

(12) Kahmann, S.; Loi, M. A., Hot Carrier Solar Cells and the Potential of Perovskites for Breaking the Shockley–Queisser Limit. *J. Mater. Chem. C* **2019,** *7* (9), 2471-2486.

(13) Kojima, A.; Teshima, K.; Shirai, Y.; Miyasaka, T., Organometal Halide Perovskites as Visible-Light Sensitizers for Photovoltaic Cells. *J. Am. Chem. Soc.* **2009,** *131* (17), 6050-6051.

(14) Zhou, H.; Chen, Q.; Li, G.; Luo, S.; Song, T.-b.; Duan, H.-S.; Hong, Z.; You, J.; Liu, Y.; Yang, Y., Interface Engineering of Highly Efficient Perovskite Solar Cells. *Science* **2014,** *345* (6196), 542-546.

(15) Stranks, S. D.; Eperon, G. E.; Grancini, G.; Menelaou, C.; Alcocer, M. J. P.; Leijtens, T.; Herz, L. M.; Petrozza, A.; Snaith, H. J., Electron-Hole Diffusion Lengths Exceeding 1 Micrometer in an Organometal Trihalide Perovskite Absorber. *Science* **2013,** *342* (6156), 341-344.

(16) Niesner, D.; Zhu, H.; Miyata, K.; Joshi, P. P.; Evans, T. J. S.; Kudisch, B. J.; Trinh, M. T.; Marks, M.; Zhu, X. Y., Persistent Energetic Electrons in Methylammonium Lead Iodide Perovskite Thin Films. *J. Am. Chem. Soc.* **2016,** *138* (48), 15717-15726.

(17) Guo, Z.; Wan, Y.; Yang, M.; Snaider, J.; Zhu, K.; Huang, L., Long-Range Hot-Carrier Transport in Hybrid Perovskites Visualized by Ultrafast Microscopy. *Science* **2017,** *356* (6333), 59-62.

(18) Li, M.; Fu, J.; Xu, Q.; Sum, T. C., Slow Hot-Carrier Cooling in Halide Perovskites: Prospects for Hot-Carrier Solar Cells. *Adv. Mater.* **2019,** *31* (47), 1802486.

(19) Nie, Z.; Gao, X.; Ren, Y.; Xia, S.; Wang, Y.; Shi, Y.; Zhao, J.; Wang, Y., Harnessing Hot Phonon Bottleneck in Metal Halide Perovskite Nanocrystals via Interfacial Electron–Phonon Coupling. *Nano Lett.* **2020,** *20* (6), 4610-4617.

(20) Yang, Y.; Ostrowski, D. P.; France, R. M.; Zhu, K.; van de Lagemaat, J.; Luther, J. M.; Beard, M. C., Observation of a Hot-Phonon Bottleneck in Lead-Iodide Perovskites. *Nat. Photonics* **2016,** *10* (1), 53-59.

(21) Fu, J.; Xu, Q.; Han, G.; Wu, B.; Huan, C. H. A.; Leek, M. L.; Sum, T. C., Hot Carrier Cooling Mechanisms in Halide Perovskites. *Nat. Commun.* **2017,** *8* (1), 1300.

(22) Manser, J. S.; Kamat, P. V., Band Filling with Free Charge Carriers in Organometal Halide Perovskites. *Nat. Photonics* **2014,** *8* (9), 737-743.

(23) Hintermayr, V. A.; Polavarapu, L.; Urban, A. S.; Feldmann, J., Accelerated Carrier Relaxation Through Reduced Coulomb Screening in Two-Dimensional Halide Perovskite Nanoplatelets. *ACS Nano* **2018,** *12* (10), 10151-10158.

(24) Zhu, H.; Miyata, K.; Fu, Y.; Wang, J.; Joshi, P. P.; Niesner, D.; Williams, K. W.; Jin, S.; Zhu, X. Y., Screening in Crystalline Liquids Protects Energetic Carriers in Hybrid Perovskites. *Science* **2016,** *353* (6306), 1409-1413.

(25) Yang, J.; Wen, X.; Xia, H.; Sheng, R.; Ma, Q.; Kim, J.; Tapping, P.; Harada, T.; Kee, T. W.; Huang, F., et al., Acoustic-Optical Phonon Up-Conversion and Hot-Phonon Bottleneck in Lead-Halide Perovskites. *Nat. Commun.* **2017,** *8* (1), 14120.

(26) Hopper, T. R.; Gorodetsky, A.; Frost, J. M.; Müller, C.; Lovrincic, R.; Bakulin, A. A., Ultrafast Intraband Spectroscopy of Hot-Carrier Cooling in Lead-Halide Perovskites. *ACS Energy Lett.* **2018,** *3* (9), 2199-2205.

(27) Papagiorgis, P.; Protesescu, L.; Kovalenko, M. V.; Othonos, A.; Itskos, G., Long-Lived Hot Carriers in Formamidinium Lead Iodide Nanocrystals. *J. Phys. Chem. C* **2017,** *121* (22), 12434-12440.

(28) Li, M.; Bhaumik, S.; Goh, T. W.; Kumar, M. S.; Yantara, N.; Grätzel, M.; Mhaisalkar, S.; Mathews, N.; Sum, T. C., Slow Cooling and Highly Efficient Extraction of Hot Carriers in Colloidal Perovskite Nanocrystals. *Nat. Commun.* **2017,** *8* (1), 14350.

(29) Chen, J.; Messing, M. E.; Zheng, K.; Pullerits, T., Cation-Dependent Hot Carrier Cooling in Halide Perovskite Nanocrystals. *J. Am. Chem. Soc.* **2019,** *141* (8), 3532-3540.

(30) Chung, H.; Jung, S. I.; Kim, H. J.; Cha, W.; Sim, E.; Kim, D.; Koh, W.-K.; Kim, J., Composition-Dependent Hot Carrier Relaxation Dynamics in Cesium Lead Halide ($CsPbX_3$, X=Br and I) Perovskite Nanocrystals. *Angew. Chem. Int. Ed.* **2017,** *56* (15), 4160-4164.

(31) Madjet, M. E.; Berdiyorov, G. R.; El-Mellouhi, F.; Alharbi, F. H.; Akimov, A. V.; Kais, S., Cation Effect on Hot Carrier Cooling in Halide Perovskite Materials. *J. Phys. Chem. Lett.* **2017,** *8* (18), 4439-4445.

(32) Wei, Q.; Yin, J.; Bakr, O. M.; Wang, Z.; Wang, C.; Mohammed, O. F.; Li, M.; Xing, G., Effect of Zinc-Doping on the Reduction of the Hot-Carrier Cooling Rate in Halide Perovskites. *Angew. Chem. Int. Ed.* **2021,** *60* (19), 10957-10963.

(33) Huang, H.; Bodnarchuk, M. I.; Kershaw, S. V.; Kovalenko, M. V.; Rogach, A. L., Lead Halide Perovskite Nanocrystals in the Research Spotlight: Stability and Defect Tolerance. *ACS Energy Letters* **2017,** *2* (9), 2071-2083.

(34) Yang, D.; Li, X.; Zhou, W.; Zhang, S.; Meng, C.; Wu, Y.; Wang, Y.; Zeng, H., $CsPbBr_3$ Quantum Dots 2.0: Benzenesulfonic Acid Equivalent Ligand Awakens Complete Purification. *Adv. Mater.* **2019,** *31* (30), 1900767.

(35) Sun, C.; Zhang, Y.; Ruan, C.; Yin, C.; Wang, X.; Wang, Y.; Yu, W. W., Efficient and Stable White LEDs with Silica-Coated Inorganic Perovskite Quantum Dots. *Adv. Mater.* **2016,** *28* (45), 10088-10094.

(36) Loiudice, A.; Strach, M.; Saris, S.; Chernyshov, D.; Buonsanti, R., Universal Oxide Shell Growth Enables in Situ Structural Studies of Perovskite Nanocrystals during the Anion Exchange Reaction. *J. Am. Chem. Soc.* **2019,** *141* (20), 8254-8263.

(37) Huang, H.; Chen, B.; Wang, Z.; Hung, T. F.; Susha, A. S.; Zhong, H.; Rogach, A. L., Water Resistant $CsPbX_3$ Nanocrystals Coated with Polyhedral Oligomeric Silsesquioxane and Their Use as Solid State Luminophores in All-Perovskite White Light-Emitting Devices. *Chem. Sci.* **2016,** *7* (9), 5699-5703.

(38) Hou, S.; Guo, Y.; Tang, Y.; Quan, Q., Synthesis and Sabilization of Colloidal Perovskite Nanocrystals by Multidentate Polymer Micelles. *ACS Appl. Mater. Interfaces* **2017,** *9* (22), 18417-18422.

(39) Wang, S.; Bi, C.; Portniagin, A.; Yuan, J.; Ning, J.; Xiao, X.; Zhang, X.; Li, Y. Y.; Kershaw, S. V.; Tian, J., et al., $CsPbI_3$/PbSe Heterostructured Nanocrystals for High-Efficiency Solar Cells. *ACS Energy Lett.* **2020,** *5* (7), 2401-2410.

(40) Zhang, X.; Lu, M.; Zhang, Y.; Wu, H.; Shen, X.; Zhang, W.; Zheng, W.; Colvin, V. L.; Yu, W. W., PbS Capped $CsPbI_3$ Nanocrystals for Efficient and Stable Light-Emitting Devices Using p–i–n Structures. *ACS Cent. Sci.* **2018,** *4* (10), 1352-1359.

(41) Zhang, J.; Liu, X.; Jiang, P.; Chen, H.; Wang, Y.; Ma, J.; Zhang, R.; Yang, F.; Wang, M.; Zhang, J., et al., Red-Emitting $CsPbBrI_2$/PbSe Heterojunction Nanocrystals with High Luminescent Efficiency and Stability for Bright Light-Emitting Diodes. *Nano Energy* **2019,** *66*, 104142.

(42) Gao, L.; Quan, L. N.; García de Arquer, F. P.; Zhao, Y.; Munir, R.; Proppe, A.; Quintero-Bermudez, R.; Zou, C.; Yang, Z.; Saidaminov, M. I., et al., Efficient Near-Infrared Light-Emitting Diodes Based on Quantum Dots in Layered Perovskite. *Nat. Photonics* **2020,** *14* (4), 227-233.

(43) Protesescu, L.; Yakunin, S.; Bodnarchuk, M. I.; Krieg, F.; Caputo, R.; Hendon, C. H.; Yang, R. X.; Walsh, A.; Kovalenko, M. V., Nanocrystals of Cesium Lead Halide Perovskites ($CsPbX_3$, X = Cl, Br, and I): Novel Optoelectronic Materials Showing Bright Emission with Wide Color Gamut. *Nano Lett.* **2015,** *15* (6), 3692-3696.

(44) Ghosh, G.; Jana, B.; Sain, S.; Ghosh, A.; Patra, A., Influence of Shape on the Carrier Relaxation Dynamics of $CsPbBr_3$ Perovskite Nanocrystals. *Phys. Chem. Chem. Phys.* **2019,** *21* (35), 19318-19326.

(45) Wu, K.; Liang, G.; Shang, Q.; Ren, Y.; Kong, D.; Lian, T., Ultrafast Interfacial Electron and Hole Transfer from $CsPbBr_3$ Perovskite Quantum Dots. *J. Am. Chem. Soc.* **2015,** *137* (40), 12792-12795.

(46) Marjit, K.; Ghosh, G.; Ghosh, S.; Sain, S.; Ghosh, A.; Patra, A., Structural Analysis and Carrier Relaxation Dynamics of 2D $CsPbBr_3$ Nanoplatelets. *J. Phys. Chem. C* **2021,** *125* (22), 12214-12223.

(47) Ghosh, G.; Dutta, A.; Ghosh, A.; Ghosh, S.; Patra, A., Ultrafast Carrier Dynamics in 2D CdSe Nanoplatelets–$CsPbX_3$ Composites: Influence of the Halide Composition. *J. Phys. Chem. C* **2020,** *124* (18), 10252-10260.

(48) Ghosh, G.; Marjit, K.; Ghosh, S.; Ghosh, A.; Ahammed, R.; De Sarkar, A.; Patra, A., Hot Hole Cooling and Transfer Dynamics from Lead Halide Perovskite Nanocrystals Using Porphyrin Molecules. *J. Phys. Chem. C* **2021,** *125* (10), 5859-5869.

(49) Klimov, V. I.; Mikhailovsky, A. A.; McBranch, D. W.; Leatherdale, C. A.; Bawendi, M. G., Quantization of Multiparticle Auger Rates in Semiconductor Quantum Dots. *Science* **2000,** *287* (5455), 1011-1013.

(50) Klimov, V.; Haring Bolivar, P.; Kurz, H., Hot-Phonon Effects in Femtosecond Luminescence Spectra of Electron-Hole Plasmas in CdS. *Phys. Rev. B: Condens. Matter Mater. Phys.* **1995,** *52* (7), 4728-4731.

(51) Kawai, H.; Giorgi, G.; Marini, A.; Yamashita, K., The Mechanism of Slow Hot-Hole Cooling in Lead-Iodide Perovskite: First-Principles Calculation on Carrier Lifetime from Electron–Phonon Interaction. *Nano Lett.* **2015,** *15* (5), 3103-3108.

(52) König, D.; Casalenuovo, K.; Takeda, Y.; Conibeer, G.; Guillemoles, J. F.; Patterson, R.; Huang, L. M.; Green, M. A., Hot Carrier Solar Cells: Principles, Materials and Design. *Phys. E: Low-Dimens. Syst. Nanostructures* **2010,** *42* (10), 2862-2866.

(53) Liao, M.; Shan, B.; Li, M., In Situ Raman Spectroscopic Studies of Thermal Stability of All-Inorganic Cesium Lead Halide ($CsPbX_3$, X = Cl, Br, I) Perovskite Nanocrystals. *J. Phys. Chem. Lett.* **2019,** *10* (6), 1217-1225.

(54) Wang, L.; Chen, Z.; Liang, G.; Li, Y.; Lai, R.; Ding, T.; Wu, K., Observation of a Phonon Bottleneck in Copper-Doped Colloidal Quantum Dots. *Nat. Commun.* **2019,** *10* (1), 4532.

(55) van Stokkum, I. H. M.; Larsen, D. S.; van Grondelle, R., Global and Target Analysis of Time-Resolved Spectra. *Biochim. Biophys. Acta* **2004,** *1657* (2), 82-104.

(56) Ghosh, S.; Ghosh, A.; Ghosh, G.; Marjit, K.; Patra, A., Deciphering the Relaxation Mechanism of Red-Emitting Carbon Dots Using Ultrafast Spectroscopy and Global Target Analysis. *J. Phys. Chem. Lett.* **2021,** *12* (33), 8080-8087.

(57) Snellenburg, J. J.; Laptenok, S.; Seger, R.; Mullen, K. M.; van Stokkum, I. H. M., Glotaran:A Java-Based Graphical User Interface for the R Package TIMP. *J. Stat. Softw.* **2012,** *49* (3), 1-22.

(58) Blöchl, P. E., Projector Augmented-Wave Method. *Phys. Rev. B* **1994,** *50* (24), 17953-17979.

(59) Perdew, J. P.; Burke, K.; Ernzerhof, M., Generalized Gradient Approximation Made Simple. *Phys. Rev. Lett.* **1996,** *77* (18), 3865-3868.

(60) Perdew, J. P.; Ruzsinszky, A.; Csonka, G. I.; Vydrov, O. A.; Scuseria, G. E.; Constantin, L. A.; Zhou, X.; Burke, K., Restoring the Density-Gradient Expansion for Exchange in Solids and Surfaces. *Phys. Rev. Lett.* **2008,** *100* (13), 136406.

(61) Perdew, J. P.; Burke, K.; Wang, Y., Generalized Gradient Approximation for the Exchange-Correlation Hole of a Many-Electron System. *Phys. Rev. B* **1996,** *54* (23), 16533-16539.

(62) Lee, W.; Li, H.; Wong, A. B.; Zhang, D.; Lai, M.; Yu, Y.; Kong, Q.; Lin, E.; Urban, J. J.; Grossman, J. C., et al., Ultralow Thermal Conductivity in All-Inorganic Halide Perovskites. *Proc. Natl. Acad. Sci. U.S.A.* **2017,** *114* (33), 8693-8697.

(63) Lanigan-Atkins, T.; He, X.; Krogstad, M. J.; Pajerowski, D. M.; Abernathy, D. L.; Xu, G. N. M. N.; Xu, Z.; Chung, D. Y.; Kanatzidis, M. G.; Rosenkranz, S., et al., Two-Dimensional Overdamped Fluctuations of the Soft Perovskite Lattice in $CsPbBr_3$. *Nat. Mater.* **2021,** *20* (7), 977-983.

(64) Guo, P.; Xia, Y.; Gong, J.; Stoumpos, C. C.; McCall, K. M.; Alexander, G. C. B.; Ma, Z.; Zhou, H.; Gosztola, D. J.; Ketterson, J. B., et al., Polar Fluctuations in Metal Halide Perovskites Uncovered by Acoustic Phonon Anomalies. *ACS Energy Lett.* **2017,** *2* (10), 2463-2469.

(65) López, C. A.; Abia, C.; Alvarez-Galván, M. C.; Hong, B.-K.; Martínez-Huerta, M. V.; Serrano-Sánchez, F.; Carrascoso, F.; Castellanos-Gómez, A.; Fernández-Díaz, M. T.; Alonso, J. A., Crystal Structure Features of $CsPbBr_3$ Perovskite Prepared By Mechanochemical Synthesis. *ACS Omega* **2020,** *5* (11), 5931-5938.

Chapter 6

Halide Composition Dependent Ultrafast Electron Transfer in 2D CdSe Nanoplatelets-$CsPbX_3$ Composites

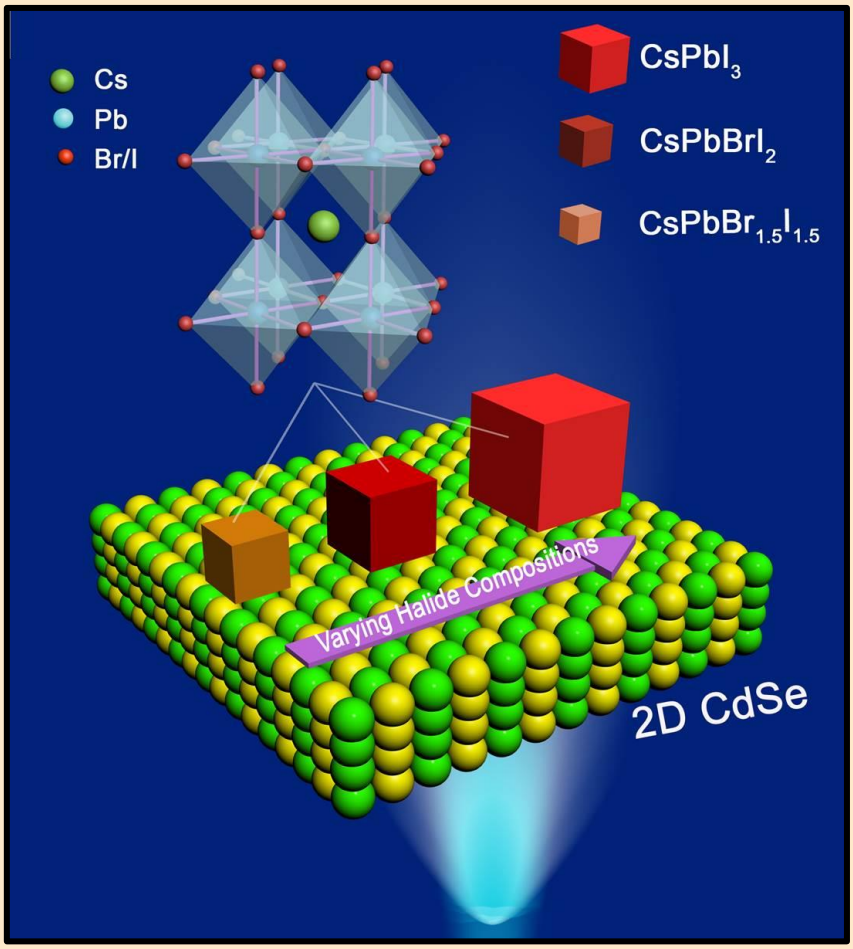

6.1. Introduction

Hetero-structured materials such as semiconductor-metal, inorganic-organic, and core-shell structures have been given significant attention for photo-catalysis and photovoltaic applications due to efficient charge separation.[1-5] Upon photo-excitation of such heterostructures, the efficient charge separation occurs due to a slow recombination process that enhances the lifetime of photo-generated carriers. Two-dimensional (2D) semiconductor nanoplatelets (NPLs) are now up-and-coming alternatives because of unique properties such as high electron-hole binding energy, giant oscillator strength, and enhanced absorption cross-section.[6-9] The efficient charge transfer happened in the CdSe–CdTe type-II NPL heterostructure where the electrons reside in CdSe and holes are in CdTe.[10] CdS NPLs/Pt heterostructures produced hydrogen gas due to the ultrafast electron transfer from the CdS conduction band to Pt.[11] The influence of various dimensions of CdS NCs on photocatalytic properties is reported and the most efficient system is 2D CdS-2D rGO hybrid.[12] An ultrafast pump-probe transient spectroscopic study reveals that the hot electron and the ultrafast electron transfer processes occur in the 2D‑2D composite of CdSe NPLs and rGO.[13] Thus, the fundamental understanding of carrier relaxation dynamics of such heterostructures is essential for light-driven photovoltaics or photo-catalysis applications.[14-16] It is established that the extraction of the hot carrier and the ultrafast electron transfer are crucial for overcoming the Shockley-Quessier limit to enhance the solar energy conversion to electrical energy.[17-18] Theoretically, the efficiency of the solar cell can be improved to 67% by utilizing the excess energy of hot carriers.[19] Thus, the efficient extraction of carriers is very important for better performance of optoelectronic devices. It is found that the hot electron cooling relaxation varies with temperature in CdSe quantum wells (QWs) which plays a crucial role in several potential optoelectronic applications.[20]

Perovskite NCs have found to be potential materials for solar cell applications because of its extraordinary absorption coefficients, high photoluminescence quantum yield (PLQY), defect tolerant nature, etc.[21-28] Few strategies have been developed to design efficient devices such as solar cells, light-emitting diodes (LED), photovoltaic and photo-catalysis using perovskite NCs and 2D semiconductor NPLs hybrid structures.[29-33] Schaller et al. have investigated the influence of dimension of NCs on electron transfer rate in $CsPbBr_3$-CdSe hybrid, and they found the most efficient electron transfer occurs in 2D $CsPbBr_3$-CdSeNPLs composites.[34] Kim et al. have reported the hot carrier dynamics varies from 310 fs to 580 fs with changing the halide composition i.e. from $CsPbBr_3$ to $CsPbI_3$.[35] Fu et al. have

reported the fluence-dependent hot carrier cooling mechanism of $MAPbI_3$ NCs.[18] Thus, the designing of composites of 2D semiconducting materials with perovskite NCs is emerging for developing efficient optoelectronic applications. To our knowledge, there is no study on halide composition-dependent ultrafast electron transfer in CdSe NPLs/$CsPbX_3$ composites.

Herein, we have designed 2D layered CdSe NPLs - $CsPbX_3$ perovskite composites to understand the influence of halide composition of perovskite NCs on the electron transfer rate. Fluorescent up-conversion measurements and transient absorption spectroscopy (TAS) are being used to study composites' ultrafast electron transfer dynamics. Transient absorption spectroscopic study reveals that the ultrafast electron transfer from CdSe NPLs to perovskite NCs with increasing iodide composition of $CsPbX_3$ NCs is studied. Ultrafast electron transfer from CdSe NPLs to $CsPbX_3$ NCs confirms the enhancement of growth time of perovskite NCs in composites. Finally, we measured the photocurrent measurement of these composites CdSe NPLs-perovskite devices under visible light illumination to open up a new avenue in solar energy conversion. Such study is vital for the fundamental understanding of charge transfer dynamics and for designing efficient light-harvesting systems.

6.2. Results and Discussion

6.2.1. Structural analysis

Figure 6.1A shows the TEM images of CdSe NPLs, $CsPbBr_{1.5}I_{1.5}$, $CsPbBrI_2$, and $CsPbI_3$ NCs, respectively, and the corresponding high-resolution transmission electron microscopy (HRTEM) images are shown in the inset. The average lateral dimensions and the thickness of the 4 ML CdSe NPLs are 200±40 nm and 1.3 nm, respectively (inset of Figure. 6.1A-a). All the perovskite NCs exhibit a highly monodispersed cubic shape. The average edge length is found to be 9± 0.8 nm for $CsPbBr_{1.5}I_{1.5}$ (inset of Figure. 6.1A-b), 12±0.5 nm is for $CsPbBrI_2$ (inset of Figure. 6.1A-c) and 22±1 nm is for $CsPbI_3$ (inset of Figure 6.1A-d) which are consistent with previous results.[13, 36]

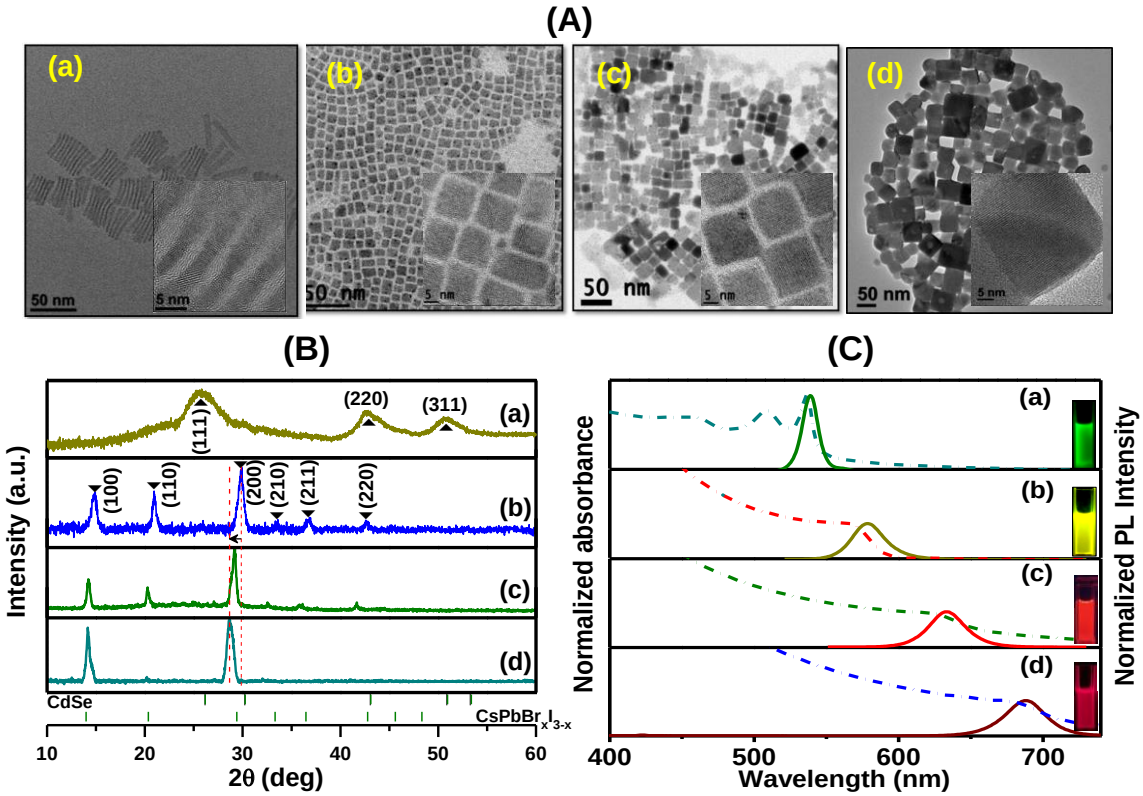

Figure 6.1. *(A) TEM and HRTEM (inset) images,(B) X-ray diffraction patterns and (C) normalized UV-Visible absorption spectra (dashed lines) and normalized PL spectra (solid lines) of (a) CdSe NPLs, (b) $CsPbBr_{1.5}I_{1.5}$, (c) $CsPbBrI_2$, and (d) $CsPbI_3$ NCs.*[37] *Reproduced with permission from reference 37 (Copyright 2020 American Chemical Society).*

The compositions of the perovskite NCs are investigated by energy-dispersive X-ray spectroscopy (EDS) (Figure 6.2).

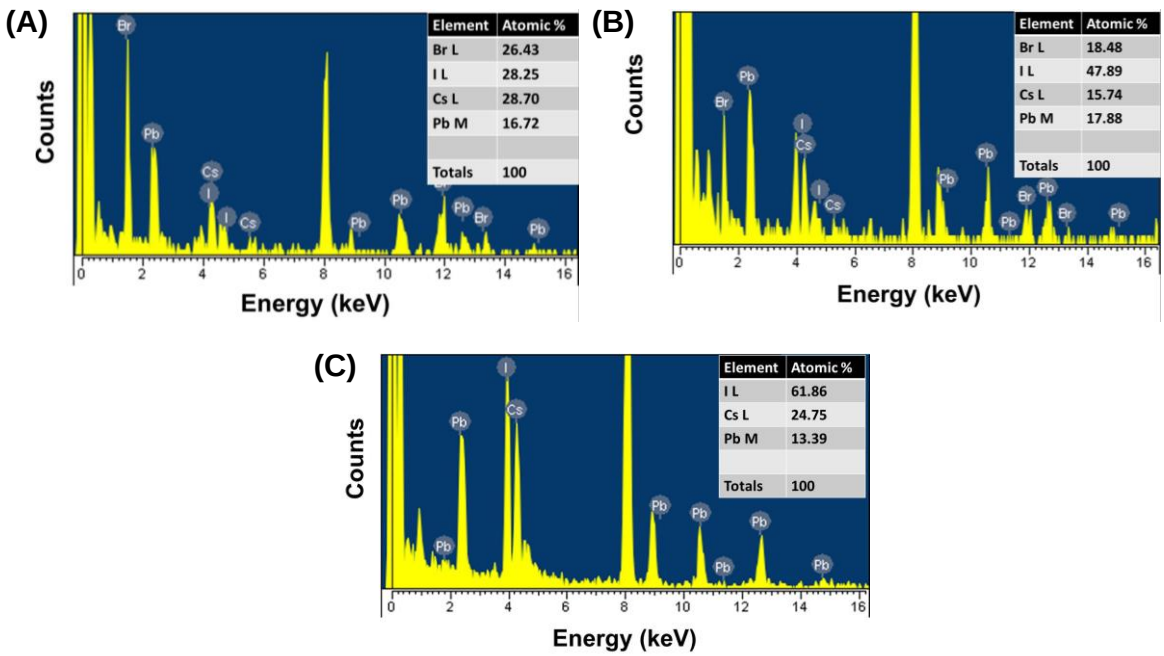

Figure 6.2. *EDS spectra and corresponding elemental analysis table (inset) of (A) $CsPbBr_{1.5}I_{1.5}$, (B) $CsPbBrI_2$ and (C) $CsPbI_3$ NCs.[37] Reproduced with permission from reference 37 (Copyright 2020 American Chemical Society).*

The formation of composites is confirmed from the TEM images of composites of CdSe-$CsPbX_3$ (Figure 6.3).

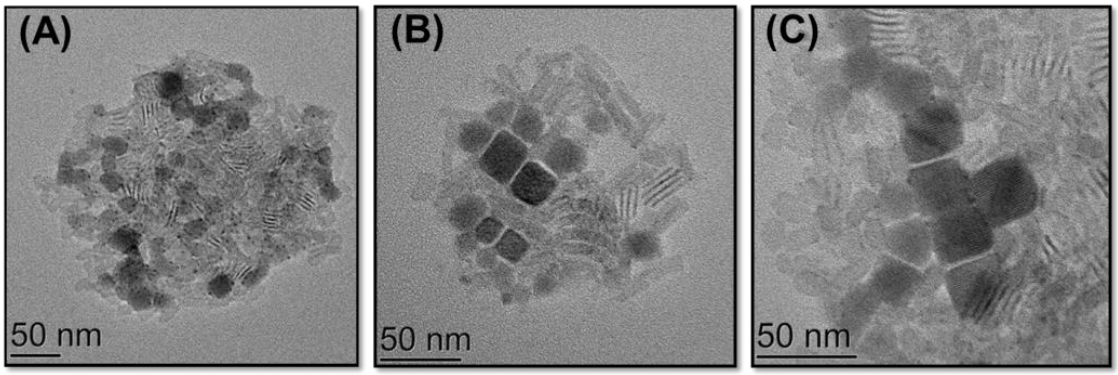

Figure 6.3. *TEM images of composites (A) CdSe-$CsPbBr_{1.5}I_{1.5}$, (B) CdSe-$CsPbBrI_2$ and (C) CdSe-$CsPbI_3$.[37] Reproduced with permission from reference 37 (Copyright 2020 American Chemical Society).*

Figure 6.1B-a shows the diffraction pattern of CdSe NPLs and Figure 6.1B (b-d) represents diffraction patterns of $CsPbBr_{1.5}I_{1.5}$, $CsPbBrI_2$ and $CsPbI_3$ NCs respectively. Analysis reveals that the crystal phase of CdSe NPLs is zinc blend, and the crystal phase of perovskite NCs is

cubic. A systematic shift of (200) plane towards lower angel (2θ) with increasing iodide composition of $CsPbX_3$ NCs indicates the change of lattice parameters.

6.2.2. Steady-state and time-resolved spectroscopy

The steady-state spectroscopic study of CdSe NPLs and all $CsPbX_3$ NCs is carried out at room temperature. The UV-visible absorption spectra are shown in dotted line, and the photoluminescence spectra are shown in solid line (Figure 6.1C). Insets show emission color under UV-light excitation (λ_{ex}=365 nm). Two absorption bands at 482 nm and 513 nm are observed for CdSe NPLs, which are due to the light hole (LH) and heavy hole (HH) excitonic transition to the conduction band, respectively (Figure 6.1C-a).[6] The PL band of CdSe NPLs is observed at 515 nm with a photoluminescence quantum yield (PLQY) of 12%. Figure 6.1C (b-d) shows the UV-visible absorption along with PL spectra of $CsPbBr_{1.5}I_{1.5}$, $CsPbBrI_2$ and $CsPbI_3$ NCs respectively. The excitonic absorption band at 569 nm and the emission band at 580 nm are observed for $CsPbBr_{1.5}I_{1.5}$ NCs. For $CsPbBrI_2$ NCs, the excitonic absorption and emission bands are found at 620 nm and 635 nm, respectively. The absorption and emission bands are at 678 nm and 688 nm for $CsPbI_3$ NCs. The red shifting of emission band with varying halide composition indicates that the bandgap of perovskite NCs changes with changing the composition.[38] The PLQY of $CsPbBr_{1.5}I_{1.5}$, $CsPbBrI_2$ and $CsPbI_3$ NCs are found to be 58%, 62% and 67%, respectively. In the case of composites, the PL quenching of CdSe NPLs (at 515 nm peak) is observed with increasing concentration (0-40 nM) of $CsPbX_3$NCs. To compare the PL quenching of CdSe NPLs in the presence of different perovskite NCs, we added a fixed amount (10 nM) of $CsPbX_3$ NCs with CdSe NPLs. The PL quenching of CdSe NPLs is found to be 51%, 67% and 94% for 10 nM $CsPbBr_{1.5}I_{1.5}$, $CsPbBrI_2$ and $CsPbI_3$ NCs, respectively which is composition dependent (Figure 6.4A). Stern-Volmer (SV) plot (inset of Figure 6.4A) is used to understand the PL quenching mechanism and the Stern-Volmer constants (K_{SV}) are found to be 1.06×10^8 M^{-1}, 1.46×10^8 $M^{-1}$and 5.18×10^8 M^{-1} for CdSe-$CsPbBr_{1.5}I_{1.5}$, CdSe-$CsPbBrI_2$ and CdSe-$CsPbI_3$ NCs, respectively; indicating strong interaction between CdSe NPLs and perovskite NCs. A time-resolved emission spectroscopic study has been carried out to understand the excited state dynamics of 2D CdSe NPLs in the presence of perovskite NCs.

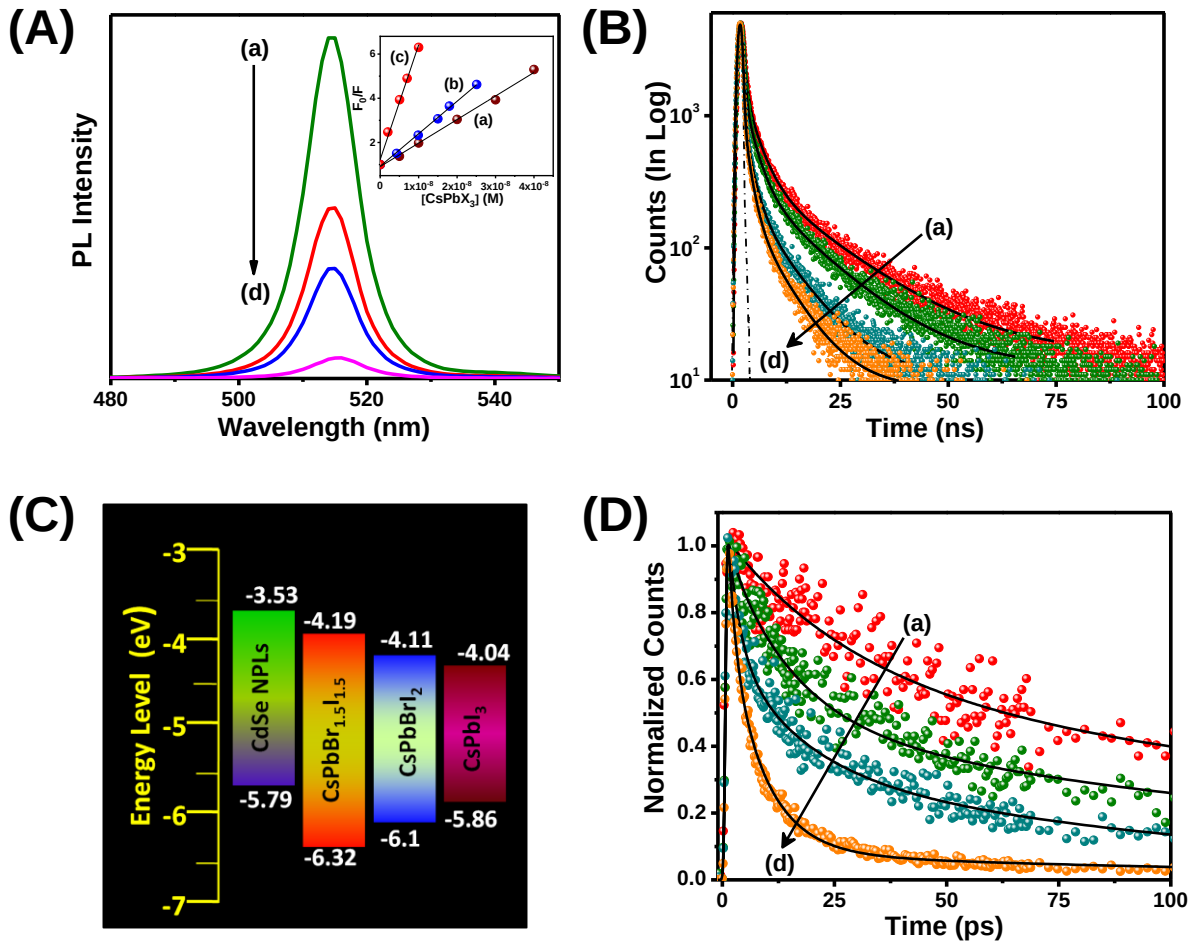

***Figure 6.4**. (A) PL quenching and Stern-Volmer plots of PL quenching against various concentration of $CsPbX_3$ NCs (inset). (B)TCSPC decay curves of CdSe NPLs in absence (a) and in presence of fixed concentration (10 nM) of $CsPbBr_{1.5}I_{1.5}$ (b), $CsPbBrI_2$ (c), and $CsPbI_3$ NCs (d)[λ_{ex}= 375 nm and λ_{em}= 515 nm], (C) Schematic energy level positions of CdSe NPLs and all three $CsPbX_3$ NCs and (D) Femtosecond fluorescence up-conversion decay profiles of CdSe NPLs in absence (a) and in presence of fixed concentration (10 nM) of $CsPbBr_{1.5}I_{1.5}$ (b), $CsPbBrI_2$ (c), and $CsPbI_3$ NCs (d) [λ_{ex}= 400 nm and λ_{em}= 515 nm].[37] Reproduced with permission from reference 37 (Copyright 2020 American Chemical Society).*

Figure 6.4B represents PL decay traces of CdSe NPLs in the absence and presence of all three $CsPbX_3$ NCs. All of the PL decay traces are fitted well with tri-exponential functions. The decay components of pure CdSe NPLs are (τ_1) 0.5 ns (85%), (τ_2) 2.9 ns (12%), and (τ_3) 16.2 ns (3%) with an average decay time of 1.2±0.23 ns. Here, τ_2 corresponds to band-edge recombination, and τ_1 and τ_3 are for trap state mediated non-radiative processes.[39] The average decay time of CdSe NPLs is shortened to 0.71±0.13 ns, 0.55±0.11 ns and 0.37±0.08 ns in presence of $CsPbBr_{1.5}I_{1.5}$, $CsPbBrI_2$ and $CsPbI_3$ NCs respectively (Table 6.1).

Table 6.1. *Time-resolved PL decay parameters of the pure CdSe NPLs and corresponding composites.*[37]

Systems	$\tau_1^x (a_1)^y$ [ns]	$\tau_2^x (a_2)^y$ [ns]	$\tau_3^x (a_3)^y$ [ns]	<τ> [ns]
CdSe NPLs	0.5 (0.85)	2.9 (0.12)	16.2 (0.03)	1.2±0.23
CdSe-$CsPbBr_{1.5}I_{1.5}$	0.35 (0.91)	2.9 (0.07)	9.8 (0.02)	0.71±0.13
CdSe-$CsPbBrI_2$	0.30 (0.93)	1.9 (0.05)	8.7(0.02)	0.55±0.11
CdSe-$CsPbI_3$	0.26 (0.95)	1.3 (0.04)	7.1(0.01)	0.37±0.08

^{x}±4% and ^{y}±5%

The PL quenching and the shortening of the decay time of CdSe NPLs in the presence of $CsPbX_3$ NCs are definitely due to the energy or charge transfer (electron or hole transfer) process. Both steady-state and the decay time data confirm the dynamics quenching process. The band positions of perovskite NCs are measured by cyclic voltammetry (CV) measurements (Figure 6.5), consistent with previous results.[40] The band positions of CdSe NPLs are taken from earlier reports.[41] Figure 6.4C shows the energy level positions of CdSe NPLs with respect to all $CsPbX_3$ NCs. The valence band (VB) position of all $CsPbX_3$ NCs lies below VB of CdSe NPLs, which rules out the possibility of hole transfer from photoexcited NPLs to $CsPbX_3$ NCs. On the other hand, the conduction band (CB) position for all three $CsPbX_3$ NCs is lower than the CB of CdSe NPLs, indicating that the electron or energy transfer process is thermodynamically feasible.

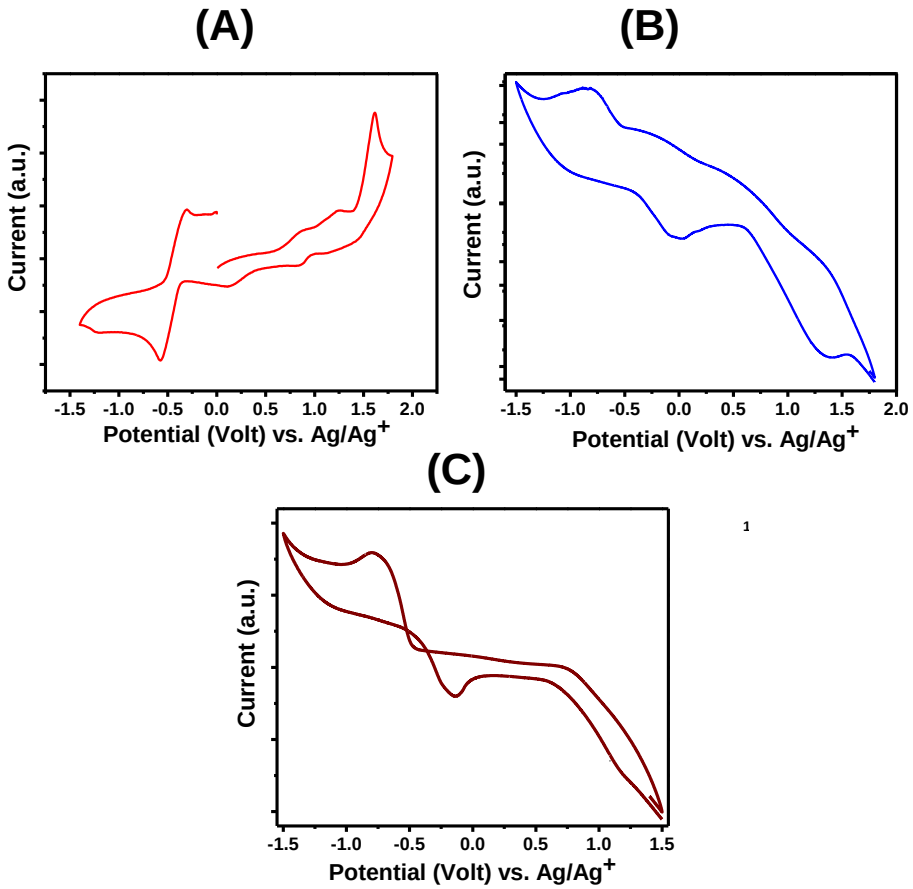

Figure 6.5. *Cyclic voltammetric (CV) curves of (A) $CsPbBr_{1.5}I_{1.5}$, (B) $CsPbBrI_2$ and (C) $CsPbI_3$ NCs with respect to Ag/Ag+ electrodes.[37] Reproduced with permission from reference 37 (Copyright 2020 American Chemical Society).*

The spectral overlap between the emission band of CdSe NPLs and the absorption spectra of all $CsPbX_3$ NCs indicates the possibility of an energy transfer process. We measured the decay times of $CsPbBr_{1.5}I_{1.5}$, $CsPbBrI_2$ and $CsPbI_3$ NCs in absence and presence of CdSe NPLs (Figure 6.6). Analysis suggests that PL quenching in composites is not due to the energy transfer from CdSe NPLs (donor) to perovskite NCs (acceptor).

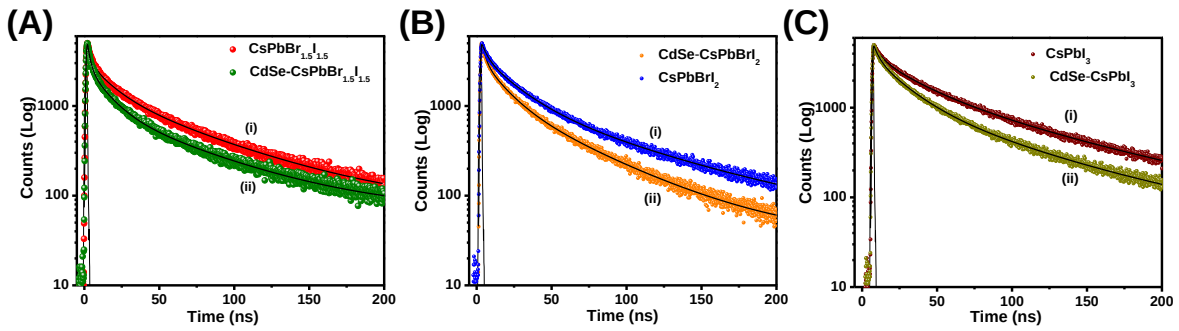

Figure 6.6. *PL decay traces of (A) $CsPbBr_{1.5}I_{1.5}$NCs (i), CdSe-$CsPbBr_{1.5}I_{1.5}$ (ii), (B) $CsPbBrI_2$ (i), CdSe-$CsPbBrI_2$ (ii) and (C) $CsPbI_3$ (i), CdSe-$CsPbI_3$ (ii) [λ_{ex} = 371 nm, λ_{em} = 580 nm for (A), 635 nm for (B) and 688 nm for (C)].*[37] *Reproduced with permission from reference 37 (Copyright 2020 American Chemical Society).*

6.2.3. Ultrafast fluorescence up-conversion spectroscopy

A femtosecond fluorescence up-conversion study has been carried out to understand the ultrafast dynamics of CdSe NPLs in the presence of perovskite NCs at 515 nm (PL maxima of CdSe NPLs), exciting the samples with 400 nm laser pulse. Figure 6.4D shows the up-conversion decay traces of CdSe NPLs in the absence and the presence of fixed concentration (10 nM) of perovskite NCs. The decay traces of pure CdSe NPLs is fitted bi-exponentially with time constants τ_1= 29.7±0.5 ps (56%) and τ_2= >100 ps (44%) (Table 6.2). In presence of $CsPbBr_{1.5}I_{1.5}$ NCs, the decay traces of CdSe NPLs is fitted with the time constants τ_1= 6.4±0.15 ps (36%), τ_2= 17.9±0.35 ps (46%) and τ_3= > 100 ps (16%).

Table 6.2. *Fluorescence up-conversion decay parameters of pure CdSe NPLs and corresponding composites with $CsPbX_3$ NCs.*[37]

Systems	τ_1 (a_1%) (ps)	τ_2 (a_2%) (ps)	τ_3 (a_3%) (ps)
Cdse NPLs	29.7 ± 0.5 (56%)	>100 (44%)	-
CdSe-$CsPbBr_{1.5}I_{1.5}$	6.4 ± 0.15 (36%)	17.9 ± 0.35 (46%)	>100 (18%)
CdSe-$CsPbBrI_2$	2.7± 0.1 (40%)	15.2 ± 0.26 (45%)	>100 (15%)
CdSe-$CsPbI_3$	1.6 ± 0.08 (48%)	12.3 ± 0.20 (40%)	>100 (12%)

For $CsPbBrI_2$ NCs, the time constants are τ_1= 2.7±0.1 ps (40%), τ_2= 15.2±0.26 ps (45%) and τ_3= >100 ps (15%), whereas τ_1= 1.6±0.08 ps (48%), τ_2= 12.3±0.20 ps (40%) and τ_3= >100 ps (12%) are found in case of $CsPbI_3$ NCs (Table 6.2). Analysis reveals that the fast component [6.4 ps for $CsPbBr_{1.5}I_{1.5}$, 2.7 ps for $CsPbBrI_2$, and 1.6 ps for $CsPbI_3$] is due to the ultrafast electron transfer process from CdSe NPLs to perovskite NCs which is eventually halide composition dependent.

6.2.4. Ultrafast Transient Absorption Spectroscopy

Furthermore, a femtosecond transient absorption (fs-TA) spectroscopic study is used to understand the charge carrier dynamics of both 2D CdSe NPLs and $CsPbX_3$ NCs. The samples are excited at 400 nm with very low fluence (< 5 μJ/cm^2) to eliminate multi-excitonic processes.

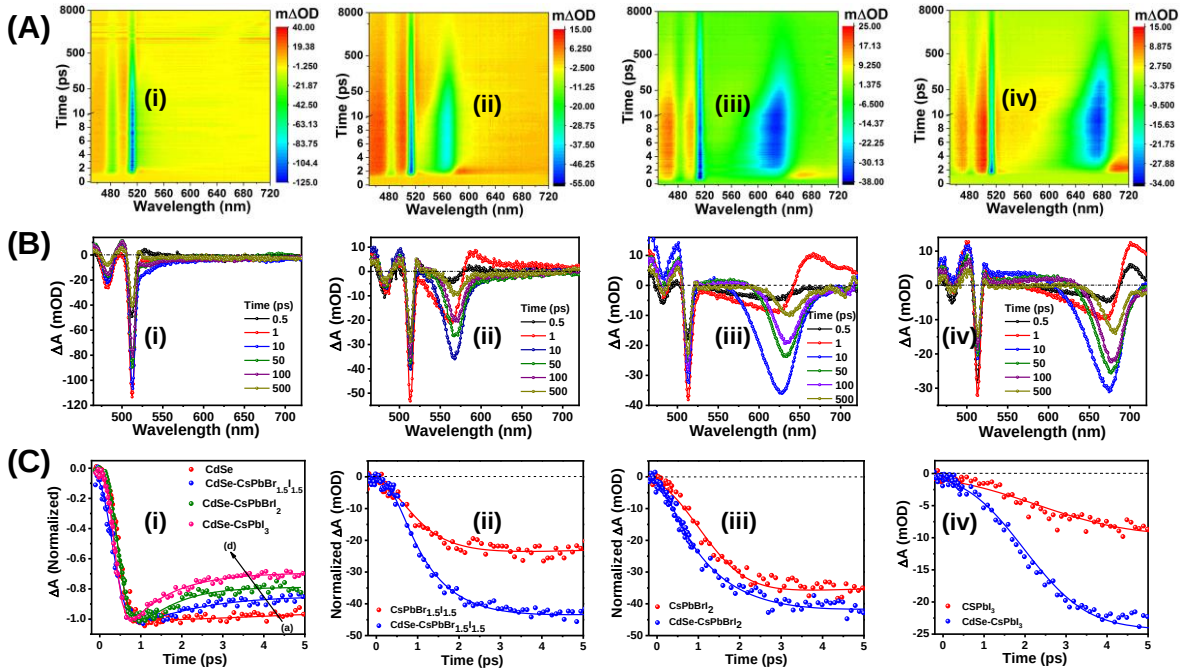

Figure 6.7. *(A) 2D heat map, (B) TA spectral profiles of (i) CdSe NPLs, (ii) CdSe-$CsPbBr_{1.5}I_{1.5}$, (iii)CdSe-$CsPbBrI_2$ and (iv) CdSe-$CsPbI_3$ composite and (C) TA dynamics of (i) CdSe NPLs (at 513 nm) [in absence of (a) and in presence of $CsPbBr_{1.5}I_{1.5}$ (b), $CsPbBrI_2$ (c), and $CsPbI_3$NCs (d)], (ii) $CsPbBr_{1.5}I_{1.5}$ at 569 nm, (iii) $CsPbBrI_2$ at 620 nm and (iv) $CsPbI_3$ at 678 nm, in absence and presence of CdSe NPLs. (λ_{ex}= 400 nm).*[37] *Reproduced with permission from reference 37 (Copyright 2020 American Chemical Society).*

Figure 6.7A (i-iv) shows the 2D heat map of TA data and Figure 6.7B (i-iv) shows TA spectral profiles of CdSe NPLs, CdSe-$CsPbBr_{1.5}I_{1.5}$, CdSe-$CsPbBrI_2$, and CdSe-$CsPbI_3$ composites, respectively. TA spectra of pure CdSe NPLs consist of two exciton bleach (EB)

at 482 nm and 513 nm correspond to the transition of the light hole (LH) and heavy hole (HH) to the conduction band, respectively. A weak photo-induced absorption (PIA) from 525-560 nm is observed at early delay times (1.5 ps) for CdSe NPLs. Figure 6.8 (A, B) shows the heat map and TA spectra of pure $CsPbX_3$ NCs with varying halide compositions. Here, the exciton bleach (EB) bands at 569 nm, 620 nm, and 678 nm are observed for $CsPbBr_{1.5}I_{1.5}$, $CsPbBrI_2$, and $CsPbI_3$ NCs, respectively; which are in good accordance with absorption spectra. A short-lived (3 ps) and long-lived (>300 ps) PIA are observed for all $CsPbX_3$ NCs, which is consistent with previous results.[35]

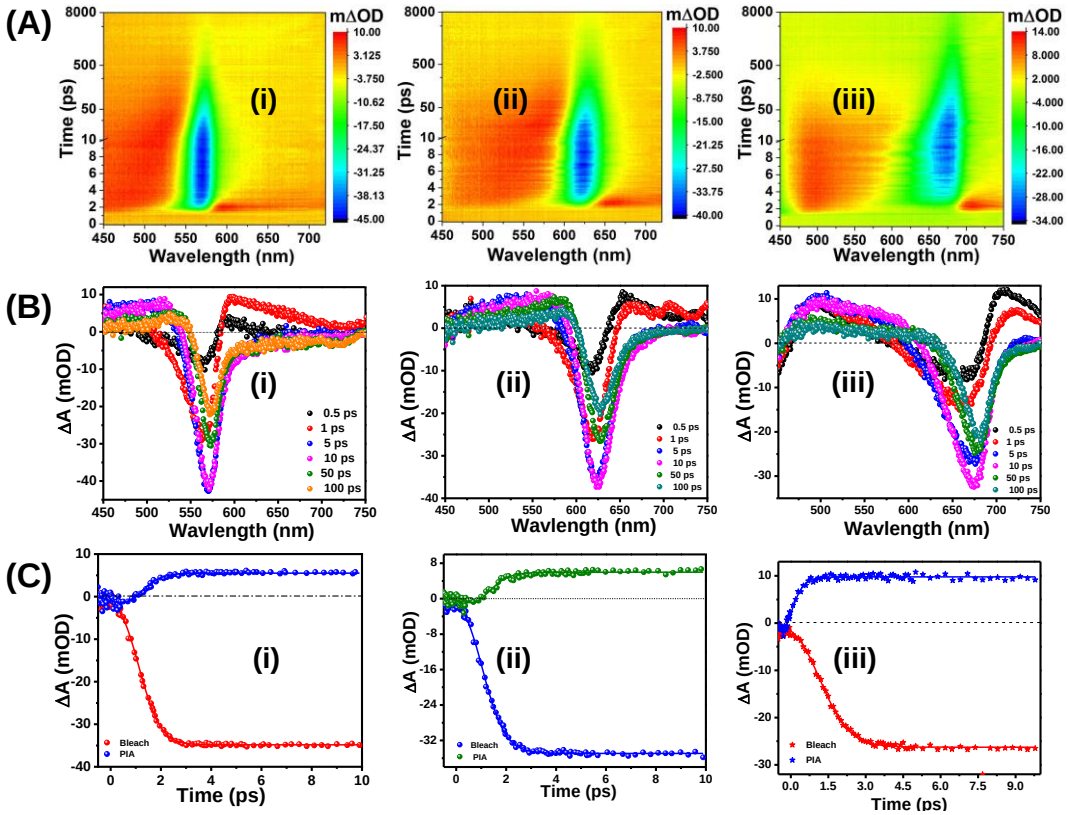

Figure 6.8. *(A) 2D heat map, (B) TA spectral profiles, and (C) TA dynamics (EB and PIA) of pure (i) $CsPbBr_{1.5}I_{1.5}$, (ii) $CsPbBrI_2$ and (iii) $CsPbI_3$ NCs.[37] Reproduced with permission from reference 37 (Copyright 2020 American Chemical Society).*

EB and PIA for both CdSe NPLs and perovskite NCs appear due to state filling and exciton-induced absorption, respectively.[36, 42] It is worth noting that EB of CdSe NPLs is dominated by state filling of electrons only (because of VB's lower effective electron mass and higher degeneracy). In contrast, both electrons and holes are responsible for EB of $CsPbX_3$ NCs due to comparable effective masses of electrons and holes.[43] TA spectra of CdSe-$CsPbX_3$ composites show additive, spectral features of CdSe NPLs and individual $CsPbX_3$ NCs

(Figures 6.7A, B). Interestingly, the bleaching amplitude of CdSe NPLs decreases. The bleach recovery kinetics of CdSe NPLs has fitted with time constants 9.3±0.2 ps (15%), 290±0.85 ps (40%), and >1 ns (45%) where the two shorter components and the longer components are due to the non-radiative trapping and radiative electron-hole recombination process, respectively (Table 6.3).[44] The bleach recovery kinetics for CdSe-$CsPbBr_{1.5}I_{1.5}$ composite are fitted with time constants of 3.8±0.15 ps (30%), 197±0.72 ps (31%) and >1 ns (39%), whereas 2.1±0.10 ps (41%), 179±0.55 ps (23%) and >1ns (36%) time constants are found for CdSe-$CsPbBrI_2$ (Table 6.3).

Table 6.3. *Fitted kinetics parameters of pure CdSe NPLs and CdSe-$CsPbX_3$ composites at 513 nm.*[37]

System	**τ_g (a_g%) (fs)**	**τ_1 (a_1%) (ps)**	**τ_2 (a_2%) (ps)**	**τ_3(a_3%) (ns)**
CdSe NPLs	800±0.5 (100%)	9.3 ± 0.2 (15%)	290±0.85 (40%)	>1(45%)
Cdse-$CsPbBr_{1.5}I_{1.5}$	<100 (100%)	3.8± 0.15 (30%)	197±0.72 (31%)	>1(39%)
CdSe-$CsPbBrI_2$	<100 (100%)	2.1± 0.10 (41%)	179±0.55 (23%)	>1(36%)
CdSe-$CsPbI_3$	<100 (100%)	1.4±0.10 (48%)	150±0.46 (19%)	>1(33%)

In case of CdSe-$CsPbI_3$, the bleach recovery kinetics is fitted with time constants 1.4±0.10 ps (48%), 150±0.46 ps (19%) and >1ns (33%). The shorter component (τ_1) becomes faster with increasing amplitude [from ~9.3 ps (15%) to ~1.4 ps (48%)] in composites which reflects the ultrafast electron transfer. Additionally, the amplitude reduction of the longer component (τ_3) suggests that electron-hole recombination decreases. We have monitored the growth dynamics of all $CsPbX_3$ NCs in the composites (at 569 for $CsPbBr_{1.5}I_{1.5}$, 620 for $CsPbBrI_2$, 678 nm for $CsPbI_3$). Figure 6.7C (ii-iv) compares growth kinetics between pure and composites at the corresponding bleach position of $CsPbX_3$ NCs. Figure 6.8C (i, ii, iii) represents the PIA decay profiles and EB growth time of all pure $CsPbX_3$ NCs. The measured growth times are 385± 0.5 fs (for $CsPbBr_{1.5}I_{1.5}$), 450 ± 0.4 fs ($CsPbBrI_2$) and 586± 0.8 fs (for $CsPbI_3$) which are consistent with previous reports.[35] It is to be noted that these growth times of perovskite NCs are associated with hot carrier relaxation. In composites, the hot carrier relaxation timescale are 770±0.6 fs, 1.1± 0.1 ps and 1.5 ±0.08 ps for $CsPbBr_{1.5}I_{1.5}$, $CsPbBrI_2$ and $CsPbI_3$, respectively. It is seen from the analysis that the growth time of $CsPbX_3$ NCs enhanced in CdSe-$CsPbX_3$ composites compared to pure $CsPbX_3$ NCs. The enhancement of

the growth time at the bleaching position for all $CsPbX_3$ NCs in the composites also supports the ultrafast electron transfer from CdSe NPLs to $CsPbX_3$ NCs. Thus, the shortening of the faster component of bleach recovery kinetics of CdSe NPLs and the enhancement of the growth time of $CsPbX_3$ NCs in composites confirm the ultrafast electron transfer from CdSe NPLs to $CsPbX_3$ NCs, which is dependent on halide compositions. The dynamics of photo-induced ultrafast electron transfer from the 2D quantum well (CdSe NPLs) to perovskite NCs with a variation of halide composition are illustrated in Scheme 6.1.

Scheme 6.1. *Schematic representation of photo-induced ultrafast electron transfer from CdSe NPLs to $CsPbX_3$ NCs with varying halide compositions*[37]

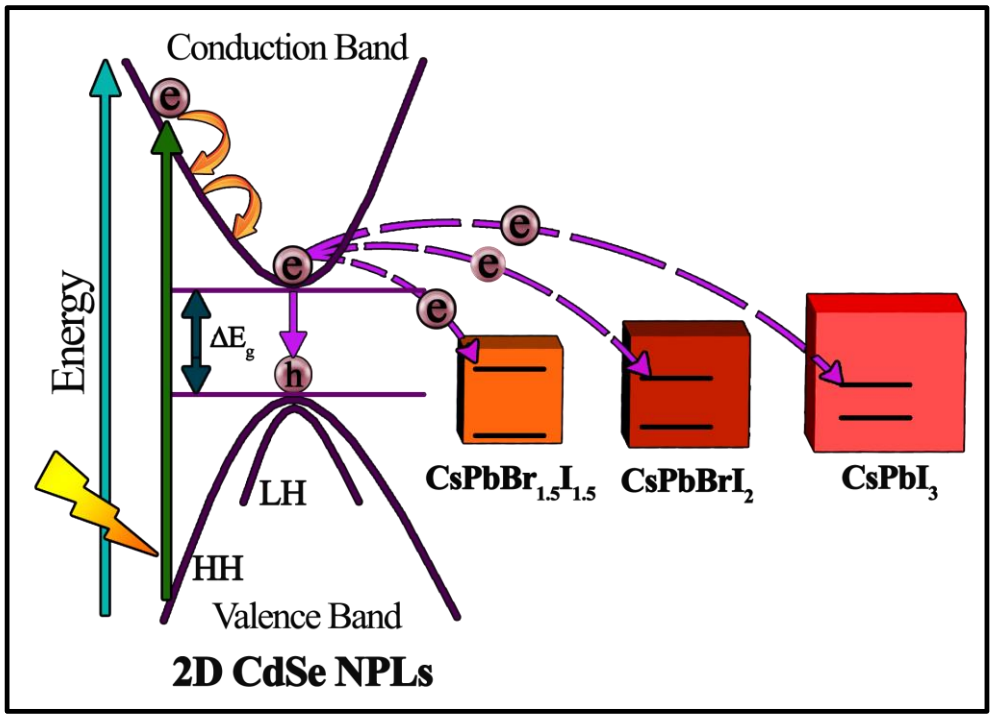

6.2.5. Photocurrent measurement

Finally, photocurrent measurement of the CdSe NPLs-perovskite composites devices under visible light illumination is investigated considering the efficient charge separation, an essential aspect for converting light into electricity. We have measured the photocurrent of the pure CdSe NPLs, pristine $CsPbX_3$ NCs, and CdSe-$CsPbX_3$ composites devices separately under one sun illumination at 100 mW cm^{-2} with a 300 W Newport Solar Simulator. Figure 6.9A shows the schematic representation of the device architecture which is fabricated by using the loading of 25 mg/ml sample with the thickness of ~100 nm. Figure 6.9B provides the mechanism of the fabricated devices. Based on the band alignment of the CdSe NPLs and perovskite NCs, the photoexcited electrons of the NPLs are promptly injected into the CB of

perovskite NCs then collected by the Al electrode. In contrast, holes of the NPLs are transported in the reverse direction towards the ITO electrode via PEDOT.PSS. The photo-response characteristics of devices are demonstrated in I-V analysis under dark and light by varying the scanning voltage up to 1.6 V.

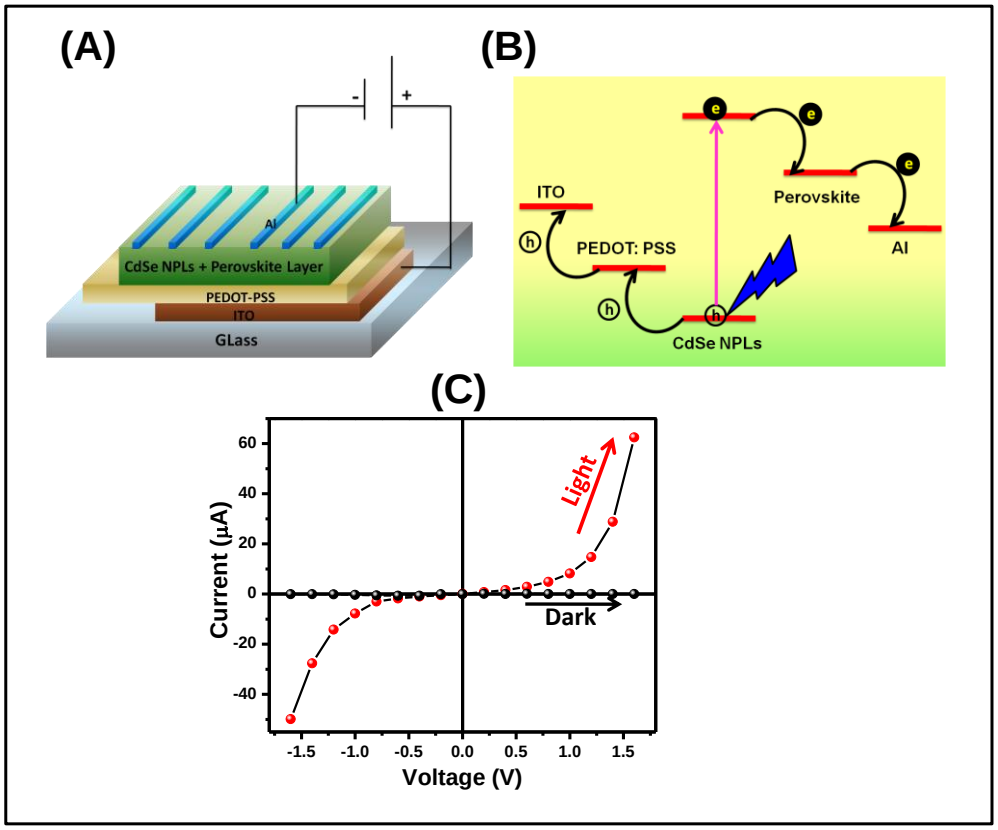

Figure 6.9. *(A) Schematic representation of device architecture, (B) schematic diagram of the charge separation mechanism of CdSe-perovskite composites at a fixed bias voltage of 1.6 V, (C) I-V characteristics curves CdSe-$CsPbI_3$ composite.*[37] *Reproduced with permission from reference 37 (Copyright 2020 American Chemical Society).*

The typical I-V characteristics of the pure CdSe NPLs are shown in Figure 6.10.

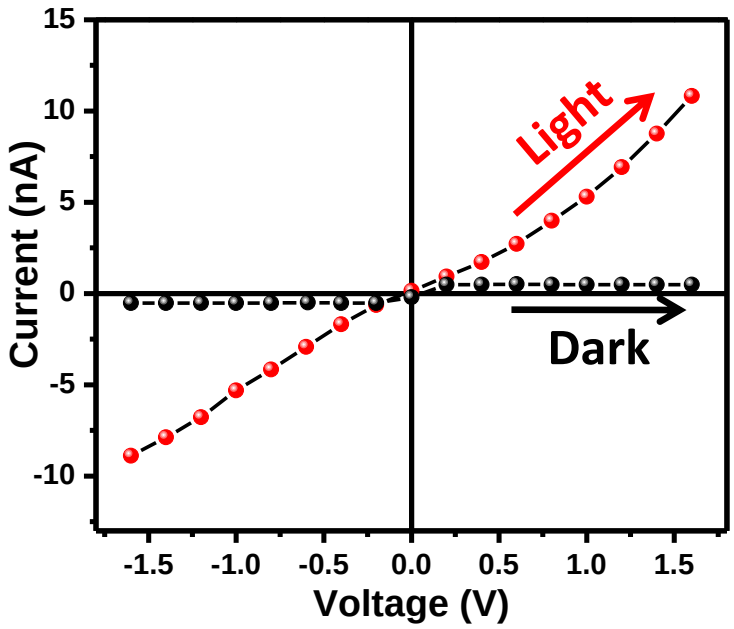

Figure 6.10. *I-V curves of pure CdSe NPLs.[37] Reproduced with permission from reference 37 (Copyright 2020 American Chemical Society).*

The obtained dark current and photocurrent of pure CdSe NPLs are 0.5 nA and 10 nA, respectively. We have received the ratio of I_L and I_D (I_L and I_D are the currents in the presence of light and the absence of light, respectively) is 21 times for pure CdSe NPLs. Figure 6.11 represents the I-V features of all three pristine $CsPbX_3$ NCs, and the measured ratio of I_L and I_D are 290 fold, 440 fold, and 930 fold for $CsPbBr_{1.5}I_{1.5}$, $CsPbBrI_2$, and $CsPbI_3$, respectively.

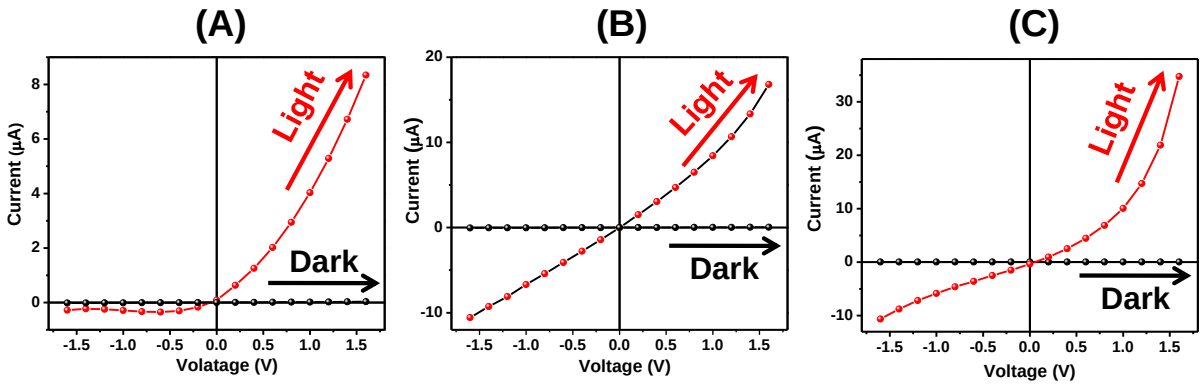

Figure 6.11. *I-V curves of pure (A) $CsPbBr_{1.5}I_{1.5}$ NCs, (B) $CsPbBrI_2$ NCs and (C) $CsPbI_3$ NCs.[37] Reproduced with permission from reference 37 (Copyright 2020 American Chemical Society).*

Figure 6.9C shows the I-V features of CdSe-$CsPbI_3$ composites and the corresponding I-V characteristics for CdSe-$CsPbBr_{1.5}I_{1.5}$, CdSe-$CsPbBrI_2$ are shown in Figure 6.12.

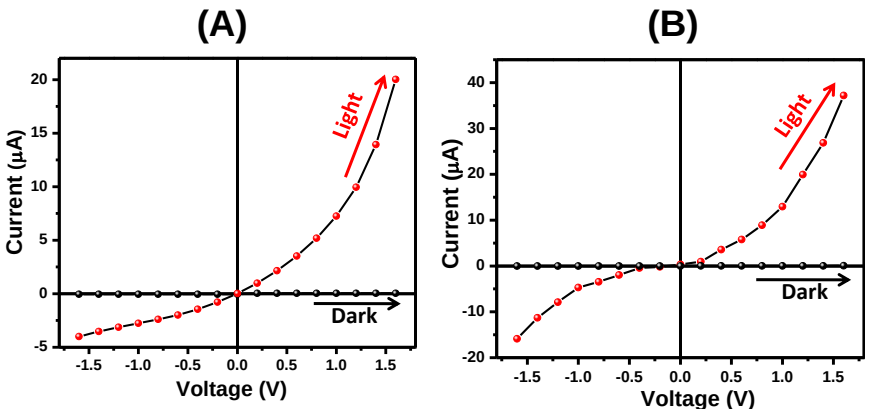

Figure 6.12. *I-V curves of composites (A) CdSe-$CsPbBr_{1.5}I_{1.5}$ and (B) CdSe-$CsPbBrI_2$.[37] Reproduced with permission from reference 37 (Copyright 2020 American Chemical Society).*

Interestingly, the resistor-type behavior of pure CdSe NPLs has been greatly influenced by changing the iodide compositions of the $CsPbX_3$ NCs under identical conditions. The measured ratio of I_L and I_D are 5 $\times 10^2$, 9 $\times 10^2$ and 1.5 $\times 10^3$ for the CdSe-$CsPbBr_{1.5}I_{1.5}$, CdSe-$CsPbBrI_2$ and CdSe-$CsPbI_3$ composites, respectively. Interestingly, all three heterostructures exhibit a greater IL and ID ratio than pure CdSe NPLs and pure $CsPbX_3$ NCs. Interestingly, the high dark current and photocurrent are 0.04 μA and 62.4 μA in the CdSe-$CsPbI_3$ composite. This improved photocurrent in the composites CdSe-$CsPbI_3$ confirms the efficient charge separation due to the ultrafast electron transfer process. The photocurrent of these composites CdSe NPLs-perovskite devices is better than that of the CdSe NPLs or perovskite only devices.

6.3. Conclusions

In summary, we have highlighted the influence of halide compositions on the ultrafast electron transfer rate in CdSe NPLs/$CsPbX_3$ composites. Time-resolved fluorescence up-conversion and absorption spectroscopic studies confirm the ultrafast electron transfer process from CdSe NPLs to perovskite NCs. The ultrafast electron transfer rate increases with increasing iodide compositions perovskite NCs. The shortening of faster components of bleach recovery kinetics of CdSe NPLs and the suppression of intra-band cooling rate of perovskite NCs is helpful for optoelectronic devices. Due to efficient charge separation, the maximum photocurrent to dark current is obtained for CdSe-$CsPbI_3$ composites. Our studies would help design highly efficient optoelectronic devices based on CdSe/perovskite composites.

6.4. References

(1) Novoselov, K. S.; Mishchenko, A.; Carvalho, A.; Castro Neto, A. H., 2D Materials and Van Der Waals Heterostructures. *Science* **2016**, *353*, aac9439.

(2) Fang, H.; Battaglia, C.; Carraro, C.; Nemsak, S.; Ozdol, B.; Kang, J. S.; Bechtel, H. A.; Desai, S. B.; Kronast, F.; Unal, A. A., et al., Strong Interlayer Coupling in Van Der Waals Heterostructures Built from Single-Layer Chalcogenides. *Proc. Natl. Acad. Sci. U.S.A.* **2014**, *111*, 6198-6202.

(3) Kundu, S.; Patra, A., Nanoscale Strategies for Light Harvesting. *Chem. Rev.* **2017**, *117*, 712-757.

(4) Pospischil, A.; Furchi, M. M.; Mueller, T., Solar-Energy Conversion and Light Emission in an Atomic Monolayer P–N Diode. *Nat. Nanotechnol.* **2014**, *9*, 257-261.

(5) Xing, G.; Mathews, N.; Lim, S. S.; Yantara, N.; Liu, X.; Sabba, D.; Grätzel, M.; Mhaisalkar, S.; Sum, T. C., Low-Temperature Solution-Processed Wavelength-Tunable Perovskites for Lasing. *Nat. Mater.* **2014**, *13*, 476-480.

(6) Ithurria, S.; Tessier, M. D.; Mahler, B.; Lobo, R. P. S. M.; Dubertret, B.; Efros, A. L., Colloidal Nanoplatelets with Two-Dimensional Electronic Structure. *Nat. Mater.* **2011**, *10*, 936-941.

(7) Delikanli, S.; Yu, G.; Yeltik, A.; Bose, S.; Erdem, T.; Yu, J.; Erdem, O.; Sharma, M.; Sharma, V. K.; Quliyeva, U., et al., Ultrathin Highly Luminescent Two-Monolayer Colloidal Cdse Nanoplatelets. *Adv. Funct. Mater.* **2019**, *29*, 1901028.

(8) Tessier, M. D.; Javaux, C.; Maksimovic, I.; Loriette, V.; Dubertret, B., Spectroscopy of Single Cdse Nanoplatelets. *ACS Nano* **2012**, *6*, 6751-6758.

(9) Guzelturk, B.; Erdem, O.; Olutas, M.; Kelestemur, Y.; Demir, H. V., Stacking in Colloidal Nanoplatelets: Tuning Excitonic Properties. *ACS Nano* **2014**, *8*, 12524-12533.

(10) Cassette, E.; Pedetti, S.; Mahler, B.; Ithurria, S.; Dubertret, B.; Scholes, G. D., Ultrafast Exciton Dynamics in 2D in-Plane Hetero-Nanostructures: Delocalization and Charge Transfer. *Phys. Chem. Chem. Phys.* **2017**, *19*, 8373-8379.

(11) Li, Q.; Zhao, F.; Qu, C.; Shang, Q.; Xu, Z.; Yu, L.; McBride, J. R.; Lian, T., Two-Dimensional Morphology Enhances Light-Driven H_2 Generation Efficiency in CdS Nanoplatelet-Pt Heterostructures. *J. Am. Chem. Soc.* **2018**, *140*, 11726-11734.

(12) Bera, R.; Kundu, S.; Patra, A., 2D Hybrid Nanostructure of Reduced Graphene Oxide–CdS Nanosheet for Enhanced Photocatalysis. *ACS Appl. Mater. Interfaces* **2015**, *7*, 13251-13259.

(13) Das, S.; Dutta, A.; Bera, R.; Patra, A., Ultrafast Carrier Dynamics in 2D–2D Hybrid Structures of Functionalized GO and CdSe Nanoplatelets. *Phys. Chem. Chem. Phys.* **2019**, *21*, 15568-15575.

(14) Sippel, P.; Albrecht, W.; van der Bok, J. C.; Van Dijk-Moes, R. J. A.; Hannappel, T.; Eichberger, R.; Vanmaekelbergh, D., Femtosecond Cooling of Hot Electrons in CdSe Quantum-Well Platelets. *Nano Lett.* **2015**, *15*, 2409-2416.

(15) Diroll, B. T.; Fedin, I.; Darancet, P.; Talapin, D. V.; Schaller, R. D., Surface-Area-Dependent Electron Transfer between Isoenergetic 2D Quantum Wells and a Molecular Acceptor. *J. Am. Chem. Soc.* **2016**, *138*, 11109-11112.

(16) Boulesbaa, A.; Wang, K.; Mahjouri-Samani, M.; Tian, M.; Puretzky, A. A.; Ivanov, I.; Rouleau, C. M.; Xiao, K.; Sumpter, B. G.; Geohegan, D. B., Ultrafast Charge Transfer and Hybrid Exciton Formation in 2D/0D Heterostructures. *J. Am. Chem. Soc.* **2016**, *138*, 14713-14719.

(17) Wang, L.; Chen, Z.; Liang, G.; Li, Y.; Lai, R.; Ding, T.; Wu, K., Observation of a Phonon Bottleneck in Copper-Doped Colloidal Quantum Dots. *Nat. Commun.* **2019**, *10*, 4532.

(18) Fu, J.; Xu, Q.; Han, G.; Wu, B.; Huan, C. H. A.; Leek, M. L.; Sum, T. C., Hot Carrier Cooling Mechanisms in Halide Perovskites. *Nat. Commun.* **2017**, *8*, 1300.

(19) Ross, R. T.; Nozik, A. J., Efficiency of Hot-Carrier Solar Energy Converters. *J. Appl. Phys.* **1982**, *53*, 3813-3818.

(20) Pelton, M.; Ithurria, S.; Schaller, R. D.; Dolzhnikov, D. S.; Talapin, D. V., Carrier Cooling in Colloidal Quantum Wells. *Nano Lett.* **2012**, *12*, 6158-6163.

(21) Stranks, S. D.; Eperon, G. E.; Grancini, G.; Menelaou, C.; Alcocer, M. J. P.; Leijtens, T.; Herz, L. M.; Petrozza, A.; Snaith, H. J., Electron-Hole Diffusion Lengths Exceeding 1 Micrometer in an Organometal Trihalide Perovskite Absorber. *Science* **2013**, *342*, 341-344.

(22) Snaith, H. J., Perovskites: The Emergence of a New Era for Low-Cost, High-Efficiency Solar Cells. *J. Phys. Chem. Lett.* **2013**, *4*, 3623-3630.

(23) Huang, H.; Bodnarchuk, M. I.; Kershaw, S. V.; Kovalenko, M. V.; Rogach, A. L., Lead Halide Perovskite Nanocrystals in the Research Spotlight: Stability and Defect Tolerance. *ACS Energy Lett.* **2017**, *2*, 2071-2083.

(24) De Roo, J.; Ibáñez, M.; Geiregat, P.; Nedelcu, G.; Walravens, W.; Maes, J.; Martins, J. C.; Van Driessche, I.; Kovalenko, M. V.; Hens, Z., Highly Dynamic Ligand Binding and Light Absorption Coefficient of Cesium Lead Bromide Perovskite Nanocrystals. *ACS Nano* **2016**, *10*, 2071-2081.

(25) Nenon, D. P.; Pressler, K.; Kang, J.; Koscher, B. A.; Olshansky, J. H.; Osowiecki, W. T.; Koc, M. A.; Wang, L.-W.; Alivisatos, A. P., Design Principles for Trap-Free $CsPbX_3$ Nanocrystals: Enumerating and Eliminating Surface Halide Vacancies with Softer Lewis Bases. *J. Am. Chem. Soc.* **2018**, *140*, 17760-17772.

(26) Wang, K.; Wang, S.; Xiao, S.; Song, Q., Recent Advances in Perovskite Micro- and Nanolasers. *Adv. Opt. Mater.* **2018**, *6*, 1800278.

(27) Zhang, N.; Fan, Y.; Wang, K.; Gu, Z.; Wang, Y.; Ge, L.; Xiao, S.; Song, Q., All-Optical Control of Lead Halide Perovskite Microlasers. *Nat. Commun.* **2019**, *10*, 1770.

(28) Xing, G.; Wu, B.; Wu, X.; Li, M.; Du, B.; Wei, Q.; Guo, J.; Yeow, E. K. L.; Sum, T. C.; Huang, W., Transcending the Slow Bimolecular Recombination in Lead-Halide Perovskites for Electroluminescence. *Nat. Commun.* **2017**, *8*, 14558.

(29) Yang, Z.; Janmohamed, A.; Lan, X.; García de Arquer, F. P.; Voznyy, O.; Yassitepe, E.; Kim, G.-H.; Ning, Z.; Gong, X.; Comin, R., et al., Colloidal Quantum Dot Photovoltaics Enhanced by Perovskite Shelling. *Nano Lett.* **2015**, *15*, 7539-7543.

(30) Ngo, T. T.; Mora-Seró, I., Interaction between Colloidal Quantum Dots and Halide Perovskites: Looking for Constructive Synergies. *J. Phys. Chem. Lett.* **2019**, *10*, 1099-1108.

(31) Zhang, C.; Lian, L.; Yang, Z.; Zhang, J.; Zhu, H., Quantum Confinement-Tunable Ultrafast Charge Transfer in a Pbs Quantum Dots/WSe_2 0D–2D Hybrid Structure: Transition from the Weak to Strong Coupling Regime. *J. Phys. Chem. Lett.* **2019**, *10*, 7665-7671.

(32) Ning, Z.; Gong, X.; Comin, R.; Walters, G.; Fan, F.; Voznyy, O.; Yassitepe, E.; Buin, A.; Hoogland, S.; Sargent, E. H., Quantum-Dot-in-Perovskite Solids. *Nature* **2015**, *523*, 324-328.

(33) Xing, G.; Kumar, M. H.; Chong, W. K.; Liu, X.; Cai, Y.; Ding, H.; Asta, M.; Grätzel, M.; Mhaisalkar, S.; Mathews, N., et al., Solution-Processed Tin-Based Perovskite for near-Infrared Lasing. *Adv. Mater.* **2016**, *28*, 8191-8196.

(34) Brumberg, A.; Diroll, B. T.; Nedelcu, G.; Sykes, M. E.; Liu, Y.; Harvey, S. M.; Wasielewski, M. R.; Kovalenko, M. V.; Schaller, R. D., Material Dimensionality Effects on Electron Transfer Rates between $CsPbBr_3$ and CdSe Nanoparticles. *Nano Lett.* **2018**, *18*, 4771-4776.

(35) Chung, H.; Jung, S. I.; Kim, H. J.; Cha, W.; Sim, E.; Kim, D.; Koh, W.-K.; Kim, J., Composition-Dependent Hot Carrier Relaxation Dynamics in Cesium Lead Halide ($CsPbX_3$, X=Br and I) Perovskite Nanocrystals. *Angew. Chem. Int. Ed.* **2017**, *56*, 4160-4164.

(36) Protesescu, L.; Yakunin, S.; Bodnarchuk, M. I.; Krieg, F.; Caputo, R.; Hendon, C. H.; Yang, R. X.; Walsh, A.; Kovalenko, M. V., Nanocrystals of Cesium Lead Halide Perovskites ($CsPbX_3$, X = Cl, Br, and I): Novel Optoelectronic Materials Showing Bright Emission with Wide Color Gamut. *Nano Lett.* **2015**, *15*, 3692-3696.

(37) Ghosh, G.; Dutta, A.; Ghosh, A.; Ghosh, S.; Patra, A., Ultrafast Carrier Dynamics in 2D CdSe Nanoplatelets–$CsPbX_3$ Composites: Influence of the Halide Composition. *J. Phys. Chem. C* **2020**, *124*, 10252-10260.

(38) Akkerman, Q. A.; D'Innocenzo, V.; Accornero, S.; Scarpellini, A.; Petrozza, A.; Prato, M.; Manna, L., Tuning the Optical Properties of Cesium Lead Halide Perovskite Nanocrystals by Anion Exchange Reactions. *J. Am. Chem. Soc.* **2015**, *137*, 10276-10281.

(39) Fitzmorris, B. C.; Cooper, J. K.; Edberg, J.; Gul, S.; Guo, J.; Zhang, J. Z., Synthesis and Structural, Optical, and Dynamic Properties of Core/Shell/Shell CdSe/ZnSe/ZnS Quantum Dots. *J. Phys. Chem. C* **2012**, *116*, 25065-25073.

(40) Tao, S.; Schmidt, I.; Brocks, G.; Jiang, J.; Tranca, I.; Meerholz, K.; Olthof, S., Absolute Energy Level Positions in Tin- and Lead-Based Halide Perovskites. *Nat. Commun.* **2019**, *10*, 2560.

(41) Li, Q.; Lian, T., Area- and Thickness-Dependent Biexciton Auger Recombination in Colloidal CdSe Nanoplatelets: Breaking the "Universal Volume Scaling Law". *Nano Lett.* **2017**, *17*, 3152-3158.

(42) Wu, K.; Liang, G.; Shang, Q.; Ren, Y.; Kong, D.; Lian, T., Ultrafast Interfacial Electron and Hole Transfer from $CsPbBr_3$ Perovskite Quantum Dots. *J. Am. Chem. Soc.* **2015**, *137*, 12792-12795.

(43) Klimov, V. I., Optical Nonlinearities and Ultrafast Carrier Dynamics in Semiconductor Nanocrystals. *J. Phys. Chem. B* **2000**, *104*, 6112-6123.

(44) Kobayashi, Y.; Pan, L.; Tamai, N., Effects of Size and Capping Reagents on Biexciton Auger Recombination Dynamics of CdTe Quantum Dots. *J. Phys. Chem. C* **2009**, *113*, 11783-11789.

Chapter 7

Conclusion

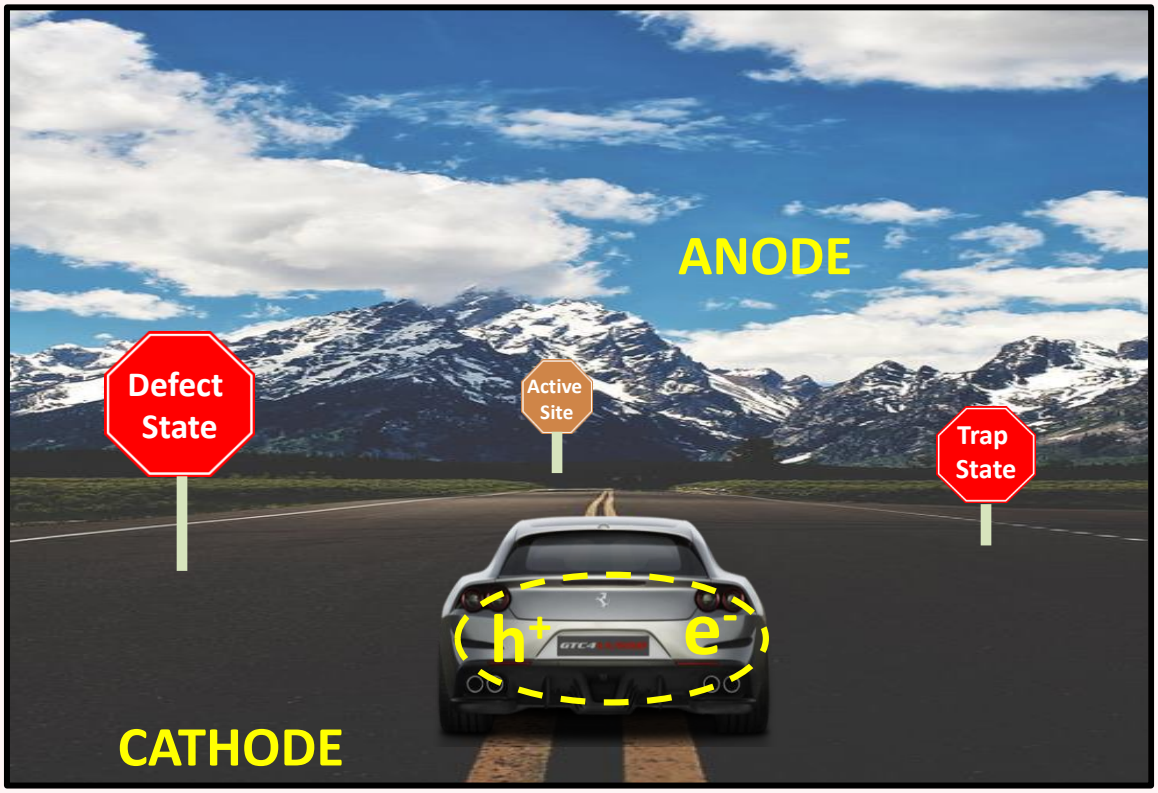

7.1. Summary of the thesis

Lead halide perovskite (LHP) NCs are the most demanding nanomaterials nowadays for optoelectronics and photovoltaics for their intriguing optical and electronic properties. Although the scientific community has witnessed a surge of research progress within a short period, there are many open questions and challenges to be addressed to move the field forward. Ultrafast spectroscopy is a valuable tool to investigate the photophysics of these novel materials, which will improve the scope of diverse applications. An overview of the recent advances of lead-based halide perovskite nanocrystals is presented in this thesis. Herein, we have addressed (a) how the shape of the LHP NCs influence the photophysics, (b) efficient hot hole extraction using suitable molecules, (c) slow down the hot carrier (HC) cooling rate, and (d) controlling the electron transfer in a heterostructure with 2D CdSe with varying the composition. The ultrafast spectroscopic method is being used to understand these fundamental processes.

The most important findings are summarized below:

- We highlight the influence of the shape of $CsPbBr_3$ NCs on carrier relaxation dynamics. Structural transformation from cubic shape to rod shape is achieved by changing the solvent from toluene to DCM. We have analyzed the detailed crystal phase by Rietveld method. A drastic increase in lifetime from 5.6 ns to 14.3 ns) is obtained by changing the toluene solvent to DCM. Furthermore, the global target kinetics model is employed to investigate individual excited state species (i.e. species associated difference spectra, SADS). Our analysis reveals that trap states play a vital role in the carrier relaxation dynamics of cubic and rod-shaped NCs. The lifetime of deep trap (DT) states changed drastically from 163 ps to 303 ps, respectively, changing the solvent from toluene to DCM. We believe that this solvent polarity-dependent tuning of morphology and the subsequent change in photophysical properties of $CsPbBr_3$ NCs may be beneficial for designing efficient light-harvesting systems.

- Furthermore, we have studied the hot hole transfer dynamics from $CsPbBr_3$ NCs to surface-attached porphyrin molecules by a combination of ultrafast transient absorption and fluorescence up-conversion spectroscopy. The drastic change of the initial carrier temperature of $CsPbBr_3$ NCs in the presence of porphyrin molecules confirms the efficient transfer of hot holes from $CsPbBr_3$ NCs to TpyP molecules. The

maximum hot hole transfer efficiency is 42% at 370 nm excitation. The experimental findings have been well supported by DFT analysis. As the hot holes are localized around the top surface of the perovskite, they can be easily extracted from the $CsPbBr_3$ by TpyP molecules compared to the hot electrons. These findings offer the possibility of utilizing porphyrin molecules as an alternative source of the hole-extracting molecule for optoelectronic devices.

- We have found a strategy to slow down the HC cooling rate of $CsPbBr_3$ perovskite NCs at a low carrier density of 10^{17} cm^{-3} in the presence of PbSe. A deep understanding of ultrafast HC cooling dynamics of metal halide perovskite is reported using ultrafast transient absorption spectroscopy, carrier-phonon scattering model, and the first-principles calculations. We have found two times slower HC relaxation (from 770 fs to 1.4 ps) and much higher initial HC temperature, T_C (1663 K, compared to 900 K) for the heterostructure compared to pure $CsPbBr_3$ at 3.64 eV excitation, under 1.86×10^{17} cm^{-3} carrier density. In addition, the fitting of HC energy loss rate in an electron- LO phonon coupling model suggests a much slower decay time of LO phonon through the Klemens channel after heterostructure formation. The first-principle calculation confirms a large energy gap between the LO and LA phonon modes in the heterostructure due to the localization of charge density near the heterojunction, which leads to retardation of HC cooling. Our findings will help design efficient HC solar cells.

- Finally, we have successfully prepared a hybrid of 2D CdSe/$CsPbX_3$ by varying halide compositions for solar light harvesting. Time-resolved fluorescence up-conversion and absorption spectroscopic studies confirm the ultrafast electron transfer process from CdSe NPLs to perovskite NCs and ultrafast electron transfer rate increases with increasing iodide compositions of perovskite NCs. The shortening of faster component of bleach recovery kinetics of CdSe NPLs in the presence of $CsPbX_3$ NCs and the suppression of intra-band cooling rate of perovskite NCs in the presence of CdSe NPLs would be beneficial for designing efficient optoelectronic devices. The maximum ratio of photocurrent to dark current is obtained for CdSe-$CsPbI_3$composites due to efficient charge separation. Further persuasive investigations on CdSe/perovskite composites can offer exciting opportunities for device technologies to provide a platform for solar light harvesting.

In summary, we have studied the excited-state dynamics, charge separation, and relaxation process of perovskite nanocrystals in detail with the help of state-of-the-art ultrafast spectroscopy. The emergence of semiconducting lead halide perovskite NCs in materials science is advantageous for the prospect of next-generation optoelectronic devices and many other potential applications.

7.2. Scope for the future work

The recent emergence of lead halide perovskite NCs is rapidly growing owing to their outstanding advantages such as extraordinary absorption coefficients, narrow full width at half maximum (FWHM), high photoluminescence quantum yield (PLQY), defect tolerant nature, and color tunability. Although tremendous research efforts have been made within the last few years, there are still several unanswered questions regarding their defect tolerant nature, characteristics of dark excitons, and slow hot carrier cooling properties. The essential concerns which need immediate research attention are the following:

- The harnessing of singlet fission from perovskite nanocrystals is a growing field of research to sensitize photochemical reactions. Furthermore, the generation of triplet exciton from the singlet fission with changing the size and different morphologies of perovskite nanomaterials remains a challenge to the scientific community. In addition, the metal halide perovskites as triplet sensitizers has generated new possibilities in optoelectronic application, and fundamental understanding of the sensitization of long-lived molecular triplets is required.
- Perovskite NCs show considerably retarded hot carrier (HC) cooling properties than other conventional semiconductors NCs. These unique properties provide strong motivation and guidance for prototype perovskite hot carrier solar cells (HCSCs). However, the HC cooling rate would be slowed down to realize practical perovskite-based HCSCs. Perovskite NCs with Ruddlesden– Popper perovskite quantum wells (QW) having low thermal conductivity, internal self-charge carrier separation, and reduced charge recombination rate would be beneficial. Furthermore, the HC cooling dynamics can be modulation by tuning the organic cations (e.g., PEA^+ = phenethylammonium, BA^+=benzylammonium, and $CHMA^+$ = cyclohexylammonium) between the inorganic lattices to vary the dielectric constants, carrier–carrier, and carrier phonon interactions, etc.

- Recently, 2D layered organic-inorganic hybrid perovskite consisting of long-chain or functionalized organic cations have been gained significant attention. This interlayer energy exchange can be leveraged for unique molecular photophysics, particularly sensitized phosphorescence. We believe that gaining control over interlayer energy exchange will ultimately open the door to many exciting new functions and applications.

- The toxicity of lead-based perovskite NCs is a severe concern for environmental sustainability. In this concern, several lead-free perovskite materials have been developed, including bismuth and tin-based perovskite, double perovskite, etc. These lead-free perovskite nanomaterials can be adapted as photocatalysts for visible-light-driven hydrogen production. Thus, designing hybrid nanostructures could pave us to increase the yield of hydrogen fuel. Furthermore, perovskite NCs can also be used as an efficient photocatalyst for CO_2 reduction.

- Furthermore, doping of various metal ions into the perovskite crystals is an intriguing research area for the modulation of optical and electronic properties. Despite significant progress into the doping of perovskite NCs, several transitions and inner transition metals remain unexplored. Additionally, while B-site doping is largely explored, the progress of A-site doping is significantly less. Most importantly, the exact location of the dopant is still unexplored.

7.3. List of publications

Publications Included in this Thesis

(1) *"Influence of shape on the carrier relaxation dynamics of $CsPbBr_3$ perovskite nanocrystals"* **Goutam Ghosh**, Bikash Jana, Sumanta Sain, and Amitava Patra*, ***Phys. Chem. Chem. Phys.***, **2019**, 21, 19318-19326**.**

(2) *"Hot Hole Cooling and Transfer Dynamics from Lead Halide Perovskite Nanocrystals Using Porphyrin Molecules"* **Goutam Ghosh**, Kritiman Marjit, Srijon Ghosh, Arnab Ghosh, Raihan Ahammed, Abir De Sarkar and Amitava Patra, ***J. Phys. Chem. C*** **2021**, 125, 10, 5859–5869.

(3) *"Revealing Slow Hot Carrier Cooling Dynamics of $CsPbBr_3$/PbSe Heterostructure at Low Carrier Density"* **Goutam Ghosh**, Raju K Biswas, Kritiman Marjit, Srijon Ghosh, Arnab Ghosh, Swapan K Pati* and Amitava Patra* (***Manuscript under revision***).

(4) *"Ultrafast Carrier Dynamics in 2D CdSe Nanoplatelets–$CsPbX_3$ Composites: Influence of the Halide Composition"* **Goutam Ghosh**, Avisek Dutta, Arnab Ghosh, Srijon Ghosh and Amitava patra*, ***J. Phys. Chem. C*** **2020**, 124, 18, 10252–10260**.**

Other Co-authored Publications

(5) "*Global and target analysis of relaxation processes of the collapsed state of P3HT polymer nanoparticles*" Arnab Ghosh, Srijon Ghosh, **Goutam Ghosh** , Bikash Jana and Amitava Patra*, ***Phys. Chem. Chem. Phys***., **2020**, 22, 2229-2237.

(6) *"Revealing Complex Relaxation Processes of Collapsed Conjugated Polymer Nanoparticles in the Presence of Different Shapes of Gold Nanoparticles Using Global and Target Analysis"* Arnab Ghosh, Srijon Ghosh, **Goutam Ghosh** , Bikash Jana and Amitava Patra*, ***J. Phys. Chem. C 2020,*** 124, 48, 26165–26173.

(7) *"Structural Analysis and Carrier Relaxation Dynamics of 2D $CsPbBr_3$ Nanoplatelets"* Kritiman Marjit, **Goutam Ghosh**, Srijon Ghosh, Sumanta Sain, Arnab Ghosh and Amitava Patra*, ***J. Phys. Chem. C*** **2021**, 125, 22, 12214–12223.

(8) *"Implications of Relaxation Dynamics of Collapsed Conjugated Polymeric Nanoparticles for Light-Harvesting Applications"* Arnab Ghosh, Srijon Ghosh, **Goutam Ghosh**, and Amitava Patra*, ***Phys. Chem. Chem. Phys,*** **2021**, 23, 14549-14563.

(9) *"Deciphering the Relaxation Mechanism of Red-Emitting Carbon Dots Using Ultrafast Spectroscopy and Global Target Analysis"* Srijon Ghosh, Arnab Ghosh, **Goutam Ghosh**, Kritiman Marjit and Amitava Patra*, ***J. Phys. Chem. Lett.*** **2021**, 12, 33, 8080–8087.

(10) *"Effect of Heterovalent Bi^{3+} Dopping on the Carrier Relaxation Dynamics of $CsPbBr_3$ Nanocrystals"* Kritiman Marjit, **Goutam Ghosh**, Srijon Ghosh, and Amitava Patra* (***Manuscript under preparation***).

7.4. Paper presented in conferences

Presentations

(1) "*Ultrafast Dynamics in Perovskite Nanocrystals: Role of Trap States*" **Goutam Ghosh,** and Amitava Patra, **Poster** presented at ***"International Conference on Nano Science and Technology (ICONSAT-2020)"***, during 5th- 7th March, 2020.

(2) "*Ultrafast Photo-induced Processes in Perovskite Nanocrystals*" **Goutam Ghosh,** Srijon Ghosh, Arnab Ghosh and Amitava Patra, **Poster** presentation at ***ACS Spring 2020 National Meeting & Expo*** during 22th-26th March, 2020.

(https://doi.org/10.1021/scimeetings.0c02068)

(3) *"Influence of Shape of on the Carrier Relaxation Dynamics of Perovskite Nanocrystals"* **Goutam Ghosh,** and Amitava Patra, **Poster** presented at ***Materials Science Day, 2020 at Indian Association for the Cultivation of Science***.

(4) "*Hot Carrier Transfer Dynamics from Lead Halide Perovskite Nanocrystals Using Porphyrin Molecules*" **Goutam Ghosh**, Kritiman Marjit, Srijon Ghosh, Arnab Ghosh, Raihan Ahammed, Abir De Sarkar and Amitava Patra, **Poster** presented at ***the 7th Theme Meeting on Ultrafast Sciences 2021 (UFS-2021)***, during 12^{th} -13^{th} November, 2021.